

# **Stony Brook University**



OFFICIAL COPY

**The official electronic file of this thesis or dissertation is maintained by the University Libraries on behalf of The Graduate School at Stony Brook University.**

**© All Rights Reserved by Author.**

**Targeting the Enoyl-ACP Reductase in *Mycobacterium tuberculosis*: Mechanism of Time  
Dependent Inhibition and Cellular Consequence of Target Engagement**

A Dissertation Presented

by

**Weixuan Yu**

to

The Graduate School

in Partial Fulfillment of the

Requirements

for the Degree of

**Doctor of Philosophy**

In

**Chemistry**

Stony Brook University

**August 2015**

**Stony Brook University**

The Graduate School

**Weixuan Yu**

We, the dissertation committee for the above candidate for the  
Doctor of Philosophy degree, hereby recommend  
acceptance of this dissertation.

**Peter J. Tonge – Dissertation Advisor  
Professor of Chemistry Department**

**Elizabeth M. Boon - Chairperson of Defense  
Associate Professor of Chemistry Department**

**Jin Wang – Committee Member of Defense  
Associate Professor of Chemistry Department**

**Stephen G. Walker – External Committee Member of Defense  
Associate Professor of School of Dental Medicines, Stony Brook University**

This dissertation is accepted by the Graduate School

Charles Taber  
Dean of the Graduate School

Abstract of the Dissertation

**Targeting the enoyl-ACP reductase in *Mycobacterium tuberculosis*: Mechanism of Time  
Dependent Inhibition and Cellular Consequence of Target Engagement**

by

**Weixuan Yu**

**Doctor of Philosophy**

in

**Chemistry**

Stony Brook University

**2015**

Tuberculosis (TB) infection is the single most lethal bacterial infections in the world. Isoniazid (INH), one of the most effective anti-TB drugs is usually administered to treat latent TB infection and is used in combination therapy to treat active TB. However resistance to INH is common and the emergence of multi-drug-resistant, extensively drug-resistant and now totally drug-resistant strains of TB, has resulted in an urgent need to develop novel anti-TB drugs. INH targets InhA, the enoyl-ACP reductase (FabI) from the Type II fatty acid biosynthesis pathway, and resistance to INH usually results from mutations in KatG, the enzyme that activates INH. Thus compounds that target InhA directly should be active against drug-resistant TB.

Drug-target residence time has recently emerged as a crucial parameter for drug discovery since drugs with long residence times on their targets will have sustained target occupancy leading to improved pharmacodynamics and safety. However, the molecular basis of drug-target residence time is poorly understood. In addition, methods to quantitate the lifetime of drug-target



complexes are also lacking. This gap in knowledge hinders the rational design of inhibitors with improved residence times.

Utilizing InhA as our model system, we have developed a robust assay to accurately quantitate drug-target residence time. Using a combination of enzyme kinetics, computational modeling and X-ray crystallography, we have rigorously characterized the structure-kinetic relationships for 24 diphenyl ether-based InhA inhibitors, and have investigated the mechanism of time-dependent enzyme inhibition at the molecular level. This has led to the development of a 2-step slow-onset inhibition model in which the InhA substrate-binding loop (SBL) undergoes an “open-to-closed” conformational change on the binding reaction coordinate. Site-directed mutagenesis suggests that the energy barrier associated with slow-onset inhibition results from a large-scale refolding of the SBL. Based on this finding, we have successfully designed a novel InhA inhibitor (PT504) with a 10-fold longer residence time compared to INH. Cellular studies suggest that PT504 is active against *Mycobacterium tuberculosis* and that the long residence time can be translated into a prolonged post-antibiotic effect. Further studies using a fragment-based approach together with phenotypic screening, have led to the identification of 3 different classes of InhA inhibitors with unique inhibition mechanisms, thus diversifying the current InhA drug candidate portfolio.

## Table of Contents

|  |    |
|--|----|
| <b>Chapter 1 Current therapeutics for tuberculosis control and the fatty acid biosynthesis FAS-II pathway as novel drug target</b> .....                 | 1  |
| Tuberculosis infection – demographic .....   | 1  |
| Frontline treatment and potential problems.....  | 3  |
| Novel drug candidate discovery and repurposed drugs.....   | 5  |
| Bacterial cell wall – fatty acid biosynthesis as drug target.....  | 10 |
| Inhibitors of FabI.....  | 13 |
| Time-dependent inhibition - mechanism, examples, target vulnerability .....  | 19 |
| Project overview .....   | 22 |
| <b>Chapter 2 Development of kinetic tools to study slow binding inhibitors for enoyl-ACP reductase in <i>Mycobacterium tuberculosis</i> (InhA)</b> ..... | 23 |
| INTRODUCTION .....   | 23 |
| MATERIALS and METHODS .....  | 28 |
| FabI protein preparation: .....  | 28 |
| Substrate synthesis: .....   | 28 |
| Inhibitor synthesis: .....   | 30 |
| [ <sup>32</sup> P]-Direct dissociation kinetics: .....   | 30 |
| Inhibitor progress curve analysis: .....   | 31 |
| Correlating the ternary complex concentration as function of time.....   | 32 |
| RESULTS AND DISCUSSION.....  | 34 |
| The [ <sup>32</sup> P]-Direct dissociation method.....   | 34 |
| Determination of drug-target residence time using the direct dissociation method and progress curve analysis.....  | 39 |
| Measuring residence time under physiological temperature is feasible by this method  | 48 |
| Recovery of ternary complex correlates with the inhibitor dissociation rate constant ..  | 49 |

|   |           |
|---|-----------|
| Direct dissociation method together with the conventional steady-state kinetics is able to cover a wide range for residence time measurement .....                    | 53        |
| Advantages and disadvantages of direct dissociation method .....  | 54        |
| CONCLUSION .....  | 58        |
| <b>Chapter 3 Unraveling the slow onset inhibition of InhA, the enoyl ACP reductase from <i>Mycobacterium tuberculosis</i>: Mechanism and inhibitor design .....</b>   | <b>59</b> |
| INTRODUCTION .....  | 59        |
| MATERIALS AND METHOD.....   | 64        |
| InhA purification: .....  | 64        |
| Progress curve analysis: .....  | 64        |
| [ <sup>32</sup> P]-NAD <sup>+</sup> direct dissociation kinetics: .....   | 66        |
| Substrate synthesis: .....  | 67        |
| Compound synthesis: .....   | 67        |
| Crystallization and structure determination of InhA ternary complexes with PT504, PT506, PT512 and PT514: .....   | 71        |
| Kinetic model: .....  | 72        |
| Arrhenius analysis: .....   | 73        |
| Eyring analysis: .....  | 74        |
| Site-directed mutagenesis, expression and purification of InhA mutants: .....   | 74        |
| Thermofluor experiments: .....  | 75        |
| RESULTS and DISCUSSION .....  | 76        |
| A comprehensive kinetic model for the InhA system suggests that the release of NAD <sup>+</sup> (k <sub>off, NAD<sup>+</sup></sub> ) is partially rate limiting ..... | 76        |
| Diphenyl ether inhibitors bind to the binary E-NAD <sup>+</sup> complex generated through enzyme catalysis and follow a two-step induced fit mechanism .....          | 77        |
| Structure-activity relationship for the 2' substituents suggests that the 2'-chloro group enhances residence time by improving binding affinity .....                 | 79        |

|  |            |
|--|------------|
| 5-Triazole substituents increase the residence time by a slower overall association rate .....   | 86         |
| The 5-triazole substituents decrease the overall onset rate constant by increasing the ground state energy of E-I. The onset rate constants of the slow binding step ( $k_2$ ) are essentially identical among diphenyl ether inhibitors .....   | 88         |
| Rational design of PT504 – A novel compound with 10 hours residence time .....   | 89         |
| Structure insight on the 2' substituents .....   | 91         |
| Comparison of PT506 and PT119 – the triazole greatly aids the interaction with the SBL .....   | 94         |
| Crystal structure of PT504 .....   | 98         |
| Comparison of PT506, PT504, PT512, PT514 PT91 and PT119 – hydrogen bond formation between Q214 and triazole ring reveals an energetically elevated intermediate state captured by 5-bulky substituent, yet the entropically-favored inward conformation of I215 represented the final ground state ..... | 101        |
| The energy barrier is predominantly from enthalpic contributions for the 5-alkyl substituents, while entropic contributions increased for the 5-triazole substituents ....   | 110        |
| The slow association barrier mainly derives from large scale refolding of $\alpha$ -helix 6: evidence from V203A, I215A, L207A InhA .....  | 115        |
| Hypothesis on the slow binding mechanism for diphenyl ether series .....   | 118        |
| The energy barrier – structural and kinetic insight .....  | 120        |
| CONCLUSION .....   | 125        |
| <b>Chapter 4 Cellular Activity of Diphenyl Ether InhA Inhibitors – Killing Kinetics and Post Antibiotic Effect .....</b>   | <b>126</b> |
| INTRODUCTION .....   | 126        |
| MATERIALS AND METHODS .....  | 129        |
| Compounds .....  | 129        |
| Bacterial strains .....  | 129        |
| MIC measurement .....  | 129        |
| Killing-kinetics .....   | 130        |

|   |     |
|---|-----|
| Post antibiotic effect (PAE).....   | 130 |
| Theoretical maximum killing rate calculation .....  | 131 |
| RESULTS AND DISCUSSION.....   | 133 |
| Diphenyl ether inhibitors are active against both <i>M. smeg</i> and <i>M. tb</i> .....   | 133 |
| Killing kinetics revealed that a slower association rate constant could be translated into a slower killing rate .....  | 133 |
| Theoretical maximum killing rate and lag-phase calculation .....  | 139 |
| Post antibiotic effect and residence time.....  | 144 |
| Theoretical target engagement .....   | 147 |
| CONCLUSION .....  | 148 |
| <b>Chapter 5 InhA inhibitor discovery: novel fragment-hits and scaffolds</b> .....  | 149 |
| INTRODUCTION .....  | 149 |
| MATERIALS AND METHODS .....   | 156 |
| Discovery of novel fragment-sized inhibitors of InhA using virtual screening .....  | 156 |
| Discovery of 4-hydroxy-2-pyridone InhA inhibitors using whole-cell high-throughput profiling.....   | 160 |
| RESULTS AND DISCUSSION.....   | 163 |
| Discovery of novel fragment-sized inhibitors of InhA using virtual screening.....   | 163 |
| Discovery of 4-hydroxy-2-pyridones using microbiological profiling .....  | 187 |
| CONCLUSIONS .....   | 197 |
| <b>Chapter 6 MUT056399 and <i>p</i>-Fluoro Diphenyl Ethers: Slow Binding Inhibitors of the Enoyl-ACP Reductase FabI from <i>Burkholderia pseudomallei</i></b> ..... | 198 |
| INTRODUCTION .....  | 198 |
| MATERIALS AND METHODS .....   | 205 |
| Materials.....  | 205 |
| Expression and purification of <i>Bp</i> FabI.....  | 205 |

|  |     |
|--|-----|
| Synthesis of substrates .....  | 205 |
| Synthesis of diphenyl ethers.....  | 206 |
| Thermal shift assay.....   | 207 |
| Preincubation inhibition assay .....   | 208 |
| Progress curve analysis .....  | 209 |
| Direct dissociation assay .....  | 211 |
| Minimum inhibitory concentration determination .....   | 211 |
| Evaluation of efficacy in acute <i>B. pseudomallei</i> mouse model of infection .....  | 212 |
| RESULTS AND DISCUSSION.....  | 214 |
| Mutabilis compound, MUT056399, is a slow-onset inhibitor of BpFabI that follows one-step binding mechanism.....  | 214 |
| The <i>p</i> -fluorine introduction may destabilize the transition state and ground state. ....  | 220 |
| <p><i>p</i>-Fluoro diphenyl ethers' B-ring substituents may affect ground and/or transition states. ....</p> .....   | 220 |
| <p><i>p</i>-Fluoro diphenyl ethers form an E-NAD<sup>+</sup>-I complex with NAD<sup>+</sup> generated from catalysis and exogenous NAD<sup>+</sup>. ....</p> ..... | 225 |
| Structural insights of PT404 in complex with BpFabI.....   | 227 |
| <i>In vivo</i> efficacy of PT405 .....   | 230 |
| CONCLUSION .....   | 232 |
| <b>Bibliography</b> .....  | 233 |
| Chapter 1.....   | 233 |
| Chapter 2.....   | 242 |
| Chapter 3.....   | 247 |
| Chapter 4.....   | 251 |
| Chapter 5.....   | 253 |
| Chapter 6.....   | 268 |

## List of Figures

|  |    |
|--|----|
| Figure 1.1 First-line antituberculosis drugs .....   | 2  |
| Figure 1.2 Selected Second-line antituberculosis drugs .....   | 3  |
| Figure 1.3 Activation of INH by KatG .....   | 5  |
| Figure 1.4 Current global pipeline of new tuberculosis drugs.....  | 8  |
| Figure 1.5 Site of action of different antituberculosis drug candidates .....  | 9  |
| Figure 1.6 Repurposed drugs for tuberculosis treatment.....  | 10 |
| Figure 1.7 Bacteria Type II fatty acid biosynthesis pathway.....   | 12 |
| Figure 1.8 Structure of InhA in complex with INH-NAD adduct .....  | 13 |
| Figure 1.9 Structure of <i>E. coli</i> FabI in complex with diazaborine-NAD <sup>+</sup> adduct .....  | 14 |
| Figure 1.10 Structure of <i>E. coli</i> FabI in complex with Triclosan .....   | 15 |
| Figure 1.11 Novel InhA inhibitors.....   | 17 |
| Figure 1.12 Structure of InhA in complex with pyridomycin .....  | 18 |
| Figure 1.13 $k_{obs}$ as a function of inhibitor concentration .....   | 21 |
| Figure 2.1 The FabI inhibitor dissociation scheme.....   | 26 |
| Figure 2.2 MS spectrum of trans-2-octenoyl coenzyme A .....  | 29 |
| Figure 2.3 The [ <sup>32</sup> P]-NAD <sup>+</sup> direct dissociation method.....   | 36 |
| Figure 2.4 Method validation.....  | 38 |
| Figure 2.5 Comparison of residence times generated by the progress curve analysis and the <sup>32</sup> P-NAD <sup>+</sup> direct dissociation method for inhibitors with residence times under 100 min..... | 40 |
| Figure 2.6 Examples where progress curve analysis cannot accurately determine $k_{off}$ .....  | 47 |

|   |     |
|---|-----|
| Figure 2.7 Comparison of $k_{\text{off}}$ values determined at 25 °C and 37 °C for inhibitors bound to <i>E. coli</i> FabI .....          | 49  |
| Figure 2.8 High throughput screening to identify slow off-rate inhibitors.....  | 52  |
| Figure 2.9 Relative timescales of methods to determine $k_{\text{off}}$ .....   | 54  |
| Figure 2.10 Comparison of approaches to directly measure ligand dissociation .....  | 57  |
| Figure 3.1 The Type II fatty acid biosynthesis pathway in <i>M. tuberculosis</i> .....  | 62  |
| Figure 3.2 InhA catalysis and inhibition kinetic model.....   | 76  |
| Figure 3.3 Comparison of progress curves under different concentrations of exogenous $\text{NAD}^+$ .....                                 | 79  |
| Figure 3.4 Overlay of experimental and simulated progress curve analyses.....   | 80  |
| Figure 3.5 A double logarithmic plot of thermodynamic and kinetic constants for 2'-substituents .....                                     | 86  |
| Figure 3.6 The relative energy level of four different diphenyl ethers on the same reaction coordinate.....                               | 90  |
| Figure 3.7 The $^{32}\text{-P}$ $\text{NAD}^+$ dissociation kinetics of PT504.....  | 91  |
| Figure 3.8 Orientation of different 2'-substituents relative to amino acids G96 and A198 within the substrate-binding pocket of InhA..... | 93  |
| Figure 3.9 The dynamic nature of interactions between InhA and PT504/PT506 .....  | 96  |
| Figure 3.10 Comparison of amino acids A201 – V203 of the SBL's $\alpha$ -helix 6.....   | 97  |
| Figure 3.11 InhA tetramer with bound cofactor and PT504.....  | 100 |
| Figure 3.12 Hydrophobic environment of the B-ring of PT504 within the substrate-binding pocket of InhA .....                              | 101 |
| Figure 3.13 Extraordinary conformation of the loop region between $\alpha$ -helices 6 and 7 .....   | 103 |
| Figure 3.14 Position of Q214 and I215 of InhA-PT512/PT514 complex.....  | 106 |



|  |     |
|--|-----|
| Figure 3.15 Position of hydrogen-bond donor E219 and I215 within the substrate-binding pocket of InhA .....                          | 107 |
| Figure 3.16 Dynamics of the substrate-binding cavity .....   | 109 |
| Figure 3.17 Thermodynamic analysis of inhibitor dissociation phase .....   | 113 |
| Figure 3.18 Progress curve analysis for the inhibition of V203A, I215A and L207A by PT70 .....                                       | 119 |
| Figure 3.19 Integrated structural – kinetic inhibition scheme .....  | 123 |
| Figure 3.20 Midpoint temperatures of the protein-unfolding transition ( $T_m$ ) for 4-pyridone.....                                  | 124 |
| Figure 4.1 Double logarithmic plot of $K_i$ vs. MIC of diphenyl ethers against <i>M. tb</i> .....                                    | 138 |
| Figure 4.2 Target engagement workflow .....  | 139 |
| Figure 4.3 Killing kinetics against <i>M. smeg</i> .....   | 141 |
| Figure 4.4 Overlay of killing curves from experiment and simulation.....   | 142 |
| Figure 4.5 Overlay of killing curves from experiment and simulation.....   | 143 |
| Figure 4.6 PAE of PT504 against <i>M. smeg</i> under different drug concentrations .....   | 145 |
| Figure 4.7 PAE of PT504 against <i>M. smeg</i> under different drug concentrations .....   | 146 |
| Figure 5.1 InhA in complex with methyl-thiazole.....   | 153 |
| Figure 5.2 Workflow Used to Discover Novel InhA Inhibitors in the Virtual Screen with the NCI Library on GO FAM.....                 | 164 |
| Figure 5.3 Summary of the 2D structures, docking scores, and InhA inhibitory activities of the eight new inhibitors discovered ..... | 171 |
| Figure 5.4 Predicted binding modes of the two most potent new InhA inhibitors discovered in GO FAM experiment .....                  | 172 |
| Figure 5.5 Predicted binding modes of the least potent new InhA inhibitors discovered in GO FAM experiment.....                      | 173 |

|   |     |
|---|-----|
| Figure 5.6 Kinetic data for the two most potent InhA inhibitors.....  | 177 |
| Figure 5.7 Comparison of the chemical space of the new InhA inhibitors to known InhA inhibitors .....                                 | 181 |
| Figure 5.8 Chemical structures and MIC <sub>50</sub> of 4-hydroxy-2-pyridone analogs .....  | 187 |
| Figure 5.9 Isothermal titration calorimetry binding of NITD-529 and NITD-564.....   | 194 |
| Figure 5.10 Structural analysis of 2-pyridone binding site in InhA-NADH complex.....  | 196 |
| Figure 6.1 Frontline <i>B. pseudomallei</i> treatment.....  | 200 |
| Figure 6.2 FabI inhibitors .....  | 204 |
| Figure 6.3 Representative plot of pseudo-first order rate constant ( $k_{\text{obs}}$ ) as a function of inhibitor concentration..... | 216 |
| Figure 6.4 Kinetic and thermodynamic correlation .....  | 224 |
| Figure 6.5 Midpoint temperatures of the protein-unfolding transition ( $T_m$ ) for PT412.....   | 227 |
| Figure 6.6 Differences in the structures for PT404 and Triclosan in complex with <i>Bp</i> FabI and NADH.....                         | 229 |
| Figure 6.7 <i>In vivo</i> efficacy of PT405 in the animal model of melioidosis.....   | 231 |

## List of Tables

|  |     |
|--|-----|
| Table 1.1 First-line and Second-line antituberculosis drugs.....   | 6   |
| Table 2.1 Comparison of direct dissociation and progress curve analysis under different FabI systems.....                              | 42  |
| Table 2.2 Parameters obtained from progress curve analysis under different inhibitor concentrations.....                               | 47  |
| Table 2.3 Parameters obtained from progress curve analysis at low inhibitor concentration.....   | 48  |
| Table 2.4 Comparison of $k_{off}$ values obtained from experiment and simulation.....  | 51  |
| Table 2.5 Advantages and disadvantages of the direct dissociation method.....  | 56  |
| Table 3.1 Kinetic parameters depicting the association and dissociation for the three common time-dependent inhibition mechanisms..... | 62  |
| Table 3.2 Rationale of kinetic parameters for InhA in the Mathematica Model.....   | 72  |
| Table 3.3 Primers for different InhA mutant constructs.....  | 74  |
| Table 3.4 Detailed kinetic characterization of 2'-substituents diphenyl ether analogs.....   | 82  |
| Table 3.5 Detailed kinetic characterization of 5-substituents diphenyl ether analogs.....  | 84  |
| Table 3.6 $k_{off}$ at difference temperatures for various inhibitors.....   | 114 |
| Table 3.7 Activation enthalpy, entropy and free energy for different inhibitors.....   | 114 |
| Table 3.8 Michaelis-Menten parameters of wild-type and variant InhA.....   | 117 |
| Table 3.9 kinetics parameters of wild-type and variant InhA generated from the computational kinetic model.....                        | 117 |
| Table 3.10 kinetic parameters of PT163 with wild-type InhA under difference pH values.....   | 120 |
| Table 4.1 MIC of diphenyl ethers against <i>M. smeg</i> and <i>M. tb</i> .....   | 135 |

|   |     |
|---|-----|
| Table 4.2 Cellular parameters computed from the killing kinetic model for PT04 and PT504 .  | 142 |
| Table 5.1 Compound ID's, 2D structures, and InhA inhibition data .....  | 168 |
| Table 5.2 Tanimoto Similarity of Each Novel Inhibitor Compared to the Other 7 New Inhibitors<br>.....                               | 174 |
| Table 5.3 Tanimoto Similarity to 154 Known InhA Inhibitors in the TB Mobile data set .....  | 180 |
| Table 5.4 Summary of Antitubercular Efficacy and Mammalian Cell Cytotoxicity .....  | 183 |
| Table 5.5 Activity of 4-hydroxy-2-pyridone analogues against different drug resistance TB<br>clinical isolates.....                 | 189 |
| Table 5.6 cross-resistance and whole genome sequencing analysis of 4-hydroxy-2-pyridone<br>resistance mutants of <i>M. tb</i> ..... | 191 |
| Table 5.7 Interaction of 4-hydroxy-2-pyridones with InhA .....  | 193 |
| Table 6.1 Kinetic and thermodynamic parameters for inhibitors against bpFabI.....   | 217 |

## List of Abbreviations

|                      |  |
|----------------------|--|
| AccABCD              | Acetyl-CoA carboxylase                           |
| AccAD                | Carboxyltransferase component of AccABCD         |
| AccB                 | Biotin carboxyl carrier protein                  |
| AccC                 | Biotin carboxylase component of AccABCD          |
| ACP                  | Acyl carrier protein                             |
| BSA                  | Bovine serum albumin                             |
| CFU                  | Colony-forming unit                              |
| CoA                  | Coenzyme A                                       |
| Cro-CoA              | Trans-2-crotonyl-CoA                             |
| Da                   | Dalton   |
| DD CoA               | Trans-2-dodecenoyl-CoA                           |
| DMSO                 | Dimethyl sulfoxide                               |
| <i>E. coli</i>       | <i>Escherichia coli</i>                          |
| EcFabI               | Enoyl-ACP reductase from <i>Escherichia coli</i> |
| EDTA                 | Ethylenediaminetetraacetic acid                  |
| <i>F. tularensis</i> | <i>Francisella tularensis</i>                    |
| FabA                 | $\beta$ -hydroxyacyl-ACP dehydrase               |
| FabB                 | $\beta$ -Ketoacyl synthase I                     |
| FabD                 | Malonyl-CoA: ACP transacylase                    |
| FabF                 | $\beta$ -Ketoacyl synthase II                    |
| FabG                 | $\beta$ -Ketoacyl-ACP reductase                  |

|                               |  |
|-------------------------------|--|
| FabH                          | $\beta$ -Ketoacyl-ACP synthase III                         |
| FabI                          | Enoyl-ACP reductase  |
| FabZ                          | $\beta$ -Hydroxyacyl-ACP dehydrase                         |
| FAS-I                         | Eukaryotic fatty acid biosynthesis                         |
| FAS-II                        | Bacterial fatty acid biosynthesis                          |
| FtFabI                        | Enoyl-ACP reductase from <i>Francisella tularensis</i>     |
| IC <sub>50</sub>              | Half maximal inhibitory concentration                      |
| INH                           | Isoniazid  |
| InhA                          | Enoyl-ACP reductase from <i>Mycobacterium tuberculosis</i> |
| IPTG                          | Isopropyl-1-thio- $\beta$ -D-galactopyranoside             |
| KatG                          | Mycobacterial catalase-peroxidase                          |
| K <sub>i</sub> <sup>app</sup> | Same as IC <sub>50</sub>                                   |
| k <sub>obs</sub>              | Pseudo-first order rate constant                           |
| MIC                           | Minimal inhibitory concentration                           |
| NAC                           | N-acetylcysteamine   |
| NAD <sup>+</sup>              | Nicotinamide adenine dinucleotide, oxidized form           |
| NADH                          | Nicotinamide adenine dinucleotide, reduced form            |
| NADPH                         | Nicotinamide adenine dinucleotide phosphate, reduced form  |
| Oct-CoA                       | Trans-2-octenoyl-CoA                                       |
| OD <sub>600</sub>             | Optical density at 600 nm                                  |
| PAE                           | Post-antibiotic effect                                     |

|                  |                                     |
|------------------|-------------------------------------|
| PD               | Pharmacodynamic                     |
| PDB              | Protein Data Bank                   |
| PK               | Pharmacokinetic                     |
| RMSD             | Root-mean-square deviation          |
| <i>S. aureus</i> | <i>Staphylococcus aureus</i>        |
| SAR              | Structure-activity relationship     |
| SBL              | Substrate binding loop              |
| SDR              | Short-chain dehydrogenase/reductase |
| TB               | Tuberculosis                        |
| TCL              | Triclosan                           |
| T <sub>m</sub>   | Melting temperature                 |
| t <sub>R</sub>   | Residence time                      |
| v <sub>i</sub>   | Initial velocity                    |
| v <sub>s</sub>   | Steady-state velocity               |
| WT               | Wild type                           |

## Acknowledgments

I would like to express my grateful and sincere gratitude to my advisor Professor Peter J. Tonge for the continuous support of my Ph.D study and research, for his immense knowledge, patience, motivation, encouragement and unconditional support. He has not only given me the latitude to explore my own research interest, but also guided me in finding out my long-term career goals, and training me as an independent thinker. I could not have imagined having a better advisor and mentor for my Ph.D study.

I would also like to thank Professor Elizabeth M. Boon, the chairperson of my dissertation committee, for teaching me one important graduate course and sharing with me her precious suggestions and insightful comments in guiding my research. I am grateful to Professor Jin Wang, the third member of my dissertation committee for all his help and advice. It is a pleasure to thank Professor Stephen G. Walker, the outside member of my committee, for all his intelligent advice and kind help.

I would like to thank all Tonge group members for your kind help and inspiring discussions. I will cherish the extraordinary happy time in Tonge group forever.

I owe my deepest gratitude to my dear parents, for your unconditional support through my life. I am proud of being a daughter of two chemists.

Words fail me to express my appreciation to my husband Yen-Ting Liu, whose great love and persistent support encourages me to complete my Ph.D work. Without you, this dissertation would not have been possible.



## Publications

- **Yu, W.**, Spagnuolo, L., Eltschkner, S., Chang, A., Li, H., Bommineni, G., Shah, S., and Tonge, P., and Kisker, C., “Unraveling the slow onset inhibition of InhA, the enoyl ACP reductase from *Mycobacterium tuberculosis*: Mechanism and Inhibitor design”, *ACS Chemical Biology*, *in preparation*
- **Yu, W.**, Bommineni, G., Neckles, C., Chang, A., Pan, P., Liu, N., Spagnuolo, L., and Tonge, P., “A [<sup>32</sup>P]-Nicotinamide Adenine Dinucleotide Method to Identify and Quantitate Long Residence Time Enoyl-ACP reductase Inhibitors”, *Journal of Analytical Biochemistry*, 2015
- **Perryman, A.L., Yu, W.**, Ekins, Sean., Forli, S., Freundlich, J.S., Tonge, P., and Olson, A.J., “GO Fight Against Malaria (GO FAM) Virtual Screen discovers novel inhibitors of *Mycobacterium tuberculosis* InhA”, *Journal of Chemical Information and Modeling*, 2015
- **Neckles, C., Yu, W.**, Bommineni, G., Cummings, J., Hirschbeck, M., Zhang, Zhuo., Kim, M., Kisker, C., Slayden, R., and Tonge, P., “MUT056399 and p-fluoro diphenyl ethers: detailed slow binding kinetic analysis on the enoyl-ACP reductase from *Burkholderia pseudomallei*”, *in preparation*
- Schiebel, J., Chang, A., Merget, B., Bommineni, G., **Yu, W.**, Spagnuolo, L., Baxter, M., Tareilus, M., Tonge, P., Kisker C., and Sotriffer, C., “Protons and hydrides – wherefrom and whereto: from a chemical binding pocket analysis to biological substrate recognition process”, *ACS chemical biology*, *submitted*, 2014

- Manjunatha, U., Rao, S.P.S., Kondreddi, R., Noble, C.G., Camacho, L.R., Tan, B.H., Ng, S.H., Ng, P., Ma, N.L., Lakshminarayana, S.B., Herve, M., Barnes, S.W., **Yu, W.**, Kuhen, Kelli., Blasco, F., Beer, D., Walker, J.R., Tonge, P., Glynne, R., Smith, P.W., and Diagana, T., “Discovery of novel direct InhA inhibitors active against *Mycobacterium tuberculosis*”, *Science Translational Medicine*, 2015
- Schiebel, J., Chang, A., Shah, S., Lu, Y., Liu, L., Pan, P., Hirschbeck, M., Tareilus, M., Eltschkner, S., **Yu, W.**, Cummings, J., Knudson, S., Bommineni, G., Walker, S., Slayden, R., Sottriffer, C., Tonge, P., and Kisker, C., “Molecular basis of the narrow-spectrum antibacterial activity of the clinical candidate CD400549 and the rational design of a potent broad-spectrum pyridine-based FabI inhibitor”, *Journal of Biological Chemistry*, 2014
- Li, H., Lai, C., Pan, P., **Yu, W.**, Liu, N., Garcia-Diaz, M., Simmerling, C., and Tonge, P., “A Structural and Energetic Model for the Slow-onset Inhibition of InhA, an enzyme drug target from *Mycobacterium tuberculosis*”, *ACS Chemical Biology*, 2014
- Cummings, J., Beaupre, Adam., Knudson, Susan., Liu, N., **Yu, W.**, Neckles, C., Wang, H., Khanna, A., Bommineni, G., Trunck, L., Schweizer, H., Tonge, P., and Slayden, R., “Substituted Diphenyl Ethers as a Novel Chemotherapeutic Platform against *Burkholderia pseudomallei*”, *Journal of Antimicrobial Agents and Chemotherapy*, 2014
- Chang, A., Schiebel, J., **Yu, W.**, Bommineni, G., Pan, P., Baxter, M., Khanna, A., Sottriffer, C., Kisker, C., and Tonge, P., “Rational Optimization of Drug-Target Residence Time: Insights from Inhibitor Binding to the *Staphylococcus aureus* FabI Enzyme-Product Complex”, *Biochemistry*, 52(24), 4217-28, 2013

## **Chapter 1 Current therapeutics for tuberculosis control and the fatty acid biosynthesis**

### **FAS-II pathway as novel drug target**

#### Tuberculosis infection – demographic

Tuberculosis (TB) is the single most lethal bacterial infection in the world. Each year, TB kills an estimated 1.7 million people and causes more than 9 million new cases of infection worldwide (2, 3). The current treatment of drug-sensitive TB requires duration of 6 months, with four drugs (isoniazid, rifampicin, pyrazinamide and ethambutol) (Figure 1.1) given in the first 2 months (intensive phase) followed by isoniazid and rifampicin in the next 4 months (continuation phase) (1). However, many factors can complicate the current TB regimen. About 12% of TB patients are co-infected with HIV and there is a convergence trend of the TB and HIV epidemic profile (2). When co-infected with HIV, the combination treatment with the antiretroviral therapy results in unwanted drug-drug interactions, toxicity, intolerance and loss of efficacy. These issues are compounding the challenge of next generation TB drug discovery (1).

The emergence of multidrug-resistant (MDR) TB as well as extensively resistant (XDR) TB has continuously added on the disease burden of TB infection. MDR TB is caused by strains of *M.tb* that are resistant to either isoniazid or rifampicin, while XDR TB is caused by MDR strains that are resistant to fluoroquinolones and one of the three injectable aminoglycosides (capreomycin, kanamycin and amikacin) (2) (Figure 1.2). In 2011, there were ~650,000 incidents of MDR-TB worldwide. The WHO recommend regimen includes at least 8 months of intensive phase treatment with at least four second-line drugs (injectable aminoglycosides, injectable

polypeptides, oral/injectable fluoroquinolones, linezolid etc.) for a total treatment duration of at least 20 months for newly diagnosed MDR-TB patients or 28 months for previously MDR-TB-infected patients (1). However, only 10% of the MDR-TB patients receive such high-quality and appropriate treatment as suggested by the WHO. The emergence of XDR-TB worsens the TB treatment in a way that the duration of treatment is substantially longer than MDR-TB treatment and involves the use of third-line antituberculosis drugs (4, 5). The drug resistance problem mitigates an urgent need for new drugs to treat drug-resistant TB infections.

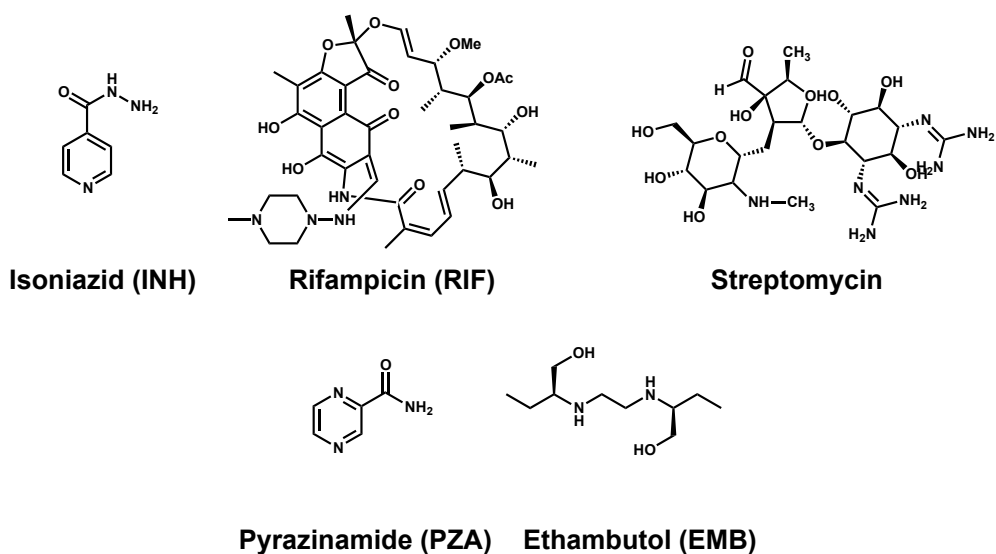


**Figure 1.1 First-line antituberculosis drugs**

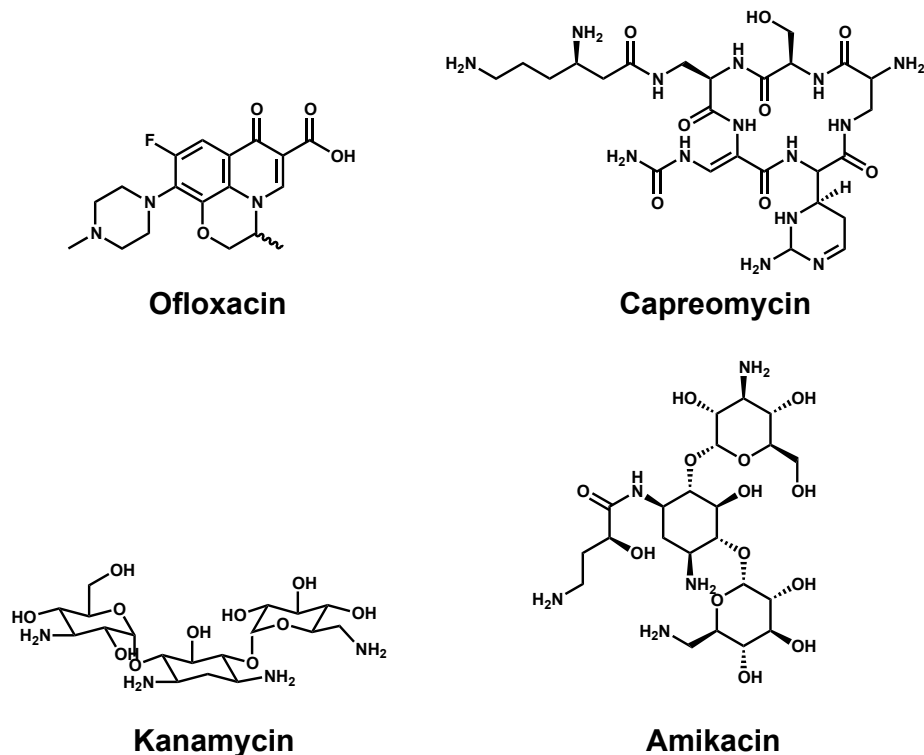


**Figure 1.2 Selected Second-line antituberculosis drugs**

### Frontline treatment and potential problems

The need for long duration of treatment results from the slow replication rate of *M. tb* (doubling time 15-20 hrs), together with the ability of *M. tb* to persist in a latent state (2). Streptomycin (Figure 1.1) was the first antibiotic discovered that showed activity against *M. tb* (6). However, as a single drug treatment for TB, the rapid emergence of drug resistance soon became problematic (6). Isoniazid (INH) is the core of the first-line antituberculosis chemotherapy (Figure 1.1). The mode of action of INH was first discovered from the correlation between diminished activity of KatG catalyse activity and INH-resistant *M. tb* strains (7). Further

studies suggested that INH was a prodrug, and it had to be activated by the catalaseperoxidase enzyme KatG in the cell (8) (Figure 1.3). The activated INH targets the enoyl-acyl-carrier-protein (enoyl-ACP) reductase (InhA) and  $\beta$ -ketoacyl-ACP synthase within the fatty acid elongation cycle (9-11). INH thus inhibits mycolic acid biosynthesis which eventually leads to the deterioration of the cell wall. However, the INH-resistant clinical isolates pose an urgent need for the discovery of InhA inhibitors that do not require activation of KatG (12). Pyrazinamide (PZA) (Figure 1.1) is one of the first-line antituberculosis drugs. The inclusion of PZA in the modern TB chemotherapy significantly reduces the treatment from 12-18 months to 6 months since PZA can kill semidormant tubercle bacilli that cannot be killed by other antituberculosis drugs (13-15). PZA is thought to be converted to the bactericidal pyrazinoic acid inside the cells by pyrazinamidase/nicotinamidase (16). Studies on PZA-resistant *M. tb* further demonstrate that mutations in the pyrazinamidase-encoded gene are responsible for PZA-resistant *M. tb* strains (17). Yet the molecular target of the active form of pyrazinoic acid (POA) is still elusive and requires further investigation. Shi *et al.* suggested that POA targets the ribosomal protein S1 (RpsA) and inhibits trans-translation, providing a possible explanation for the eradication of the dormant bacilli by the drug (18). Another first-line antituberculosis drug is ethambutol (EMB) (Figure 1.1). The molecular target of EMB is thought to be the arabinosyltransferase. The drug functions by inhibiting the incorporation of arabinogalactan into the cell wall and eventually results in detrimental alteration of the mycobacterial cell wall structure (19, 20). The fourth first-line antituberculosis drug is rifampicin (RIF) (Figure 1.1), which inhibits the bacterial DNA-dependent RNA polymerase (21). Most of the RIF-resistant strains have mutations in the *rpoB* gene (22). The following table shows the current first-line and second-line TB regimen and their mechanism of action.

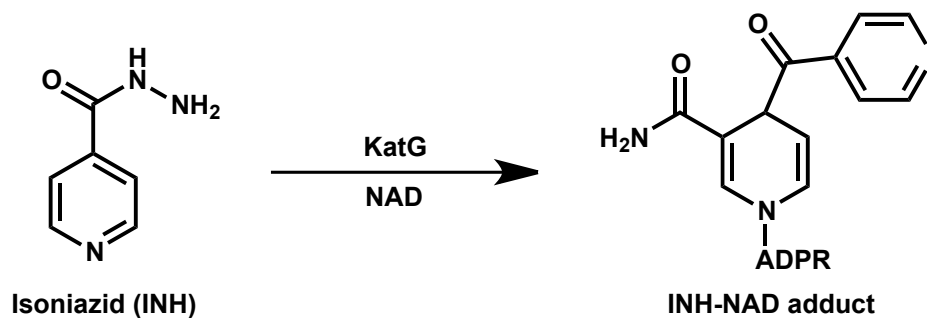


**Figure 1.3 Activation of INH by KatG**

#### Novel drug candidate discovery and repurposed drugs

Next generation TB drugs have several requirements including the ability to shorten the duration of treatment, ease of delivery, compatibility with antiretroviral therapy and with other TB drugs, low toxicity and low cost (1, 2). Over the past 5 years, there have been some promising drug candidates emerging in the TB drug pipeline (Figure 1.4 and 1.5). For example, diarylquinoline (TMC-207, or bedaquiline) which targets the mycobacterial ATP synthase has been recently approved as new chemical entity for TB treatment (23-25) (Figure 1.5). Bedaquiline has an MIC value equivalent to INH and RIF and is active against both drug-sensitive and drug-resistant strains. Interestingly, the evaluation on the clinical efficacy of bedaquiline further validates ATP synthase as a highly vulnerable target of *M. tb* (23).

Table 1.1 First-line and Second-line antituberculosis drugs

| Drug                      | Administration | Year of Discovery | Protein target   | Mechanism                                |
|---------------------------|----------------|-------------------|--|--|
| Isoniazid (26)            | Oral           | 1952              | Enoyl-ACP reductase                                    | Inhibit mycolic acid biosynthesis        |
| Rifampicin (26)           | Oral           | 1963              | RNA polymerase, beta subunit                           | Inhibit transcription                    |
| Pyrazinamide (18)         | Oral           | 1954              | S1 component of 30S ribosomal subunit                  | Inhibit translation, acidifies cytoplasm |
| Ethambutol (26)           | Oral           | 1961              | Arabinosyl transferases                                | Inhibit arabinogalactan biosynthesis     |
| Para-amino salicylic (27) | Oral           | 1948              | Dihydroteroate synthase                                | Inhibit folate biosynthesis              |
| Streptomycin (26)         | Injectable     | 1944              | S12 and 16S rRNA components of 30S ribosomal subunit   | Inhibits protein synthesis               |
| Ethionamide (26)          | Oral           | 1961              | Enoyl-ACP reductase                                    | Inhibit mycolic acid biosynthesis        |
| Ofloxacin (26, 28)        | Oral           | 1980              | DNA gyrase and DNA topoisomerase                       | Inhibit DNA supercolling                 |
| Capreomycin (29)          | Injectable     | 1963              | Interbridge B2a between 30S and 50S ribosomal subunits | Inhibit protein synthesis                |
| Kanamycin (30)            | Injectable     | 1957              | 30S ribosomal subunit                                  | Inhibits protein synthesis               |
| Amikacin (29)             | Injectable     | 1972              | 30S ribosomal subunit                                  | Inhibits protein synthesis               |
| Cycloserine (31)          | Oral           | 1955              | D-alanine racemase and ligase                          | Inhibits peptidoglycan synthesis         |



Another example of promising new TB drugs are the nitroimidazoles – i.e. PA824 and OPC-67683 (or delamanid) (Figure 1.5). Both PA824 and delamanid are active against both drug-sensitive and drug-resistant *M. tb* strains (32). These nitroimidazoles are prodrugs that require activation by deazaflavin-dependent nitroreductase (Ddn) and subsequently form the des-nitroimidazole active form that produces toxic active nitrogen radicals within the cell (33-37). PA-824 functions through inhibition of mycolic acid under aerobic conditions and could also poison the respiratory system by generating NO radicals under anaerobic conditions (38). The mechanism of delamanid is more straightforward where it stems from the inhibition of mycolic acid biosynthesis (33). Since nitroimidazoles are also active against both non-replicating and replicating *M. tb*, they bring up the possibility of shortened treatment duration (39). Currently, these nitroimidazoles are under clinical phase II (PA-824) and phase III (delamanid) development for the treatment of MDR-TB.

A third example is SQ109 (Figure 1.5). SQ109 is a membrane protein MmpL3 inhibitor and its mode of inhibition stems from the inhibition of mycolic acid biosynthesis (40). Remarkably, SQ109 has shown synergistic effect when dosed together with bedaquiline (41). Other than SQ109, there are several different MmpL3 inhibitors that are currently in the development pipeline, such as AU1235, BM212, C215, NITD-304 and 349 (42-45) (Figure 1.4).

Other than novel drug candidate discovery, tremendous efforts have also been made on repurposed drugs – i.e. antimicrobial agent are initially discovered for the purpose of other bacterial infections but are reevaluated against TB infection (Figure 1.6). For example, a Phase III clinical trial was initiated to investigate whether the treatment of drug-sensitive TB could be

shortened from 6 months to 4 months by substituting ETH or INH with gatifloxacin or moxifloxacin (24). Another Phase III clinical trial was on rifapentine, where twice-weekly rifapentine was used in combination with moxifloxacin during continuation phase (24, 46). However, it is important to note that rifapentine might induce cytochrome P450 and lead to drug-drug interactions with antiretroviral therapy or other TB drugs such as bedaquiline (25). In addition, oxazolidinones such as linezolid and sutezolid were shown to be effective against MDR-TB where sutezolid showed synergistic effects with other drug candidates, opening up the possibility for the development of novel combination therapies (47-49).

Although much effort has been made to accelerate the development of novel antituberculosis regimen, the pipeline is still thin and challenges that need to be addressed for prospective drug candidates include shortening duration of therapy and tackling the drug resistance problem.

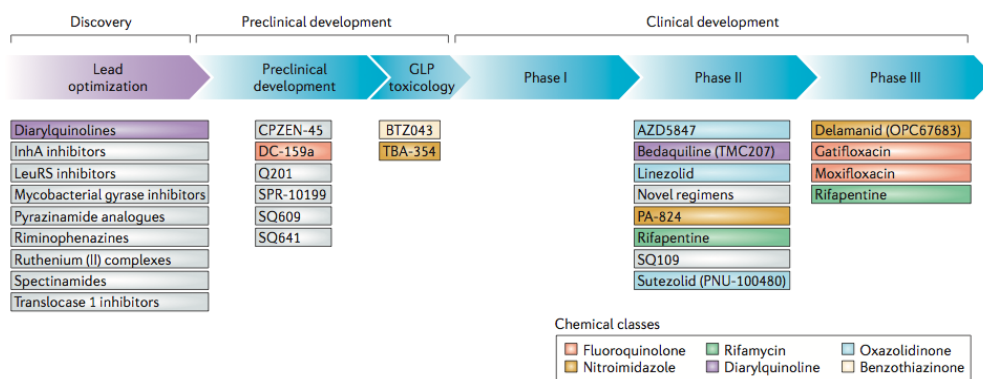


**Figure 1.4 Current global pipeline of new tuberculosis drugs**  
adapted from (1)

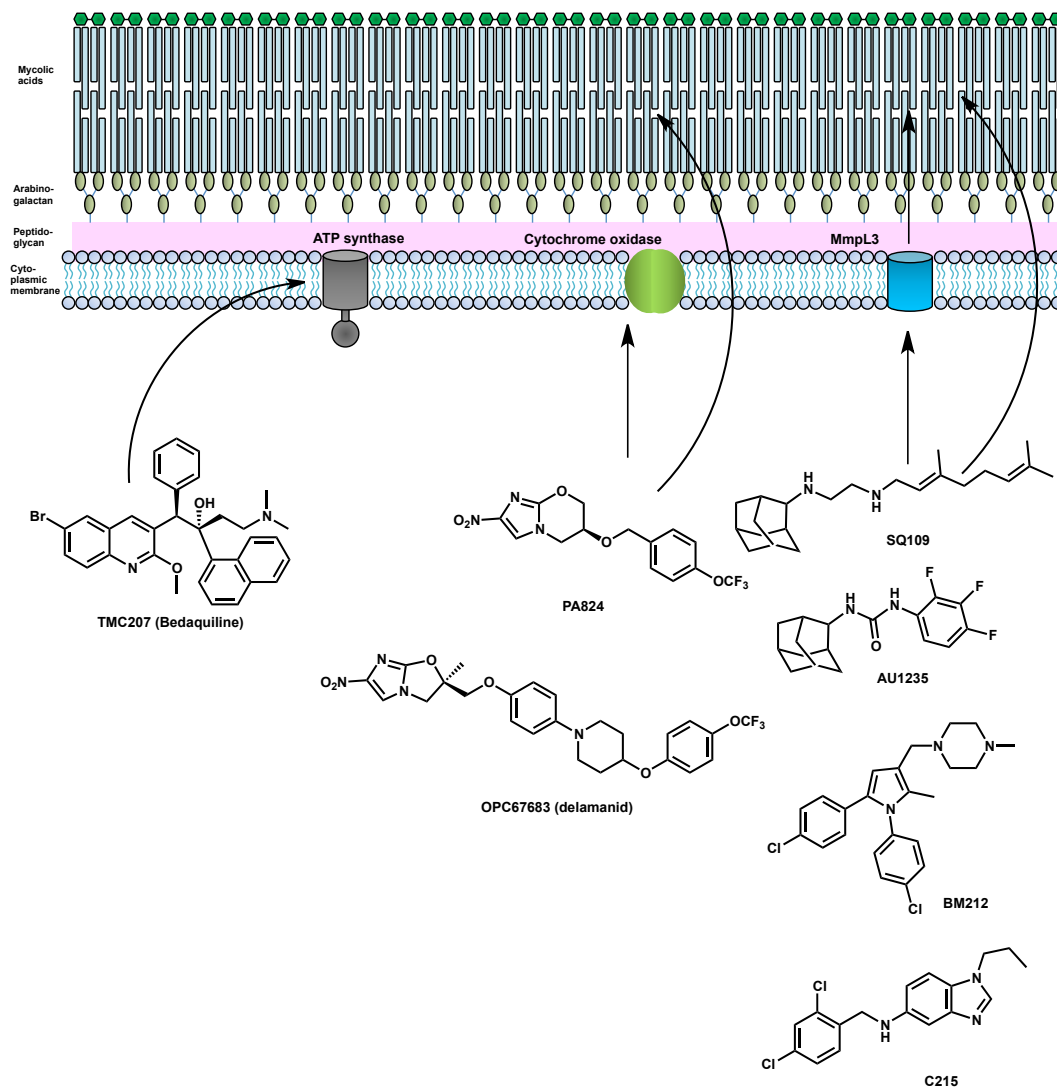
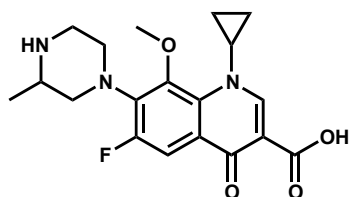
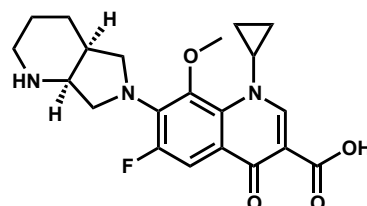


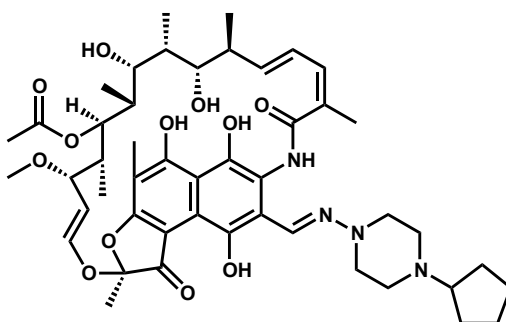
**Figure 1.5 Site of action of different antituberculosis drug candidates adapted from (1)**



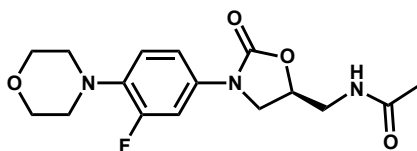
**Gatifloxacin**



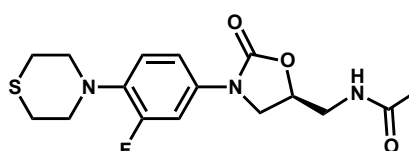
**Moxifloxacin**



**Rifapentine**



**Linezolid**



**Sutezolid**

**Figure 1.6 Repurposed drugs for tuberculosis treatment**

Bacterial cell wall – fatty acid biosynthesis as drug target

The bacterial cell membrane not only protects the interior of the cell from the outside environment, but also participates in many crucial cellular activities. Therefore, the cell membrane is essential for cell viability. The fatty acid biosynthesis pathway of bacteria (Figure 1.7) is responsible for the first step in the formation of membrane lipids, thus playing a pivotal role in cell physiology (50). In addition, bacteria are generally not able to obtain sufficient fatty acids

from the environment hence the need for *de novo* fatty acid biosynthesis (51). This is particularly true for *M. tb* which has long chain mycolic acids in the cell membrane which cannot be obtained from the human host. In addition, bacterial fatty acid biosynthesis has distinct structural and functional characteristics from the mammalian fatty acid biosynthesis. In bacteria, fatty acid biosynthesis is performed by the FAS II pathway, where a set of discrete enzymes with different functions is responsible for each step within the pathway (Figure 1.7). In contrast to bacteria, mammalian fatty acid biosynthesis follows the FAS I pathway where reactions are catalyzed by a single multifunctional polypeptide (52). Such low sequence homology between FAS II and FAS I allows a high selectivity and low toxicity profile for inhibitors targeting FAS II. Lastly, the individual enzymes involved in FAS II have high sequence similarities across different bacteria species, opening up the possibility of developing broad-spectrum antimicrobial by targeting this pathway. Overall, the FAS II pathway serves an attractive pathway for novel antimicrobial discovery.

The FAS II pathway occurs in two main steps catalyzed by the initiation cycle and the elongation cycle. The initiation cycle starts with acetyl-CoA carboxylase (AccABCD), which is a multi-subunit protein that carboxylates acetyl-CoA to form malonyl-CoA (53-58). The malonate group on malonyl-CoA is then transferred to ACP by malonyl-CoA: ACP transacylase (FabD) to form malonyl-ACP (59, 60). The elongation cycle is initiated by  $\beta$ -ketoacyl-ACP synthase III (FabH), which condenses the acetyl-CoA with malonyl-ACP to form  $\beta$ -ketobutyryl-ACP (61). The  $\beta$ -ketoacyl-ACP is subsequently reduced by  $\beta$ -ketoacyl-ACP reductase (FabG) to product  $\beta$ -hydroxyacyl-ACP (62). The  $\beta$ -hydroxyacyl-ACP is further dehydrated by FabA or FabZ to generate trans-2-enoyl-ACP (63-65). Finally, the enoyl-ACP is reduced to acyl-ACP by the

enoyl-ACP reductase (FabI, or InhA in *M. tb*) to finish up the elongation cycle (66). Subsequent elongation cycles are initiated by  $\beta$ -ketoacyl-ACP synthase I or II (FabB/FabF, or KasA/KasB in *M. tb*) (67). These condensing enzymes have unique substrate specificities to balance the flux and distribution of fatty acid products. Fatty acid biosynthesis in *M. tb* is atypical, where it contains both FAS I and FAS II pathway. The FAS I is responsible to generate shorter saturated alkyl chain fatty acid (C16 – C26), then these fatty acids are transferred to FASII to be elongated up to C56 as precursors of mycolic acid (68).

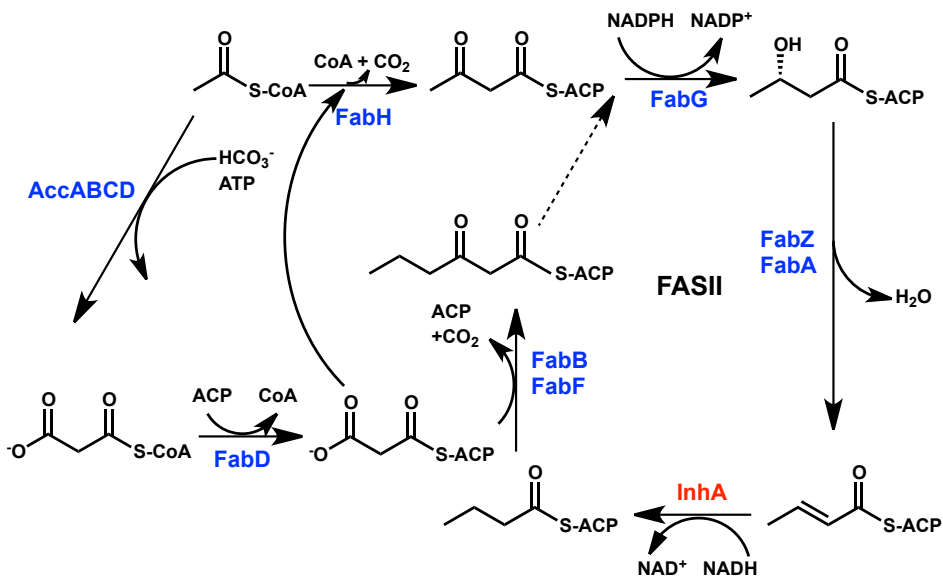


Figure 1.7 Bacteria Type II fatty acid biosynthesis pathway

## Inhibitors of FabI

Among all the enzymes involved in the FAS-II pathway, the enoyl-ACP reductase (FabI) is the most extensively studied target for potential drug development. The FabI is called InhA in *M. tb* and is the primary target of INH. Other than INH, there are several different classes of InhA inhibitors and below we will summarize the efforts that have been to inhibit this enzyme.

## Isoniazid

INH must be activated by the *Mtb* catalase-peroxidase (KatG) (69, 70). KatG activates INH to enable formation of a covalent adduct with NAD<sup>+</sup> or NADH (69) (Figure 1.8). The INH-NAD adduct is a time-dependent inhibitor of InhA with a  $K_i^*$  value of 0.75 nM and residence time of 62.5 min (71). However, most clinical isolates of INH-resistant *M. tb* contain mutations in KatG. Therefore, novel InhA inhibitors that do not require prior activation by KatG are not vulnerable to this key mechanism of INH resistance (72).

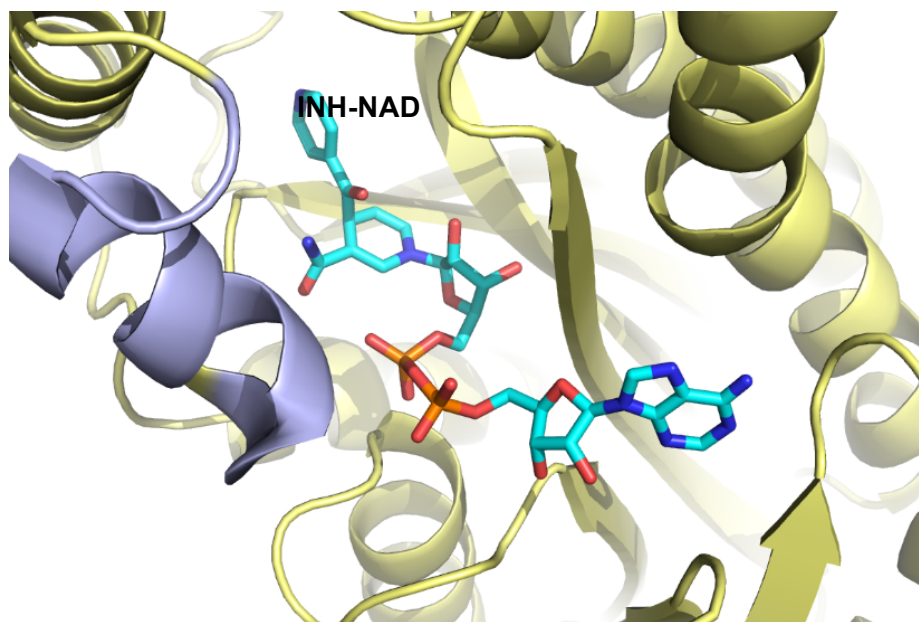


**Figure 1.8 Structure of InhA in complex with INH-NAD adduct** (pdb code: 1ZID) The substrate binding loop is shown in lightblue ribbon, the INH-NAD adduct is shown cyan sticks

## Diazaborines

The diazaborines are a class of heterocyclic boron-containing compounds that inhibit FabI by forming a covalent bond between the boron atom and the 2'-hydroxyl group of the NAD<sup>+</sup> nicotinamide ribose, allowing for the formation of a non-covalently bound inhibitor-product complex (Figure 1.9). The boron hydroxyl forms a hydrogen bond with Y156 of *E. coli* FabI. In addition, the drug has  $\pi$ -stacking interaction with the nicotinamide ring of NAD<sup>+</sup> and also forms a network of van Der Waals interactions within the hydrophobic substrate-binding pocket (73). Previous studies have also shown that the diazaborines are active against *M. tb* (74).

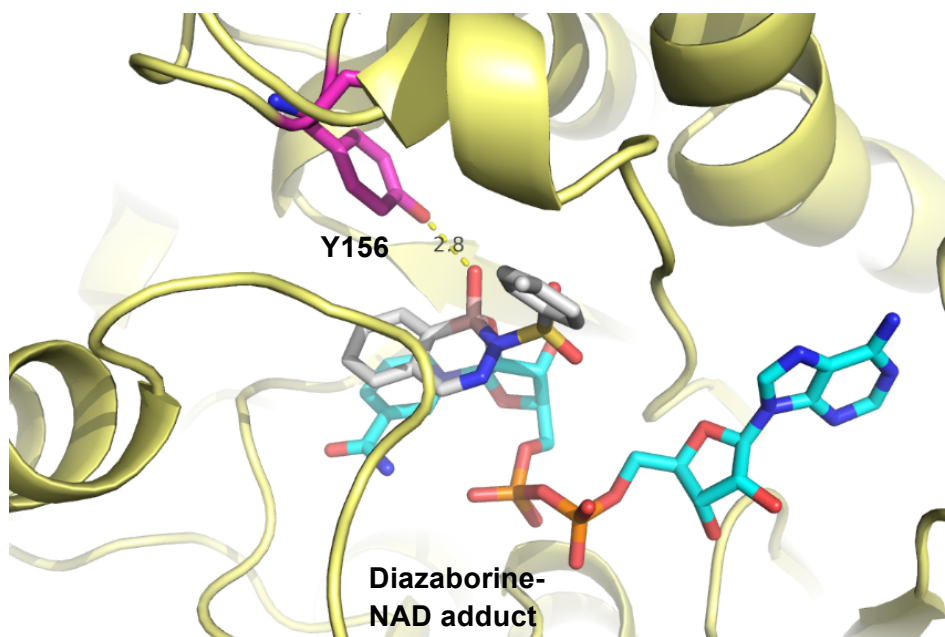


**Figure 1.9 Structure of *E. coli* FabI in complex with diazaborine-NAD<sup>+</sup> adduct**

(pdb code: 1DFG) NAD<sup>+</sup> is shown in cyan sticks, diazaborine is depicted in grey sticks, Y156 is shown in magenta and forms a hydrogen with the phenolic hydroxyl on the inhibitor.



## Triclosan

Triclosan is a time-dependent, tight-binding inhibitor of *E. coli* FabI with a  $K_i^*$  value of 7 pM. The X-ray crystal structure of the enzyme-inhibitor complex shows that the phenol ring of triclosan makes a  $\pi$ -interaction with the nicotinamide ring of  $\text{NAD}^+$ , and that the hydroxyl group forms a hydrogen bond with the catalytic residue Y156 as well as the 2'-hydroxyl of the nicotinamide ribose (Figure 1.10). Triclosan is not a time-dependent inhibitor of InhA, however previous work in our lab together with the studies described in chapter 3 have led to the development of much more potent InhA inhibitors based on the diphenyl ether scaffold.

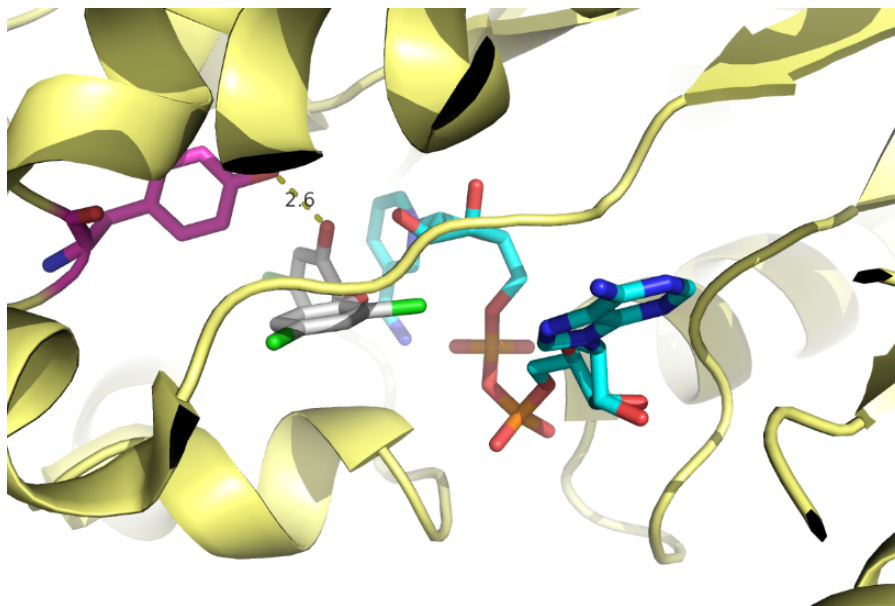
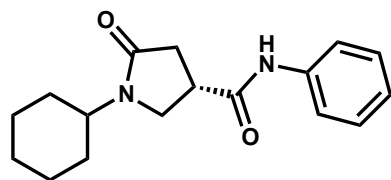


**Figure 1.10 Structure of *E. coli* FabI in complex with Triclosan**

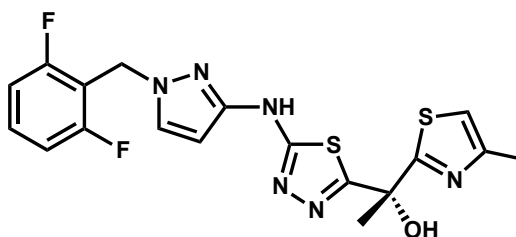
(pdb code: 1QSG) NAD is shown in cyan, triclosan is shown in grey, and Y156 is shown in magenta. A hydrogen bond is shown between Y156 and the hydroxyl of triclosan

### Other InhA inhibitors under development

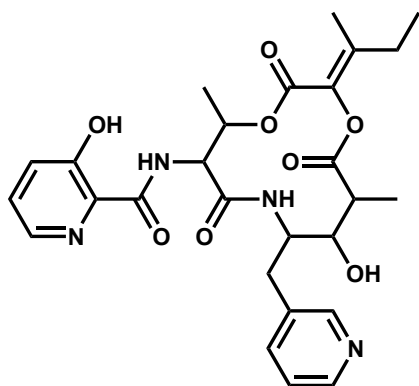
There have been many efforts to identify direct InhA inhibitors to overcome the KatG-mediated resistance (Figure 1.11). He *et al.* reported the discovery of a series of pyrrolidine carboxamides as novel class of direct InhA inhibitors through a combination of high-throughput screening and microarray parallel synthesis (75). AstraZeneca discovered a series of methylthiazoles that bind to the “Y158-out” conformation of InhA (76). In addition, these methylthiazole inhibitors bound to the E-NADH complex, in contrast to previously reported InhA inhibitors that bind to E-NAD<sup>+</sup>. Subsequently, GSK reported a class of potent and selective aminoproline InhA inhibitors using DNA encoded library technology (77). Hit-to-lead optimization yielded a potent InhA inhibitor with promising pharmacokinetic profile. In addition to synthetic compounds, several natural product FabI inhibitors have been identified including pyridomycin, which has potent antituberculosis activity (78). These investigators also determined the X-ray crystal structure of pyridomycin in complex with InhA and found that pyridomycin adopted a unique binding mode that blocked both the cofactor and enoyl substrate binding sites (79) (Figure 1.12). In separate work, Mattheus *et al.* identified a functional FabI isozyme that enables the producer strain to resist the natural product kalimantacin/batumin (80). These examples of natural product inhibitors against InhA/FabI suggest that FabI is an attractive drug target.



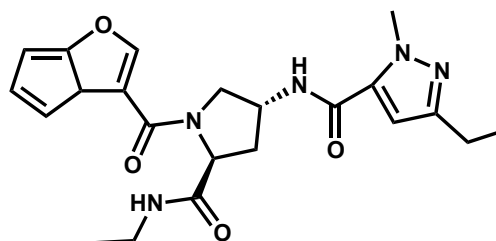
**Pyrrolidine carboxamide**



**Methylthiazole**



**Pyridomycin**



**Aminoproline**

**Figure 1.11 Novel InhA inhibitors**

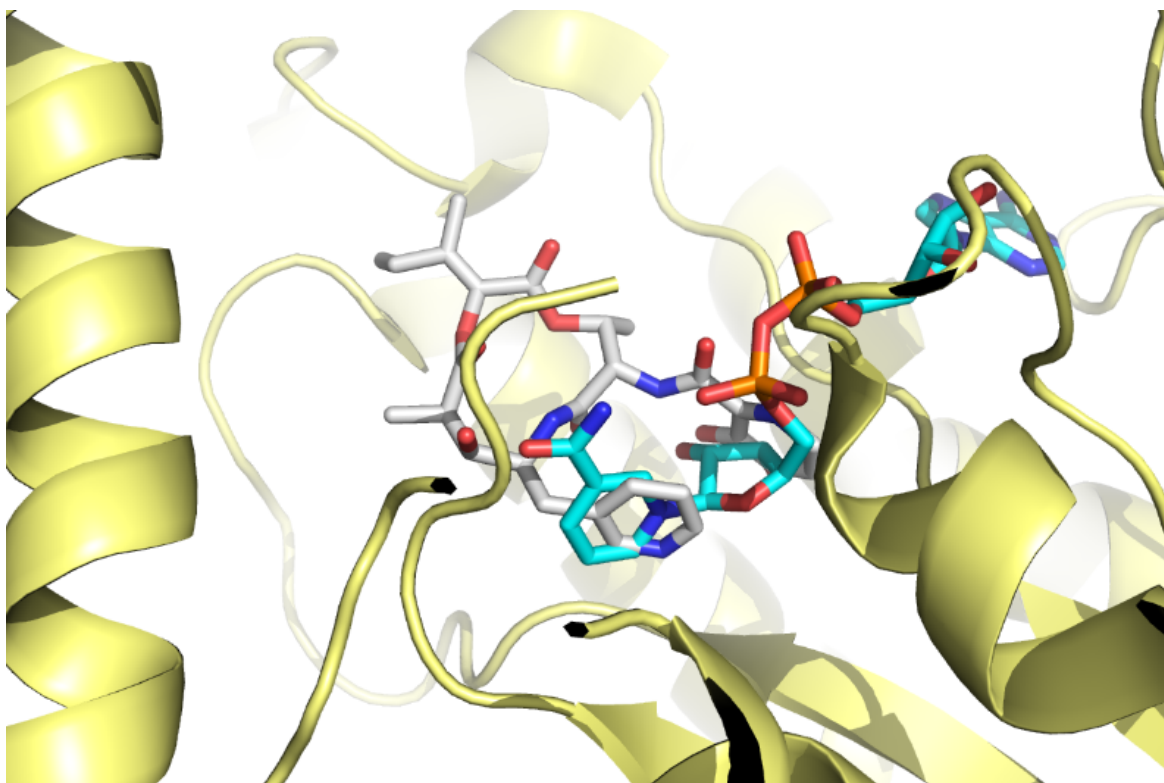


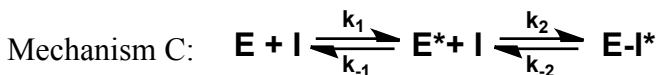
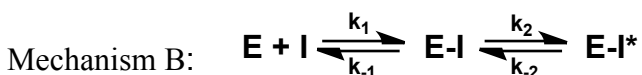
**Figure 1.12 Structure of InhA in complex with pyridomycin**  
(pdb code: 4BII) NAD is shown in cyan, pyridomycin is shown in grey. The structure suggests that pyridomycin partially occupies the NAD binding pocket.

## Time-dependent inhibition - mechanism, examples, target vulnerability

Although novel chemical entities are populating the pipeline, the low success rate at moving compounds in late stage development through clinical trials remains a major problem (1). Historically, the *in vitro* assessment of drug-target interactions are quantified in terms of binding parameters, such as half-maximal inhibitory concentration ( $IC_{50}$ ), or more correctly, by the equilibrium dissociation constant for the drug-complex complex ( $K_d$ ). Generally, these *in vitro* measurements are performed under closed-system conditions, which means the concentration of ligand and receptor can be considered invariant throughout the period of measurement. Under such conditions, the equilibrium dissociation constant is an appropriate metric for the level of target engagement (81). However, in open systems such as those found *in vivo*, the ligand concentration to which the target receptor is exposed is no longer constant, but changes as a function of (82). In this situation, the *in vitro* equilibrium dissociation constant can no longer fully describe the duration of target occupancy. Instead drug-target kinetics must also be used including the target-ligand dissociation rate constant, or off-rate ( $k_{off}$ ) (83). Since residence time by the definition is only related to the rate of complex dissociation, it can be quantified by the reciprocal of this dissociation rate constant ( $1/k_{off}$ ). Therefore,  $k_{off}$  can be considered as a direct method of residence time measurement.

Since drug-target residence time is such an important determinant of drug action, inhibitors should be optimized for both the dissociation rate constant ( $k_{off}$ ) and the equilibrium dissociation constant ( $K_d$ ). Currently, there are three different kinds of inhibition mechanisms that can generate a slow off rate.

The first mechanism (mechanism A) is a simple one-step binding-dissociation process in which E and I combine to form EI (Scheme 1.1) (82). If the equilibrium dissociation constant ( $K_d$ ) is a very small (nanomolar to picomolar), then by necessity the off rate will also be small. For example assuming that the on rate is diffusion controlled ( $k_{on} = 5 \times 10^8 \text{ M}^{-1} \text{ s}^{-1}$ ) then a 1 pM inhibitor will have a  $k_{off}$  value of  $5 \times 10^{-4} \text{ s}^{-1}$  and hence a residence time of  $\sim 33.3 \text{ min}$ .



Scheme 1.1 demonstrates the three different types of slow onset inhibition mechanism: mechanism A depicts the one-step model; mechanism B depicts the induced-fit model; mechanism C depicts the conformation selection mechanism

The second mechanism (mechanism B) is the slow onset induced-fit mechanism (Scheme 1.1) (82). This two-step binding mechanism involves the initial formation of the enzyme-inhibitor complex (EI) followed by a slow enzyme isomerization to the final enzyme-inhibitor complex EI\* (84). Since the isomerization step is the slowest and hence limiting the complex

dissociation,  $k_{-2}$  can be considered as the off rate. Mechanism B is a very common mechanism in the cases of long residence time inhibitors.

The third mechanism (mechanism C) is also called slow onset conformational selection mechanism (Scheme 1.1) (82). In this mechanism, the enzyme undergoes a slow conformational exchange between two states E and E\*, only one of which (E\*) binds the inhibitor. This mechanism is rarely encountered in the enzyme-inhibitor binding studies.

To distinguish between these three mechanisms the observed pseudo-first-order rate constant ( $k_{\text{obs}}$ ) is plotted as a function of inhibitor concentration. As shown in Figure 1.13, plotting  $k_{\text{obs}}$  as a function of inhibitor concentration for mechanism A is linear, for both mechanism B and C are a hyperbolic curves.

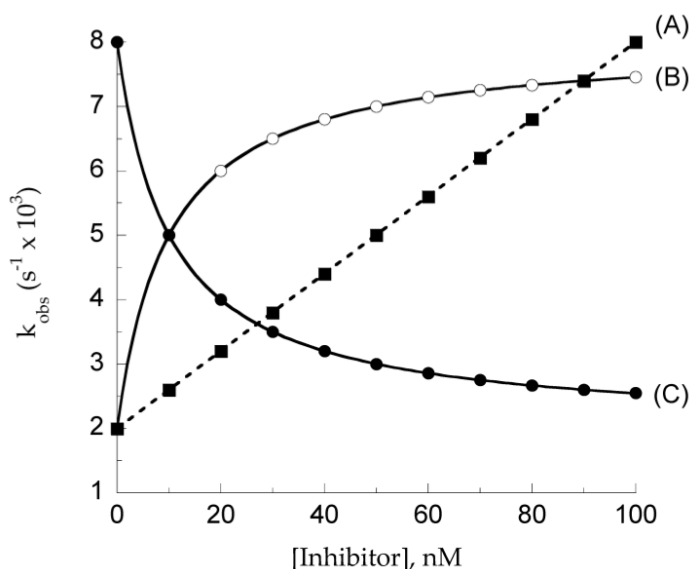


**Figure 1.13**  $k_{\text{obs}}$  as a function of inhibitor concentration

## Project overview

My thesis project has involved the discovery and analysis of slow-binding FabI inhibitors. The majority of these studies have focused on the FabI from *M. tb* (InhA). In chapter 2, I describe a robust method to directly and accurately measure residence time in the FabI system. In chapter 3, I use this method together with traditional steady-state enzyme kinetics to perform a thorough kinetic characterization of different sets of InhA inhibitors based primarily on the diphenyl ether scaffold. In Chapter 4 I then evaluate the cellular activity of some of the inhibitors described in Chapter 3. In chapter 5, I describe the discovery of novel InhA inhibitor scaffolds by leveraging the power of computational biology and high-throughput screening. Finally, in Chapter 6, I extend the analysis to the FabI enzymes from bioweapon pathogens such as *Burkholderia pseudomallei*.



## **Chapter 2 Development of kinetic tools to study slow binding inhibitors for enoyl-ACP reductase in *Mycobacterium tuberculosis* (InhA)**

This chapter is based on part of work that has been published in:

**Yu, W.**, Bommineni, G., Neckles, C., Chang, A., Pan, P., Liu, N., Spagnuolo, L., and Tonge, P., “A [<sup>32</sup>P]-Nicotinamide Adenine Dinucleotide Method to Identify and Quantitate Long Residence Time Enoyl-ACP reductase Inhibitors”, *Journal of Analytical Biochemistry*, 2015

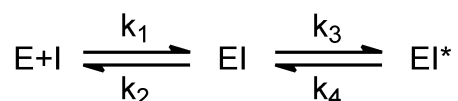
### **INTRODUCTION**

Widespread resistance to front-line and combinatorial antibiotic therapies continuously demands the development of new drugs (1-4). In the standard drug development pipeline, the strategy for developing lead compounds has mainly focused on the optimization of drug-target thermodynamics and *in vivo* pharmacokinetics (5, 6), while little attention has been paid to drug-target binding kinetics due to the assumption that the dissociation rate of the drug from the complex ( $k_{\text{off}}$ ) is too rapid to play a significant role in drug pharmacodynamics (7). However, the high attrition rate of many lead compounds from high toxicity and/or lack of efficacy (8) suggests a lack of mechanistic understanding when translating *in vitro* lead optimization to later-stage efficacy models and clinical trials. Recently, it has been suggested that drug-target residence time ( $t_R = 1/k_{\text{off}}$ ) should be included in the traditional affinity-driven drug development

strategy, since the lifetime of the drug-target complex can modulate drug efficacy, selectivity and target occupancy under non-equilibrium conditions (5, 6, 9, 10).

Drug-target residence time can be determined using a number of methods, including kinetic assays from which  $k_{\text{off}}$  values can be extracted or approaches that measure  $k_{\text{off}}$  directly. As slow-off ligands are commonly seen in time-dependent rather than in rapid equilibrium inhibition mechanisms (Scheme 2.1), progress curve analysis can be used to accurately determine  $k_{\text{off}}$  values of greater than  $0.01 \text{ min}^{-1}$  by monitoring the slow onset of inhibition in a standard enzyme assay. Although this type of analysis is information-rich since other kinetic and thermodynamic constants can be determined (Scheme 2.1), it is also an indirect method for determining  $k_{\text{off}}$ . In addition, it is limited by the pseudo-first-order rate constant ( $k_{\text{obs}}$ ) and steady-state velocity ( $v_s$ ) when characterizing low nanomolar to picomolar affinity inhibitors. For example, inhibition of polypeptide deformylase (PDF) by the natural product antibacterial agent actinonin, which has a  $K_i$  value of  $\leq 0.23 \text{ nM}$ , can result in progress curves where the steady-state velocity in the presence of inhibitor approaches zero, resulting in difficulties in estimating  $k_{\text{off}}$  and distinguishing a potent reversible inhibitor from a true irreversible inactivator (11). While, jump dilution assays can be used as an alternative and more direct method to obtain residence time through the recovery of enzyme activity (12), high affinity and slow  $k_{\text{off}}$  inhibitors pose similar problems to this approach. For instance, only partial recovery of enzyme activity was reported for the inhibition of PDF by actinonin and of hepatitis C virus NS3 protease by ITMN-191 (11, 13). Even though the  $k_{\text{off}}$  can still be estimated through fixing the steady-state velocity to 100% of the enzyme activity, iterative data fitting is required to generate a relatively accurate estimate. In addition, data acquisition time under such conditions usually requires hours

or longer, which brings into question the stability of the substrate and/or enzyme (13). In general, the classical  $k_{\text{off}}$  measurements using loss or regain of enzyme activity in progress curve kinetics are largely limited when inhibitors have residence times of many hours or days.



Scheme 2.1 time dependent inhibitor binding scheme In the two-step induced-fit inhibition mechanism, the initial EI complex is formed rapidly followed by a much slower enzyme isomerization to form the final EI\* complex.  $k_1$  and  $k_2$  depict the association and dissociation rate constants for the binding step, respectively;  $k_3$  and  $k_4$  represent the forward and reverse rate constants for the isomerization step. In many cases  $k_4 \approx k_{\text{off}}$  since the enzyme isomerization step occurs much more slowly than the initial binding event. Relevant thermodynamic constants for this mechanism include  $K_i$  and  $K_i^*$  where  $K_i = \frac{k_2}{k_1}$  and  $K_i^* = \frac{K_i}{1 + \frac{k_3}{k_4}}$

Surface plasmon resonance (SPR) is a popular alternative method for directly analyzing drug-target binding kinetics. SPR relies on changes in the refractive index of the solvent during complex formation and dissociation to directly measure molecular interactions, which includes binding affinity and binding kinetics in real time without labeling the ligand (14, 15). While SPR is a sensitive method, deployment of this approach can be hindered by mass transport and the ability to detect the interaction of small molecules with the target protein (15). Due to such limitations, SPR is generally able to produce reliable data for ligands with molecular sizes ranging from ~300 Da to polypeptides or proteins (15, 16), with reported  $k_{\text{off}}$  values normally ranging from  $2 \times 10^{-4} \text{ s}^{-1}$  to  $1 \text{ s}^{-1}$  and a total data acquisition time of up to 1200 seconds (15, 17). To our knowledge  $k_{\text{off}}$  values smaller than  $10^{-4} \text{ s}^{-1}$  have not yet been accurately reported using SPR because of technical limitations with monitoring slowly dissociating ligands (18, 19).

Therefore, alternative methods to accurately measure slow  $k_{\text{off}}$  values need to be developed for long residence time and high affinity inhibitors.

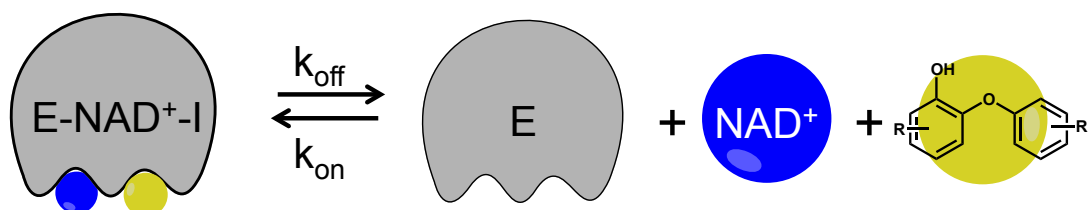


**Figure 2.1 The FabI inhibitor dissociation scheme**

As the FabI inhibitors require NAD<sup>+</sup> for binding, [<sup>32</sup>P]-NAD<sup>+</sup> was chosen as the molecule to monitor inhibitor dissociation.

Here we report a direct method for slow  $k_{\text{off}}$  measurement based on Penefsky spin columns (20-22). This method has been successfully applied to the inhibition of the fatty acid biosynthesis enoyl-ACP reductase (FabI) enzyme by a series of diphenyl ether inhibitors. The diphenyl ethers are uncompetitive inhibitors, forming a ternary complex with the enzyme and NAD(P)<sup>+</sup> (Figure 2.1). Since NAD(P)<sup>+</sup> has a millimolar dissociation constant for the enzyme (23-26), [<sup>32</sup>P]-NAD<sup>+</sup> can be used as a reporter of inhibitor dissociation. We demonstrate that this direct dissociation method is reliable and more accurate than progress curve analysis for long residence time inhibitors. We discuss the applicability and sensitivity of this method for measuring  $t_R$  values of 5 minutes to more than 10 hours. Additionally, we address how temperature affects the dissociation rate. Finally, we demonstrate how this approach can be used to screen for long residence time inhibitors in the FabI system. This new assay is suitable for the

whole FabI class of enzymes, and facilitates the identification and characterization of novel FabI inhibitors.

## **MATERIALS and METHODS**

### FabI protein preparation:

The FabI proteins from *Mycobacterium tuberculosis*, *Staphylococcus aureus*, *Escherichia coli* and *Burkholderia pseudomallei* were expressed following the protocols described previously (25, 27, 28). Briefly, the FabI gene was expressed in *E. coli* BL21(DE3) pLysS cells. Each protein was purified by affinity and size-exclusion chromatography, using His-bind Ni<sup>2+</sup>-NTA resin (Invitrogen) and Superdex 200 resin (AKTA purifier), respectively. The purity of the protein was analyzed using 12% SDS-PAGE gels and the protein was stored at -80°C in buffer containing 30 mM PIPES pH 6.8 150 mM NaCl and 1 mM EDTA.

### Substrate synthesis:

*Trans*-2-octenoyl coenzyme A (Oct-CoA) was synthesized using the mixed anhydride method (25, 29). Briefly, 277 mg (1.95 mmol) *trans*-2-octenoic acid was dissolved in 3 mL tetrahydrofuran with 140 mg (1.38 mmol) triethylamine under nitrogen. 148 mg of ethyl chloroformate (1.36 mmol) was added dropwise into the solution leading to the formation of salt crystals. The reaction was stirred at room temperature for 3 hr under nitrogen, and the mixed anhydride solution was then centrifuged at 5000 rpm for 15 min to remove the precipitate. The mixed anhydride was then added dropwise into a 2 mL solution of 20 mg (0.03 mmol) CoA in 50 mM Na<sub>2</sub>CO<sub>3</sub> (pH 8.0) and tetrahydrofuran (1:1). The reaction was stirred at room temperature for 2 hr after which excess organic solvent was removed by rotary evaporation and the Oct-CoA purified using a CombiFlash 4.3 g C18 column. The column was equilibrated with 20 mM ammonium acetate (buffer A), and Oct-CoA eluted after 20 column volumes using a linear

gradient of buffer A to 100% acetonitrile at a flow rate of 18 mL/min. Fractions containing Oct-CoA were pooled and characterized by electrospray ionization mass spectrometry (Figure 2.2). *Trans*-2-crotonyl CoA (Cr-CoA) was purchased from Sigma Aldrich (Cat# 28007).

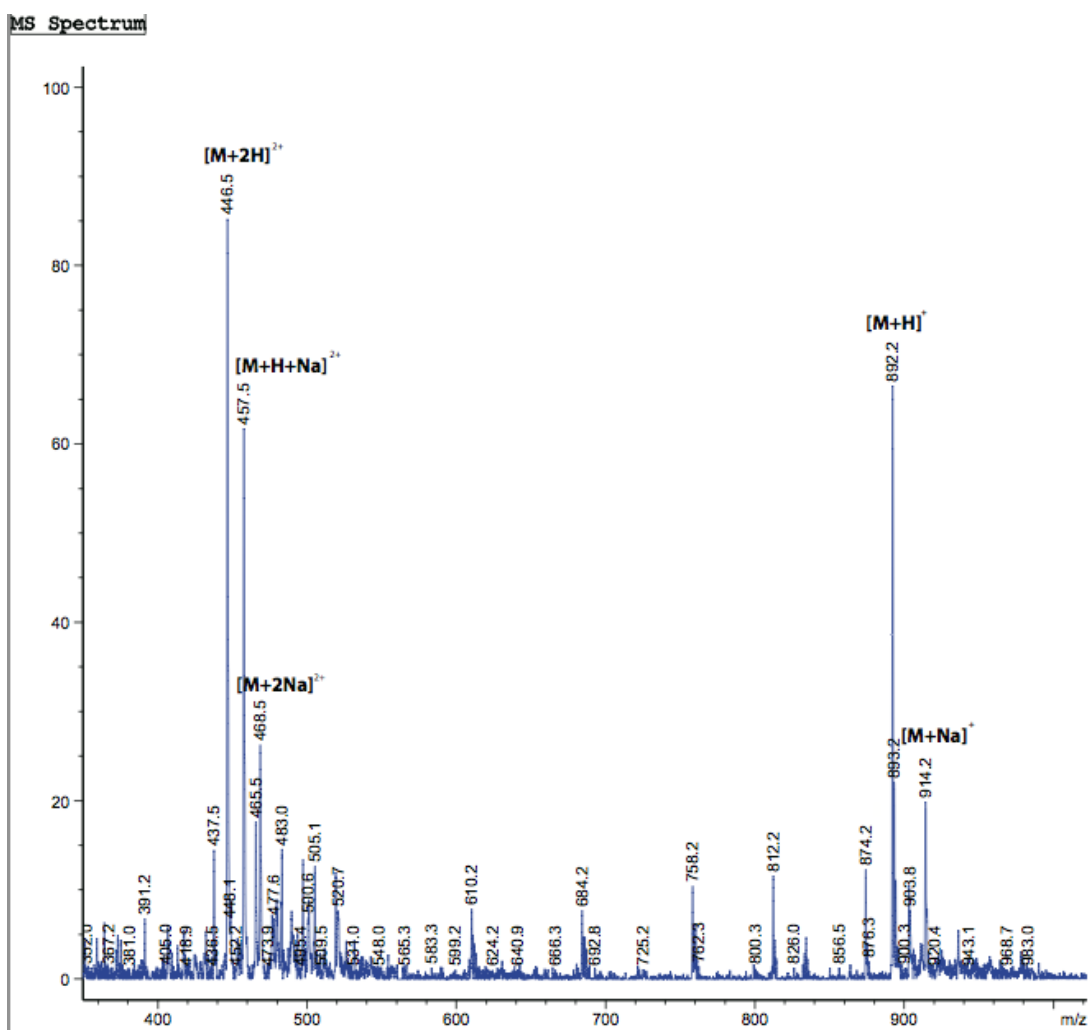


Figure 2.2 MS spectrum of *trans*-2-octenoyl coenzyme A

### Inhibitor synthesis:

Triclosan was purchased from Fisher Scientific (Cat# NC 9022139). MUT056399 was a gift from Anacor. PT01, PT02, PT03, PT04, PT05, PT52, PT70, PT103, PT113, PT91 and PT92 were synthesized as previously described (30-33), as were PT447 and PT119 (34). The synthesis of PT163, PT501, PT403, PT404, PT411, PT412 and PT417 is described in detail in the corresponding paper (35).

### [<sup>32</sup>P]-Direct dissociation kinetics:

A mixture of 15  $\mu$ M FabI, 20  $\mu$ M NAD<sup>+</sup>, [<sup>32</sup>P]-NAD<sup>+</sup> (800 Ci/ml American Radiolabeled Chemicals) and 200  $\mu$ M inhibitor were incubated in 30 mM PIPES reaction buffer pH 6.8 containing 150 mM NaCl and 1 mM EDTA at room temperature for 16 hr to allow full ternary complex formation. G25 resin (Sephadex) was hydrated in the reaction buffer and 2.5 mL resin was used to pack the Penefsky spin column. Five hundred microliters of the ternary complex was loaded onto the column which was then centrifuged using a swinging bucket rotor at 2500 rpm for 2 min to remove excess free ligand. The total radioactivity of the purified complex (~500  $\mu$ L) was determined ( $C_{\max}$  in Equation 2.1) and then the solution was rapidly diluted into 60 mL of reaction buffer to initiate ligand dissociation. Subsequently, 600  $\mu$ L aliquots of the diluted mixture were collected as a function of time, and immediately centrifuged in a Sartorius concentrator (10 kDa) at 13,400 rpm for 90 seconds. The amount of <sup>32</sup>P in the flow-through was quantified using a scintillation counter (LS5801). Data were fit to equation 1 where  $C(t)$  and  $C(0)$  are the radioactive counts (cpm) at time points  $t$  and 0, respectively,  $C_{\max}$  is the maximum radioactive counts and  $k_{\text{off}}$  is the inhibitor dissociation rate constant. This approach assumes that



NAD<sup>+</sup> dissociates rapidly from the enzyme (millimolar K<sub>d</sub>) once the inhibitor has dissociated from the ternary complex. All curve fitting was performed with KaleidaGraph 4.1.

$$C_{(t)} = C_{(o)} + C_{max} * (1 - e^{-k_{off}t})$$

Equation 2.1

Inhibitor progress curve analysis:

Progress curve analysis was performed on a Cary 100 spectrophotometer (Varian). The reaction was performed at 20 °C by adding the enzyme (75 nM) to an assay solution consisting of Oct-CoA or Cr-CoA (200 μM – 1.5 mM), NAD(P)H (250 μM – 350 μM), NAD(P)<sup>+</sup> (200 μM), DMSO (2% v), inhibitor (0 – 4000 nM) and 8% glycerol. The substrate concentration used in the assay ensured that the progress curve in the absence of inhibitor was essentially linear for the first 10% of the reaction. NAD(P)<sup>+</sup> (200 μM) was included in the assay since each inhibitor forms a ternary complex with the enzyme and the oxidized cofactor. Progress curve data were fit to equation 2.2 to obtain k<sub>obs</sub>,

$$A_t = A_0 - v_s t - (v_i - v_s) * \frac{1 - e^{-k_{obs}t}}{k_{obs}}$$

Equation 2.2

where A<sub>t</sub> and A<sub>0</sub> are the absorbance at times t and 0, respectively, v<sub>i</sub> is the initial velocity, v<sub>s</sub> is the steady state velocity, and k<sub>obs</sub> is the pseudo-first order rate constant for the approach to the steady state. Equation 2.3 was then used to obtain k<sub>off</sub>, which is the dissociation rate constant of the inhibitor from the enzyme. In a single step mechanism, the v<sub>i</sub> corresponds to the initial

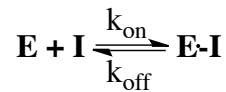
velocity when no inhibitor is present; while in the two-step induced fit mechanism,  $v_i$  represents the initial velocity when the inhibitor initially binds to the enzyme.

$$k_{off} = k_{obs} * \frac{v_s}{v_i}$$

Equation 2.3

### Correlating the ternary complex concentration as function of time

A set of curves describing the change of enzyme-drug ternary complex concentration as a function of time was constructed and plotted using KaleidaGraph 4.1. The equation used to generate these curves is derived as following:



$$v = \frac{d[EI]}{dt} = -k_{off} * [EI]$$

$$\frac{1}{[EI]} * d[EI] = -k_{off} * dt$$

$$\int_{[EI]_1}^{[EI]_2} \frac{1}{[EI]} * d[EI] = \int_{t_1}^{t_2} -k_{off} * dt$$

$$\ln[EI]_2 - \ln[EI]_1 = -k_{off} * (t_2 - t_1)$$

$$\frac{[EI]_2}{[EI]_1} = e^{-k_{off} * (t_2 - t_1)}$$

$$\frac{[EI]_t}{[EI]_0} = e^{-k_{off}t}$$

$\frac{[EI]_t}{[EI]_0}$  represents the drug-target ternary complex

recovery after operating time “t”,

therefore,

$$y = e^{-k_{off}x}$$

## RESULTS AND DISCUSSION

### The [<sup>32</sup>P]-Direct dissociation method

The [<sup>32</sup>P]-direct dissociation method was designed to directly monitor the dissociation of the inhibitors in the FabI system assuming that the limiting step was dissociation of inhibitor from the ternary complex and that release of NAD<sup>+</sup> from the resulting binary complex was rapid (Figure 2.3). FabI was incubated with excess amounts of NAD<sup>+</sup>, [<sup>32</sup>P]-NAD<sup>+</sup> and inhibitor overnight at room temperature to generate the ternary complex. Since wild-type *S. aureus* FabI (saFabI) utilizes NADPH rather than NADH, the R40Q/K41N/S44L saFabI variant was used since the kinetic parameters of this mutant are similar to the wild-type enzyme except that the cofactor preference has been switched from NADP<sup>+</sup> to NAD<sup>+</sup> (34). After incubation, the E-([<sup>32</sup>P])NAD<sup>+</sup>-I ternary complex was purified by size-exclusion spin column chromatography (20, 21) to remove free ligands (Figure 2.3). The complex was rapidly diluted to initiate ternary complex dissociation, and the amount of unbound [<sup>32</sup>P]-NAD<sup>+</sup> was quantified as a function of time following centricon separation (Figure 2.3). Although a small amount of radioactivity was present at time point 0, the subsequent change in the amount of [<sup>32</sup>P]-NAD<sup>+</sup> released accurately described the release of the ligand. Data collection was continued until the amount of [<sup>32</sup>P]-NAD<sup>+</sup> in the centricon flow-through reached a maximum.

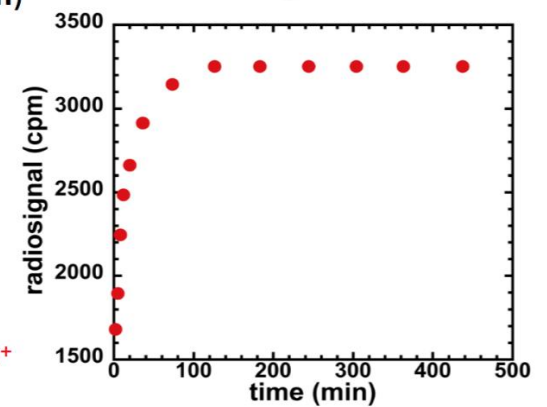
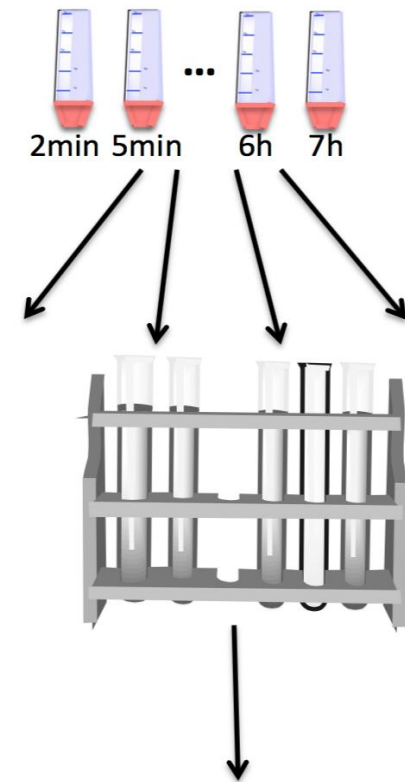
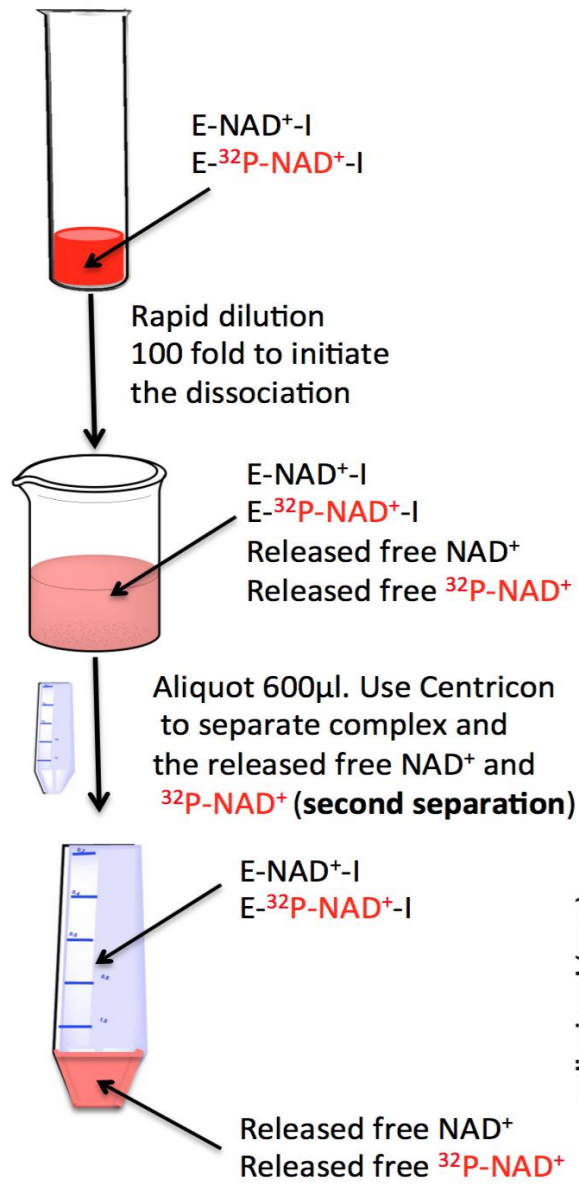
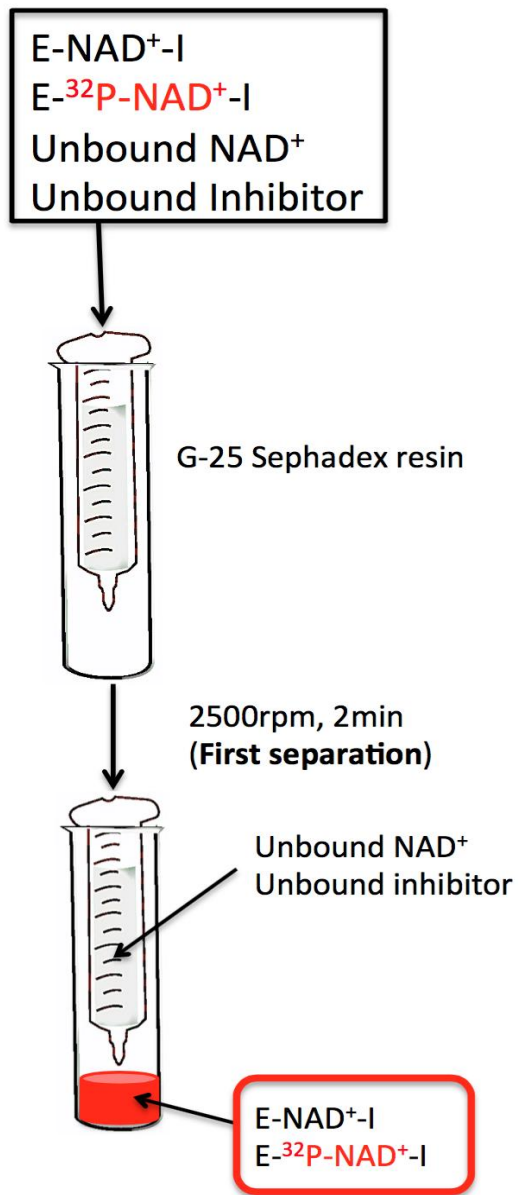


**Figure 2.3 The [<sup>32</sup>P]-NAD<sup>+</sup> direct dissociation method**

15 μM FabI, 20 μM NAD<sup>+</sup>, [<sup>32</sup>P]-NAD<sup>+</sup> and 200 μM inhibitor were incubated at room temperature overnight before loading onto the G25 Sephadex spin column. The ternary complex was purified from excess ligand using a 2 min spin at 2500 rpm. The complex was rapidly diluted 100-fold to initiate dissociation. 600 μL aliquots of the diluted inhibitor complex were collected as a function of time points loaded onto a centricon concentrator to separate the dissociated ligand from the enzyme-inhibitor complex. Free ligand was subsequently quantified using a scintillation counter to detect <sup>32</sup>P.

The challenges of this direct dissociation method arise through the development of the two separation steps (Figure 2.3). The purification of the ternary complex from the reaction mixture (Figure 2.3 first separation) must be performed with only limited dilution, since this will trigger ligand dissociation thus leading to inaccurate results. Therefore, we introduced a gel filtration technique using the spin column described before (20) in which size exclusion chromatography is performed using centrifugation. Several steps had to be optimized during development of this procedure to efficiently separate the protein from the ligand. This included adjustments to the bed resin volume of the size-exclusion spin column, the volume of sample that was loaded onto the column, the spin speed and the separation time. Figure 2.4 A shows the UV absorbance of the sample containing 15 μM protein before and after loading onto the spin column. While the A<sub>280</sub> of a 15 μM FabI sample (500 μL) decreased from 0.15 before the spin to 0.1 after the spin (Figure 2.4 A), the A<sub>260</sub> of a 25 μM NAD<sup>+</sup> solution (500 μL) decreased from 0.44 to 0.04 after the spin (Figure 2.4 B). Using this procedure the ratio of A<sub>280</sub> or A<sub>260</sub> before and after the spin was used to determine the recovery of protein or NAD<sup>+</sup>, respectively, in each experiment. In Figure 2.4 C, it can be seen that recovery of the protein was as high as 70% - 80%

for the four different FabIs, while the recovery of  $\text{NAD}^+$  was only  $\sim 5\%$ , indicating the efficiency of the column for separating large and small molecules.

The ability of the spin column to isolate the ternary  $\text{E:NAD}^+:\text{I}$  complex was then evaluated (Figure 2.4 D). While recovery of the ternary complex was as high as 80% (Figure 2.4 D), omission of inhibitor from the enzyme incubation mixture resulted in only  $\sim 5\%$  recovery of  $\text{NAD}^+$ , in agreement with the expectation that  $\text{NAD}^+$  binds only weakly to the free enzyme.

In the second separation (Figure 2.3 second separation), the  $\text{NAD}^+$  and  $[\text{}^{32}\text{P}]\text{-NAD}^+$  that has dissociated from the complex needs to be separated from the remaining ternary complex. Since dissociation is still occurring during the second separation, purification of free  $\text{NAD}^+ / [\text{}^{32}\text{P}]\text{-NAD}^+$  has to be performed significantly faster than the rate of inhibitor dissociation from the ternary complex. Although dialysis has previously been used to monitor radiotracer dissociation (36), we found this method to be too slow and instead adopted an approach that uses a centricon where the centrifugation time was shorter than the time interval between two different time points.

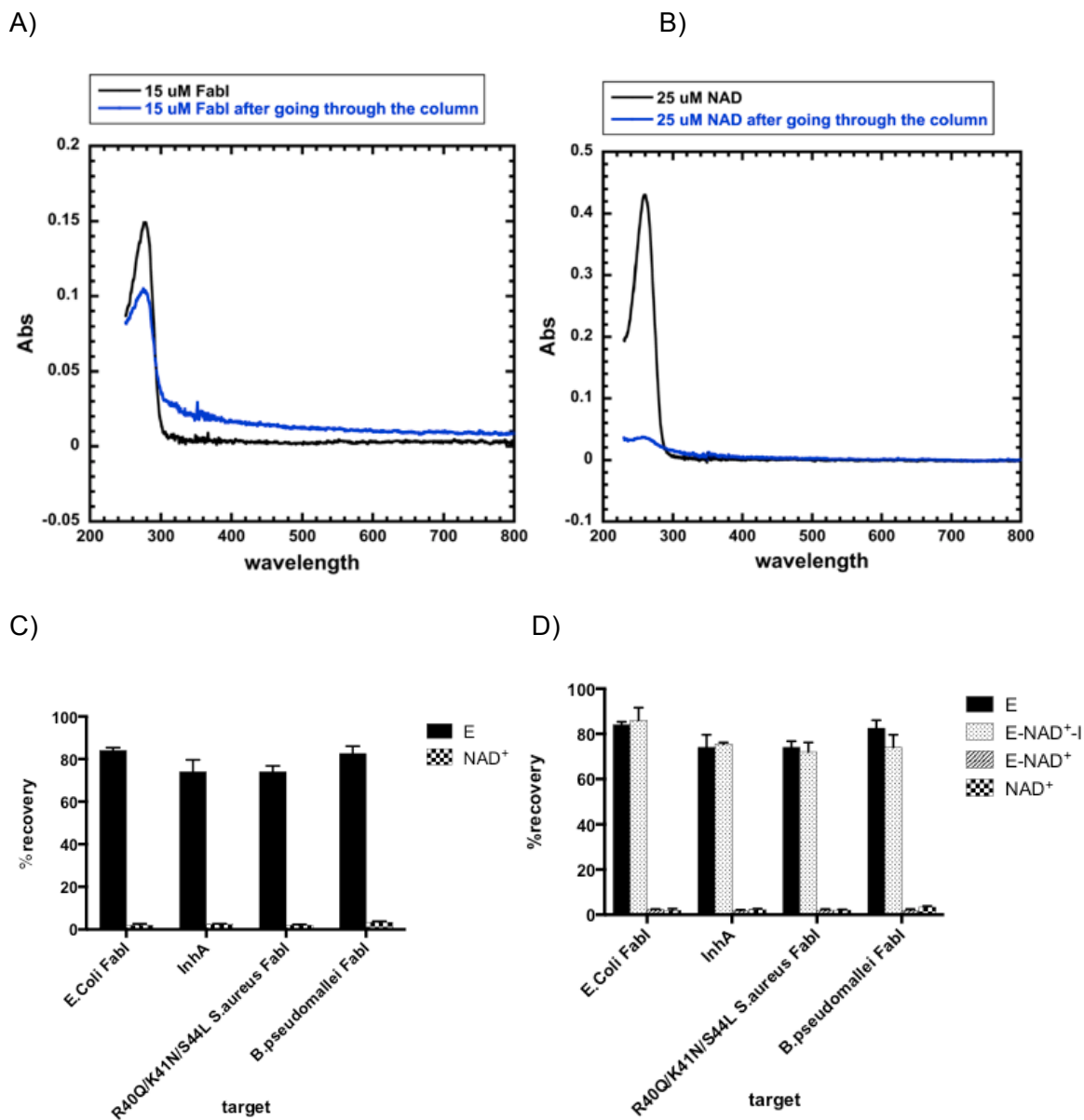


**Figure 2.4 Method validation**

A) The absorbance of enzyme at 280 nm before and after the spin column.

B) The absorbance of NAD<sup>+</sup> at 260 nm before and after the spin column

C) The percent recovery of the enzyme and NAD<sup>+</sup> was quantified by calculating the ratio of the absorbance before and after loading onto the G25 Sephadex spin column at 280 nm and 260 nm, respectively.

D) The percent recovery of the E-NAD<sup>+</sup> complex and E-NAD<sup>+</sup>-I complex was quantified by calculating the radioactive counts before and after loading onto the G25 Sephadex spin column.



## Determination of drug-target residence time using the direct dissociation method and progress curve analysis

Residence times determined using the direct dissociation method developed here were compared with those measured using progress curve analysis, which is widely used method for analyzing time-dependent enzyme inhibition (11, 13, 37-39). The direct dissociation method was first evaluated using a series of diphenyl ether inhibitors of the *M. tuberculosis* FabI (InhA). In Figure 2.5 A it can be seen that there is excellent agreement between the  $t_R$  values obtained from the direct dissociation method and progress curve analysis when  $t_R$  is under 100 minutes ( $R^2$  0.99). The method was then extended to *B. pseudomallei* FabI (bpFabI), saFabI and *E. coli* FabI (ecFabI). As shown in Figure 2.5 B, 2.5 C and 2.5 D, this method was able to accurately determine  $t_R$  values for bpFabI, saFabI and ecFabI inhibitor complexes ( $R^2$  0.78, 0.90 and 0.74, respectively). In Figure 2.5 E, all FabI datasets were compiled, which verified the accuracy of the new method and its applicability to different FabI systems.

While good agreement between the methods was generally observed for drug-target complexes with  $t_R$  values below 100 min, the direct dissociation method consistently gave larger  $t_R$  values than progress curve analysis for longer residence time inhibitors (Figure 2.5 F). For example, the direct dissociation method gave a  $t_R$  value of (148.4±13.4) min for PT91 bound to InhA, while progress curve analysis provided a shorter  $t_R$  of (102.1±11.4) min (Table 2.1). Additionally, progress curve analysis gave  $t_R$  values of 238.0 min and 68.6 min for PT404 and PT417 bound to bpFabI, while the direct dissociation method gave significantly longer  $t_R$  values of 713.0 min and 198.5 min, respectively (Table 2.1). Similarly, in the saFabI system, progress

curve analysis underestimated the  $t_R$  values of PT04 and PT119 (97 min and 120.3 min, compared to 461.5 min and 833.3 min, respectively, Table 2.1).

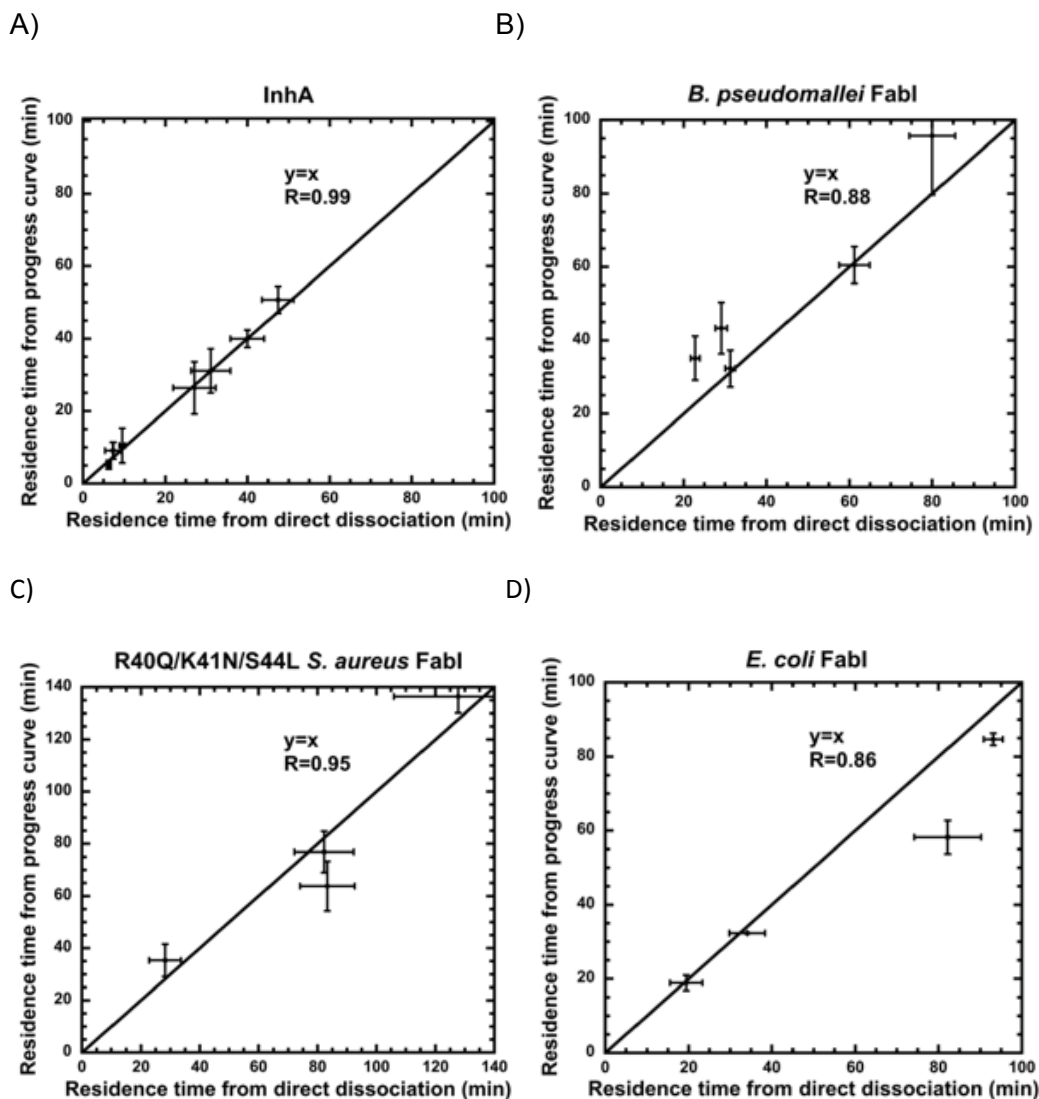


**Figure 2.5 Comparison of residence times generated by the progress curve analysis and the  $^{32}\text{P-NAD}^+$  direct dissociation method for inhibitors with residence times under 100 min**

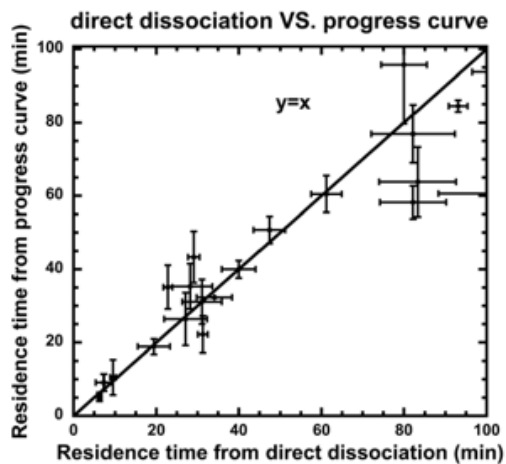
A) Data for *M. tuberculosis* FabI (InhA). Linear fit of the data gave  $R^2 = 0.99$ .

B) Data for *B. pseudomallei* FabI. Linear fit of the data gave  $R^2 = 0.78$ .

C) Data for R40Q/K41N/S44L *S. aureus* FabI. Linear fit of the data gave  $R^2 = 0.90$ .

D) Data for *E. coli* FabI. Linear fit of the data gave  $R^2 = 0.74$ .

E)



F)

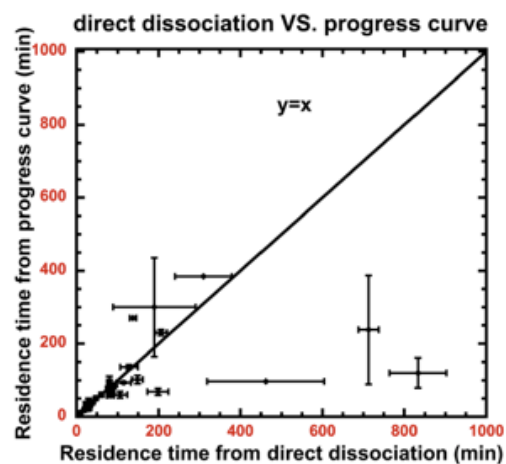


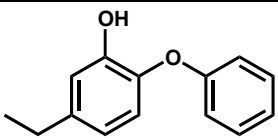
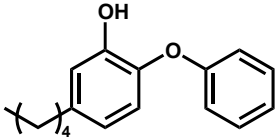
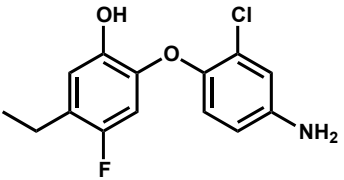
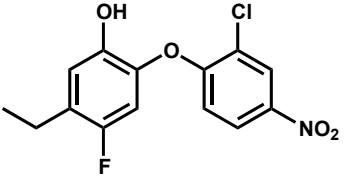
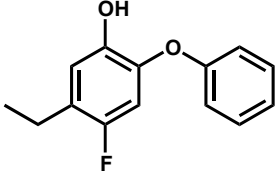
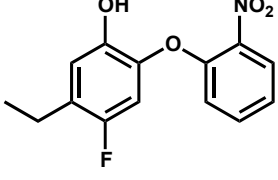
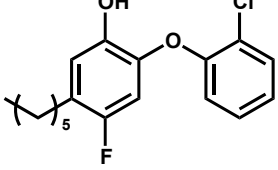
Figure 2.5 E) Comparison of all data obtained using the direct dissociation method and progress curve analysis for inhibitors with residence times under 100 min.

F) Comparison of all data obtained using the direct dissociation method and progress curve analysis for inhibitors with residence times up to 1000 min.

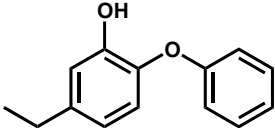
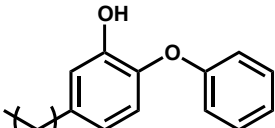
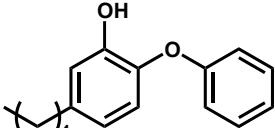
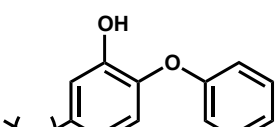
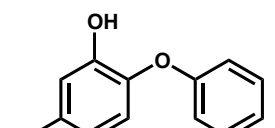
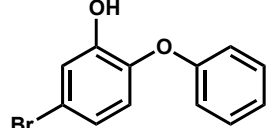
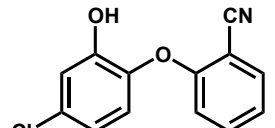
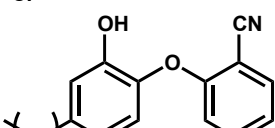
Table 2.1 Comparison of direct dissociation and progress curve analysis under different FabI systems

*M. tuberculosis* FabI

| Compound | Structure | Residence time from progress curve analysis (min) <sup>1</sup> | Residence time from direct dissociation (min) <sup>2</sup> |
|----------|-----------|--|--|
| PT04     |           | 10.5±4.8   | 9.5±0.7  |
| PT05     |           | 26.4±7.2   | 27.1±5.2   |
| PT70     |           | 40.0±2.4   | 40.0±4.1   |
| PT119    |           | 50.7±3.7   | 47.4±3.8   |
| PT113    |           | 31.1±6.1   | 31.1±4.8   |
| PT91     |           | 102.1±11.4   | 148.4±13.4   |
| PT13     |           | 5.2±1.2  | 6.3±0.5  |
| PT96     |           | 9.1±2.3  | 7.3±1.9  |
| PT163    |           | 93.8±2.6   | 114.3±17.8   |
| PT501    |           | 230.1±7.9  | 206.0±14.6   |

| Compound | Structure   | Residence time from progress curve analysis (min) <sup>1</sup> | Residence time from direct dissociation (min) <sup>2</sup> |
|----------|---|--|--|
| PT01     |    | 22.5±5.0   | 31.3±1.2   |
| PT04     |    | 35.1±6.0   | 22.8±1.1   |
| PT403    |    | 60.5±5.0   | 61.2±3.7   |
| PT404    |    | 238±149  | 713.0±24.7   |
| PT411    |  | 43.3±7.0   | 29.1±1.4   |
| PT412    |  | 95.7±16.0  | 80.0±5.5   |
| PT417    |  | 68.6±9.1   | 198.5±25.6   |

*S. aureus* FabI

| Compound | Structure   | Residence time from progress curve analysis (min) <sup>3</sup> | Residence time from direct dissociation (min) <sup>2</sup> |
|----------|---|--|--|
| PT01     |    | 63.8±9.5   | 83.3±9.5   |
| PT02     |    | 60.6±9.2   | 105.8±17.5   |
| PT03     |    | 300.3±135.3  | 189.5±100.8  |
| PT04     |    | 97 <sup>4</sup>  | 461.5±142.7  |
| PT52     |   | 35.3±6.2   | 28.2±5.4   |
| PT103    |  | 76.9±7.9   | 82.2±10.1  |
| PT447    |  | 136.4±6.2  | 127.7±21.7   |
| PT119    |  | 120.3±41.3   | 833.3±69.4   |

| Compound  | Structure | Residence time from progress curve analysis <sup>1</sup><br>(min) | Residence time from direct dissociation <sup>2</sup><br>(min) |
|-----------|-----------|---|---|
| PT01      |           | 32.3±0.07   | 34.1±4.3  |
| PT04      |           | 17.6±2.1  | 19.4±3.9  |
| MUT056399 |           | 62.9±1.6  | 93.1±2.3  |
| PT103     |           | 53.2±4.5  | 82.2±8.0  |
| Triclosan |           | 270.3 <sup>4</sup>  | 137.7±8.04  |
| PT447     |           | 384.6 <sup>4</sup>  | 309.6±69.4  |

<sup>1</sup> mean value calculated from individual progress curves. Errors represent the standard deviation from the mean.

<sup>2</sup> value calculated by taking the inverse of  $k_{\text{off}}$  where  $k_{\text{off}}$  is obtained by equation 3. Errors are propagated from  $k_{\text{off}}$

<sup>3</sup> values from reference (34)

<sup>4</sup> values estimated from a single progress curve at a specific inhibitor concentration

Progress curve assays are robust and have been widely used to analyze time-dependent inhibition in systems such as FabI (11, 13, 37-39). While thermodynamic and kinetic constants can be derived from progress curves yielding a detailed picture of the inhibition reaction coordinate (40), some caution should be exercised when applying this approach to highly potent compounds with very long residence times. In reality, progress curves are only accurate within a certain range of inhibitor concentrations. At high inhibitor concentration,  $k_{obs}$  can be very fast and the low signal/noise of  $v_s$  and/or solubility issues can limit the analysis. For instance, an 8-fold difference in  $k_{off}$  is observed in the PT119 inhibition of saFabI (Table 2.1). As shown in Figure 2.6 A and Table 2.2, this is because no significant change in  $v_s$  can be detected at high inhibitor concentrations. Conversely, at low inhibitor concentrations,  $k_{obs}$  will be small mitigating long detection times in order for  $v_s$  to be reached but leading to issues with the time window of progress curve linearity. As shown in Figure 2.6 B and Table 2.3, the time window of progress curve linearity is  $\sim 30$  min in the absence of inhibitor; however, the  $k_{obs}$  value at low inhibitor concentration is  $0.036 \text{ min}^{-1}$ , meaning that the conversion from  $v_i$  to  $v_s$  occurs in  $\sim 27$  min. Under such conditions, it is difficult to distinguish whether  $k_{obs}$  represents the rate constant for the conversion of EI to EI\*, or substrate consumption due to the limited linearity in the experimental window. In addition, since small  $k_{obs}$  values usually lead to longer data acquisition times required to reach the steady state, this brings into question the stability of the substrate or the enzyme, and the accuracy of  $v_s$ . Finally, obtaining  $k_{off}$  through hyperbolic fitting of  $k_{obs}$  and  $[I]$  can be indirect and inaccurate. For instance, a potent reversible inhibitor may not be distinguished from an irreversible inhibitor due to an extremely small  $k_{off}$  value (11). Hence, these limitations hinder the use of progress curve analysis in the characterization of high affinity, long residence time inhibitors.



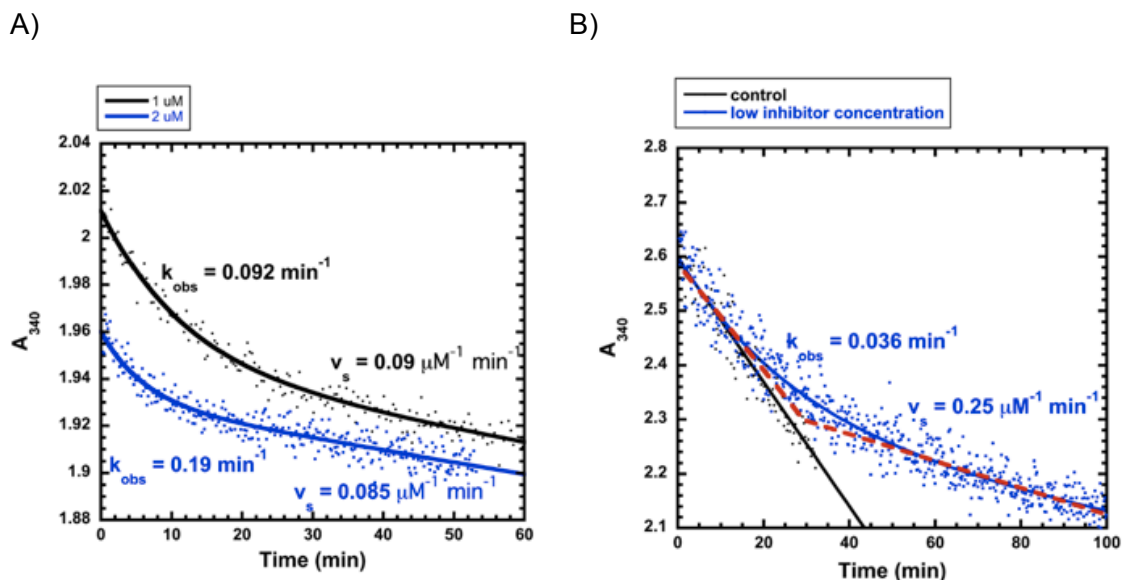


**Figure 2.6** Examples where progress curve analysis cannot accurately determine  $k_{\text{off}}$

A)  $k_{\text{obs}}$  and  $v_s$  when inhibitor concentration is increased from 1  $\mu\text{M}$  to 2  $\mu\text{M}$ .

B)  $k_{\text{obs}}$  and  $v_s$  determined using low inhibitor concentration. The intersection of the red dash line represents the time corresponding to the conversion of EI to EI\*.

Table 2.2 Parameters obtained from progress curve analysis under different inhibitor concentrations

| Inhibitor concentration<br>( $\mu\text{M}$ ) | $k_{\text{obs}}$ ( $\text{min}^{-1}$ ) | $v_s$ ( $\mu\text{M}^{-1} \text{ min}^{-1}$ ) |
|--|--|---|
| 1  | 0.092                                  | 0.090   |
| 2  | 0.19                                   | 0.085   |

Table 2.3 Parameters obtained from progress curve analysis at low inhibitor concentration

| Low inhibitor concentration | $k_{\text{obs}}$ ( $\text{min}^{-1}$ ) | $v_s$ ( $\mu\text{M}^{-1} \text{min}^{-1}$ ) |
|-----------------------------|--|--|
|                             | 0.036                                  | 0.25   |

Measuring residence time under physiological temperature is feasible by this method

The direct dissociation method can be readily adapted to studying  $k_{\text{off}}$  values as a function of temperature. In principal, this enables residence times to be determined under physiologically relevant conditions (37 °C) (41), and also facilitates Arrhenius type analysis for extracting enthalpic and entropic contributions to binding. Such analyses are problematic with progress curve kinetics, where long acquisition times required to capture formation of the final EI\* complex are confounded by the decrease in NAD(P)H stability observed at elevated temperatures (42, 43). Since the direct dissociation method utilizes  $\text{NAD}^+$  rather than NADH, this method can be utilized at different temperatures, and in Figure 2.7 it can be seen that the residence time is ~ 4-fold shorter at 37 °C compared to 25 °C for inhibitors bound to ecFabI (Figure 2.7).

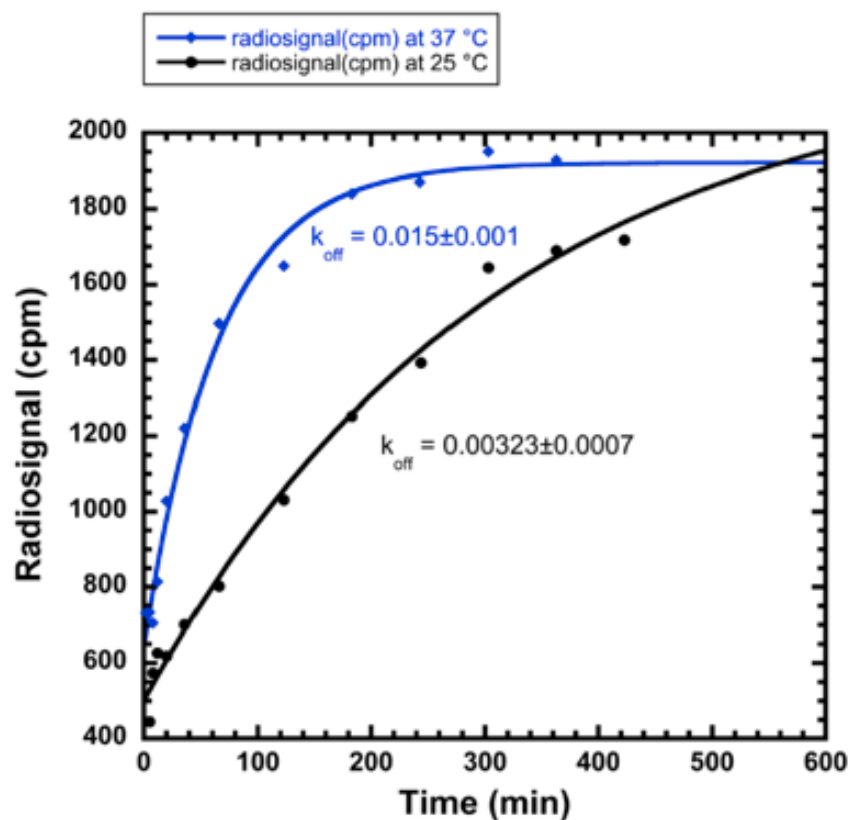


Figure 2.7 Comparison of  $k_{off}$  values determined at 25 °C and 37 °C for inhibitors bound to *E. coli* FabI

Recovery of ternary complex correlates with the inhibitor dissociation rate constant

Interestingly, we found a correlation between the amount of ternary complex recovered following centrifugation and the inhibitor off-rate (Table 2.4). After optimizing the procedure, we estimated that the minimum time from the start of chromatography to collection of the centricon flow-through was ~ 2 min. Ternary complexes that were isolated in less than 30% yield

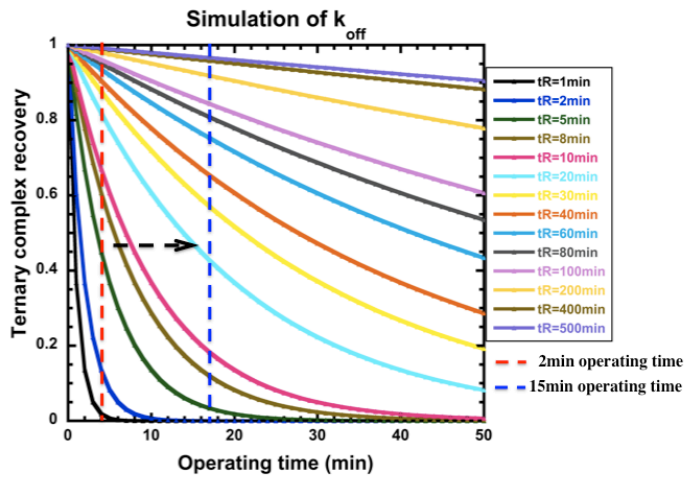
involved inhibitors with  $t_R$  values less than 10 min. Subsequent increases in  $t_R$  led to higher recovery of the ternary complex. Based on this observation, we simulated a set of curves to investigate the relationship between ternary complex recovery and inhibitor  $k_{off}$  values (Figure 2.8 A). Using these simulated curves, we were able to estimate a theoretical  $k_{off}$  range based on the yield of ternary complex. Surprisingly, we found a good agreement between the theoretical  $k_{off}$  values and those determined experimentally by monitoring the dissociation of [ $^{32}P$ ]-NAD<sup>+</sup> (Table 2.4). Compounds that gave ternary complexes in less than 30% yield corresponded to residence times of 1 – 2 min from the simulated curves, while experimental data indicated a  $t_R$  value of ~1 min. For higher recoveries, the simulation yielded an estimate of  $t_R$  values from 10 to 20 min, while experimental values were 20.0 min, 19.6 min and 22.7 min respectively. Thus, we were able to estimate  $t_R$  by simply analyzing the ternary complex recovery after a 2 min spin time. A replot of Figure 2.8 A, at a 2 min operating time, reveals that the yield of ternary complex recovery is greater than 80% when  $t_R$  values are longer than 10 min (Figure 2.8 B). Thus, the percent of complex recovery cannot easily distinguish complexes with residence times longer than 10 min. However, the dynamic range of this method can be increased by altering the time period of the gel filtration step. If the separation time is increased from 2 min to 15 min, a replot of Figure 2.8 A (Figure 2.8 C) shows that the recovery of a 10 min  $t_R$  enzyme-inhibitor complex decreases from 82% to 22% (Figure 2.8 B vs. Figure 2.8 C). However, the recovery of a 60 min  $t_R$  enzyme-inhibitor complex only decreases from 97% to 78% (Figure 2.8 B vs. Figure 2.8 C). Therefore, while the spin column method is optimized for rapid separation of free and bound ligands, in principle it could be adapted to generate longer separation times by changing parameters such as the operating time and bed volume (data not shown). In addition, the longer  $t_R$  enzyme-inhibitor complexes could also be differentiated by performing the separation at

different temperatures. Since a 4-fold increase in  $k_{\text{off}}$  is expected as shown in Figure 2.7, the inhibitor that still shows high complex recovery under higher temperature indicates long residence time.

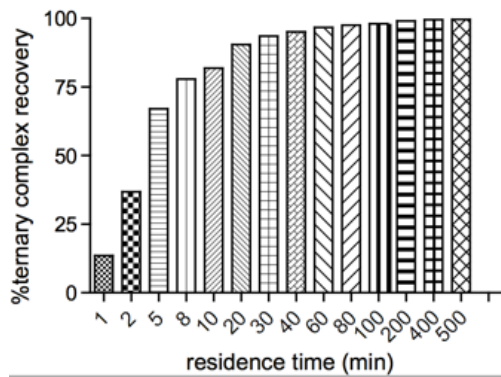
Table 2.4 Comparison of  $k_{\text{off}}$  values obtained from experiment and simulation

| Ternary complex recovery from experiment | $k_{\text{off}}$ from experiment ( $\text{min}^{-1}$ ) | Residence time from experiment (min) | Residence time range from theoretical curve (min) |
|--|--|--------------------------------------|---|
| 18%                                      | 1.10   | 0.91                                 | < 1   |
| 28%                                      | 1.10   | 0.90                                 | 1 – 2   |
| 58%                                      | 0.140  | 7.14                                 | 2 – 5   |
| 82%                                      | 0.050  | 20.0                                 | 10 – 20   |
| 84%                                      | 0.051  | 19.6                                 | 10 – 20   |
| 87%                                      | 0.044  | 22.7                                 | 10 – 20   |

A)



B)



C)

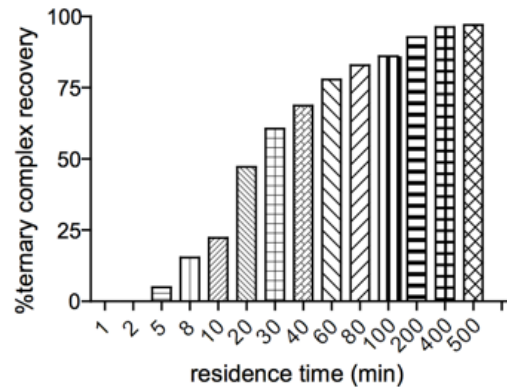


**Figure 2.8 High throughput screening to identify slow off-rate inhibitors**

A set of simulated curves depicts the change of drug-target complex concentration over time.

A) Using a 2 min and 15 min operating time, respectively

B) A replot of ternary complex recovery following 2 min separation as a function of  $t_R$

C) A replot of ternary complex recovery following 15 min separation as a function of  $t_R$

Direct dissociation method together with the conventional steady-state kinetics is able to cover a wide range for residence time measurement

Since the direct dissociation method reported here avoids the use of steady-state kinetics measurements, it does not have the shortcomings found in classical progress curve or jump dilution methods. The  $k_{\text{off}}$  is obtained by fitting the rate of formation of free [ $^{32}\text{P}$ ]NAD $^{+}$  using a simple exponential decay function (Equation 2.1) without additional calculation or derivation. In principle, this direct dissociation method can be expanded by using other methods of detecting free ligand such as fluorescence. In this regard, Goolijarsingh *et al* determined the residence time of BDGA for heat shock protein (Hsp) 90 by monitoring the time-dependent change in BDGA fluorescence anisotropy following dilution of a BDGA-Hsp90 complex to trigger dissociation (44). In our system, the use of a radioactive ligand allows the method to be applied to very potent inhibitors where high levels of dilution are required to initiate complex dissociation. Using this method, we are able to measure  $t_{\text{R}}$  values from 1 min (Table 2.4) to 800 min (Figure 2.5 F and Table 2.1). Recently, we have identified a diphenyl ether-based inhibitor that has a  $t_{\text{R}}$  value of more than 2 days by this direct dissociation method (data not shown). Combined with steady-state kinetics and SPR, the current methods are able to cover a broad timescale of  $k_{\text{off}}$  from as short as seconds to several days (Figure 2.9).

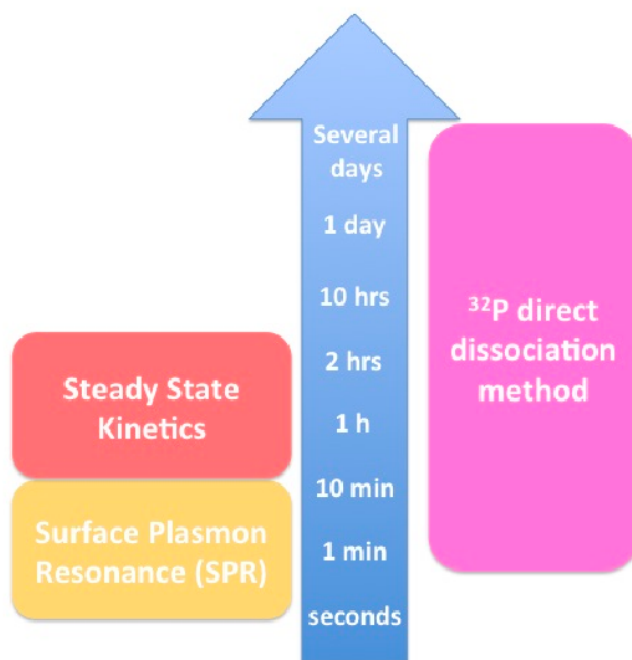


**Figure 2.9 Relative timescales of methods to determine  $k_{off}$**   
 A representation of the time range that each method can cover on the  $k_{off}$  timescale

### Advantages and disadvantages of direct dissociation method

Based on the correlation between the ternary complex recovery and inhibitor off-rate (Figure 2.8 and Table 2.4), we defined “slow off” inhibitors in the FabI system as those with at least 10 min residence time, which translates the qualitative terminology “slow” to a more quantitative concept. Furthermore, it is possible to use the method to identify compounds in a



library with relatively small off-rates. For example, compounds could be incubated with the enzyme and [<sup>32</sup>P]-NAD<sup>+</sup> in a 96 well-plate format. After a fast spin, slow off inhibitors could be identified and residence times estimated by simply analyzing the complex recovery quantified scintillation counting. If necessary, one can perform the fast spin at a higher temperature, to study the effect of temperature on  $k_{\text{off}}$ . The rate constant will be shortened at elevated temperatures thereby reducing the amount of ternary complex that is recovered. To our knowledge, this type of information is lacking in the determination of off-rates using high throughput screening (45). Therefore this method would be very valuable and useful for pharmaceutical industry at the early stage of drug development.

There are still potential weaknesses of the method reported here (Table 2.5). First, our approach requires NAD<sup>+</sup> as the cofactor when the inhibitor binds to the enzyme. If the inhibitor does not require a cofactor or is bound together with alternative cofactors, this method has to be modified. Secondly, this method is not as accurate for very short  $t_R$  inhibitors. As discussed above, for inhibitors with short  $t_R$ , we will lose considerable amounts of the ternary complex during the first separation. This will result in a relatively low yield of complex recovery. Also, we need to be cautious about the second separation step (Figure 2.3). Since inhibitor dissociation cannot be halted during the second separation, the amount of the free NAD<sup>+</sup> that is quantified will be less accurate for short  $t_R$  inhibitors due to their fast dissociation. For these short  $t_R$  inhibitors, alternative strategies can be readily used, including progress curve analysis and jump dilution assays (Figure 2.9). Lastly, there could still be potential rebinding problems in this method (46). The way the method has been designed is to remove the excess ligand before rapid dilution without adding any competing ligand after the dilution (Figure 2.10 B)., One way to

improve this method for extremely potent inhibitors is to add a competing ligand to prevent ligand rebinding (Figure 2.10 C and 2.10 D). Motulsky *et al* has discussed in detail the determination of dissociation rates using a competitive binding assay (47).

Table 2.5 Advantages and disadvantages of the direct dissociation method

| <b>Advantages</b>   | <b>Disadvantages</b>                                   | <b>How to improve</b>                                       |
|---|--|---|
| Direct method   | Requires NAD <sup>+</sup> as cofactor for binding      | Synthesize radiolabeled cofactor through enzymatic reaction |
| Accurate for long residence time inhibitors                   | Not very sensitive to short residence time measurement | N/A   |
| Applicable for FabI system                                    | Could have rebinding issue                             | Adding competing ligand                                     |
| Potentially can be used as a high throughput screening method |  |   |

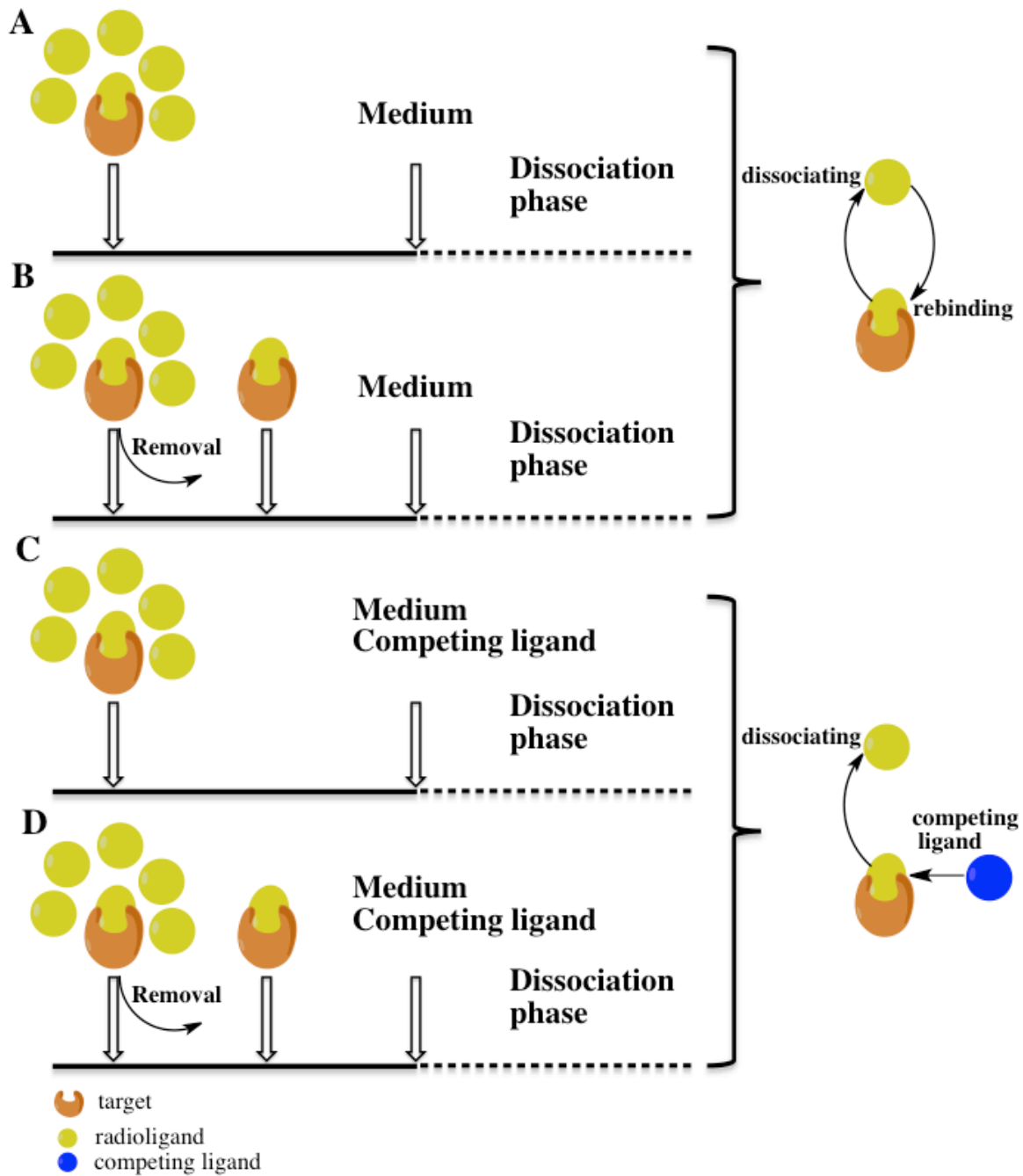


**Figure 2.10 Comparison of approaches to directly measure ligand dissociation**

- A) A dissociation scheme without removal of excess ligands and no competing ligand
- B) A dissociation scheme with removal of excess ligands but no competing ligand
- C) A dissociation scheme without removal of excess ligands but with competing ligand
- D) A dissociation scheme with removal of excess ligands and in the presence of a competing ligand

## CONCLUSION

A novel method for the direct measurement of residence time has been developed and applied to the enoyl-ACP reductase system. The method showed very reliable results compared to classical steady-state kinetic analyses, and was more accurate than progress curve analysis for inhibitors with very long residence times. A correlation was found between the drug-target ternary complex recovery and off-rate enabling the method to be expanded to a high throughput format. An advantage of this method is the use of radiolabeled ligand that permits accurate quantitation of low ligand concentrations thus enabling off-rates to be determined for very potent compounds. Even though this method is designed specifically for the enoyl-ACP reductase system, our approach could be adapted to other systems in order to validate kinetic approaches to determination of drug-target residence times and also as a potential strategy for the high throughput discovery of long residence time inhibitors.

### **Chapter 3 Unraveling the slow onset inhibition of InhA, the enoyl ACP reductase from *Mycobacterium tuberculosis*: Mechanism and inhibitor design**

This chapter is based on the publication that under preparation:

**Yu, W., Spagnuolo, L., Eltschkner, S.,** Chang, A., Li, H., Reddy, G., Shah, S., Kisker, C., and Tonge, P. J. “Unraveling the slow onset inhibition of InhA, the enoyl ACP reductase from *Mycobacterium tuberculosis*: Mechanism and inhibitor design ”, *under preparation, 2015*

Co-first author contributions:

**Yu, W.** – Enzyme kinetics, mutagenesis

Eltschkner, S. – X-ray crystallography

Spagnuolo, L. – triazole diphenyl ether synthesis

### **INTRODUCTION**

High attrition rates in the late stages of the drug development pipeline mitigate an analysis of aspects of drug discovery that are underappreciated and/or not fully exploited. In particular, drug-target kinetics has recently emerged as an important facet of the drug discovery process (1-4). Drug-target residence time, the reciprocal of the drug-target complex dissociation rate constant, is a key factor in modulating the efficacy of drug

action (1, 4). Three common mechanisms associated with time-dependent inhibition are listed in Table 3.1 (5). According to the New Molecular Entities (NME) approved by the US FDA between 2001 and 2004 (6), only 20% of the NMEs follow the mass action-sensitive equilibrium binding, whereas 80% utilize conformational changes and/or non-equilibrium kinetic mechanisms, indicating equilibrium binding alone is not sufficient to fully predict drug pharmacodynamics. Optimized binding kinetics can result in a variety of promising end results, such as greater efficacy, longer duration of response, differentiation of therapeutic indications and/or greater tolerability (4). Many systems have shown the importance of drug-target kinetics in bridging *in vitro* drug property with cellular or *in vivo* efficacy and safety (4). For example, Walkup *et al* studied a series of LpxC inhibitors that demonstrate slow binding kinetics *in vitro* and proposed that this contributes to prolonged inhibition of bacterial growth both in cellular and *in vivo* infection models after compound removal (7). In addition, the discovery of kinetically selective HDAC 2 inhibitors by Wagner *et al* indicated that the isoform selective inhibitors might mitigate some known mechanism-based toxicological effects associated with the inhibition of multiple HDACs (8). Furthermore, a small molecule IGF-1R inhibitor with a slow off-rate produced significant tumor growth inhibition at a remarkably low dose, suggesting the significant influence of drug-receptor off-rate on the overall profile of drug activity (9). In order to optimize drug-target off-rate, or residence time, a detailed mechanistic understanding of the formation and dissociation of drug-target complex on the molecular level is required. However, a detailed description of the slow onset inhibition kinetics is often elusive, due to the transient nature of the initial EI

complex (10). So far, there is only limited number of systems where this process has been elucidated in detail (11-13).

Using the enoyl-ACP reductase (FabI) (Figure 3.1) as our model system, we have shown a direct correlation between drug-target residence time and *in vivo* efficacy in a Tularemia mice infectious model (14). This finding indicated the importance of drug-target residence time as a pivotal parameter in the FabI inhibitor lead optimization. Further, we have evolved a series of slow onset inhibitors of InhA, the FabI homolog in *Mycobacterium tuberculosis* (15), and solved a number of crystal structures to provide a structural basis for understanding this slow onset inhibition mechanism (16). The structural framework suggested that the transition state energy barrier associated with the slow onset inhibition from EI to EI\* was a result of large-scale protein conformational change caused by the diphenyl ether class of compounds. This structural change corresponded to an open to closed conformation of the substrate binding loop (SBL) helix 6, transforming the protein from a catalytic-active open active site into a closed structural state that incapable of natural substrate turnover (16).

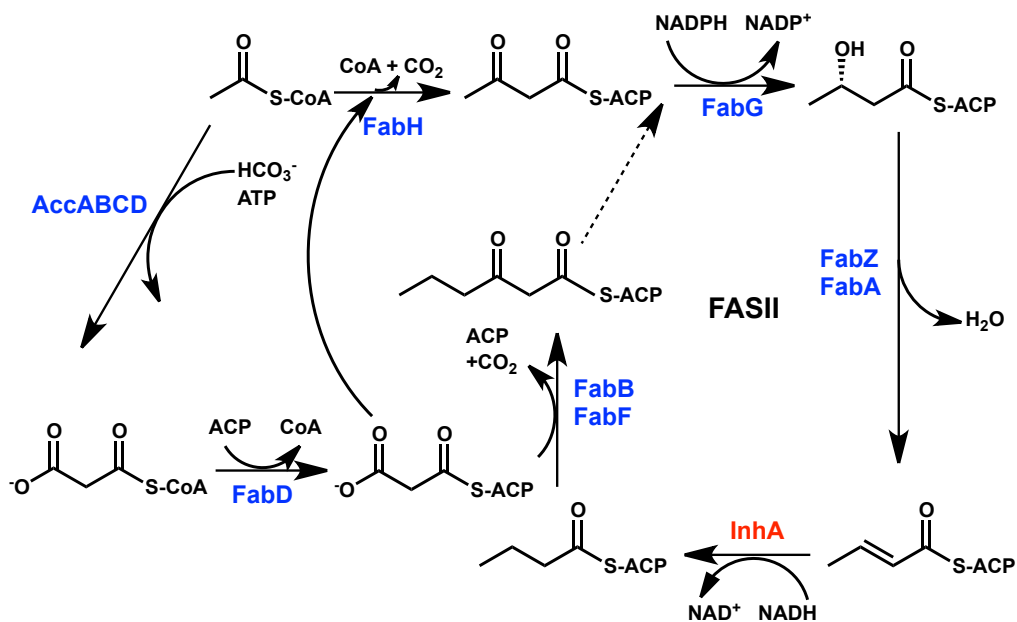


**Figure 3.1** The Type II fatty acid biosynthesis pathway in *M. tuberculosis*

InhA is the enoyl-ACP reductase in this pathway, where it reduces the enoyl ACP substrate into acyl ACP.

Table 3.1 Kinetic parameters depicting the association and dissociation for the three common time-dependent inhibition mechanisms

| Parameter | Mechanism                                    |   |   |
|-----------|--|---|---|
|           | A  | B   | C   |
|           | $E + I \xrightleftharpoons[k_{-1}]{k_1} E-I$ | $E + I \xrightleftharpoons[k_{-1}]{k_1} E^* + I \xrightleftharpoons[k_{-2}]{k_2} E-I^*$ | $E + I \xrightleftharpoons[k_{-1}]{k_1} E-I \xrightleftharpoons[k_{-2}]{k_2} E-I^*$ |
| Half-life | $1/k_{-1}$                                   | $(k_{-1} + k_2 + k_{-2})/k_1 k_2$   | $1/k_{-2}$  |
| $k_{obs}$ | $k_1[I] + k_{-1}$                            | $k_{-2} + (k_2 / (1 + K_i^{app}/[I]))$  | $k_1 + (k_{-1} / (1 + [I]/K_i^{*app}))$   |
| $K_i$     | $k_{-1}/k_1$                                 | $k_{-1}/k_1$  | --  |
| $K_i^*$   | --   | $k_1 k_2 / (k_1(k_2 + k_{-2}))$   | $k_{-2}/k_2$  |



In the present work, we have established a comprehensive kinetic model to delineate all the kinetic parameters in the 2-step induced-fit slow onset inhibition model. We further break down the different attributes that can potentially contribute to a prolonged off-rate. Together with a more detailed structural-kinetic and structural-thermodynamic study, we have successfully designed a novel inhibitor with a residence time of 10 hrs. Most importantly, mutagenesis on the substrate binding loop revealed a diminished energy barrier from EI to EI\*, supporting the structural hypothesis that the isomerization between EI and EI\* corresponds to the conformational change of the substrate binding loop. Finally, we have demonstrated that a long-lived enzyme-product complex as well as a relative high potency of the initial EI species enables information to be gained on the structure of the transition state. In summary, we have successfully established a comprehensive structural and kinetic framework to understand the molecular details of the slow onset inhibition mechanism in the InhA system. Our findings can potentially provide insight into and shed light on other time-dependent inhibition systems.

## MATERIALS AND METHOD

### InhA purification:

InhA was cloned and purified as described previously (17). Briefly, the FabI gene from *Mycobacterium tuberculosis* was cloned into the pET 23b plasmid (Novagen) and transformed into *E. coli* BL21(DE3) pLysS cells. After protein expression, the cells harvested and lysed, and the soluble FabI protein was purified using His-bind Ni<sup>2+</sup>-NTA resin (Invitrogen). Size exclusion chromatography using 30 mM PIPES buffer, pH 6.8 containing 150 mM NaCl and 1 mM EDTA as the eluant gave protein with > 97% purity. Fractions containing InhA were combined and then fractionated and stored at -80 °C.

### Progress curve analysis:

Progress curve kinetics were performed on a Cary 100 UV-Vis spectrophotometer (Varian) at 20 °C using a procedure that has recently been published (18). Reaction velocities were measured by monitoring the oxidation of NADH to NAD<sup>+</sup> at 340 nm. The enzyme reaction was initiated by adding 75 nM enzyme to the reaction buffer (30 mM PIPES, pH 6.8, 150 mM NaCl and 1 mM EDTA) containing trans-2-Oct-CoA (200 μM), NADH (250 μM), NAD<sup>+</sup> (200 μM), DMSO (2% v/v), inhibitor (0 – 4000 nM) and 8% glycerol. The reaction was monitored until the progress curve became linear, suggesting that the steady state had been reached. High concentrations of substrate and low concentrations of enzyme were used to minimize substrate consumption and ensure that progress curves were essentially linear in the absence of inhibitor. The progress curve was fit into the Morrison & Walsh integrated rate equation,

$$A_t = A_0 - v_s t - (v_i - v_s) * \frac{1 - e^{-k_{obs}t}}{k_{obs}}$$

Equation 3.1

where  $A_t$  and  $A_0$  are the absorbance at time  $t$  and  $0$ , respectively,  $v_i$  and  $v_s$  are the initial velocity and steady state velocity, respectively, and  $k_{obs}$  is the pseudo-first order rate constant for the approach to the steady state. To calculate  $k_{off}$  from the progress curve, which corresponds to the dissociation rate constant of the inhibitor, equation 3.2 was used:

$$k_{off} = k_{obs} * \frac{v_s}{v_i}$$

Equation 3.2

$K_i^{app}$ , which corresponds to the apparent value of  $K_i$  for the formation of the initial encounter complex (EI), was determined by plotting the fractional initial velocities as a function of inhibitor concentration and fitting to the isotherm equation:

$$\frac{v_i}{v_0} = \frac{1}{1 + \frac{[I]}{K_i^{app}}}$$

Equation 3.3

where  $v_0$  is the control velocity, from the uninhibited progress curve.  $K_i^{*app}$ , which represents the  $IC_{50}$  value for the final (steady state) EI\* complex formed was determined by plotting the fractional steady-state velocities as a function of inhibitor concentration and fitting to the isotherm equation:

$$\frac{v_s}{v_0} = \frac{1}{1 + \frac{[I]}{K_i^{*app}}}$$

Equation 3.4

[<sup>32</sup>P]-NAD<sup>+</sup> direct dissociation kinetics:

The direct dissociation kinetic experiments were performed as described as recently described (18). In general, 500 μL of reaction mixture containing 15 μM InhA, 20 μM NAD<sup>+</sup>, [<sup>32</sup>P]-NAD<sup>+</sup> and 200 μM inhibitor in the reaction buffer mentioned above was loaded onto a spin column followed by a 2 min centrifugation at 2500 rpm. The purified ternary complex solution was rapidly diluted into 60 mL of the same reaction buffer at different temperatures to initiate ligand dissociation. Subsequently, 600 μL aliquots from the diluted mixture were collected as a function of time and immediately loaded onto an ultrafiltration concentrator (Satorious, 10kDa) which was centrifuged at 13,400 rpm for 90 seconds. The amount of <sup>32</sup>P in the flow through was then quantified using a scintillation counter (LS5801). The inhibitor dissociation rate constant  $k_{off}$  was obtained by fitting the data to equation 3.5, where  $C(t)$  and  $C(0)$  are the radioactive counts at time  $t$  and time 0, respectively,  $C_{max}$  is the maximum radioactive counts and  $k_{off}$  is the inhibitor dissociation rate constant.

$$C(t) = C(0) + C_{max} \times (1 - e^{-k_{off}t})$$

Equation 3.5

### Substrate synthesis:

Trans-2-octenoyl coenzyme A (Oct-CoA) was synthesized using the mixed anhydride method as described previously (18). Briefly, 1.95 mmol of *trans*-2-octenoic acid was dissolved in 3 mL dry tetrahydrofuran with 1.38 mmol triethylamine under nitrogen. Following the addition of 1.36 mmol ethyl chloroformate, salt crystals formed and the reaction was stirred at room temperature for 3 hours under nitrogen. Subsequently, the reaction mixture was centrifuged at 5000 rpm for 15 min to remove the precipitate and the anhydride was added dropwise into a solution of CoA containing 50 mM Na<sub>2</sub>CO<sub>3</sub> (pH 8.0) and tetrahydrofuran (1:1) while being stirred at room temperature. After 2 hours excess organic solvent was removed by rotary evaporation and the sample was purified using a CombiFlash 4.3g C18 column. Chromatography was performed with 20 mM ammonium acetate as buffer A and 100% acetonitrile as buffer B over 60 min at a flow rate of 18 mL/min. Elution was monitored at 260 nm, and oct-CoA eluted at 20 column volumes over a linear gradient from buffer A to 100% acetonitrile. Fractions containing Oct-CoA were pooled and lyophilized. To remove all ammonium acetate, the substrate was dissolved in distilled H<sub>2</sub>O and lyophilized twice more. The product was characterized by electrospray ionization mass spectrometry. MS: 891; Found: 892.2

### Compound synthesis:

PT04, PT05, PT70, PT113, PT91, PT92, PT163 and PT501 were synthesized as described before (18).

PT162 was synthesized from vanillin as follows. Addition of benzylmagnesium bromide to vanillin, followed by Barton's deoxygenation, and hydrogenolytic debenzylation afforded 2-methoxy-4-phenethylphenol, which was then treated with 1-fluoro-4-nitrobenzene in the presence of  $K_2CO_3$ , DMF, 18-crown-6 at  $110^\circ C$  to give 2-methoxy-1-(2-methyl-4-nitrophenoxy)-4-phenethylbenzene. PT162 was subsequently obtained by reduction of the nitro group, followed by denitration and demethylation. Positive ESI-MS ( $m/z$ ):  $[M+H]^+$  calcd. 304.3, found 305.4.

Synthesis of PT501: A solution of 1.0 M boron tribromide in  $CH_2Cl_2$  (0.60 mL, 0.60 mmol) was added dropwise to a solution of [4-cyclopropyl-1-(3-methoxy-4-(*o*-tolylxy)benzyl)-1H-1,2,3-triazole] (30 mg, 0.089 mmol) in dry  $CH_2Cl_2$  (10.00 mL) at  $-78^\circ C$ . The reaction mixture was stirred under nitrogen for 19 h. The reaction was quenched with MeOH (5 mL) and the methanol was removed under reduced pressure. Dichloromethane was added to the mixture, which was poured into a saturated  $NaHCO_3$  solution in a separatory funnel. The organic layer was obtained, washed with water, and then with brine. The combined organic layers were dried over  $MgSO_4$ . Volatiles were removed under reduced pressure and the crude solid was purified by flash chromatography ( $SiO_2$ ; petroleum ether / acetone 85:15 to 70:30) to yield **PT501** as a white powder (10.6 mg, 37 %). Positive ESI-MS ( $m/z$ ):  $[M+H]^+$  calcd. 322.16, found 322.2.

Synthesis of PT503: A solution of 1.0 M boron tribromide in CH<sub>2</sub>Cl<sub>2</sub> (1.00 mL, 1.0 mmol) was added dropwise to a solution of [1-(3-methoxy-4-(*o*-tolylloxy)benzyl)-4-(*m*-tolyl)-1H-1,2,3-triazole] in dry CH<sub>2</sub>Cl<sub>2</sub> (10.00 mL) at - 78 °C. The reaction mixture was stirred under nitrogen for 17 h. The reaction was quenched with MeOH (5 mL) and the methanol was removed under reduced pressure. Dichloromethane was added to the mixture, which was poured into a saturated NaHCO<sub>3</sub> solution in a separatory funnel. Layers were separated and the aqueous layer was washed with dichloromethane while the organic layer was washed with water. The combined organic layers were dried over MgSO<sub>4</sub>. Volatiles were removed from the filtrate under reduced pressure and the crude solid was purified by flash chromatography (SiO<sub>2</sub>; petroleum ether / ethyl acetate 80:20 to 60:40) to yield PT503 as a white powder (5.4 mg, 6 %). Positive ESI-MS (*m/z*): [M+H]<sup>+</sup> calcd. 372.17, found 372.1.

Synthesis of PT504: A solution of 1.0 M boron tribromide in CH<sub>2</sub>Cl<sub>2</sub> (2.1 mL, 2.1 mmol) was added dropwise to a solution of [4-cyclopropyl-1-(3-methoxy-4-(*o*-tolylloxy)benzyl)-1H-1,2,3-triazole] (700 mg, 1.97 mmol) in dry CH<sub>2</sub>Cl<sub>2</sub> (15 mL) at - 78 °C. The reaction mixture was stirred for 18 hr and quenched with water (5 mL). Layers were separated and the aqueous layer was extracted twice with dichloromethane (10 mL portions). The combined organic layer was washed with saturated NaHCO<sub>3</sub> and subsequently dried over MgSO<sub>4</sub>. Volatiles were removed from the filtrate under reduced pressure and the crude solid was purified by flash chromatography (SiO<sub>2</sub>; CH<sub>2</sub>Cl<sub>2</sub>:MeOH 100:0 to 95:5) to yield PT504 as an off-white powder (35 mg, 5 %). Positive ESI-MS (*m/z*): [M+H]<sup>+</sup> calcd. 336.16, found 336.2.

Synthesis of PT512: A solution of 1.0 M boron tribromide in CH<sub>2</sub>Cl<sub>2</sub> (0.90 mL, 0.90 mmol) was added dropwise to a solution of [2-(4-((4-cyclopentyl-1H-1,2,3-triazol-1-yl)methyl)-2-methoxyphenoxy)benzotrile] (110 mg, 0.289 mmol) in dry CH<sub>2</sub>Cl<sub>2</sub> (5 mL) at - 40 °C. The reaction mixture was stirred for 18 h and quenched with water (5 mL). Layers were separated and the aqueous layer was extracted twice with dichloromethane (10 mL portions). The combined organic layer was washed with saturated NaHCO<sub>3</sub> and subsequently dried over MgSO<sub>4</sub>. Volatiles were removed from the filtrate under reduced pressure. The crude solid was purified by flash chromatography (SiO<sub>2</sub>; petroleum ether:acetone 70:30 to 0:100) to yield PT512 as an off-white powder (35 mg, 33 %).

Synthesis of PT514: A solution of 1.0 M boron tribromide in dichloromethane (1.35 mL, 1.35 mmol) was added dropwise to a solution of [4-ethyl-1-(3-methoxy-4-(o-tolyloxy)benzyl)-1H-1,2,3-triazole] (170 mg, 0.451 mmol) in dry dichloromethane (10.00 mL) at - 78 °C. After stirring for 19 h, the reaction was quenched with water (5 mL). The reaction mixture was poured into a 10 mL saturated NaHCO<sub>3</sub> solution in a separatory funnel. Layers were separated and the aqueous layer was washed twice with 5 mL portions of dichloromethane. The combined organic layers were washed with brine, then dried over MgSO<sub>4</sub>. Volatiles were removed from the filtrate under reduced pressure. The crude solid was purified by flash chromatography (SiO<sub>2</sub>; petroleum ether / acetone 85:15 to 70:30) to yield PT514 as a pale yellow powder (15 mg, 9 %).



Crystallization and structure determination of InhA ternary complexes with PT504, PT506, PT512 and PT514:

After 2 h of incubation on ice and centrifugation for 20 min at 16000 x g and 4 °C the PT504-, PT506- PT512- and PT514-NAD<sup>+</sup>-InhA complexes were crystallized by the hanging-drop vapor diffusion method at 20 °C. Crystals of the [InhA·NAD<sup>+</sup>·PT504] and [InhA·NAD<sup>+</sup>·PT512] complexes were obtained in 1.6 M sodium acetate, pH 7.0 with a 5-fold molar excess of cofactor and 50-fold molar excess of inhibitor over InhA at a protein concentration of 0.33 mM. The [InhA·NAD<sup>+</sup>·PT506] complex crystallized under similar conditions at a higher sodium acetate concentration (2.4 M), but required only a 20-fold molar excess of PT506. Crystals of the InhA-PT514 complex grew in conditions containing 3 M sodium chloride and 100 mM Tris-HCl, pH 9.0 at a 5-fold molar excess of cofactor and 50-fold molar excess of inhibitor. Prior to data collection the crystals were transferred to a cryoprotectant solution containing the mother liquor plus 30 – 35 % ethylene glycol.

Data sets were collected at beamline BL 14.1 at the BESSY II synchrotron using a Pilatus 6M detector. The datasets were processed either with Mosflm 7.0.9 (PT504, PT512) or XDS (PT506, PT512) and the structures solved by molecular replacement utilizing the [InhA·NAD<sup>+</sup>·PT70] complex structure (PDB entry 2X23) as search model. Structure refinement was performed using the CCP4 works suite with Refmac version 5.7.0029 for PT506 and PT504, and Refmac 5.7.0032 for PT512 and PT514.

### Kinetic model:

Based on the kinetic mechanism described before, a set of ordinary differential equations were formulated and solved numerically through Wolfram *Mathematica* 8.0. Each kinetic parameter in this mathematical model was carefully analyzed and the rationale was provided in Table 3.2.

Table 3.2 Rationale of kinetic parameters for InhA in the Mathematica Model

| Parameter     | Estimate  | Rationale   |
|---------------|---|---|
| $K_S$         | 0.67 mM for oct-CoA                             | Approximated based on a previously reported $K_m$ value (19).   |
| $K_{NADH}$    | 0.48 $\mu$ M                                    | Based on a previously reported $K_d$ value (20).  |
| $K_{NAD}$     | 4 mM  | Based on a previously reported $K_i$ value (19).<br>This arbitrary estimate is within an order of magnitude of the diffusion-limited rate constant, which represents the theoretical ceiling. The value will only affect the kinetic system if it is low enough to be rate limiting (approx. $6 \cdot 10^6 \text{ M}^{-1} \text{ min}^{-1}$ ).  |
| $k_{on,S}$    | $6 \times 10^8 \text{ M}^{-1} \text{ min}^{-1}$ | This value approximates previously reported $K_{m,NADH}$ values (19, 20).<br>We assumed that PT52 and PT70 have similar affinities for saFabI and InhA, respectively, based on their similar drug-target residence times. To replicate the InhA progress curve, this is the value of $k_{off,NAD}$ that was derived. Consistently, this value makes $\text{NAD}^+$ release partially rate limiting as previously suggested (19, 20). Additionally, mutations that likely accelerate $\text{NAD}^+$ release (e.g. S94A) result in increased $k_{cat}$ values (21). |
| $k_{off,NAD}$ | $8 \times 10^2 \text{ min}^{-1}$                |   |
| $k_{cat}$     | 185 $\text{min}^{-1}$ for oct-coA               | Based on a previously reported $k_{cat}$ value (19, 20).  |

Arrhenius analysis:

The Arrhenius analysis was performed to determine the activation energy ( $E_a$ ) and pre-exponential factor ( $A$ ) for the rate constants during the inhibitor dissociation phase, by linear regression analysis. [ $^{32}\text{P}$ ]-NAD $^+$  direct dissociation kinetics were used to determine  $k_{\text{off}}$  over a series of temperatures and data were analyzed using equation 3.6:

$$k = Ae^{-E_a/RT}$$

Equation 3.6

After taking the natural logarithms of equation 3.6,  $A$  corresponded to the y-intercept while  $E_a$  denoted the slope of the linear fitting in the Arrhenius plot.

The activation enthalpies ( $\Delta H^\ddagger$ ) and entropies ( $\Delta S^\ddagger$ ) for the dissociation rate constant were also determined through the Arrhenius-Eyring hybrid analysis. The activation enthalpy was calculated from  $E_a$  using equation 3.7:

$$\Delta H^\ddagger = E_a - RT$$

Equation 3.7

while the activation entropy was estimated from the pre-exponential factor  $A$ , using the following equation:

$$A = \left(\frac{Tk_B e^1}{h}\right)e^{\Delta S^\ddagger/R}$$

Equation 3.8

where T is the temperature,  $k_B$  is the Boltzmann's constant, h is Planck's constant and R is the gas constant.

Eyring analysis:

Eyring analysis was also used to analyze the thermodynamic parameters for the dissociation phase from the rate constants by linear regression. The  $k_{off}$  values obtained as a function of temperature were fit to the following equation:

$$\ln\left(k_{off} \frac{h}{k_B T \kappa}\right) = -\frac{\Delta H_{off}^\ddagger}{RT} + \frac{\Delta S_{off}^\ddagger}{R}$$

Equation 3.9

where  $\kappa$  is the transmission coefficient. A value of 1 was used for  $\kappa$ .

Site-directed mutagenesis, expression and purification of InhA mutants:

For the InhA mutant sV203A, I215A and L207A, site-directed mutagenesis was performed using the QuikChange site-directed mutagenesis method with the primers listed in Table 3.3. The sequence of each mutant construct was confirmed by DNA sequencing. The expression and purification of these variants followed the same protocol as described above.

Table 3.3 Primers for different InhA mutant constructs

| <b>Name</b>         | <b>Sequence</b>                  |
|---------------------|----------------------------------|
| InhA V203A forward  | 5' GAGTGCATCGCGGGCGGTGCGCTC 3'   |
| InhA V203A reversed | 5'GAGCGCACCGCCCGCGATCGCACTC 3'   |
| InhA I215A forward  | 5' CCGGCGCCAGGCGCAGCTGCTCGAG 3'  |
| InhA I215A reversed | 5' CTCGAGCAGCTGCGCCTGGGCGCCGG 3' |
| InhA L207A forward  | 5' ATCGTCGGCGGTGCGGCCGGCGAGGA 3' |
| InhA L207A reversed | 5' TCCTCGCCGGCCGCACCGCCGACGAT 3' |

Thermofluor experiments:

ThermoFluor experiments were performed as previously described to determine the inhibitor cofactor preference (22). A total volume of 20  $\mu$ L containing 7.4  $\mu$ M InhA, 2.5 mM cofactor (NADH or NAD<sup>+</sup>) and 25  $\mu$ M inhibitor (2% DMSO) was added to a 96-well think-wall PCR plate (Concord) in the same reaction buffer. After 1.5 hrs incubation at 25 °C, 1  $\mu$ L of 100 x Sypro Orange (Sigma) was added and the plate was sealed with microseal “B” Film (Bio-Rad). The samples were heated from 25 to 90 °C in increments of 0.2 °C/10 s. Data was processed on Bio-Rad CFX manager.

## RESULTS and DISCUSSION

A comprehensive kinetic model for the InhA system suggests that the release of NAD<sup>+</sup> ( $k_{\text{off}, \text{NAD}^+}$ ) is partially rate limiting

Based on the previous literature (19-21), we were able to establish a comprehensive enzymatic catalysis kinetic model (Figure 3.2). The rationale for the value of each kinetic constant used is listed in Table 3.1. One thing to note is that the last step within the catalytic cycle, which corresponds to the release of NAD<sup>+</sup> from the E-NAD<sup>+</sup> complex ( $k_{\text{off}, \text{NAD}^+}$ ) was directly related to the turnover of the enzyme catalytic cycle. Interestingly, the  $k_{\text{off}, \text{NAD}^+}$  for InhA had the same order of magnitude as the  $k_{\text{cat}}$  and was a lot slower than observed for other FabI homologs, suggesting that the release of NAD<sup>+</sup> was partially rate limiting during turnover (22). In support of this propose, previously it has been noted that mutations that likely accelerate NAD<sup>+</sup> release (e.g. S94A) also result in increased  $k_{\text{cat}}$  values (21).

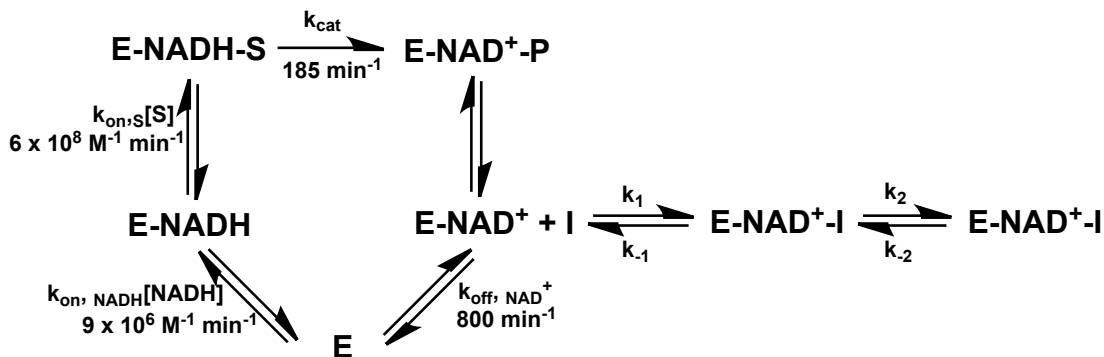


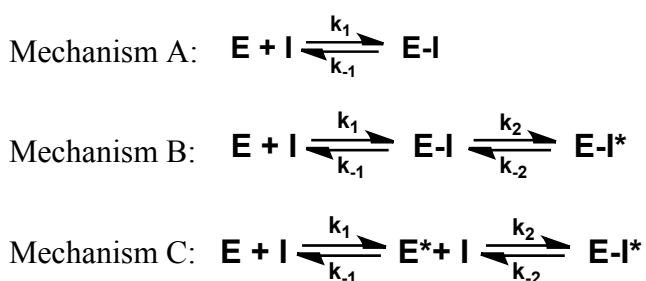
**Figure 3.2 InhA catalysis and inhibition kinetic model**

The scheme depicts the diphenyl ether inhibition mechanism along the enzymatic catalytic cycle.

Diphenyl ether inhibitors bind to the binary E-NAD<sup>+</sup> complex generated through enzyme catalysis and follow a two-step induced fit mechanism

As suggested by previous studies, diphenyl ether inhibitors prefer binding to the NAD<sup>+</sup> cofactor and bind uncompetitively with respect to NAD<sup>+</sup> to form the ternary inhibition complex (19, 23-25). In order to complete the inhibition mechanism scheme, we investigated the source of the NAD<sup>+</sup> relevant to inhibitor binding. Progress curves for enzyme inhibition performed in the presence of 200  $\mu\text{M}$  or 2000  $\mu\text{M}$  exogenous NAD<sup>+</sup> were essentially identical, indicating that the NAD<sup>+</sup> product from enzyme catalytic cycle rather than exogenous NAD<sup>+</sup> was the main source of the E-NAD<sup>+</sup> complex to which inhibitors bind (Figure 3.3). In addition, we were able to validate the two-step induced fit mechanism for InhA inhibition by experimentally distinguishing  $v_i$  and  $v_s$  from the progress curve assay. Normally, the slow-binding inhibition follows one of the three kinetic mechanisms (Scheme 3.1). In mechanism A, the inhibitor forms the EI complex through a one-step slow association process. In mechanism B, the inhibitor usually forms the initial EI complex through a rapid process followed by a much slower process which involves in large-scale protein conformation change to yield a much more potent EI\* species. Alternatively, the large-scale protein conformation change can happen before the rapid binding of inhibitor (mechanism C). To elucidate the mechanism of the slow binding inhibition,  $k_{\text{obs}}$  obtained from individual progress curves was replotted as a function of inhibitor concentration. The hyperbolic fit unambiguously suggests that inhibition occurs through the two-step induced fit slow binding mechanism (Figure 3.4) (mechanism B). In addition, we were able to extrapolate  $K_i^{\text{app}}$  and  $K_i^{*\text{app}}$  by plotting  $v_i/v_0$

and  $v_s/v_0$  as a function of inhibitor concentration, further validating the two-step mechanism. It is interesting to note that other FabI homologs follow a special case of mechanism B where the initial inhibition is not detected at low inhibitor concentrations. In the case of InhA, the ability to observe two-step inhibition might result from the observation that the E-NAD<sup>+</sup> InhA species is much longer-lived than for other FabI homologs – i.e. the  $k_{\text{off,NAD}^+}$  for InhA is 800 min<sup>-1</sup> while  $k_{\text{off,NAD}^+}$  for other FabI homologs is  $\sim 10^4$  min<sup>-1</sup> (22, 26). Consequently, the concentration of E-NAD<sup>+</sup> during the InhA catalyzed reaction is relatively high, while the initial EI complex still has a relatively low free energy. As a result, it is easier to capture the initial inhibition when the inhibitor first encounters the enzyme complex. Because of this reason, in a recent paper we were able to structurally characterize both EI and EI\* along the reaction coordinate (16). We will discuss this point later in the chapter. The kinetic model we established was also validated thoroughly as shown in Figure 4 and thus a powerful predictive kinetic model has been successfully developed for a complex enzyme inhibition system.



Scheme 3.1 Three different types of slow onset inhibition mechanism: mechanism A depicts the one-step model; mechanism B depicts the induced-fit model; mechanism C depicts the conformation selection mechanism



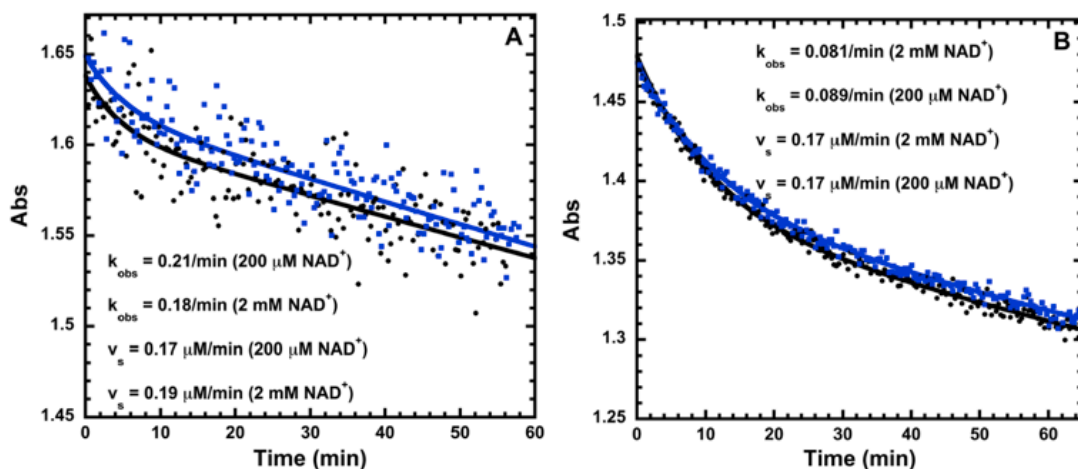


**Figure 3.3 Comparison of progress curves under different concentrations of exogenous NAD<sup>+</sup>**

A) The progress curves for the inhibition of InhA inhibition by 200 nM PT70 at 200  $\mu\text{M}$  NAD<sup>+</sup> (black) and 2000  $\mu\text{M}$  NAD<sup>+</sup> (blue). The pseudo-first order rate constant  $k_{\text{obs}}$  and steady state velocity  $v_s$  from the fit were 0.21  $\text{min}^{-1}$  and 0.17  $\mu\text{M min}^{-1}$ , respectively, at 200  $\mu\text{M}$  NAD<sup>+</sup>, and 0.18  $\text{min}^{-1}$  and 0.19  $\mu\text{M min}^{-1}$  respectively at 2000  $\mu\text{M}$  NAD<sup>+</sup>. B) The progress curves interpreted InhA inhibition by 2  $\mu\text{M}$  PT163 at 200  $\mu\text{M}$  NAD<sup>+</sup> (black) and 2000  $\mu\text{M}$  NAD<sup>+</sup> (blue). The pseudo-first order rate constant  $k_{\text{obs}}$  and steady state velocity  $v_s$  from the fit were 0.081  $\text{min}^{-1}$  and 0.17  $\mu\text{M min}^{-1}$ , respectively, at 200  $\mu\text{M}$  NAD<sup>+</sup>, and 0.089  $\text{min}^{-1}$  and 0.17  $\mu\text{M min}^{-1}$  at 2000  $\mu\text{M}$  NAD<sup>+</sup>.

Structure-activity relationship for the 2' substituents suggests that the 2'-chloro group enhances residence time by improving binding affinity

Since  $k_{\text{off}}$  is a crucial parameter for *in vitro* drug evaluation, it is important to understand the factors that can potentially affect  $k_{\text{off}}$ . As shown in scheme 3.2, the  $k_{\text{off}}$  in a 2-step slow binding model is affected by the  $K_i^*$  and  $k_{\text{on,overall}}$ . Based on our previous promising drug candidate PT70, we developed a series of compounds with the same hexyl-acyl chain on the A ring but different substituents on the B ring for structure-activity relationship comparison. Using a combined approach of kinetic model and

mechanistically informed kinetic assay, we analyzed a series of 7 InhA inhibitors with different

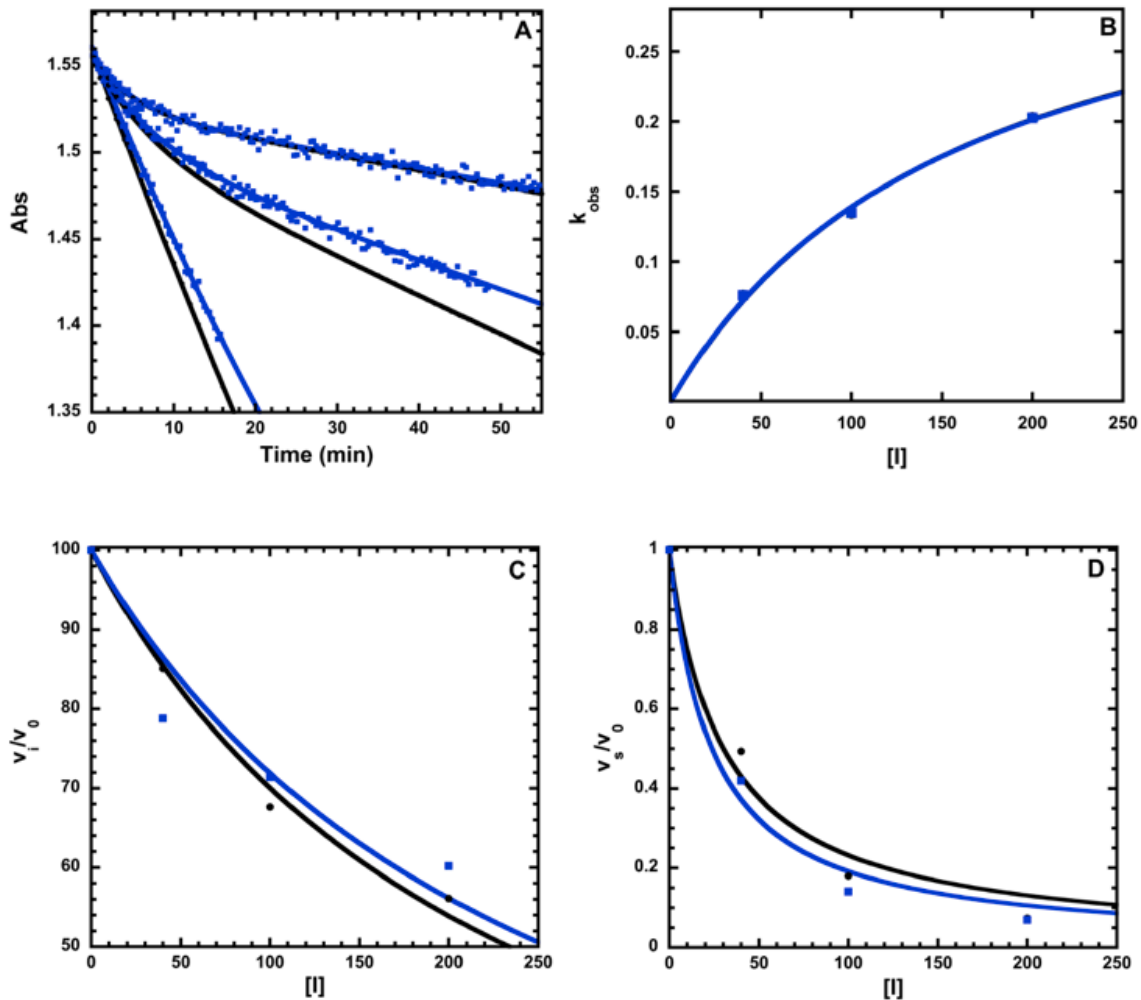
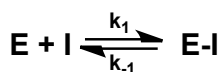


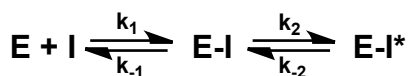
**Figure 3.4 Overlay of experimental and simulated progress curve analyses**

A) Experimental progress curves (blue) denoted PT70 inhibition at 100 nM and 200 nM. The simulated progress curves (black) were generated based on the parameters provided in Table 3.1. B) The plot of  $k_{obs}$  as a function of  $[I]$  unambiguously distinguish Mechanism B from Mechanism A and C. C) Experimental  $K_i^{app}$  (blue) and simulated  $K_i^{app}$  (black) was determined based on the  $v_i$  from individual progress curve. D) Experimental  $K_i^{*app}$  (blue) and simulated  $K_i^{*app}$  (black) was calculated based on the  $v_s$  from individual progress curve.

2'-substituent. As suggested in Table 3.4, the overall association rate constant ( $k_{on,overall}$ ) for the 7 inhibitors was essentially identical, indicating a very similar overall transition state energy barrier. This has also been reported in the saFabI system although it should be noted that saFabI inhibitors follow a 1-step slow binding mechanism. While  $t_R$  was not affected by  $k_{on,overall}$ , the  $K_i^*$  which represents the final binding affinity of the inhibitor varied across these inhibitors and displayed strong linear correlation with  $t_R$  in the double reciprocal plot (Figure 3.5), suggesting that  $t_R$  was directly related to the stabilization of the final complex. The best inhibitor in the series, PT91 had a  $K_i^*$  of 34 pM, indicating more than 10-fold tighter binding to InhA compared to the parent inhibitor PT70 ( $K_i^*$  of 560 pM).



$$k_{off} = k_{-1} (min^{-1}) = K_i(M) \times k_1 (M^{-1} min^{-1})$$



$$\frac{d[EI^*]}{dt} = k_{on,overall} \times [E] \times [I] = k_2 \times [EI]$$

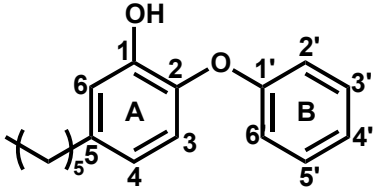
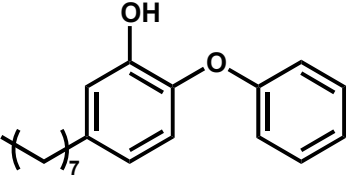
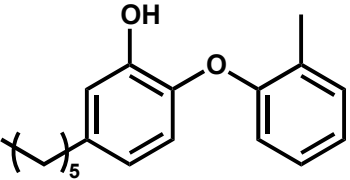
$$k_{on,overall} = \frac{k_2}{K_i}$$

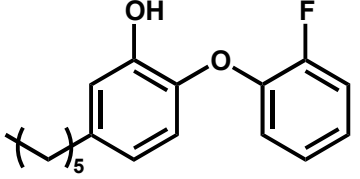
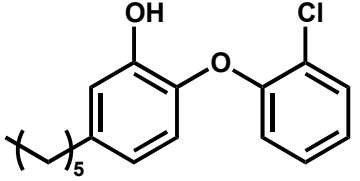
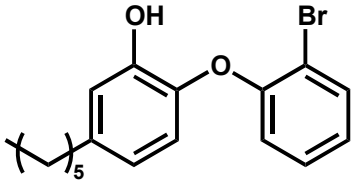
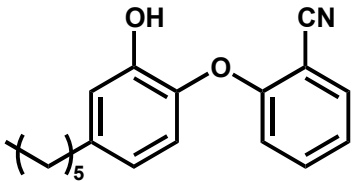
$$k_{off} \approx k_{-2} (min^{-1}) = K_i^* (M) \times k_{on,overall} (M^{-1} min^{-1})$$

$$= K_i^* (M) \times \frac{k_2 (min^{-1})}{K_i (M)}$$

Scheme 3.2 Different parameters that affect  $k_{off}$ . In the simple one step mechanism, both the binding affinity of EI and the association kinetics contribute to  $k_{off}$ . In the induced-fit 2-step mechanism,  $k_{off}$  is given by the thermodynamic affinity of the EI\* complex and the overall association kinetics. Note that the overall association kinetics can be further deconvoluted into the association rate of the second step and the thermodynamic affinity of the EI complex.

Table 3.4 Detailed kinetic characterization of 2'-substituents diphenyl ether analogs

| Compound | Structure  | $K_i^{app}$<br>(nM) | $K_i$<br>(nM) | $K_i^{*app}$<br>(nM) | $K_i^*$<br>(nM) | $k_2$<br>(min <sup>-1</sup> ) | $k_{on, overall}$<br>$k_2/K_i$<br>(M <sup>-1</sup> min <sup>-1</sup> ) | $k_{-2}$ (min <sup>-1</sup> ) | $t_R$ (min)               |
|----------|--|---------------------|---------------|----------------------|-----------------|-------------------------------|--|-------------------------------|---------------------------|
| PT04     |   | 112.6±<br>10.7      | 3.5           | 38.7±<br>2.8         | 1.9             | 0.17±<br>0.12                 | 5.0 x<br>10 <sup>7</sup>   | 0.095±<br>0.044 <sup>a</sup>  | 10.5±<br>4.8 <sup>a</sup> |
|          |  |                     |               |                      |                 |                               |  | 0.10±<br>0.007 <sup>b</sup>   | 9.5±<br>0.7 <sup>b</sup>  |
| PT05     |   | 134.9±<br>28.5      | 2.5           | 14.3±<br>0.7         | 0.49            | 0.19±<br>0.07                 | 7.8 x<br>10 <sup>7</sup>   | 0.038±<br>0.01 <sup>a</sup>   | 26.4±<br>7.2 <sup>a</sup> |
|          |  |                     |               |                      |                 |                               |  | 0.037±<br>0.007 <sup>b</sup>  | 27.1±<br>5.2 <sup>b</sup> |
| PT70     |  | 256.2±<br>38.0      | 9             | 23.7±<br>3.6         | 0.56            | 0.4±<br>0.01                  | 4.4 x<br>10 <sup>7</sup>   | 0.025±<br>0.001 <sup>a</sup>  | 40±<br>2.4 <sup>a</sup>   |
|          |  |                     |               |                      |                 |                               |  | 0.025±<br>0.002 <sup>b</sup>  | 40±<br>4.1 <sup>b</sup>   |

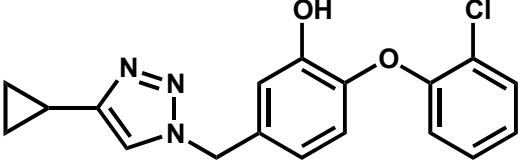
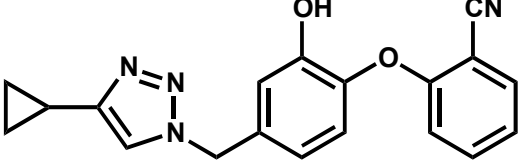
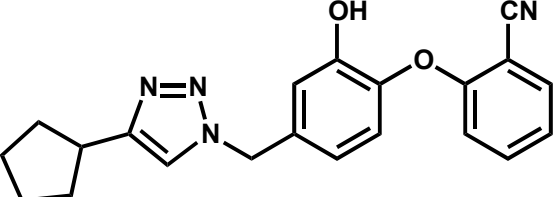
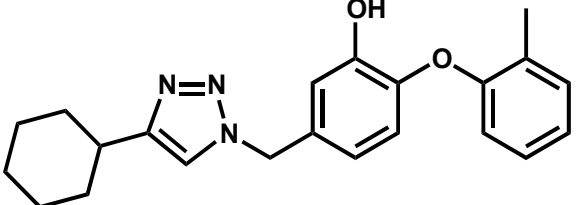
|       |  |                |     |              |       |               |                          |                                |                             |
|-------|--|----------------|-----|--------------|-------|---------------|--------------------------|--------------------------------|-----------------------------|
| PT113 |   | 134.9±<br>28.5 | 4.2 | 18.8±<br>1.7 | 0.64  | 0.21±<br>0.06 | 5.0 x<br>10 <sup>7</sup> | 0.032±<br>0.006 <sup>a</sup>   | 31.1±<br>6.1 <sup>a</sup>   |
|       |  |                |     |              |       |               |                          | 0.032±<br>0.005 <sup>b</sup>   | 31.1±<br>4.8 <sup>b</sup>   |
| PT91  |   | 58.8±<br>2.8   | 0.8 | 4.3±<br>0.6  | 0.034 | 0.20±<br>0.06 | 2.5 x<br>10 <sup>8</sup> | 0.01±<br>0.001 <sup>a</sup>    | 102.1±<br>11.4 <sup>a</sup> |
|       |  |                |     |              |       |               |                          | 0.0067±<br>0.0006 <sup>b</sup> | 148.4±<br>13.4 <sup>b</sup> |
| PT92  |   | 142.5±<br>28.3 | 4   | 31.1±<br>2.6 | 1.1   | 0.23±<br>0.02 | 5.8 x<br>10 <sup>7</sup> | 0.066±<br>0.008 <sup>a</sup>   | 15.1±<br>1.8 <sup>a</sup>   |
|       |  |                |     |              |       |               |                          | 0.024±<br>0.004 <sup>b</sup>   | 42.3±<br>6.8 <sup>b</sup>   |
| PT119 |  | N/A            | N/A | 27.5±<br>0.8 | 1.1   | N/A           | N/A                      | 0.02±<br>0.001 <sup>a</sup>    | 50.7±<br>3.7 <sup>a</sup>   |
|       |  |                |     |              |       |               |                          | 0.02±<br>0.001 <sup>b</sup>    | 47.4±<br>3.8 <sup>b</sup>   |

<sup>a</sup> value determined from progress curve analysis

<sup>b</sup> value determined from [<sup>32</sup>P]-NAD<sup>+</sup> direct dissociation kinetics

Table 3.5 Detailed kinetic characterization of 5-substituents diphenyl ether analogs

| Compound | Structure | $K_i^{app}$<br>(nM) | $K_i$<br>(nM) | $K_i^{*app}$<br>(nM) | $K_i^*$<br>(nM) | $k_2$<br>( $\text{min}^{-1}$ ) | $k_2/K_i$<br>( $\text{M}^{-1}\text{min}^{-1}$ ) | $k_{-2}$<br>( $\text{min}^{-1}$ ) | $t_R$<br>(min)              |
|----------|-----------|---------------------|---------------|----------------------|-----------------|--------------------------------|---|-----------------------------------|-----------------------------|
| PT162    |           | 324.9±<br>19.4      |               | N/A                  | N/A             | N/A                            | N/A   | rapid                             | <1                          |
| PT163    |           | 8382.9±<br>365.2    | 310           | 185.2±<br>8.6        | 7.7             | 0.44±<br>0.06                  | 1.3 x<br>10 <sup>6</sup>                        | 0.01±<br>0.003 <sup>a</sup>       | 93.8±<br>2.6 <sup>a</sup>   |
|          |           |                     |               |                      |                 |                                |   | 0.009±<br>0.001 <sup>b</sup>      | 114.3±<br>17.8 <sup>b</sup> |
| PT501    |           | 10792±<br>857       | 450           | 69.4±<br>1.5         | 3.0             | 0.65±<br>0.10                  | 1.4 x<br>10 <sup>6</sup>                        | 0.0043±<br>0.0001 <sup>a</sup>    | 230.1±<br>7.9 <sup>a</sup>  |
|          |           |                     |               |                      |                 |                                |   | 0.0048±<br>0.0003 <sup>b</sup>    | 206.0±<br>14.6 <sup>b</sup> |
| PT503    |           | 22633±<br>2416      | 930           | 106.1±<br>9.3        | 4.9             | 1.65±<br>0.31                  | 1.8 x<br>10 <sup>6</sup>                        | 0.0088±<br>0.0009 <sup>a</sup>    | 114.3±<br>11.6 <sup>a</sup> |
|          |           |                     |               |                      |                 |                                |   | 0.01±<br>0.001 <sup>b</sup>       | 96.6±<br>11.9 <sup>b</sup>  |

|       |  |                |    |                |    |               |    |                                |                             |
|-------|--|----------------|----|----------------|----|---------------|----|--------------------------------|-----------------------------|
| PT504 |   | 1249±<br>226   | ND | 54.3±<br>6.9   | ND | 0.11±<br>0.02 | ND | 0.0047±<br>0.001 <sup>a</sup>  | 211.1±<br>44.5 <sup>a</sup> |
| PT506 |   | NA             | ND | NA             | ND | NA            | ND |                                | 161.0±<br>48.0 <sup>a</sup> |
| PT512 |   | 68069±<br>7634 | ND | 369.9±<br>36.7 | ND | 0.70±<br>0.08 | ND | 0.0042±<br>0.0003 <sup>a</sup> | 238.1±<br>17.0 <sup>a</sup> |
| PT514 |  | 12116±<br>845  | ND | 248.1±<br>16.2 | ND | 0.32±<br>0.03 | ND | 0.0071±<br>0.001 <sup>a</sup>  | 140.8±<br>19.8 <sup>a</sup> |

<sup>a</sup> value determined from progress curve analysis

<sup>b</sup> value determined from [<sup>32</sup>P]-NAD<sup>+</sup> direct dissociation kinetics

NA: Not available

ND: Not determined

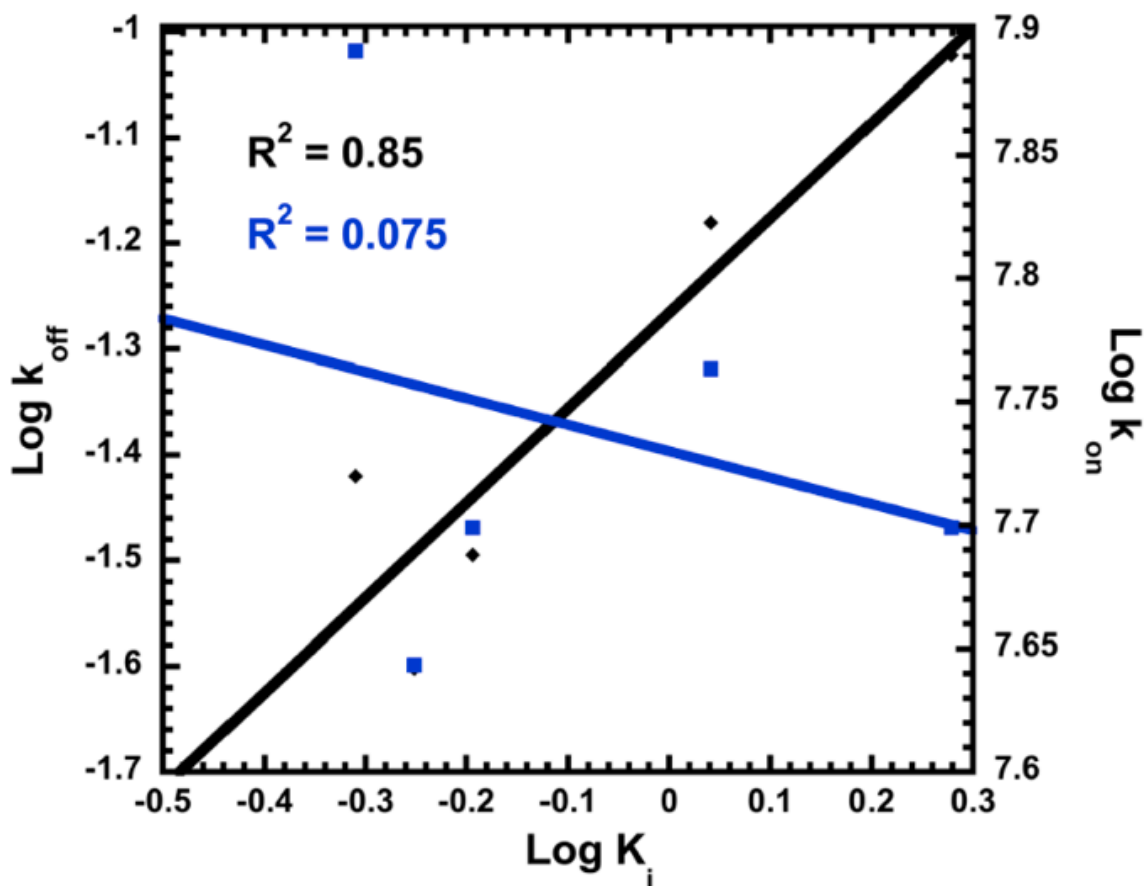


**Figure 3.5** A double logarithmic plot of thermodynamic and kinetic constants for 2'-substituents

The plot suggests a strong correlation between thermodynamic affinity and dissociation kinetics (black) and a weak correlation between thermodynamic affinity and association kinetics (blue).

#### 5-Triazole substituents increase the residence time by a slower overall association rate

After the analysis of  $K_i^*$ , we further look into the effect of  $k_{on,overall}$  on  $k_{off}$ . Inspired by the crystal structure of InhA-PT70 complex (17), we hypothesized that the triazole ring will create an additional pharmacophore element to the diphenyl ether scaffold, providing rigidity when interacting with the protein target, therefore enhance the associate energy barrier by a decreased



association rate constant. Using click chemistry as our strategy, we incorporated a triazole ring at the 5-position and synthesized 7 compounds to interrogate the hydrophobic and van der Waals interactions about the A ring side chain that might affect  $k_{\text{off}}$ . As we expected, the overall association rate  $k_{\text{on, overall}}$  of PT163 decreased by 10-fold compared to PT70 (Table 3.5), the chemical structure of which only differed by the nature of the substituent at the 5-position. Yet the binding affinity was also weakened at the same time – i.e. the  $K_i^*$  of PT163 was 7.7 nM, which was 14-fold weaker than PT70. As a result, the residence time was only prolonged by ~2.6-fold from 40 min to ~100 min. With this knowledge in hand, we performed additional SAR studies on these bulky 5-substituents. Interestingly, when we replaced the triazole ring in PT163 with an ethyl group (PT162), the latter completely lost slow binding behavior and became a rapid reversible inhibitor. We think the triazole might create a specific interaction for inhibitor binding such that it helps to anchor the inhibitor effectively into the binding pocket. In addition, the triazole ring helps modulate the steric bulk of the 5-substituent about the A-ring tail provided that the tail is oriented favorably with respect to the hydrophobic residues lining the pocket. For the rest of the triazole analogs, we found the substituted aromatic ring (PT503) was comparable to PT163, both in binding affinity and residence time (Table 3.4). In comparing the cyclopropyl to the cyclohexyl substituents (PT501 and PT514), the cyclopropyl had the best size for binding affinity, with a  $K_i^*$  value of 3.0 nM, about 2.5 fold improvement from PT163. Consequently, the residence time was also improved by ~2.5 fold. Based on our findings together with a recent publication, the data suggest that the triazole is an important pharmacophore for InhA inhibitors and that click chemistry might be an attractive strategy for InhA inhibitor design (27-30).

The 5-triazole substituents decrease the overall onset rate constant by increasing the ground state energy of E-I. The onset rate constants of the slow binding step ( $k_2$ ) are essentially identical among diphenyl ether inhibitors

As mentioned earlier, a stabilized ground state (i.e. a good  $K_i$ ) as well as a destabilized transition state (i.e. a higher energy barrier) can both contribute to a slower dissociation rate of the drug. Therefore, finding out the molecular cause of the transition state energy barrier is very important for further design of slow binding drugs. As discussed earlier, both  $K_i^*$  and  $k_{on,overall}$  can affect  $k_{off}$  in a 2-step slow-onset inhibition model. Moreover,  $k_{on, overall}$  can be further dissected into  $k_2/K_i$ , where  $k_2$  corresponds to the association barrier for the second step and  $K_i$  is the equilibrium constant for initial binding (Scheme 3.2). Regarding  $k_{on, overall}$ , it is interesting to note that the triazole-diphenyl ethers displayed about a magnitude slower overall association rate compared to the acyl-diphenyl ethers ( $\sim 5.5 \times 10^7 \text{ M}^{-1} \text{ min}^{-1}$  compared to  $\sim 1.5 \times 10^6 \text{ M}^{-1} \text{ min}^{-1}$ , respectively). If we further deconvolute the  $k_{on, overall}$  into  $k_2$  and  $K_i$ , we find that the association rate constant for the second step ( $k_2$ ) is  $\sim 0.2 \text{ min}^{-1}$ , which is essentially identical among all compounds (Table 3.3 and 3.4). Although a 2-3 fold fluctuation was observed for  $k_2$ , we don't think this needs to be taken into consideration. Remarkably, there was a  $\sim 100$  fold difference in  $K_i$  between the triazole and acyl diphenyl ethers. For example, the  $K_i$  for PT04 was 3.5 nM, while and  $K_i$  for PT163 was 310 nM. This significant difference in  $K_i$  predominantly accounts for the one magnitude slower overall association rate.

Figure 3.6 further illustrates the relative energy levels on the same reaction coordinate. The ground state of EI among all the aliphatic diphenyl ethers is about the same, therefore we

chose PT70 as our representative. The one exception is PT91, for which both the ground state of EI and EI\* is <10 fold more stable than the rest of the acyl diphenyl ethers. For triazole diphenyl ethers e.g. PT163, the  $K_i$  value is significantly raised so that the energy level of the EI state is raised ~35 fold, while the EI\* state for this set of compounds is about the same as the EI of the aliphatic diphenyl ethers. As a result, the overall association rate constant for PT163 is slower by approximately 10-fold, yet the association barrier for the slow step ( $k_2$ ) is essentially identical, with only a 2-fold increase. From this figure, we can visualize that both  $K_i$  and  $K_i^*$  can act synergistically to maximize the dissociation barrier of the drug in a way such that  $K_i^*$  should be stabilized while  $K_i$  should be destabilized.

#### Rational design of PT504 – A novel compound with 10 hours residence time

Based on our previous observation that the 2'- chloro substituent can significantly improve  $K_i^*$  and that the triazole 5-substituent can lower the overall association rate  $k_{on,overall}$ , we expect that an inhibitor with a triazole on the A ring and a Cl on the B ring should have a significantly increased residence time due to the additive effect of an improved  $K_i^*$  (a smaller  $K_i^*$ ) and a slower overall association rate (a smaller  $k_{on,overall}$ ) (Scheme 3.2). Based on this hypothesis, we designed the inhibitor PT504, and demonstrated that the residence time has been successfully increased to about 10 hrs with a low picomolar  $K_i^*$  (Table 3.4). Because of the high potency of this compound, the progress curve analysis has difficulty accurately delineating  $k_{off}$ , and so the [ $^{32}$ P] direct dissociation assay was used to quantify residence time (Figure 3.7) (18). The true affinity  $K_i^*$  was computed through the kinetic model described above. To sum up, we were able to design a novel InhA inhibitor with a residence time as long as 10 hrs based on our

kinetic analysis, which improved the residence time by 10 fold compared to the first-line anti-TB drug isoniazid (31).

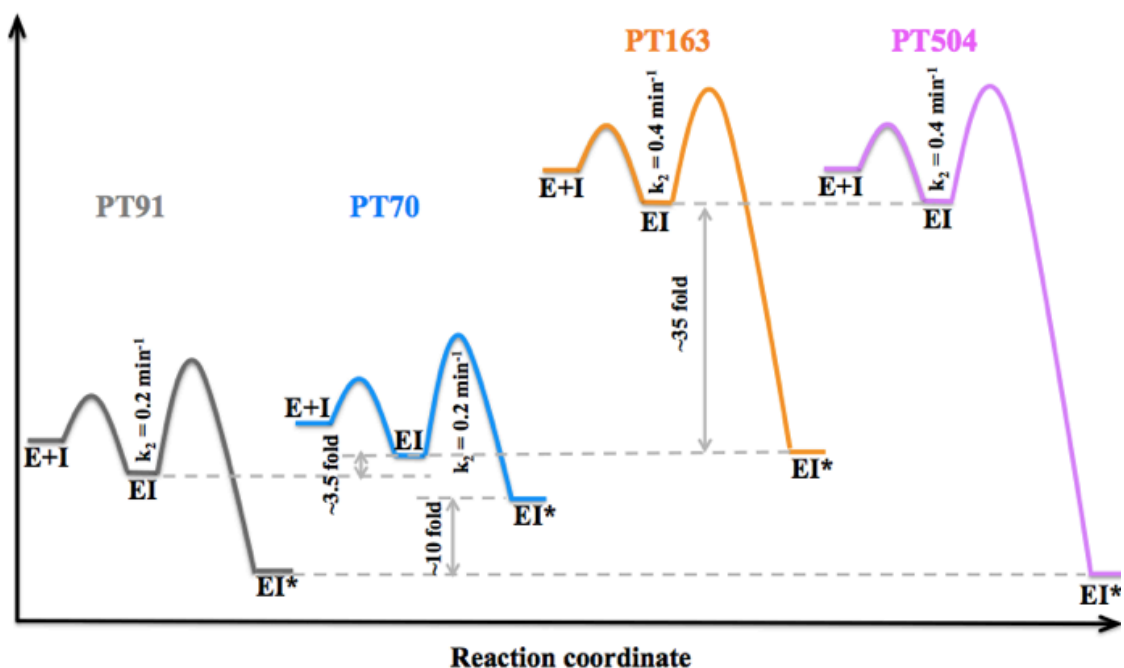


**Figure 3.6 The relative energy level of four different diphenyl ethers on the same reaction coordinate**

The association barriers are within the same magnitude. The  $K_i$  for both PT70 and PT91 are similar, representing by an essentially identical ground state of EI. While the  $K_i$  for PT163 and PT504 are much weaker, depicting by a ~35 fold higher energy level of EI. The  $K_i^*$  of PT91 is the strongest, corresponding to the lowest ground state energy level of EI\*. PT70 is 10 fold weaker than PT91, while EI\* of PT163 is around the level of EI in PT70 and PT91. Based on this observation, PT504 is designed to maximize the dissociation barrier by securing a high energy level of EI while maintaining a low energy level of EI\*.

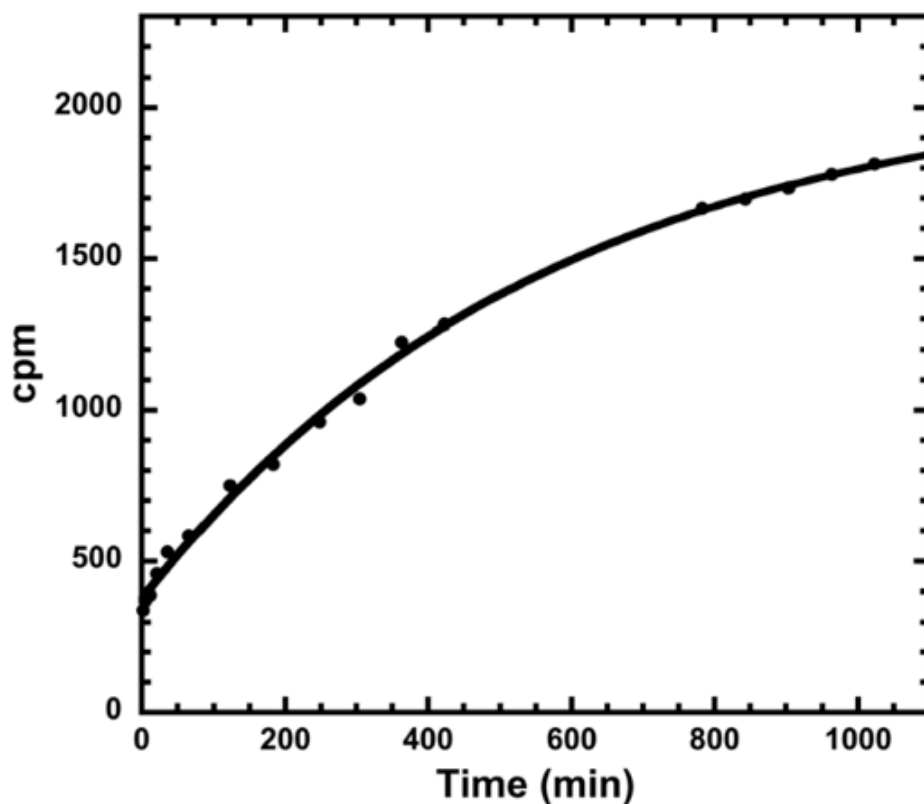


**Figure 3.7** The  $^{32}\text{-P NAD}^+$  dissociation kinetics of PT504

### Structure insight on the 2' substituents

A comparison of the environment and positioning of the 2'-substituents in different InhA-diphenyl ether complex structures reveals significant differences, particularly between the 2'-CN and 2'-Cl groups. Both substituents are generally located in close proximity to the phosphate-ribose portion of the cofactor, and also to amino acid residues A198 as part of  $\alpha$ -helix 6 of the substrate-binding loop (SBL), and additionally to G96. However, the most striking difference can be seen in the distances of the 2'-substituents and the position of the  $\text{C}_\beta$  of A198. The 2'-Cl

substituents of PT91 and PT504 and also the 2'-methyl group of PT514 tend to be oriented more towards A198 (Figure 3.8 A and B), thereby forming close van-der-Waals contact with the C<sub>β</sub> of A198. Considering only subunits with fully defined SBLs, van-der-Waals distances ranging from 3.17 Å (PT504) to 3.48 Å (PT91), and 3.35 Å to 3.48 Å within the InhA-PT514 complex structures can be observed. In contrast, the 2'-CN groups are oriented further away from A198 and located in closer proximity to G96 (Figure 3.8 C and D), but only at a weak hydrogen-bonding distance to the backbone NH of G96, ranging from 3.12 to 3.46 Å in the InhA-PT512 complex and reach a maximum of 3.63 Å for PT506. Further approximation to the backbone NH would also be accompanied by a reduced distance to the backbone carbonyl moiety of G96, which would in turn lead to a repulsion between both negatively charged entities and thus the formation of a stronger hydrogen-bond may not be feasible.

Our data therefore suggest that hydrophobic 2'-substituents, especially a 2'-Cl group, are engaged in van-der-Waals contacts with A198 belonging to  $\alpha$ -helix 6, which leads to a better stabilization of the SBL in a more closed state upon inhibitor binding. The more polar 2'-CN substituents instead, are faced with offsetting attracting as well as repulsive forces. These structural observations are in good agreement with our kinetic results discussed earlier, where the 2'-Cl substituent leads to a significantly improved binding affinity.

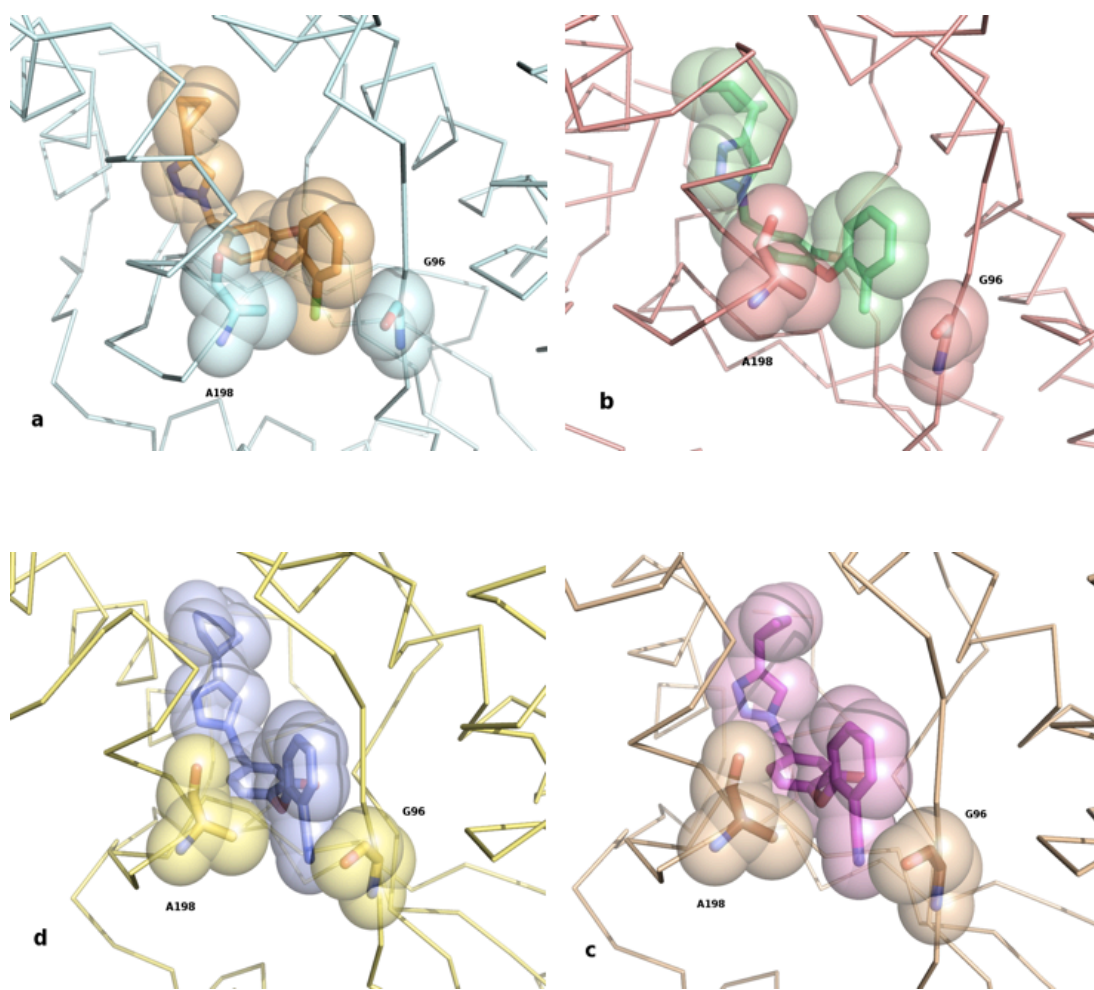


**Figure 3.8 Orientation of different 2'-substituents relative to amino acids G96 and A198 within the substrate-binding pocket of InhA**  
 (a: PT504, b: PT514, c: PT506, d: PT512)

## Comparison of PT506 and PT119 – the triazole greatly aids the interaction with the SBL

PT119 and PT506 both consist of the common diphenyl ether scaffold known for slow-onset inhibitors and possess in addition a cyano substituent at the 2'-position of the B ring. A striking difference between both compounds is the nature of the 5-position substituents on ring A: for PT119 it is a hydrophobic hexyl substituent whereas for PT506 it is a more bulky and not exclusively hydrophobic triazole moiety, supplemented by a cyclopropane ring. Due to this substitution pattern clear differences concerning the residence times of both inhibitors for their target enzyme InhA can be observed. PT506 shows an approximately 3.4 – 4.4-fold ( $t_R = 161 \pm 48$  min) higher residence time compared to PT119 ( $t_R = 47.4$  min), which can be explained by the extensive interactions of the 5-substituent with InhA, leading to the superior inhibitory potential of PT506 relative to PT119.

In general, all interactions known to be characteristic for the binding of diphenyl-ether inhibitors to InhA, such as the hydrogen-bonding network and the typical  $\pi$ - $\pi$ -stacking interactions established by the A ring are maintained by the core structure of PT506. In contrast to the hexyl substituent of PT119, which makes van-der-Waals contacts with F149, M199, I202 and L218, the protein – inhibitor interactions of the 5-substituent of PT506 are more extensive and more diverse in nature: The triazole ring is in close vicinity to the aromatic ring of Y158, and also to F149 and I202.  $C_\zeta$  of the aromatic ring of F149 is located within a C-H –  $\pi$ -interaction distance (3.81 Å) relative to  $N_{AY}$  of the PT506 triazole. In addition, the electron density in the crystal structure clearly shows a hydrogen bond to E219. E219 is located in close proximity to the 5-substituent ( $O_{\epsilon 2, E219} - N_{AO, PT506}$  distance = 3.01 Å) in the PT506 structure



(Figure 3.9 A), whereas the distances between  $O_{\epsilon 2, E219}$  and C3 and C4 of the hexyl substituent in the PT119 complex range from 5.62 to 5.68 Å, respectively.

Because of its spatial requirements the cyclopropane ring of PT506, compared to the hexyl moiety of PT119, creates a larger interaction surface within the substrate binding pocket of the protein, which is reflected by numerous hydrophobic interactions with the residues of  $\alpha$ -helix 6 (I202) and  $\alpha$ -helix 7 (I215, L218) in the SBL, as well as with other regions in InhA's substrate binding cavity (M155, Y158). These additional interactions further stabilize the protein-inhibitor complex formed with PT506 and lead to a longer residence time of PT506 compared to PT119.

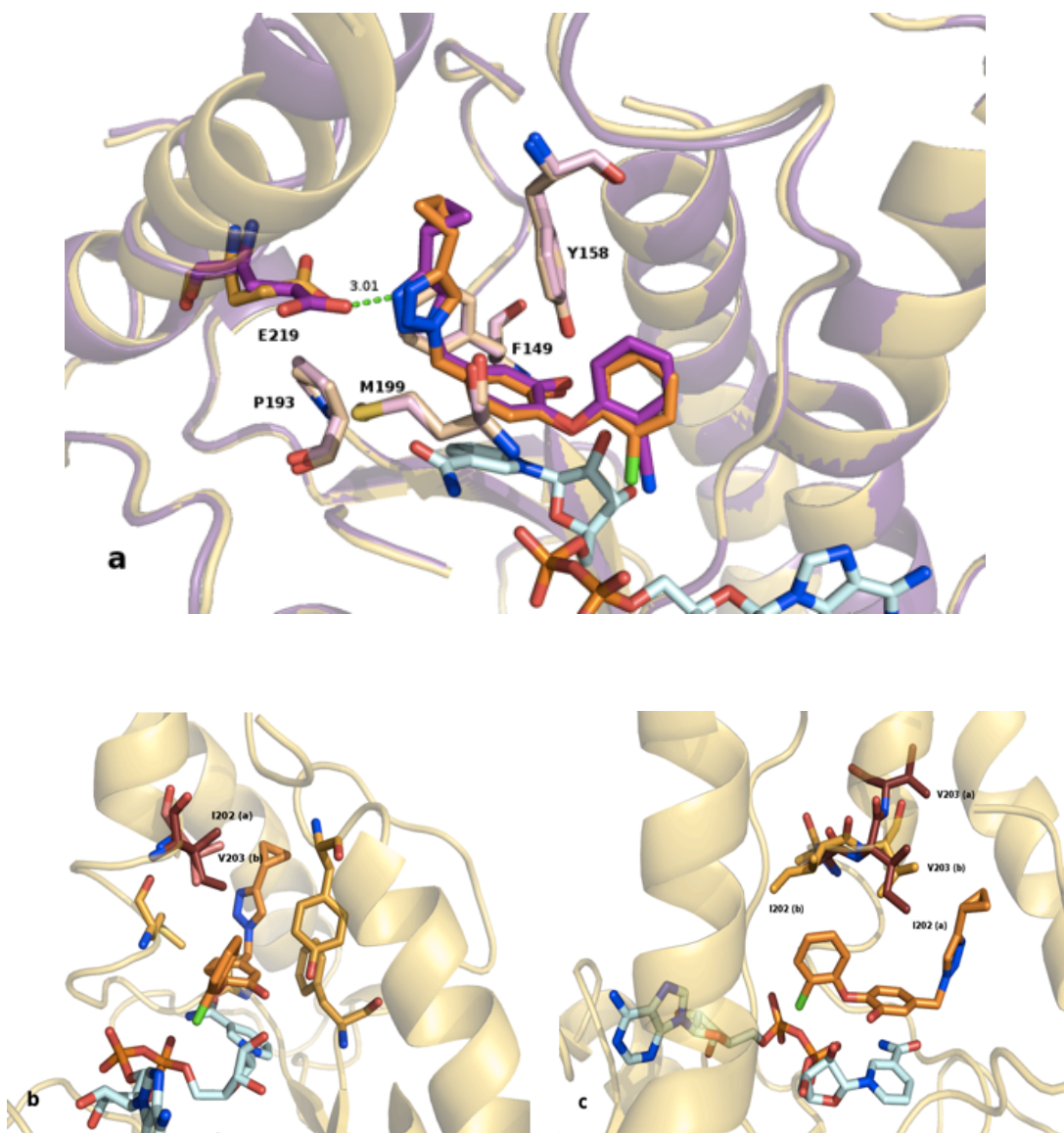


**Figure 3.9 The dynamic nature of interactions between InhA and PT504/PT506**

A: Hydrogen bond between E219 and triazole moieties of PT504 (orange) and PT506 (magenta) and protein surrounding of the triazole ring; hydrogen-bonding distance (green) is shown for PT506; B: Interaction of the triazole with either I202 (a, more open SBL conformation) or V203 (b, closed SBL); C: Amino acid shift between more open (a, dark red) and closed (b, gold) SBL conformation

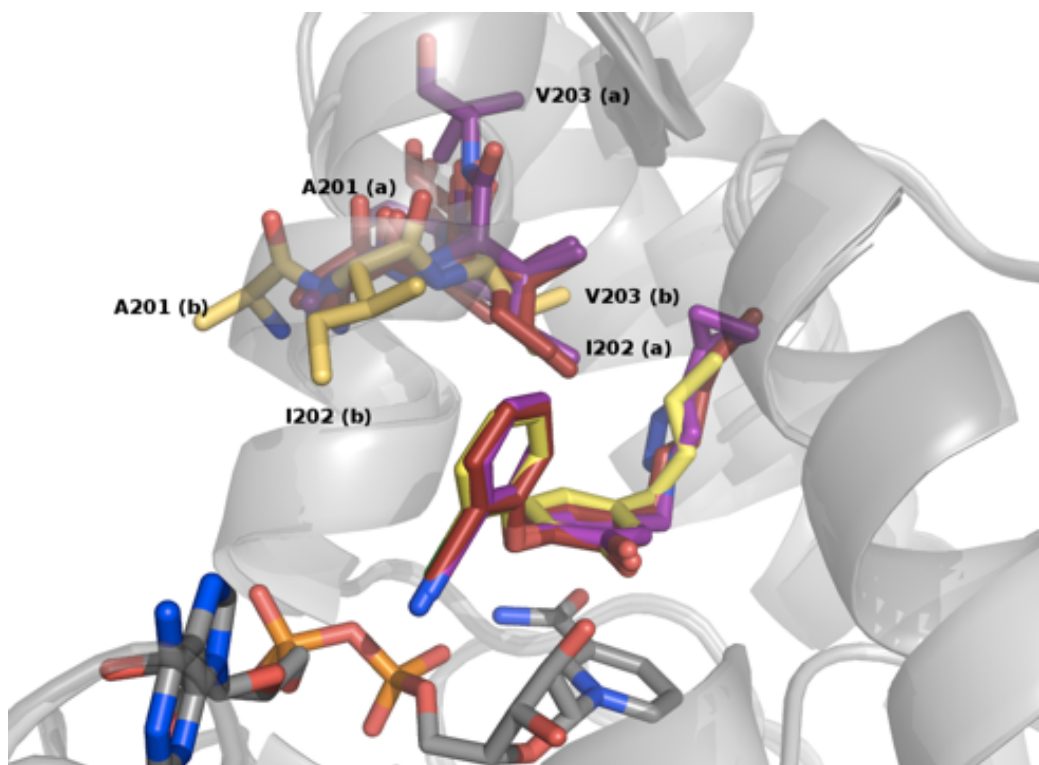


Figure 3.10 **Comparison of amino acids A201 – V203 of the SBL's  $\alpha$ -helix 6**  
 The closed conformation for PT91 is shown in yellow, the more open conformations are depicted in red (PT119) and magenta (PT506)

Compared to the [InhA·NAD<sup>+</sup>·PT91] complex, which adopts a completely closed state of the SBL, both the PT506 and the PT119 complexes show a shift of amino acids A201 – V203 by approximately one amino acid (Figure 3.10). This shift leads to reduced contact interface between the inhibitor and  $\alpha$ -helix 6 of the protein, excluding V203 from hydrophobic interactions with the compound. Instead, V203 now partially occupies the space within the hydrophobic cavity, which in the totally closed SBL state of [InhA·NAD<sup>+</sup>·PT91] would be occupied by I215 of  $\alpha$ -helix 7. To prevent clashes between these residues, I215 has moved closer

to the 5-substituent of the respective inhibitor, thus leading to a global rearrangement of the entire SBL in the PT506 and PT119 complex structures.

#### Crystal structure of PT504

The crystal structure of InhA in complex with NAD<sup>+</sup> and PT504 belongs to space group I 2 and contains one tetramer in the asymmetric unit (Figure 3.11). The inhibitor is bound to all four subunits in the tetramer, and the interactions known to be crucial for inhibitor binding to the binary [InhA·NAD<sup>+</sup>] complex are present in all four molecules of the crystal structure. These interactions consist of  $\pi$ - $\pi$ -stacking interactions between ring A of PT504 and the nicotinamide ring of NAD<sup>+</sup>; accompanied by hydrogen bonds created by the 1-OH substituent of ring A with the hydroxyl group of Y158 as well as with the 2'-OH of the nicotinamide ribose. Ring B of PT504 is embedded in a hydrophobic environment created by residues G96, F97, M98, M103 and Y158, as well as by I202 belonging to the SBL  $\alpha$ -helix 6. The 2'-chlorine substituent is accommodated in a mostly hydrophobic pocket made up by G96, A198 as an integral part of  $\alpha$ 6, but also the ribose pyrophosphate portion of the cofactor (Figure 3.12).

Similar to the ternary [InhA·NAD<sup>+</sup>·PT506] complex, O <sub>$\epsilon$ 1</sub> of E219 of InhA is directed towards the triazole N<sub>AN</sub> to form a hydrogen bond with distances between 2.64 and 2.96 Å in all subunits. Additionally, the triazole moiety is involved in several interactions with its surrounding. The nitrogen portion of the ring is in hydrophobic contact with P193 and M199; whereas the carbon half interacts with F149 and Y158 (Figure 3.9 A). Interestingly, the inhibitor is bound to all four subunits in the tetramer, but the SBL adopts different conformational states

in each subunit and differences in the protein- cofactor – inhibitor contacts can be observed in all four binding variants. In monomers A and E with a completely ordered SBL, this region of the triazole additionally interacts more closely with V203, whereas in the partially ordered state in monomers B and G, an interaction with I202 can be observed. This is due to the more open SBL conformation (Figure 3.9 B (a)) in subunits B and G which leads to a shift of I202 to the position where V203 would be located at a fully closed SBL state (Figure 3.9 B (b)).

The cyclopropane interactions with the protein surrounding differ in some detail between the monomers, because the substituent can assume slightly different orientations within the hydrophobic pocket. In general, hydrophobic contacts can be observed with residues A157, Y158, I215 or L218. The differences in the interaction patterns of both, the triazole and the cyclopropane moieties correspond to the observed shift of amino acids A201 – V203 by one amino acid when comparing the subunits with partially disordered and completely ordered SBLs. In the closed state of subunits A and E (Figure 3.9 C (b)) the positioning of these amino acids matches the one observed for the completely closed [InhA·NAD<sup>+</sup>·PT91] ternary complex. In contrast, monomers B and G display an orientation of I202 more towards the direction of the hydrophobic pocket accommodating the inhibitor's 5-substituent, which resembles the SBL states mostly seen for the 2'-CN substituted inhibitors PT119, PT506 and in part PT512 (Figure 3.9 C (a)).

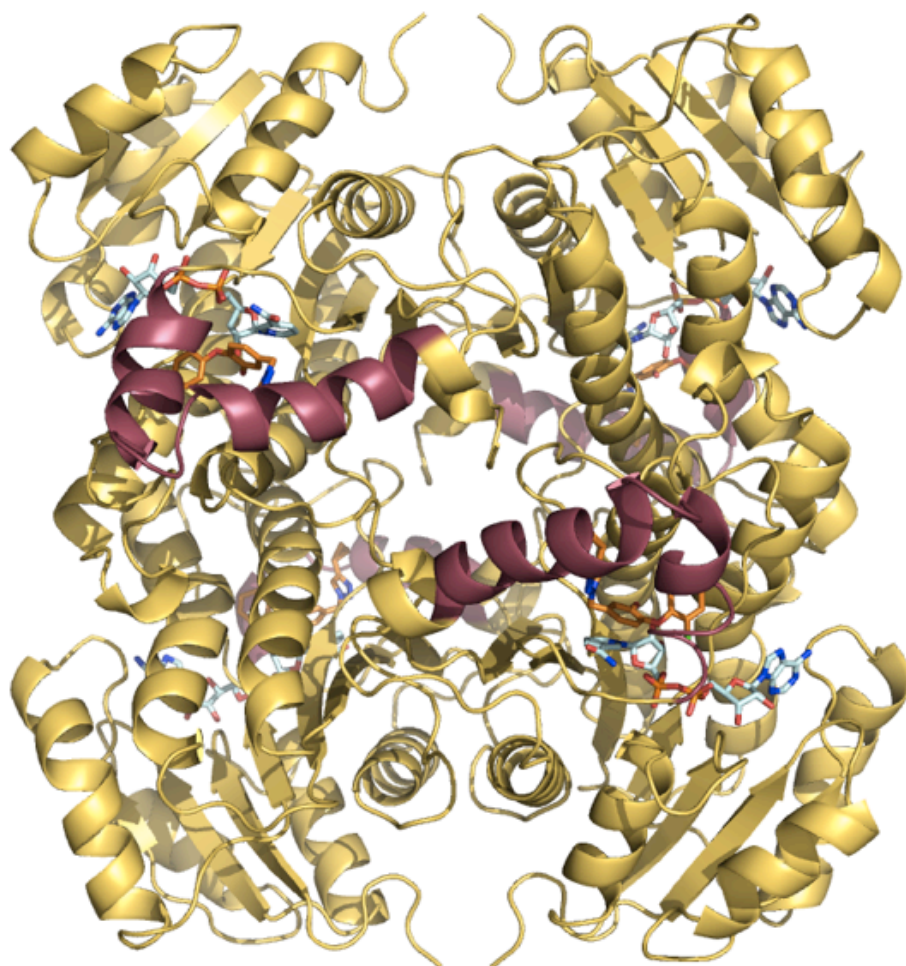


**Figure 3.11 InhA tetramer with bound cofactor and PT504**

Cofactor is shown in pale green and PT504 in orange; SBL is depicted in raspberry

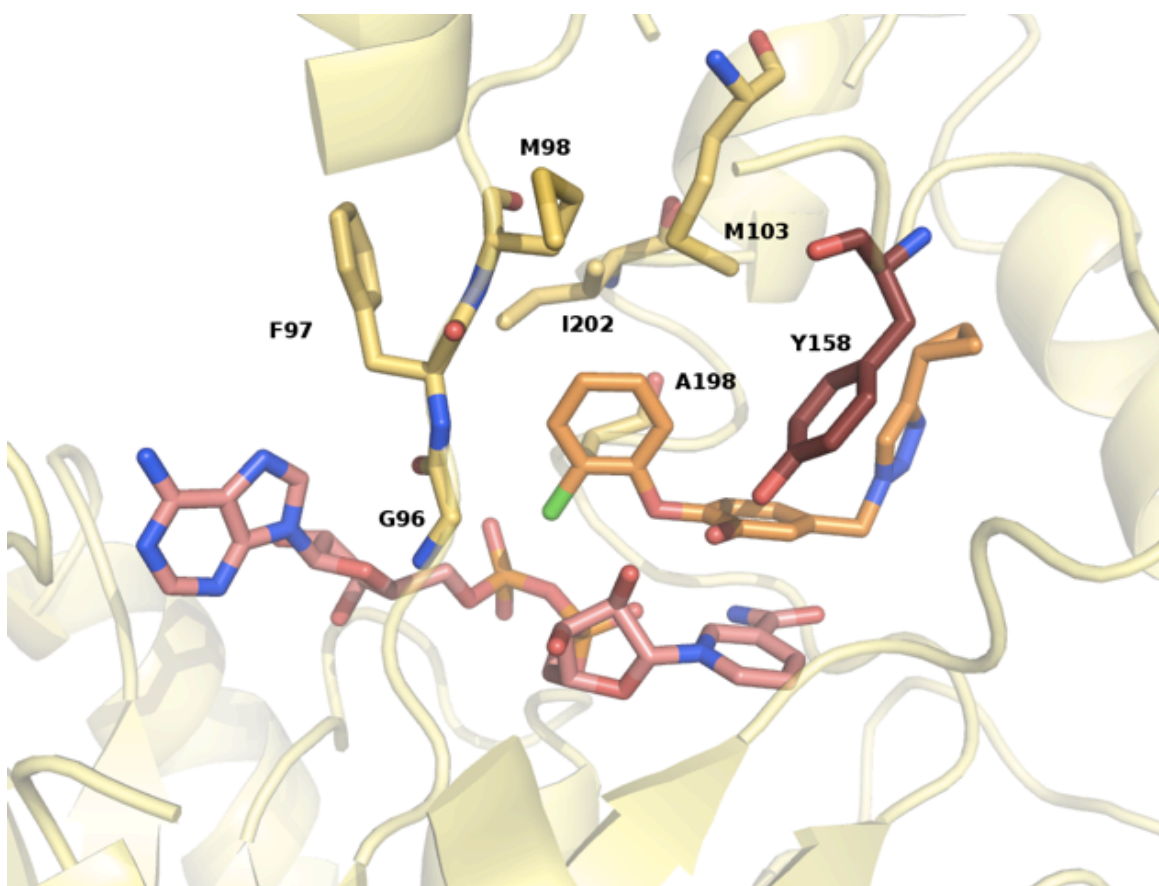


**Figure 3.12 Hydrophobic environment of the B-ring of PT504 within the substrate-binding pocket of InhA**

Catalytic Y158 is depicted in dark red

Comparison of PT506, PT504, PT512, PT514 PT91 and PT119 – hydrogen bond formation between Q214 and triazole ring reveals an energetically elevated intermediate state captured by 5-bulky substituent, yet the entropically-favored inward conformation of I215 represented the final ground state

The positioning of ring A and B within the substrate-binding pocket of all observed structures is similar and the previously described interactions of ring A with the cofactor and the

target enzyme known to be essential for inhibitor binding are maintained in each of the reviewed complexes. The general environment of ring B of all herein described structures is created by residues G96, F97, M98, M103, M161, Y158, and I202 ( $C_{\gamma 2}$ ) as part of the SBL and assumes a mainly hydrophobic character.

The conformations of the SBLs in chains B and D of [InhA·NAD<sup>+</sup>·PT512] and [InhA·NAD<sup>+</sup>·PT514] are very similar to each other, and differ from the other subunits concerning the loop region between  $\alpha 6$  and  $\alpha 7$  (G205 - L207), assuming a more open state, which is not observed in any of the other complex structures (Figure 3.13). For all the other subunits of InhA in complex with PT504, PT506, PT512 or PT514 either a closed conformation (subunits A and E; A, C, F and A, C, E with PT504, PT512 and PT514, respectively) is observed as it is present in the [InhA·NAD<sup>+</sup>·PT91] complex or an intermediate state of the loop similar to [InhA·NAD<sup>+</sup>·PT119] (subunit E of the PT512 structure and the [InhA·NAD<sup>+</sup>·PT506] monomer) can be seen. Interestingly, the conformation of the loop region can be locally modulated without necessarily leading to an altered alignment of  $\alpha$ -helices 6 or 7 between monomers of the same complex structure.



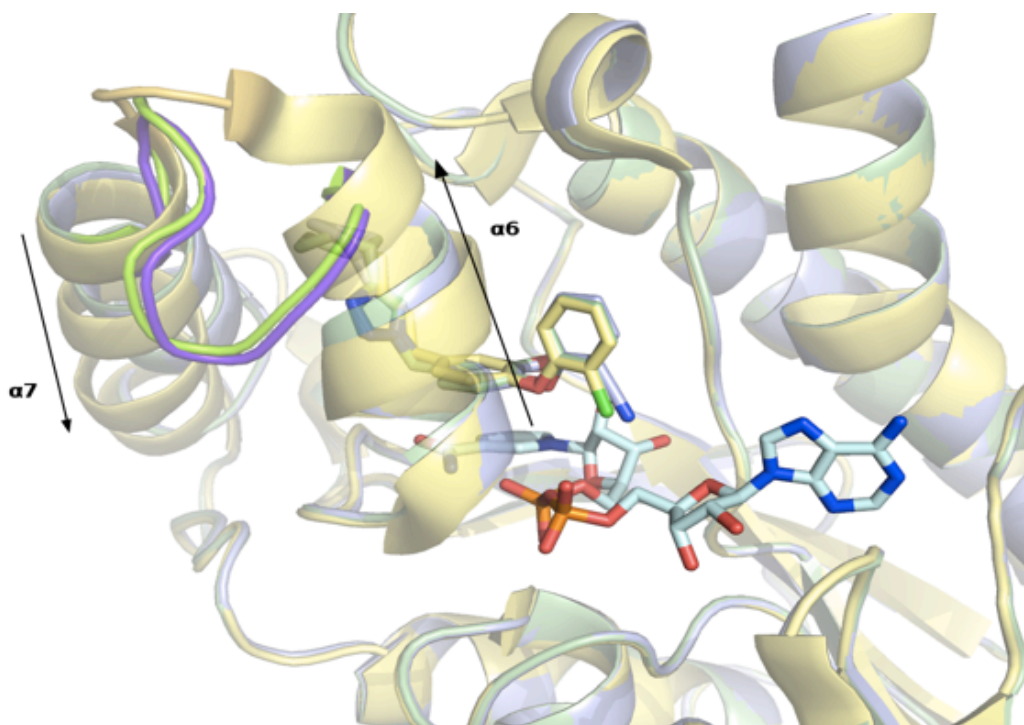


**Figure 3.13 Extraordinary conformation of the loop region between  $\alpha$ -helices 6 and 7**

The SBL within subunits B of the PT512 is shown in purple and PT514 in green; the PT91 (yellow) structure is shown as reference

Compared to the ternary  $[\text{InhA}\cdot\text{NAD}^+\cdot\text{PT91}]$ ,  $[\text{InhA}\cdot\text{NAD}^+\cdot\text{PT119}]$  and  $[\text{InhA}\cdot\text{NAD}^+\cdot\text{PT506}]$  complex structures, the SBLs of the InhA structures with PT504, PT512 and PT514 differ within their position of  $\alpha$ -helix 7. The N-terminal part of  $\alpha$ -helix 7 more closely resembles the orientation of  $\alpha$ -helix 7 as observed in the  $[\text{InhA}\cdot\text{NAD}^+\cdot\text{PT91}]$  complex, whereas the C-terminal region of  $\alpha$ -helix 7 in these structures rather approximates the alignment present within the  $[\text{InhA}\cdot\text{NAD}^+\cdot\text{PT119}]$  and  $[\text{InhA}\cdot\text{NAD}^+\cdot\text{PT506}]$  complex structures. Additionally, the orientation of  $\alpha$ -helix 7 in the complexes with PT512 and PT514 is stabilized by a hydrogen-bond formed between Q214 and the triazole moiety (Figure 3.14 A), which displays a clear

difference to the observation for the [InhA·NAD<sup>+</sup>·PT504] and [InhA·NAD<sup>+</sup>·PT506] complexes involving E219 in hydrogen-bonding interactions instead (Figure 3.9 A).

In the C-terminal region of  $\alpha$ -helix 6, monomers of [InhA·NAD<sup>+</sup>·PT504], [InhA·NAD<sup>+</sup>·PT512] and [InhA·NAD<sup>+</sup>·PT514], possessing a rather closed SBL, more closely resemble the conformational character of the [InhA·NAD<sup>+</sup>·PT91] ternary complex. However, within the more open chains of [InhA·NAD<sup>+</sup>·PT512] (subunits B, D, E) and [InhA·NAD<sup>+</sup>·PT514] (subunits B, D), those regions present a higher similarity to the [InhA·NAD<sup>+</sup>·PT119] and [InhA·NAD<sup>+</sup>·PT506] structures; also relating to the altered arrangement of amino acids A201 – V203, making reduced hydrophobic contacts with the diphenyl-ether ring system in these monomers. In contrast to these differences in  $\alpha$ -helix 6 and the loop region in the individual subunits of the [InhA·NAD<sup>+</sup>·PT512] complex,  $\alpha$ -helix 7 is oriented in an identical slightly opened fashion in all subunits, except monomer C. In this subunit  $\alpha$ -helix 7 is more closed and for that reason closer, but not fully, approximates the conformational state of [InhA·NAD<sup>+</sup>·PT91]. In this case no hydrogen-bond exists between the triazole ring of PT512 and Q214, because the position of Q214 is occupied by I215 instead (Figure 3.14 B). This inward-rotated state of I215 is also present in the [InhA·NAD<sup>+</sup>·PT91] complex, which is thought to represent the final [EI]\* state of the inhibitor-binding process, suggesting that the triazole hydrogen-bonded state to Q214 displays another intermediate state during the SBL ordering process, which is captured by the presence of bulkier groups at 5-position of ring A. Additionally, amino acids A201 – V203 of monomer C assume the same conformation as in the PT91 complex, indicating that here the final, energetically most favorable state is reached. Since the inward orientation of I215 can also be observed within the [InhA·NAD<sup>+</sup>·PT504] and

[InhA·NAD<sup>+</sup>·PT506] structures, together with an additional hydrogen bond between the triazole moiety and E219 (Figure 3.15), this buried state of I215 seems to be entropically favored. The inward-rotation of I215 in combination with the hydrogen-bond formed to E219 might have a positive synergistic effect on the residence times of these inhibitors. However, this phenomenon only seems to be possible for the inhibitors PT504 and 506 which possess a more flexible and less bulky cyclopropyl substituent compared to PT512 and PT514. This observation provided structural support in our kinetic characterization regarding the final ground state and reinforced the rational design of PT504.

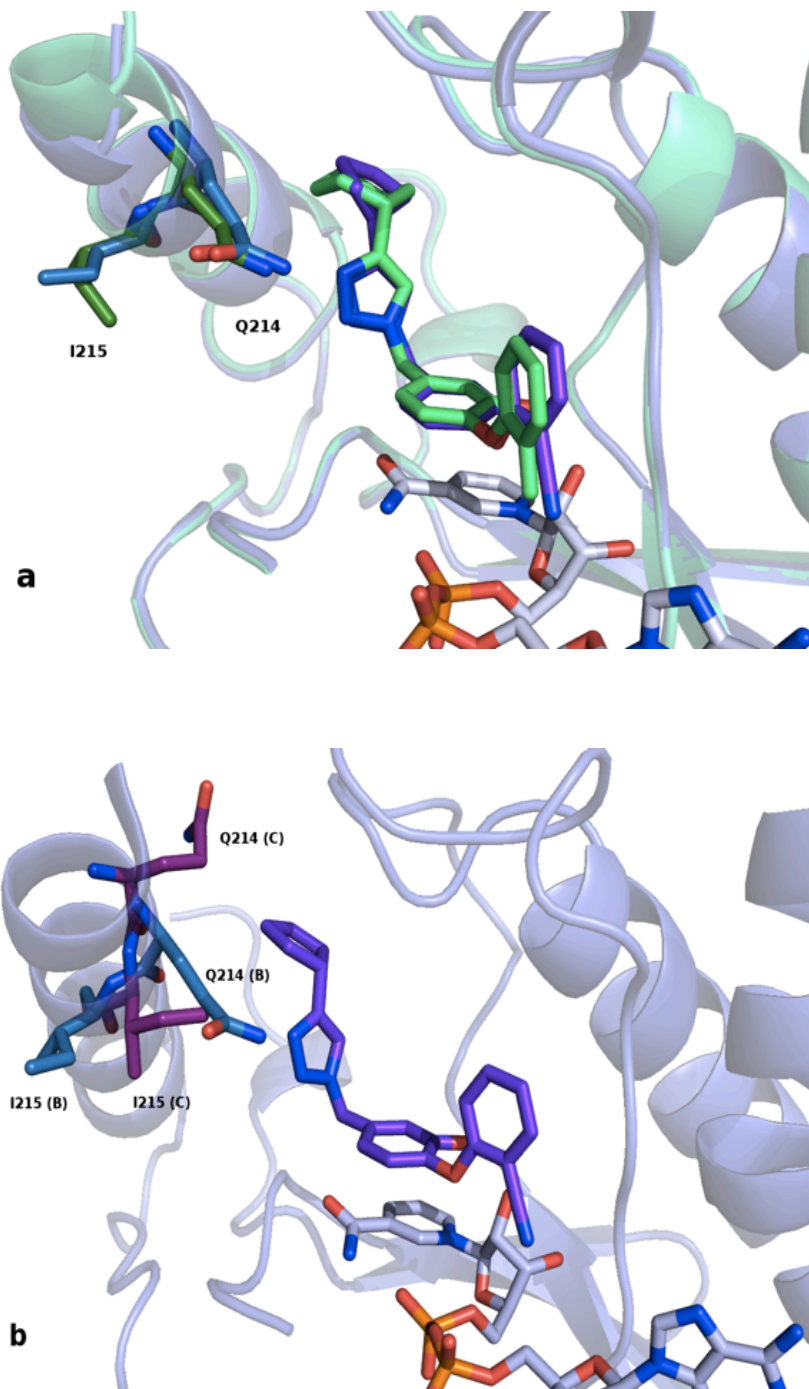


**Figure 3.14 Position of Q214 and I215 of InhA-PT512/PT514 complex**

a: Position of hydrogen-bond donor Q214 and I215 relative to PT512 (purple/ blue) and PT514 (green); b: Position of Q214 and I215 in the special case of monomer C (dark magenta) compared to monomer B (blue) within the PT512 structure

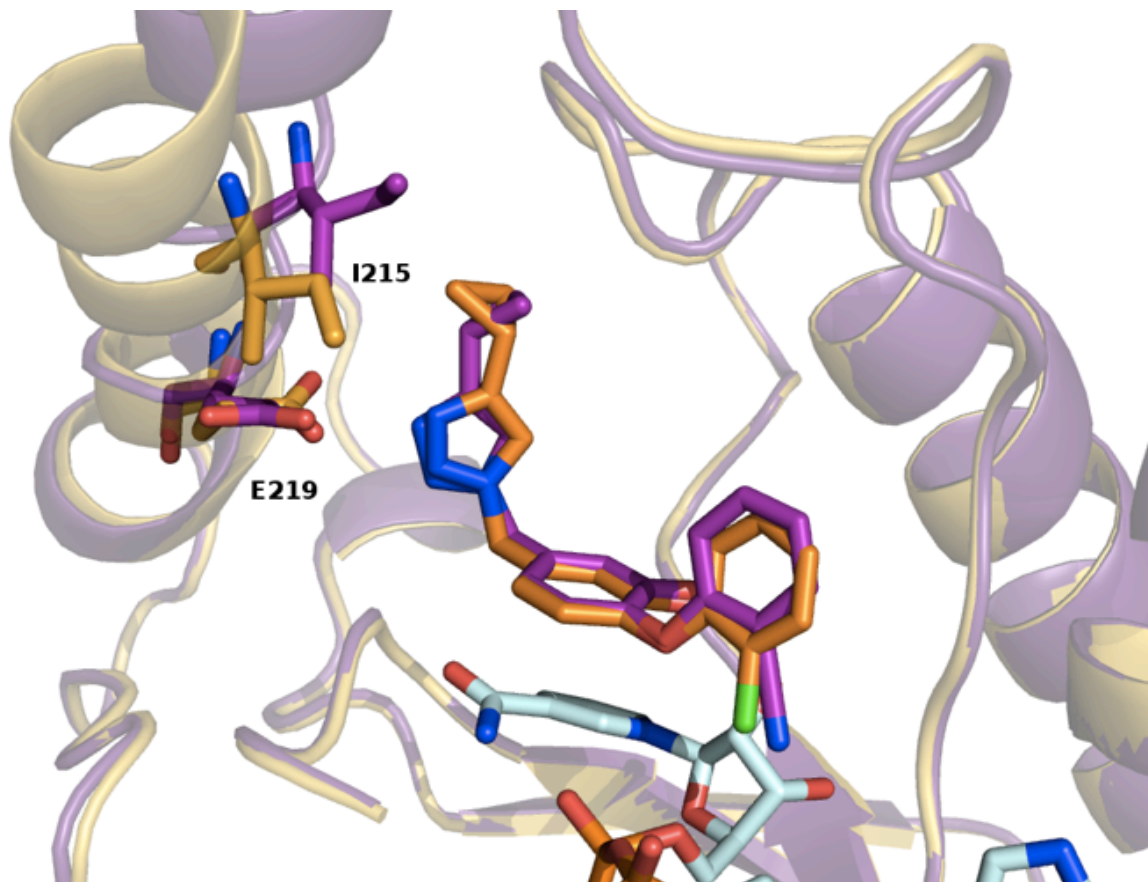


**Figure 3.15** Position of hydrogen-bond donor E219 and I215 within the substrate-binding pocket of InhA

PT504 is shown in orange and PT506 in magenta.

The multiple SBL conformations observed in the  $[\text{InhA}\cdot\text{NAD}^+\cdot\text{PT512}]$  complex provided a good platform in understanding the transition state conformation captured by the triazole series along the reaction coordinate. In case of the  $[\text{InhA}\cdot\text{NAD}^+\cdot\text{PT512}]$  and  $[\text{InhA}\cdot\text{NAD}^+\cdot\text{PT514}]$  complexes it might be an entropical advantage to have Q214 instead of I215 solvent-exposed, again indicating that the hydrogen-bond formation of the triazole substituent with Q214 might

stabilize an intermediate, energetically elevated state during the binding process, but does not represent the final [EI]\* state. However, within [InhA·NAD<sup>+</sup>·PT514] the buried state of I215 is not observed in any of the monomers, although residues A201 – V203 also assume a conformation similar to the PT91-complex structure in some of the subunits. This might be due to the fact that the cyclohexyl substituent requires more space within the hydrophobic cavity, thereby forcing  $\alpha$ -helix 7 to assume a different conformation. The role of the size of the cycloalkyl substituents is again underlined by the fact that for the inhibitors PT504 and PT506 possessing only a cyclopropane ring, the inward-rotation of I215 is still possible. Considering the [InhA·NAD<sup>+</sup>·PT91] SBL conformation, including the typical orientation of residues A201 – V203 in  $\alpha_6$  as final [EI]\* state one can assume that the second most frequently occurring conformation of residues A201 – V203 as it is primarily observed for 2'-CN-substituted inhibitor complexes or subunits of 2'-Cl or 2'-methyl-substituted InhA-inhibitor complexes containing a partially disordered SBL depicts an energetically elevated [EI] state along the path towards the final [EI]\* state of the inhibitor binding process, representing a local energy minimum. In case of the PT512-inhibitor complex the transition into an entropically favored (I215) conformation with a maximum of protein-inhibitor interactions (A201 – V203) might be facilitated by the hydrogen-bond formation between the triazole moiety and Q214.

Another interesting difference arises in the orientation of the triazole ring's nitrogen portion of PT504 and PT506 compared to PT512 and PT514. A torsion angle of  $\approx 49^\circ$  can be observed between the triazole ring plains of PT504 and PT506 and the ones of PT512 and PT514 around an axis through C<sub>AK</sub> parallel to the ring plain (Figure 3.16 A and B). This orientation

further provides explanation for the different interactions of PT504 and PT506 with  $\alpha 7$  occur compared to PT512 and PT514. While the nitrogen portions of PT504

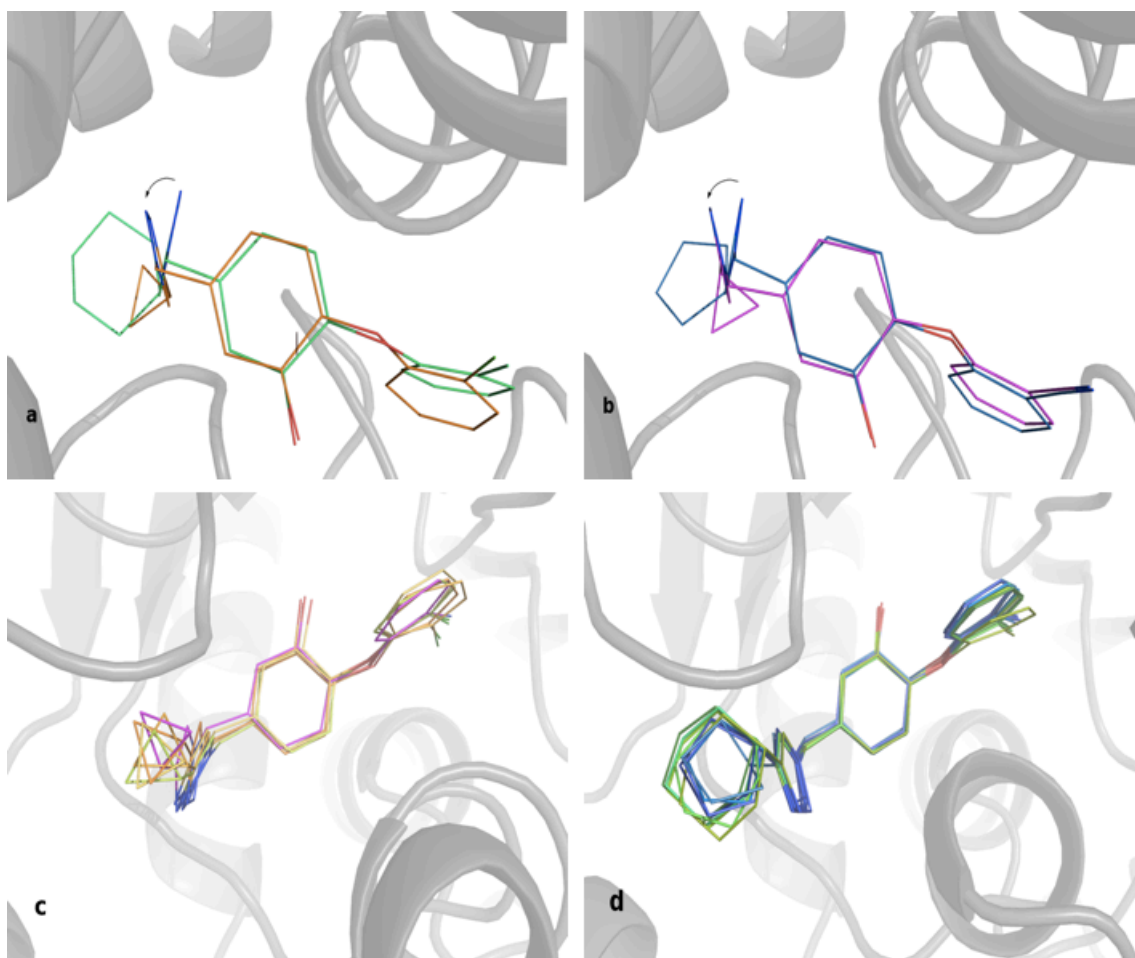


**Figure 3.16 Dynamics of the substrate-binding cavity**

a - b: Comparison of the orientation of the triazole moiety within the substrate-binding cavity between inhibitors with smaller and larger cycloalkyl-substituents (a: PT504 (orange) vs. PT514 (green), b: PT506 (magenta) vs. PT512 (blue)); c - d: Comparison of the conformational freedom of the cycloalkyl-substituents within the substrate-binding cavity (c: PT504 (light green/ yellow/ orange) and PT506 (magenta), d: PT512 (blue) and PT514 (green))

and PT506 form a hydrogen bond to E219 of the SBL, the torsion of the ring plains in PT512 and PT514 leads to the formation of a hydrogen bond with Q214. The variation of the interaction partner of the triazole moiety seems to locally influence the tilt of  $\alpha$ -helix 7 and stabilize it in a distinct conformation. The different orientation modes of the triazole moieties may have their origin in the altered positions of the cyclopropane groups compared with the bulkier cyclopentane and cyclohexane substituents within the substrate-binding pocket. Due to their lower spatial requirements, the plains of the cyclopropane rings of PT504 and PT506 possess a higher rotational freedom within the substrate-binding pocket (Figure 3.16 C) and are thereby able to assume different orientations. The cyclopentane and -hexane rings of PT512 and PT514, however, adopt one distinct orientation in all subunits within the substrate-binding pocket (Figure 3.16 D), creating an altered contact interface with  $\alpha$ 7 by interacting with L217 rather than with I215.

The energy barrier is predominantly from enthalpic contributions for the 5-alkyl substituents, while entropic contributions increased for the 5-triazole substituents

Enhancing thermodynamic potency is a primary goal of any drug discovery effort. However, little effort is often expended to understand the underlying enthalpic and entropic components that contribute to the free energy. The  $^{32}\text{P}$  direct dissociation method, which we developed in Chapter 2 allowed us to measure the dissociation rate constant at different temperatures, making it possible to investigate the energy component during the drug dissociation process using the Arrhenius analysis and Eyring equation. We chose PT05, PT113



and PT119 as our acyl-chain analog representatives, and PT163, PT501 and PT503 as triazole-analog representatives. The compounds of interest were assessed at 5 different temperatures, ranging from 4 °C to 25 °C. A large temperature interval is critical for the quality of the linear regression in determining the activation energy, but these conditions are rarely fulfilled with proteins (32). As expected, the kinetic rate constants increased with increasing temperature, yet at different rates and starting points among different inhibitors (Table 3.6). The activation energy (activation enthalpy) was extrapolated from the linear regression of the Arrhenius equation. As shown in Figure 3.17 A and Table 3.7, the energy component of PT05 and PT113 were similar to each other. The activation enthalpies were 13.96 kcal/mol and 15.62 kcal/mol, respectively; while the  $-\Delta TS^\ddagger$  were 7.98 kcal/mol and 6.21 kcal/mol. When the 5-substituent becomes more rigid and hydrophobic, the  $-\Delta TS^\ddagger$  has a bigger contribution in the activation free energy. The  $-\Delta TS^\ddagger$  of PT501 increased to 8.12 kcal/mol, and further increased to 10.17 kcal/mol and 10.21 kcal/mol for PT163 and PT503, respectively. It is interesting to note that the entropy enthalpy compensation is observed for all of these compounds, as the activation free energies are around the magnitude across all inhibitors. Surprisingly, when compared to PT05 and PT113, PT119 has a much higher activation enthalpy of 27.88 kcal/mol and a negative  $\Delta TS^\ddagger$  of -5.97 kcal/mol. As the major difference among these compounds is the 2'-substituent, we speculate that the cyano group on PT119 creates a very strong repulsive interaction with the protein, leading to an increase in enthalpy and a less favorable entropy. This was confirmed with the previous structural analysis (Figure 3.8 C and D). To take a closer look at the enthalpy and entropy contribution to the Gibbs free energy, we replotted Figure 3.17A into Figure 3.17 B. As suggested in Figure 3.17 B, the activation enthalpy of dissociation,  $\Delta H^\ddagger$  contributes to most of the Gibbs free energy for the acyl-chain diphenyl ethers. The enthalpy component for the

dissociation of PT05 and PT113 is 64% and 72%, respectively. The entropic contribution to  $k_{\text{off}}$  increased with hydrophobicity and rigidity. As the 5-substituent becomes more rigid and hydrophobic, the entropic component increases from 28% and 36% for PT113 and PT05, to ~50% for PT163 and PT503, respectively. The effects of these hydrophobic interactions are possible evidence for a dissociation process in which a more rigid and more hydrophobic substituent yields a slower off-rate. One could imagine creating the smallest possible solvent accessible area in the crevice between the loop region and A ring of the compound and thereby shielding the hydrophobic residues from interacting with the solvent, thus resulting in a lower  $k_{\text{off}}$  (32). This observation rationalizes the extremely long residence time of PT504, as Ring A of PT504 creates hydrophobic contacts with residues A157, Y158 and L218, while Ring B is also embedded in a hydrophobic environment created by residues G96, F97, M98, M103, Y158 and I202. Our conclusion is further supported by Meinhold *et al* (PERSONAL COMMUNICATION) from GSK who reported that larger, more hydrophobic and rigid compounds tend to have slower off-rates as the physical properties of the compound limits the escape trajectory as well as excludes water in a more efficient manner.

Figure 3.17 C further illustrates the enthalpy entropy compensation that was observed in the system. The plot comparing  $\Delta H^\ddagger$  and  $-T\Delta S^\ddagger$  shows a negative correlation. Since free energy is the sum of  $\Delta H^\ddagger$  and  $-T\Delta S^\ddagger$  and is held constant among different inhibitors, therefore enthalpy and entropy must be numerically negatively correlated (33).

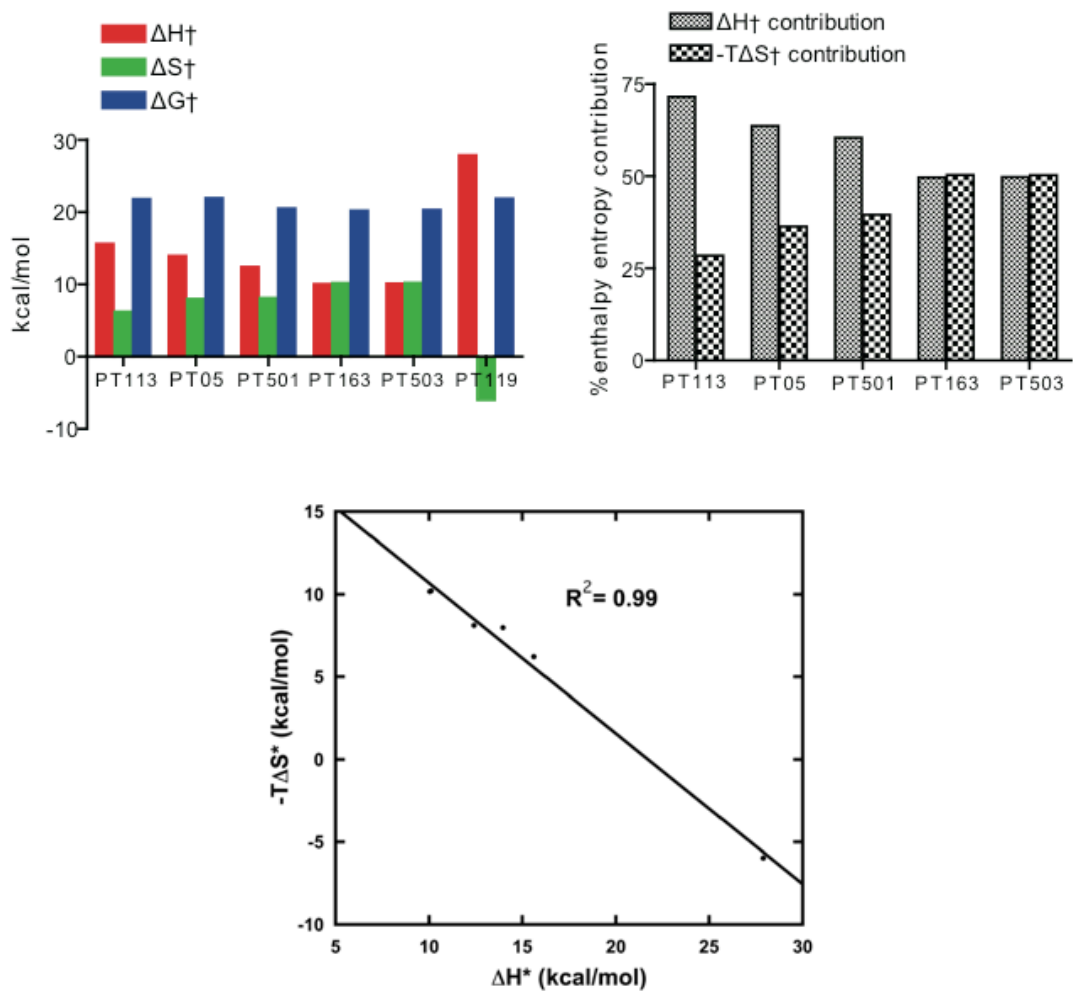


**Figure 3.17 Thermodynamic analysis of inhibitor dissociation phase**

A) Thermodynamic profiles for selected diphenyl ethers from  $^{32}\text{-P NAD}^+$  dissociation kinetics:  $\Delta H^\ddagger$  (red),  $-T\Delta S^\ddagger$  (green), and  $\Delta G^\ddagger$  (blue). B) The percentage contribution of activation enthalpy or entropy to total activation free energy. C) Plot of activation enthalpy ( $\Delta H^\ddagger$ ) VS. entropy ( $-T\Delta S^\ddagger$ )

Table 3.6  $k_{\text{off}}$  at difference temperatures for various inhibitors

| Compound | $k_{\text{off}}$ at 24 °C<br>( $\text{min}^{-1}$ ) | $k_{\text{off}}$ at 20 °C<br>( $\text{min}^{-1}$ ) | $k_{\text{off}}$ at 15 °C<br>( $\text{min}^{-1}$ ) | $k_{\text{off}}$ at 10 °C<br>( $\text{min}^{-1}$ ) | $k_{\text{off}}$ at 4 °C<br>( $\text{min}^{-1}$ ) |
|----------|--|--|--|--|---|
| PT113    | 0.032  | 0.021  | 0.013  | 0.0074   | 0.0044  |
| PT05     | 0.038  | 0.018  | 0.011  | 0.0073   | 0.0056  |
| PT501    | 0.0048   | 0.0039   | 0.0027   | 0.0016   | 0.0010  |
| PT163    | 0.0087   | 0.0065   | 0.0053   | 0.0035   | 0.0024  |
| PT503    | 0.01   | 0.0081   | 0.0059   | 0.0043   | 0.0028  |
| PT119    | 0.014  | 0.0075   | 0.0040   | 0.0020   | 0.00084   |

Table 3.7 Activation enthalpy, entropy and free energy for different inhibitors

| Compound | $E_a$ (kcal/mol) | $\Delta H^\ddagger$ (kcal/mol) | $-T\Delta S^\ddagger$<br>(kcal/mol) | $\Delta G^\ddagger$ (kcal/mol) |
|----------|------------------|--------------------------------|-------------------------------------|--------------------------------|
| PT113    | 16.21            | 15.62                          | 6.21                                | 21.83                          |
| PT05     | 14.55            | 13.96                          | 7.98                                | 21.94                          |
| PT501    | 12.99            | 12.41                          | 8.12                                | 20.53                          |
| PT163    | 10.63            | 10.04                          | 10.17                               | 20.21                          |
| PT503    | 10.70            | 10.11                          | 10.21                               | 20.32                          |
| PT119    | 28.48            | 27.88                          | -5.97                               | 21.89                          |

The slow association barrier mainly derives from large scale refolding of  $\alpha$ -helix 6: evidence from V203A, I215A, L207A InhA

Based on the above analysis, we further investigated the molecular mechanism associated with the energy barrier for the second step ( $k_2$ ) (Scheme 3.2). According to our previous observations on the conformation between time-dependent inhibitors and rapid reversible inhibitor, we proposed in a recently published paper that the open conformation of  $\alpha$ -helix 6 represents the EI state, whereas the closed conformation represents the EI\* state (16). From the extensive crystallographic analysis provided here, we were able to capture and distinguish different conformations of the substrate binding loop ( $\alpha$ -helix 6) within different subunits of the InhA-inhibitor complex, which might depict the unstable intermediates along the reaction pathway. Therefore, we hypothesized that the energy barrier associated with the second step results from the loop motion change between  $\alpha$ -helix 6 (SBL) (residue 197 to 210) and the adjacent  $\alpha$ -helix 7 (residue 211 to 220), and that helix 6 has a larger scale of motion compared to helix 7 as the SBL closes over the active site from an open conformation to a closed conformation. In order to test the hypothesis and link the structural insights with enzyme kinetics, we constructed alanine mutations on residue V203, L207 and I215, as structural analysis suggested that hydrophobic residues namely M199, I202, V203, L207 on helix 6 and I215 on helix 7 had close interactions with the ligand. These alanine mutations will allow us to explore the relationship between the loop motion and the barrier-crossing activity in inhibitor kinetics.

The Michaelis-Menten parameters for wild-type InhA, V203A, I215A and L207A variants were listed in Table 3.8. The  $k_{\text{cat}}/K_m$  values for all constructs were almost identical, with one exception - that of V203A where a  $\sim 3$ -fold change in  $k_{\text{cat}}/K_m$  was observed compared to wild-type InhA. To investigate how these alanine mutations would affect the second step slow onset barrier, we used PT70 as our model ligand to explore the change in the association barrier using progress curve analysis. As the progress curve analysis is limited to determining only particular kinetic and thermodynamic constants – i.e.  $K_i^{\text{app}}$ ,  $K_i^{*\text{app}}$ ,  $k_{-2}$ , we use the kinetic model described earlier to obtain all the kinetic parameters. Overlay of the experimental and simulated progress curves for all the variants, (Figure 3.18 A to Figure 3.18 C), it was shows that the model is in good agreement with the experimental data, suggesting that the kinetic parameters generated from the model accurately represent the experimental values. In Table 3.9, we summarize all the kinetic constants from the model. Consistent with  $K_m$  in the experiment, the  $K_s$  values from the model were almost identical between wild-type InhA, I215A and L207A, while the  $K_s$  of V203A was less than 3 fold higher than the value for the wild-type enzyme. The  $k_{\text{cat}}$  generated from the model also follows a similar trend compared to experimental values. The most direct effect we would expect from a change of energy barrier would be a faster drug dissociation rate ( $k_{\text{off}}$ ), or a shortened residence time. However, as we discussed earlier in Scheme 3.2, both  $K_i^*$  and  $k_2$  could contribute to the overall  $k_{\text{off}}$ . The model can be used to determine if the change in  $k_{\text{off}}$  is due to a change in the value of  $k_2$ . The V203A variant has a 4-fold faster  $k_{\text{off}}$  compared to wild-type InhA. Although the transition state barrier is reduced slightly (a less than 2-fold difference in  $k_2$ ), the change in  $k_{\text{off}}$  is predominantly due to a destabilization of the EI\* ground state. The I215A mutant has a 3-fold faster  $k_{\text{off}}$  for the dissociation of PT70, however the  $k_2$  value is essentially identical to that from the wild-type enzyme, suggesting that the change in  $k_{-2}$ , or the reduced

residence time is mainly the result of a destabilized ground state. The difference in kinetic parameters between V203A and I215A indicates that  $\alpha$ -helix 7 does not contribute to the energy barrier for the slow step, since  $k_2$  for I215A is identical to that of wild-type InhA, and instead that motion of  $\alpha$ -helix 6 might be involved in the transition state barrier. Yet the change in  $k_2$  was insignificant and the loss of potency made it difficult to disentangle the true reason of change in dissociation rate constant. Crystal structure suggested that V203 and I215 were in close contact with the ligand (16); therefore it was not surprising to see a loss of potency effect.

Table 3.8 Michaelis-Menten parameters of wild-type and variant InhA

| <b>Construct</b> | <b><math>k_{cat}</math> (<math>\text{min}^{-1}</math>)</b> | <b><math>K_m</math> (<math>\mu\text{M}</math>)</b> | <b><math>k_{cat}/K_m</math> (<math>\mu\text{M}^{-1} \text{min}^{-1}</math>)</b> |
|------------------|--|--|---|
| <b>Wild-type</b> | 116±9  | 14±3   | 9.0±1.8   |
| <b>V203A</b>     | 121±16   | 37±7   | 3.3±0.7   |
| <b>I215A</b>     | 95±4   | 9±1  | 10.6±1.3  |
| <b>L207A</b>     | 184±14   | 20±3   | 9.2±1.5   |

Table 3.9 kinetics parameters of wild-type and variant InhA generated from the computational kinetic model

| <b>Construct</b> | <b><math>K_s</math> (<math>\mu\text{M}</math>)</b> | <b><math>k_{cat}</math> (<math>\text{min}^{-1}</math>)</b> | <b><math>K_i</math> (nM)</b> | <b><math>K_i^*</math> (nM)</b> | <b><math>k_2</math> (<math>\text{min}^{-1}</math>)</b> | <b><math>k_{-2}</math> (<math>\text{min}^{-1}</math>)</b> |
|------------------|--|--|------------------------------|--------------------------------|--|---|
| Wild-type        | 800  | 185  | 9                            | 0.6                            | 0.4  | 0.025   |
| V203A            | 2000   | 185  | 15                           | 2.2                            | 0.7  | 0.10  |
| I215A            | 900  | 145  | 20                           | 3.6                            | 0.4  | 0.071   |
| L207A            | 900  | 185  | 31                           | 1.5                            | 4  | 0.20  |

We speculated that residues on  $\alpha$ -helix 6 relatively far from the ligand might be the ideal place to investigate this loop motion without compromising the binding with the ligand. Based on this rationale, we designed the L207A variant. As we expected, the dissociation barrier was lowered by 10-fold ( $k_{-2}$  was 10-fold faster than wild-type), and this change was mainly from the lowered barrier of the transition state, rather than the loss of binding affinity. To visualize we have plotted  $k_{on}$  and  $k_{off}$  of each variant in Figure 3.18 D), where it can be seen that a faster  $k_{off}$  (or a shortened  $t_R$ ) is observed for I215A and V203A, while the  $k_{on}$  value is essentially identical for these two mutants, suggesting the change of  $k_{off}$  was not due to the change of the transition state energy barrier. In contrast, for the L207A variant, an increase in  $k_{off}$  is accompanied by a dramatic change in  $k_{on}$ , indicating that the change in  $k_{off}$  is a result of a weakened energy barrier. This suggests that the motion of  $\alpha$ -helix 6 is associated with the energy barrier for the slow onset inhibition, coinciding with our previous structural hypothesis that the barrier corresponds to a large scale refolding process of  $\alpha$ -helix 6.

#### Hypothesis on the slow binding mechanism for diphenyl ether series

Previously, we proposed that the diphenyl ethers are transition state analogs and that the deprotonated diphenyl ether mimics the substrate enolate intermediate. To test this proposal, we used PT163 as our model ligand and measured the  $K_i$  and  $K_i^*$  values at pH 6.8 and 8.5: since the pKa for the diphenyl ethers is  $\sim 7-8$ , an increase in pH should increase the population of ionized inhibitor and potentially result in improved affinity. We first evaluated the enzymatic activity at pH 8.5. As shown in Table 3.10, the enzyme activity was very similar at pH 6.8 and 8. We then performed progress curve analysis and observed a 3-fold enhancement of the apparent binding



affinity for the ligand (Table 3.10), in agreement with our proposal. This supports our argument that the diphenyl ethers bind to the protein in their deprotonated forms and thus are transition state analog inhibitors.

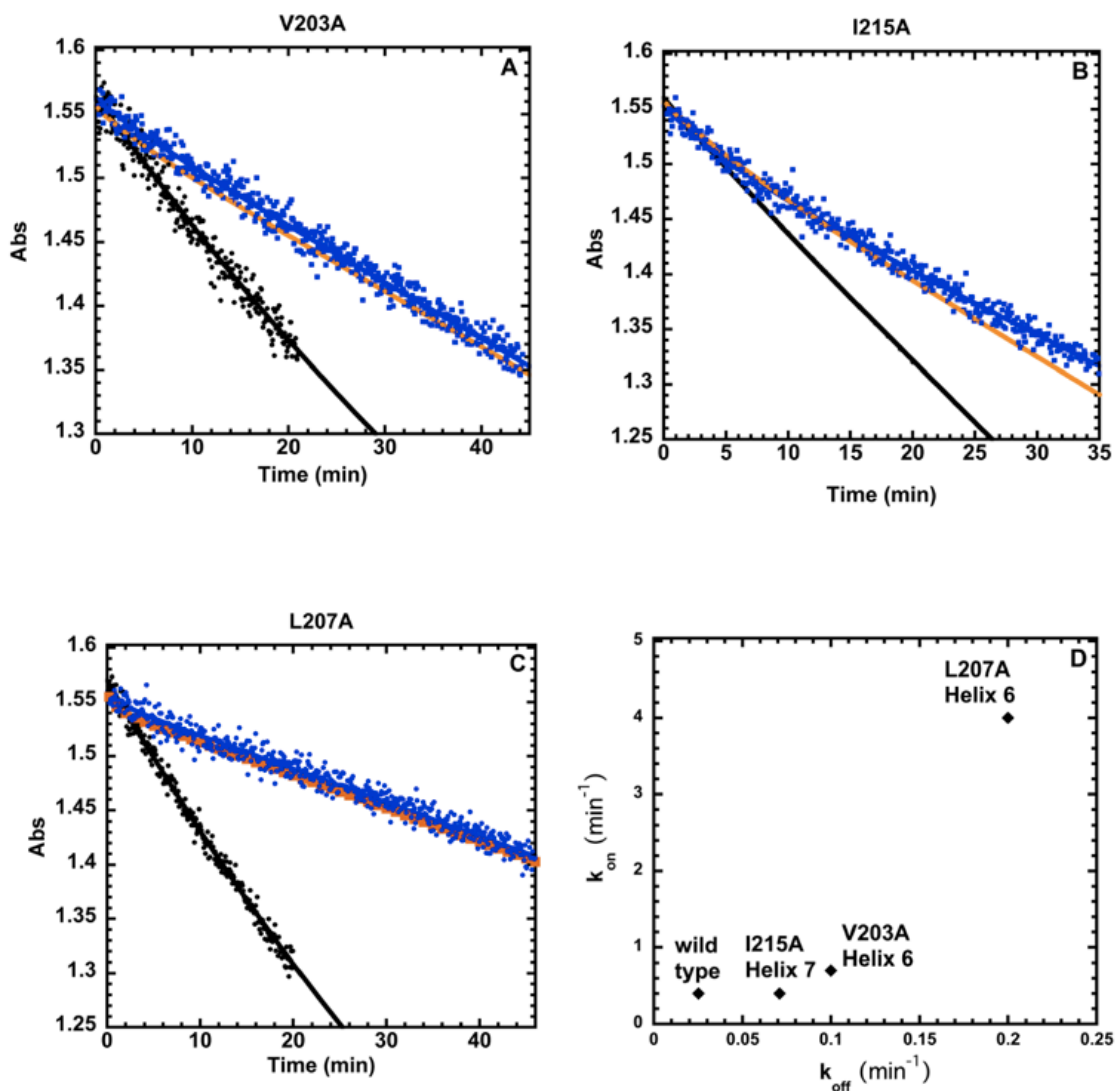


**Figure 3.18 Progress curve analysis for the inhibition of V203A, I215A and L207A by PT70**

A) V203A, B) I215A, C) L207A. For A-C the control in the absence of inhibitor is shown in black whereas the experimental progress curves with inhibitors are depicted in blue, and the simulated progress curves based on parameters listed in Table 3.9 are shown in orange. D) Plot of  $k_{on}$  and  $k_{off}$  for each variant and wild-type InhA

Table 3.10 kinetic parameters of PT163 with wild-type InhA under difference pH values

| pH condition | $k_{\text{cat}}$ ( $\text{min}^{-1}$ ) | $K_m$ ( $\mu\text{M}$ ) | $\frac{k_{\text{cat}}}{K_m}$ ( $\mu\text{M}^{-1} \text{min}^{-1}$ ) | $K_i^{\text{app}}$ of PT70 (nM) | $K_i^{*\text{app}}$ of PT70 (nM) |
|--------------|--|-------------------------|---|---------------------------------|----------------------------------|
| pH = 6.8     | 116±9                                  | 14±3                    | 9.0±1.8   | 8383±365                        | 185±8                            |
| pH = 8.5     | 159±13                                 | 18±3                    | 8.8±1.6   | 4513±158                        | 54±2                             |

### The energy barrier – structural and kinetic insight

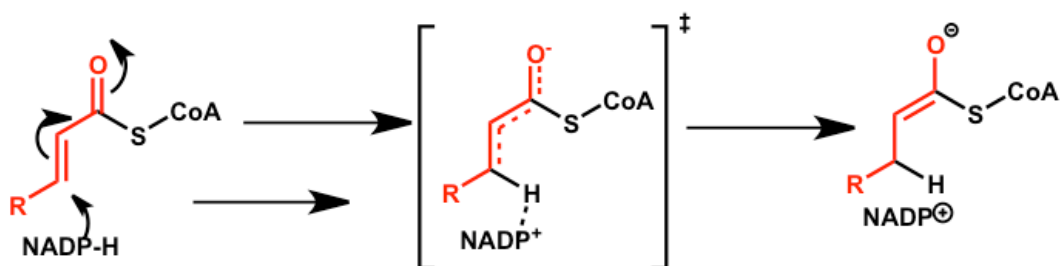
As discussed in our previous paper, we proposed that “self” inhibition of InhA occurs when  $\alpha$ -helix 6 is in the closed conformation such that A201, I202 and V203 on  $\alpha$ -helix 6 mimic a portion of the fatty acid substrate, while L197 mimics part of the phosphopantetheine group. In other words, helix 6 itself becomes an inhibitor and contributes to the potency of the bound small molecule such as PT70 (16). Together with the finding that diphenyl ethers bind to the enzyme-product complex (E-NAD<sup>+</sup> complex) generated during substrate turnover, we speculate that the transition state mimic of the enolate tricks the enzyme as it binds to the substrate and undergoes catalysis (Figure 3.19 A), therefore the substrate binding loop (helix 6) closes up to fill in the space where the fatty acid tail and phosphopantetheine arm occupy. The close-up of helix 6 corresponded to a large-scale of refolding process, occupied portion of the active site, and this motion eventually resulted in the energy barrier along the reaction coordinate. This argument is supported by studies with the 4-pyridone class of FabI inhibitors. Thermofluor experiments suggest that 4-pyridones bind to the initial enzyme-cofactor complex (E-NADH) (Figure 3.20). In addition, 4-pyridones do not have an ionizable group and the crystal structure of the a 4-

pyridone inhibitor in complex with the enzyme show that helix6 is in an open conformation. Putting all pieces of data together, it was suggested that deprotonation of the compounds made them as transition state analogs and bound with enzyme-product complex after enzyme turnover, such behavior triggered the protein closed up the substrate binding loop and resulted in an energy barrier and a largely improved binding affinity (EI\*) (Figure 3.19 B). On the other hand, compounds that not able to deprotonate are substrate analogs and bind to the E-NAD H complex, leaving the substrate binding loop open and not showing time-dependent inhibition (no EI\* state) (Figure 3.19 B).

We can also compare the InhA system with other FabI homologs. In this regard, it is interesting to note that the time-dependent inhibition in other FabI homologs is thought to be a one-step slow onset mechanism, where the initial enzyme-inhibitor complex EI cannot be observed and is thus a special case of 2-step induced-fit mechanism. Moreover, there is no significant structural change for the inhibition of other FabIs and thus no support for the existence of two different enzyme conformation states (viz EI and EI\*). In contrast, it is clear that the InhA inhibitors follow a 2-step induced fit mechanism. Progress curve analysis clearly shows differences between the initial and steady state velocities, suggesting two distinguishable enzyme-inhibitor complexes; in support, X-ray structural analysis is clearly able to capture both the EI state as an open SBL conformation and the EI\* state as a closed SBL conformation along the reaction coordinate. We try to understand why there is such discrepancy between InhA and other FabI homologs. As suggested by the kinetic parameters computed from our kinetic model, it is interesting to see that the dissociation rate constant of  $\text{NAD}^+$  from the enzyme-product complex E-NAD<sup>+</sup> varies significantly amongst the different FabIs. For example, the  $k_{\text{off}, \text{NAD}^+}$  is

$10^4 \text{ min}^{-1}$  for *Staphylococcus aureus* FabI (22), and around the same magnitude in *Escherichia coli* FabI (26); however the  $k_{\text{off, NAD}^+}$  for InhA is only  $800 \text{ min}^{-1}$ , and is thus partially rate-limiting. The dissociation of  $\text{NAD}^+$  from E- $\text{NAD}^+$  determines the lifetime of the enzyme-product complex and the slower dissociation of  $\text{NAD}^+$  results in a longer half-life of E- $\text{NAD}^+$  in InhA, which, together with low nanomolar to micromolar binding affinity for the first enzyme-inhibitor complex  $K_i$ , allows us to capture the EI species. Based on our finding, we conclude that the time-dependent inhibition in the InhA system is a unique behavior of diphenyl ethers such that the deprotonation of diphenyl ethers mimics the transition state of the substrate analog in complex with the enzyme-product species and further triggers the large refolding process of the SBL from the open state to the closes state, resulting in an energy barrier along the reaction coordinate.

A)



B)

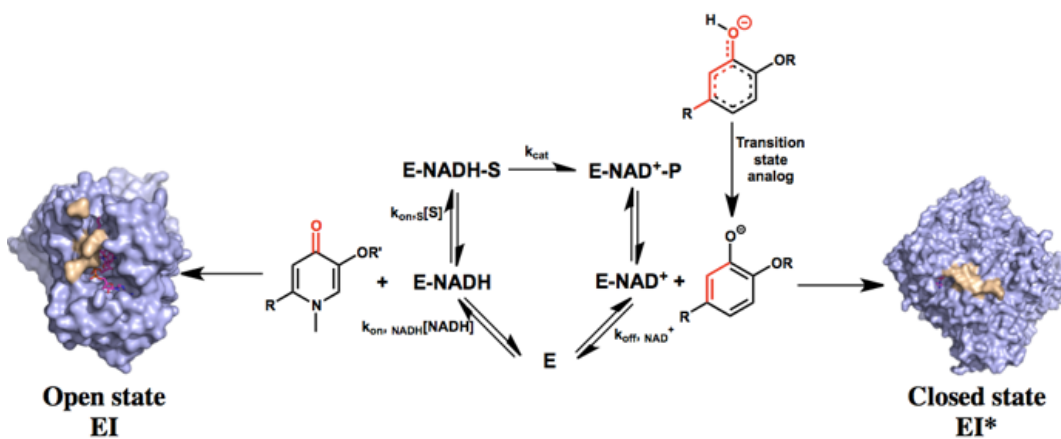


**Figure 3.19 Integrated structural – kinetic inhibition scheme**

A) illustrates the substrate enolate transition state. B) depicts the structural – kinetic relationship of diphenyl ethers and 4-pyridones, respectively. InhA is shown as surface in purple, the substrate binding loop (SBL) is represented in yellow. The ligands are shown as sticks in magenta.

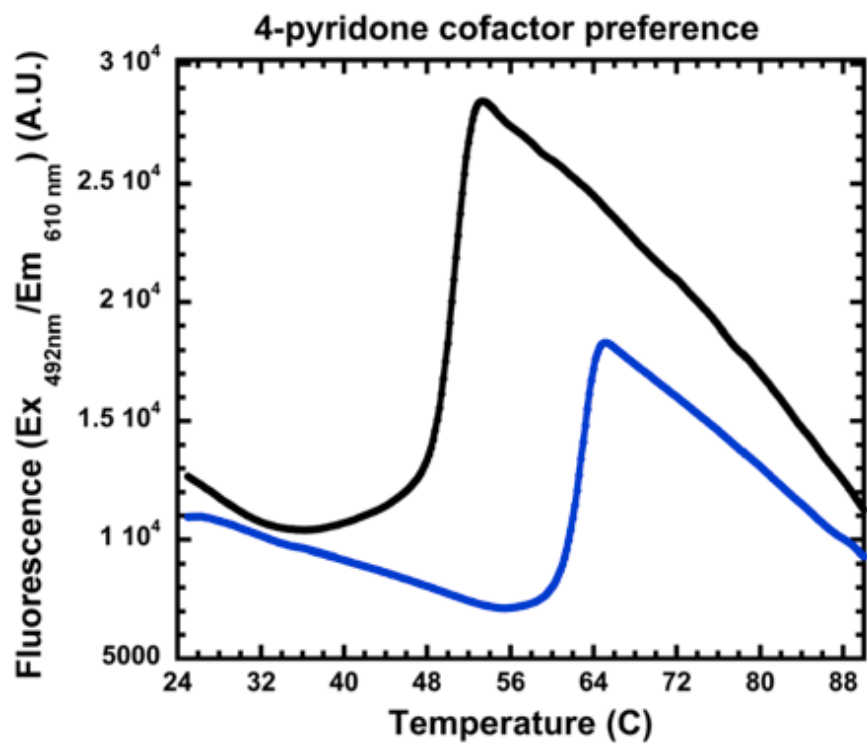


**Figure 3.20** Midpoint temperatures of the protein-unfolding transition ( $T_m$ ) for 4-pyridone  
 In the presence of NADH is shown in blue and NAD in black

## CONCLUSION

Using a combination approach of enzyme kinetics, computational kinetic modeling and X-ray crystallography, we have rigorously characterized 24 diphenyl ether inhibitors of InhA and determined the kinetic parameters for each step on the reaction pathway. Based on the mechanistic insight we gained from our thorough analysis, we have designed PT504 which has a 10-fold improvement on residence time compared to INH. Arrhenius analysis reveals that the energy barrier ( $E_a$ ) associated with the slow step is  $\sim 10$  kcal/mol. Further analysis using the Eyring equation suggests that the activation free energy for the dissociation process predominantly derives from the activation enthalpy. Site-directed mutagenesis supports the hypothesis that the energy barrier associated with time-dependent enzyme inhibition results from a large scale refolding of the SBL from an open to a closed conformation, linking kinetics with the structural hypothesis. Lastly, we determined that diphenyl ethers are transition state analogs and bind in their deprotonated states to the enzyme with a preference for the E-NAD<sup>+</sup> product complex. This transition state mimic triggers the refolding process of the SBL, resulting in a partial overlap with the natural substrate and “self” inhibition, which greatly improves the binding affinity of the final EI complex. Finally, we conclude that unlike other FabI enzymes InhA displays 2-step induced-fit time-dependent inhibition, due to the fact that E-NAD<sup>+</sup> complex to which inhibitors bind has a significantly longer half-life than in other FabI homologs. These findings will aid the future design of additional compounds with long residence times.

## Chapter 4 Cellular Activity of Diphenyl Ether InhA Inhibitors – Killing Kinetics and Post Antibiotic Effect

### INTRODUCTION

Lead optimization has traditionally focused on thermodynamic properties for the interaction of compounds with their targets such as  $IC_{50}$ ,  $K_i$ , and MIC values (1, 2). However the high attrition rate of compounds in late stage development and clinical trials suggests that one or more fundamental concepts have been neglected when translating *in vitro* lead optimization to late-stage efficacy models and clinical trials (3). One neglected area is the role of drug-target kinetics in modulating the efficacy of drugs in humans and as a result there is a growing interest in understanding and incorporating the time-dependence of target engagement into the drug development pipeline. If it is assumed that drugs only work when they are bound to their targets, then the rate at which the drug-target complex dissociates ( $k_{off}$ ) or the duration of time the drug remains bound to the target (residence time  $t_R = 1/k_{off}$ ) will have a critical impact on the duration of drug action.

A significant fraction of marketed drugs have residence times ranging from minutes to days (1, 4). In addition, we previously demonstrated a direct relationship between residence time and drug *in vivo* efficacy for inhibitors of the *F. tularensis* FabI (5). This stimulated our interest in exploring the translation of drug-target kinetics to antibacterial activity for FabI enzymes from other pathogens.



Recently, Walkup *et al* demonstrated that the *in vitro* slow-binding kinetic profile of LpxC inhibitors could contribute to the prolonged suppression of bacterial growth (post antibiotic effect, or PAE) both at the whole cell level and also in a murine model of *P. aeruginosa* infection (6). Their finding provides the foundation for validating the link between target kinetics and *in vivo* efficacy. However, studies in the *S. aureus* and *E. coli* FabI systems revealed a very shallow correlation between drug-target residence time and PAE, (7) suggesting that factors such as target turnover and target vulnerability will impact the coupling between residence time and PAE. By constructing a mathematical metabolic flux model, Chang made the argument that FabZ instead of FabI, was the rate-limiting step that balanced the flux within the FAS-II elongation cycle. Moreover, Chang also pointed out that in fast-growing bacteria – i.e. *S. aureus* or *E. coli*, target re-synthesis acted as a significant challenge in the translation of drug-target residence time to the suppression of bacterial growth. Interestingly, Rubin *et al* examined the vulnerability of 6 protein targets in *M. smegmatis* and demonstrated that degradation of InhA completely inhibited growth (8). Together with the fact that InhA is the primary target of the successful frontline antituberculosis drug INH (9, 10), this observation has further stimulated our interest in determining the vulnerability of InhA and understanding whether InhA would be an appropriate system to analyze the connection between target kinetics and growth inhibition.

As elaborated in Chapter 3, we have extensively characterized two sets of diphenyl ether InhA inhibitors which have distinct binding kinetics. These analyses set the foundation for us to add an additional layer of complexity in the cellular context. The aim of this project is to

determine whether InhA is a vulnerable target and how well observations on one bacteria system can be applied to other bacteria species.

## MATERIALS AND METHODS

### Compounds

PT04, PT05, PT91, PT70, PT119 were synthesized by Dr. Pan Pan (11). PT163 was synthesized by Dr. Gopal Reddy (12). PT500 series were synthesized by Ms. Lauren Spagnuolo, as described in Chapter 3. Isoniazid and Rifampicin were both purchased from Sigma Aldrich.

### Bacterial strains

*Mycobacterium smegmatis* (*M. smeg*) MC<sup>2</sup> 155 and *Mycobacterium tuberculosis* (*M. tb*) H37rV strains were used for MIC measurement. *M. smeg* was used for cellular killing kinetics and post-antibiotic effect experiments.

### MIC measurement

MIC values were determined by the microbroth dilution method followed by visual inspection according to the Clinical and Laboratory Standards Institute (CLSI) (13). Compounds were dissolved in DMSO and diluted in DMSO to prepare 10 two-fold dilutions at 2% final DMSO (v/v) in broth media. An equivalent volume (100  $\mu$ L) of broth medium was added to a 96-well round-bottomed microtitre plate (Thermo Scientific), followed by addition of another 100  $\mu$ L of bacterial broth containing  $\sim 10^6$  CFU/mL cells. Final concentrations of drug from  $\sim 0.05$   $\mu$ g/mL upwards were added to each well and the plate was incubated aerobically at 35.5  $^{\circ}$ C for 3 days. The MIC was the minimum drug concentration that prevented visible growth.

### Killing-kinetics

An aliquot of  $\sim 10^9$  CFU/mL of *M. smeg* cells was diluted 100 fold in 7H9 media (Sigma Aldrich) supplemented with glycerol (0.4% v/v) and Tween 80 (0.1% v/v). The culture was shaken at 35.5 °C for  $\sim 20$  hrs until an OD<sub>600</sub> at  $\sim 0.6$  was reached. Subsequently, this starter culture was diluted 200-fold into fresh 7H9 media containing either drug or an equal volume of DMSO. The culture was shaken at 35.5 °C, and 100  $\mu$ L was removed every 2 hrs, serially diluted in fresh 7H9 media and plated on 7H10 agar plates. The number of viable colonies were then counted following a 3-day aerobic incubation at 35.5 °C. Killing kinetic curves were analyzed in KaleidoGraph Version 4.1.

### Post antibiotic effect (PAE)

An aliquot of  $\sim 10^9$  CFU/mL *M. smeg* cells was diluted 100 fold in the 7H9 media supplemented with glycerol (0.4% v/v) and Tween 80 (0.1% v/v). The culture was shaken at 35.5 °C for  $\sim 20$  hrs until an OD<sub>600</sub> of  $\sim 0.6$  was reached. Subsequently, this starter culture was diluted 200-fold into fresh 7H9 media containing either drug (4X, 8X and 16X MIC) or an equal volume of DMSO. The cultures were then shaken at 35.5 °C for 2 hrs, and subsequently, both treated and untreated cultures were diluted 1000-fold into fresh 7H9 media to remove the drug. Regrowth was monitored by removing an aliquot of 100  $\mu$ L culture every 4 hrs and plating the serial dilutions on 7H10 agar plate. The number of viable colonies were counted after 3-day incubation at 35.5 °C. The PAE was calculated following the equation  $PAE = T - C$ , where T is the time it takes for the drug exposed culture to increase 1 log<sub>10</sub> CFU after removal of the drug, and C is the

corresponding time it takes for the control group to increase 1 log<sub>10</sub> CFU following dilution (14). Data processing was performed using KaleidoGraph Version 4.1.

#### Theoretical maximum killing rate calculation

This work was performed by Dr. Fereidoon Daryaei. A mathematical model was constructed to model the lag-phase during killing kinetics (15). It was assumed that the rate of killing is a time-dependent process and reached the maximum killing rate at steady-state.

$$k_t = k_{max} * (1 - e^{-\alpha*t})$$

Equation 4.1

In Equation 4.1,  $k_t$  is the killing rate-constant at time  $t$ ;  $k_{max}$  stands for the maximum killing rate-constant;  $\alpha$  is the killing induction rate-constant. Assuming that bacterial death/growth defect is directly related to the fraction of bacterial target engagement level, the following equation was derived

$$\frac{dN}{dt} = (k_{growth} - k_t * TO) * N = (k_{growth} - TO * k_{max} * (1 - e^{-\alpha*t})) * N$$

Equation 4.2

In Equation 4.2,  $k_{\text{growth}}$  is the growth rate-constant in the absence of drug;  $TO$  is target occupancy, which represents the fraction of the target that is occupied at a fixed drug concentration;  $N$  is the total bacterial population.

Equation 4.3 was generated after numerically solving Equation 4.2.

$$\log_{10} N_t = \log_{10} N_0 + 0.434 * \left( (k_{\text{growth}} - TO * k_{\text{max}}) * t + \frac{TO * k_{\text{max}}}{\alpha} * (1 - e^{-\alpha * t}) \right)$$

Equation 4.3

Subsequently, all the experimental data were fit to Equation 4.3 to calculate the killing induction rate-constant  $\alpha$ , where the reciprocal of  $\alpha$  corresponds to the lag-phase time.

## RESULTS AND DISCUSSION

### Diphenyl ether inhibitors are active against both *M. smeg* and *M. tb*

In chapter 3, we have discussed the kinetic characterization of the diphenyl ether InhA inhibitors and have described the development of a series of triazole substituted diphenyl ethers. Subsequently, we have evaluated the antibacterial activity of these compounds against both *M. smeg* and *M. tb* (Table 4.1). As expected from our previous work, the alkyl chain diphenyl ether analogs were active against *M. tb* H37rv (11), and also against *M. smeg* with MIC values in the range of 0.95  $\mu\text{g/mL}$  to 7.45  $\mu\text{g/mL}$  (Table 4.1). Interestingly, the triazole substituents demonstrated a better MICs against *M. tb* compared to the alkyl analogs, with MIC values from 0.16  $\mu\text{g/mL}$  to 2.42  $\mu\text{g/mL}$ . The lipophilicity (ClogP) suggests that the triazole series has better cellular permeability than the corresponding alkyl chain analogues indicating a possible reason of the observed MIC trend. In addition, a double logarithmic plot of  $K_i$  vs. MIC showed a linear correlation, providing evidence that these compounds act on the same target and had similar cellular profile (Figure 4.1).

### Killing kinetics revealed that a slower association rate constant could be translated into a slower killing rate

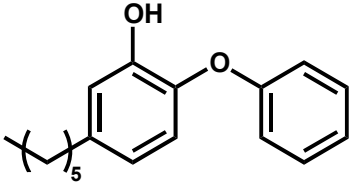
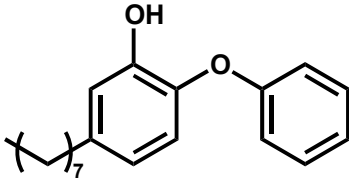
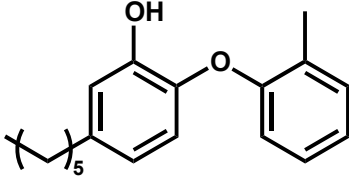
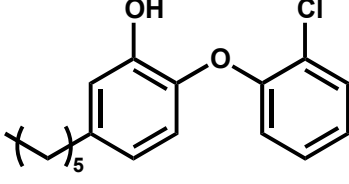
As MIC measurements are used for preliminary cellular activity evaluation and have many limitations (16), we used killing kinetics to investigate the cellular activity of the compounds at a fixed drug concentration. In the following analysis we chose PT04 and PT504 as representatives from the two sets of inhibitors (alkyl and triazole, respectively) to interrogate the link between target engagement and cellular activity.

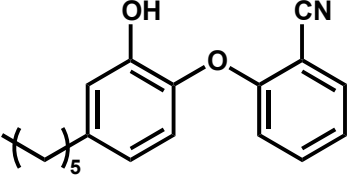
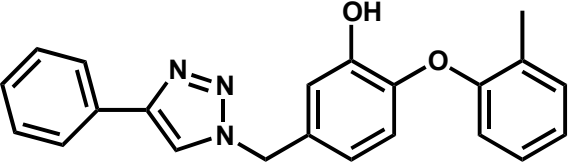
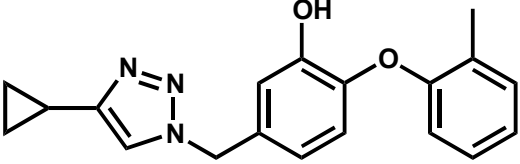
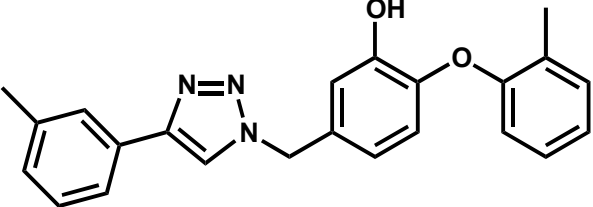
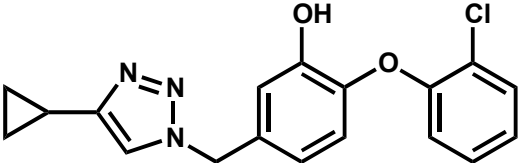
The killing curve for PT04 is shown in Figure 4.3 A. A moderate dose response is observed. At 4X MIC, there was a 15 hr growth suppression followed by growth recovery comparable to the control group, suggesting the cells have not been fully saturated by the drug. Remarkably, a rapid killing effect was observed starting at 8X MIC concentration after a 15-hr lag phase. Similar result was observed at 16X MIC, with a faster killing rate. In general, it took 25 hrs for PT04 to achieve a 4 log<sub>10</sub> CFU bacteria reduction.

A similar dose-dependent effect was observed for PT504 (Figure 4.3 B). However, instead of the static effect and regrowth reported at 4X MIC of PT04, a moderate killing effect can be seen at the same concentration for PT504. The killing rate was faster at higher drug concentrations (8X and 16X MIC). Intriguingly, the lag phase was ~18 hrs, slightly longer compared to PT04, and bacteria sterilization was never achieved. Generally, it took ~20 hrs for PT504 to reach a 4 log<sub>10</sub> CFU reduction.

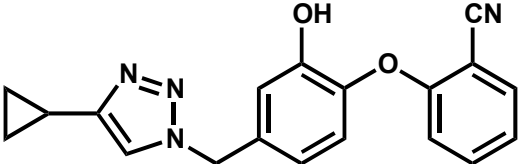
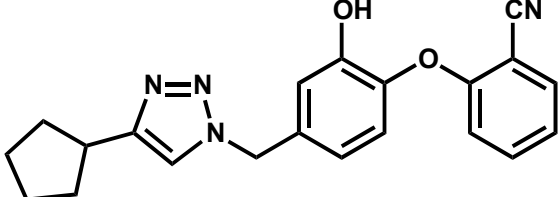
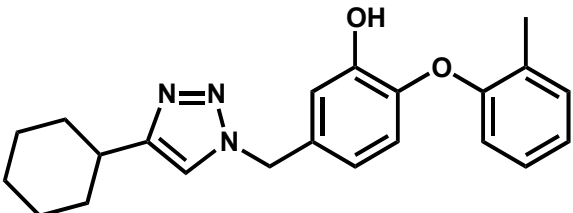


Table 4.1 MIC of diphenyl ethers against *M. smeg* and *M. tb*

| Compound | Structure   | MIC <sub>99</sub> in<br><i>M. smeg</i><br>(µg/mL) | MIC <sub>99</sub> in<br><i>M. smeg</i><br>(µM) | MIC <sub>99</sub> in<br><i>M. tb</i><br>(µg/mL) | MIC <sub>99</sub> in<br><i>M. tb</i><br>(µM) | CLogP |
|----------|---|---|--|---|--|-------|
| PT04     |    | 1.69  | 6.26   | 2.10  | 7.80   | 5.81  |
| PT05     |    | 7.45  | 25.00  | 3.13  | 10.49  | 7.53  |
| PT70     |   | 3.60  | 12.70  | 1.56  | 5.49   | 6.97  |
| PT91     |  | 0.95  | 3.10   | 0.39  | 1.28   | 6.95  |

|       |  |      |       |      |      |      |
|-------|--|------|-------|------|------|------|
| PT119 |     | 3.70 | 12.50 | 2.50 | 8.46 | 5.90 |
| PT163 |    | 8.90 | 25.00 | ND   | ND   | 5.02 |
| PT501 |    | 2.00 | 6.22  | 0.39 | 1.21 | 3.60 |
| PT503 |   | ND   | ND    | 2.38 | 6.41 | 5.50 |
| PT504 |  | 1.06 | 3.10  | 0.16 | 0.47 | 3.62 |

---

|       |  |    |    |      |      |      |
|-------|--|----|----|------|------|------|
| PT506 |  | ND | ND | 0.27 | 0.81 | 4.00 |
| PT512 |  | ND | ND | 0.29 | 0.80 | 4.20 |
| PT514 |  | ND | ND | ND   | ND   | 4.90 |

---

ND: Not Determined

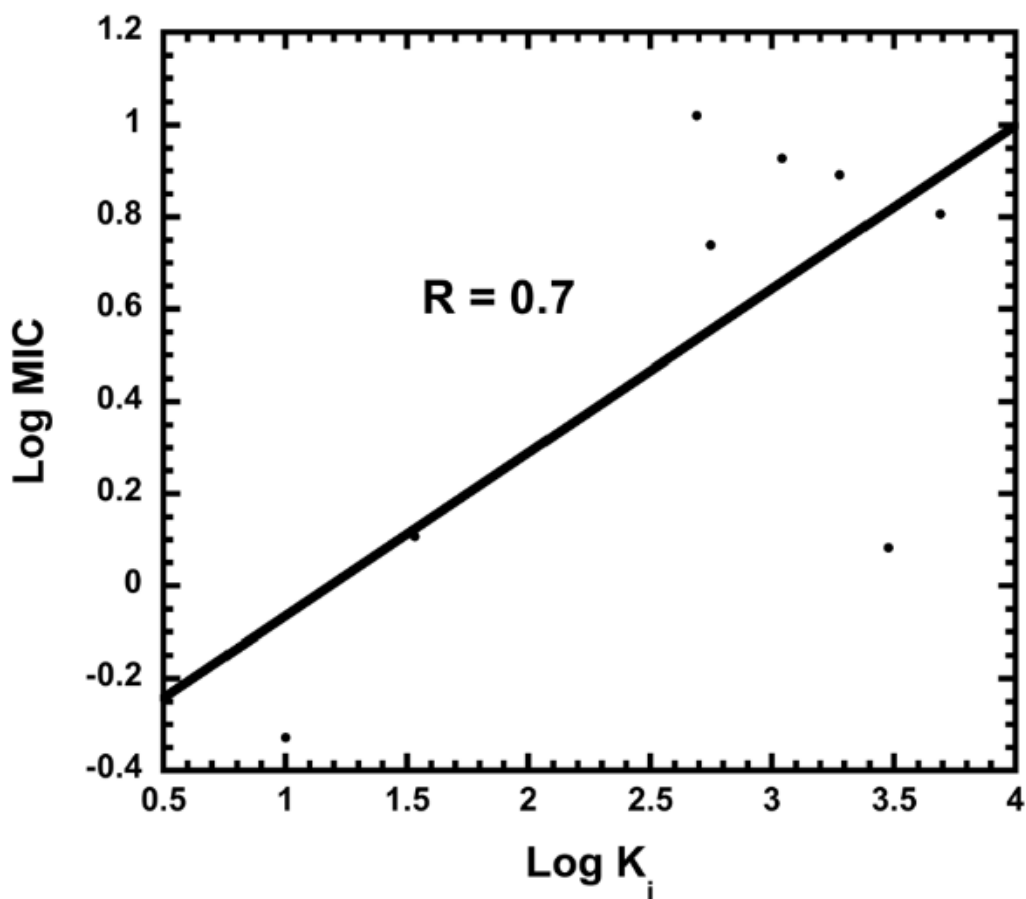


**Figure 4.1 Double logarithmic plot of  $K_i$  vs. MIC of diphenyl ethers against *M. tb***  
 The MIC values were obtained against *M. tb* H37rV strain. The linear correlation depicted the best fit with R-value of 0.7.

As shown by the killing kinetics, the diphenyl ether InhA inhibitors are bacteriacidal drugs against mycobacterial species, which contrasts with their bacteriostatic behavior against other pathogens such as *S. aureus* and *E. coli* (7). The lag phase is an estimate of the time that it takes for the downstream cascade to generate the full killing effect. We speculate that the 10-fold slower association rate of PT504 translates to the ~3 hr increase in the lag phase. It is worth noting that whereas a slower association rate is an alternative strategy to improve residence time,

it could paradoxically lead to a slower target onset in the cellular context. In the meanwhile, PT504 is slightly more cidal than PT04, which could be a result of a combination effect of superior binding affinity and dissociation kinetics.

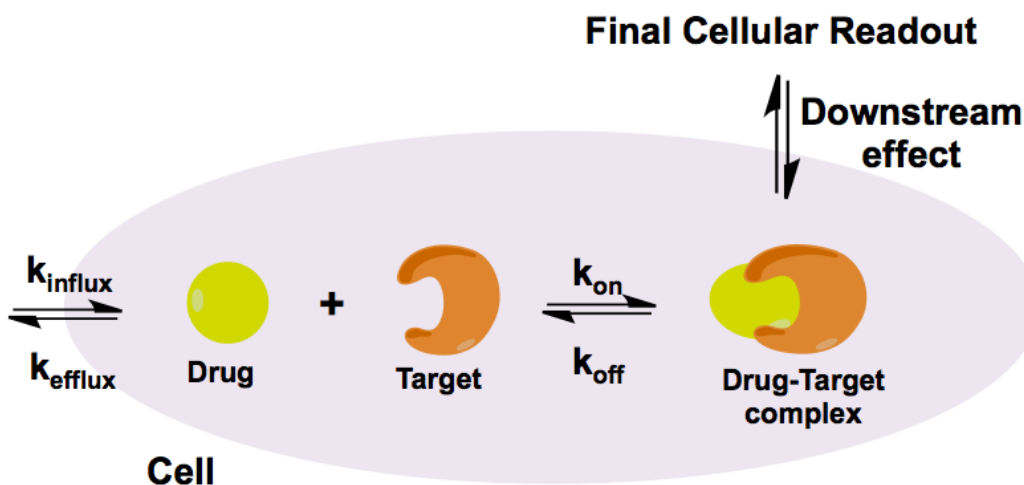


**Figure 4.2 Target engagement workflow**

Drug-target kinetics is an crucial factor for final cellular readout

### Theoretical maximum killing rate and lag-phase calculation

The lag-phase observed in the bacteria killing curves is not uncommon. As illustrated in Figure 4.2, several processes can lead to the lag-phase observed in killing kinetics such as drug permeability, drug-target complex formation and more importantly, the time needed for the translation of target engagement into the final cellular outcome. To understand this process in a more comprehensive manner, we constructed a mathematical model to extrapolate the lag-phase

time and theoretical killing rate for each compound. As shown in Figure 4.4 A and B, the model shows good agreement with the experimental killing curves for PT04 at both 8X MIC and 16X MIC. The  $k_{\text{growth}}$  calculated from the model was  $0.269 \text{ hr}^{-1}$  (Table 4.2), corresponding to a doubling time of 3.7 hrs, which is consistent with the literature (17). The killing induction rate-constant  $\alpha$  was  $0.3079$  and  $0.25 \text{ hr}^{-1}$  at 8X and 16X MIC, respectively. These observations subsequently yielded a lag-phase of  $\sim 3.6$  hrs. Interestingly, if we assume that target occupancy at 16X MIC is 100%, then the maximum killing rate  $k_{\text{max}}$  is  $\sim 0.75 \text{ Log CFU/mL/hr}$ .

Along the same lines, the theoretical killing curve for PT504 is shown in Figure 4.5 A, B and C. Remarkably, the  $\alpha$  was  $\sim 3$ -fold slower than PT04, translating to a much longer lag-phase time (Table 4.2). The simulation result was in good agreement with our experimental observations and corroborates the argument that a slower inhibitor onset rate constant is reflected at the cellular level in a much longer duration of the lag-phase. Moreover, the maximum killing rate  $k_{\text{max}}$  of PT504 was  $1 \text{ Log CFU/mL/h}$ , slightly faster than PT04. This simulation result also agrees with the fact that it takes a shorter time for PT504 to reach the same reduction in Log CFU compared to PT04.

We were able to validate our model through 2 sets of killing kinetic curves and extrapolated informative cellular parameters from the model. PT504 suggested a longer lag-phase time and a faster maximum killing rate than PT04, in line with its target kinetic characteristics. It is critical to note the correlation of target level kinetics and killing kinetic curve, as the lag-phase might shed some light in determining the exposure time during PAE experiment. The maximum killing rate is comparable for both PT04 and PT504, consistent with the

knowledge that the kill rate is more closely related to thermodynamic parameters rather than kinetics at constant drug exposure.

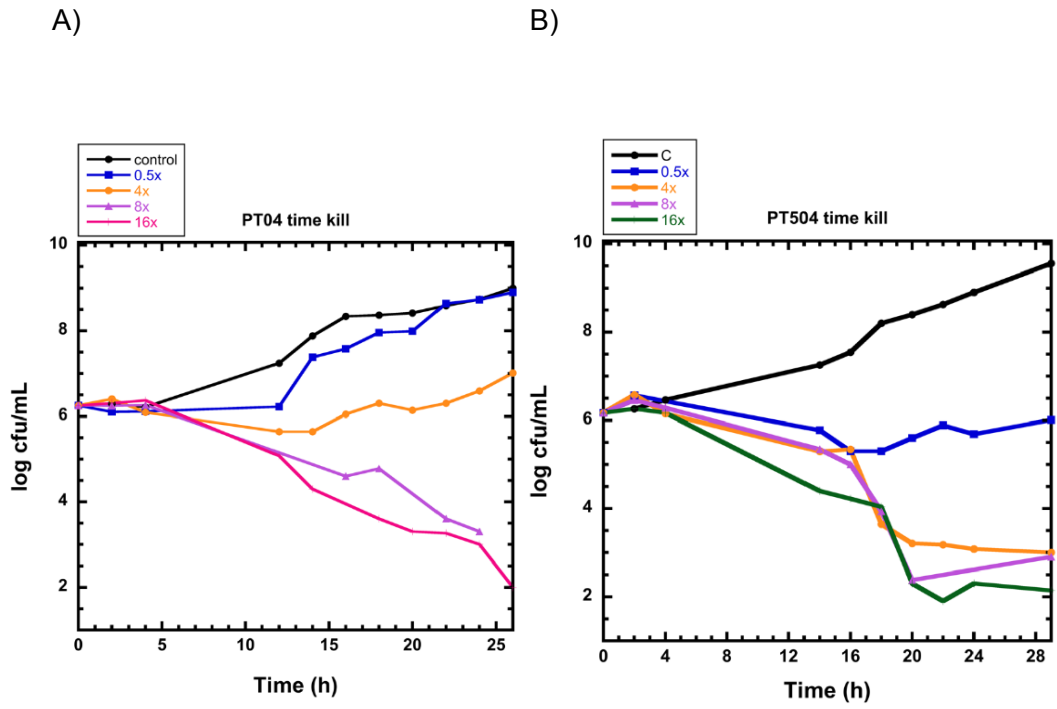


**Figure 4.3 Killing kinetics against *M. smeg***  
A) Killing curve of PT04 B) Killing curve of PT504

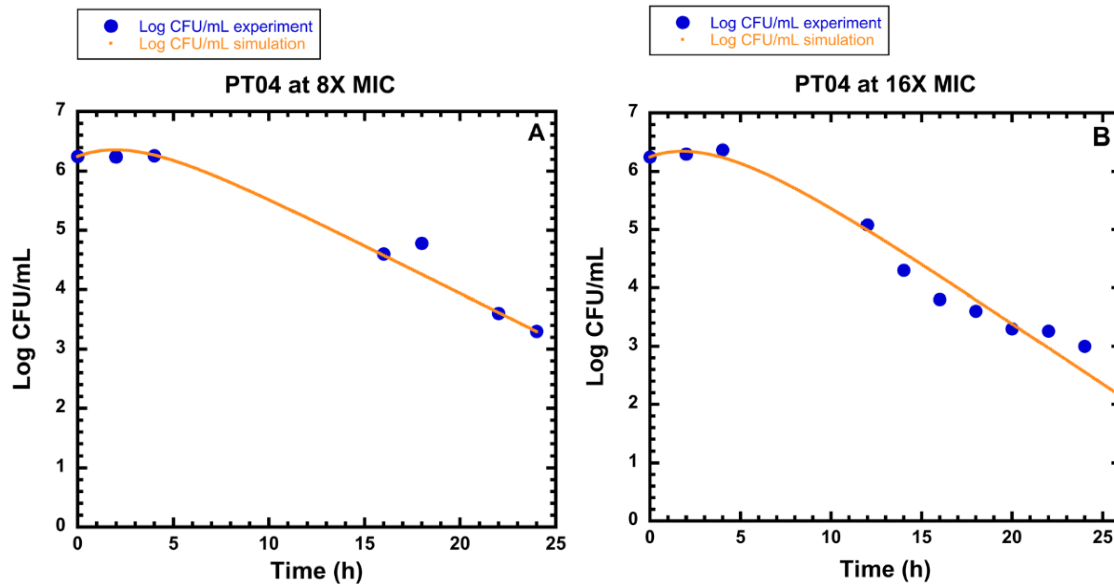


**Figure 4.4 Overlay of killing curves from experiment and simulation**  
 A) PT04 at 8X MIC B) PT04 at 16X MIC

Table 4.2 Cellular parameters computed from the killing kinetic model for PT04 and PT504

|       |                                  | 4X MIC | 8X MIC | 16X MIC |
|-------|----------------------------------|--------|--------|---------|
| PT04  | $k_{\max}$ (Log CFU/mL/h)        | --     | 0.64   | 0.75    |
|       | $\alpha$ ( $h^{-1}$ )            | --     | 0.31   | 0.25    |
|       | Lag phase (h)                    | --     | 3.23   | 4.00    |
|       | $k_{\text{growth}}$ ( $h^{-1}$ ) | --     | 0.27   | 0.27    |
| PT504 | $k_{\max}$ (Log CFU/mL/h)        | 1      | 1      | 1       |
|       | $\alpha$ ( $h^{-1}$ )            | 0.10   | 0.11   | 0.14    |
|       | Lag phase (h)                    | 10.0   | 9.09   | 7.14    |
|       | $k_{\text{growth}}$ ( $h^{-1}$ ) | 0.27   | 0.27   | 0.27    |



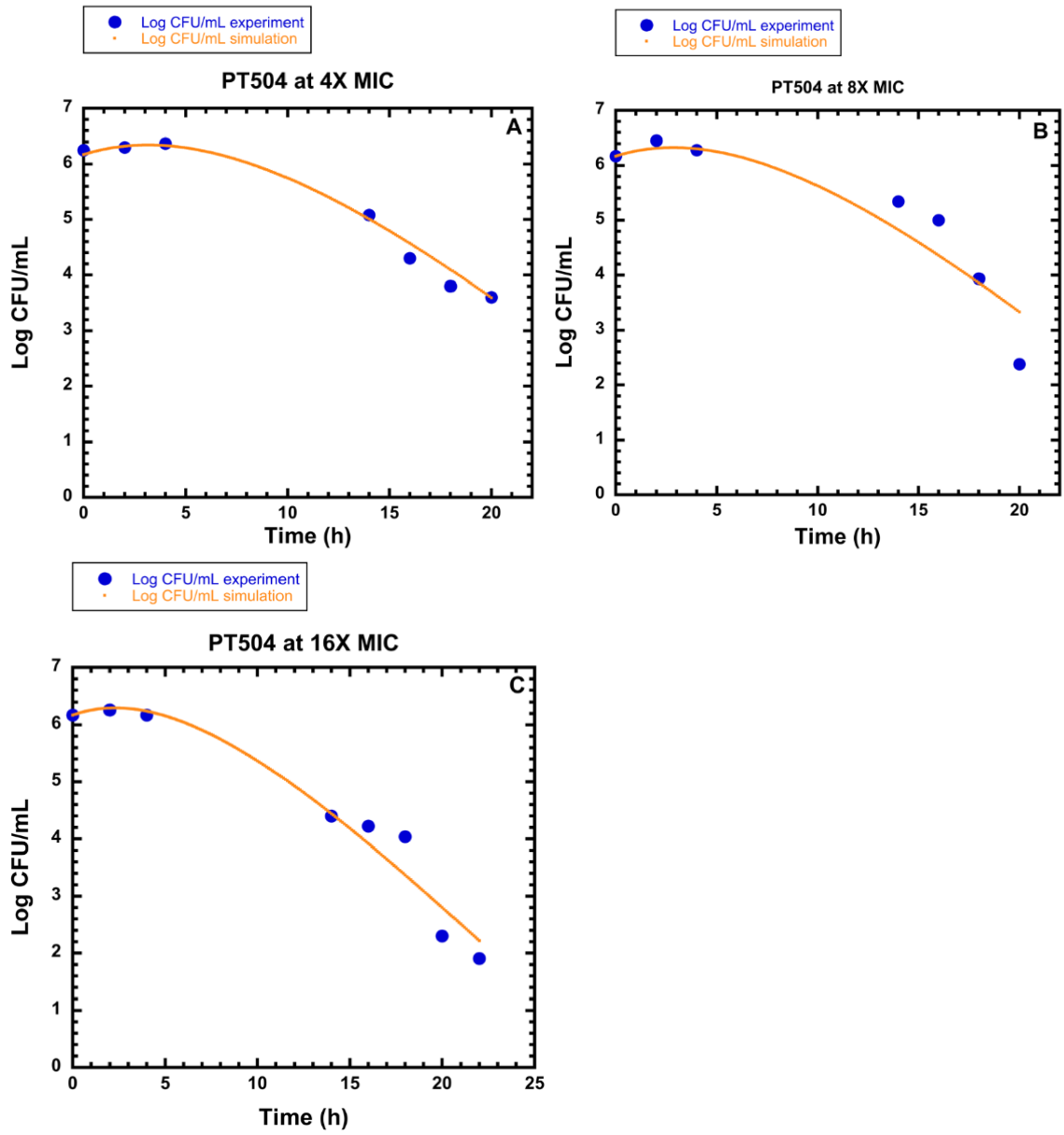


**Figure 4.5 Overlay of killing curves from experiment and simulation**

A) PT504 at 4X MIC B) PT504 at 8X MIC C) PT504 at 16X MIC

## Post antibiotic effect and residence time

To investigate the relationship between post antibiotic effect and residence time in mycobacteria, we chose PT04 and PT504, 2 compounds which display drastically different residence times for preliminary studies. Based on the above killing kinetics and literature precedent, the drug exposure time was set to 2 hrs despite the slow doubling time of mycobacteria. The PAEs were run at 4X, 8X and 16X MICs (Figure 4.5). Interestingly, a drop in  $\text{Log}_{10}$  CFU was observed after removal of the drug under different drug concentrations as well as the control. The linear fit of the control revealed that it took 10 hrs for normal growing bacteria to achieve a 1  $\text{log}_{10}$ CFU increase in growth, translating to a doubling time of  $\sim 3.5$  hrs, comparable to the value reported from the literature. Similar to the killing kinetics, a dose-dependent effect was also observed under different drug concentrations. At 4X MIC, the PAE was  $\sim 12.3$  hrs before recovery of normal growth (Table 4.3). At 8X and 16X MIC, we assume that the target is saturated with drug, so that no significant difference in PAE was observed. Intriguingly, the PAE at saturating drug concentrations shows a 1:1 relationship with the drug-target residence time.

Inspired by the result for PT504, we further examined the PAE of PT04, which has residence time of 10 min. Interestingly, a lag in normal growth was observed under different drug concentrations, as well as in the control group (Figure 4.6). In addition, the PAE was similar across all tested drug concentrations, which was  $\sim 10$  hrs. Further experiment needs to be performed for a more comprehensive analysis, yet the preliminary results suggest that a shorter residence time leads to a shorter PAE.

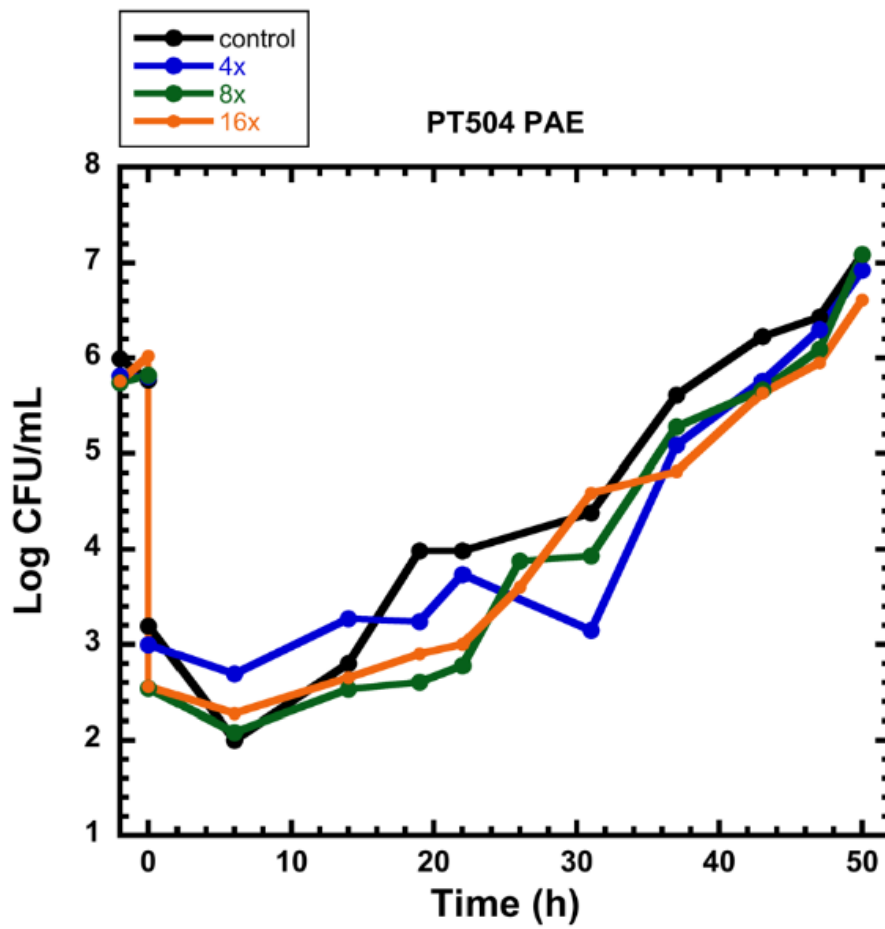


Figure 4.6 PAE of PT504 against *M. smeg* under different drug concentrations

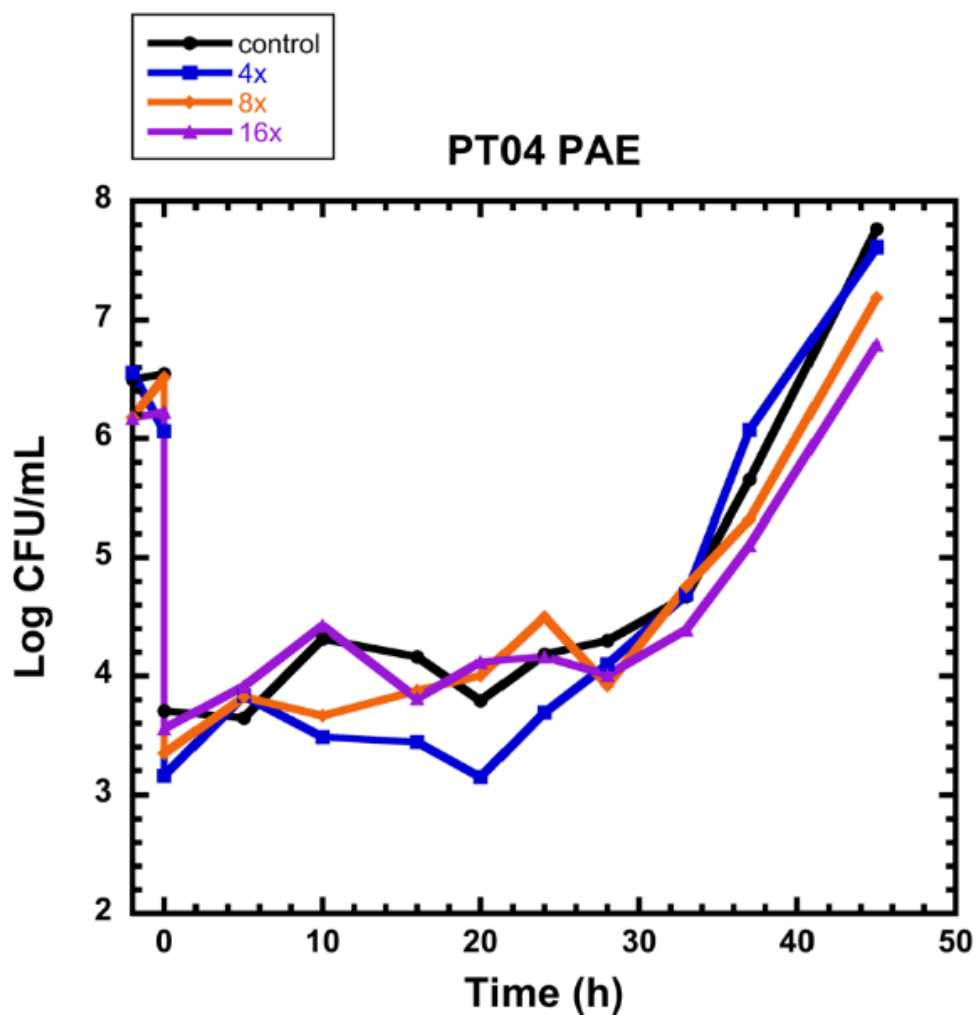


Figure 4.7 PAE of PT504 against *M. smeg* under different drug concentrations

Table 4.3 Kinetic and cellular parameters of PT504 against *M. smeg*

| Compound | MIC <sub>99</sub> <i>M. smeg</i> (µg/mL) | Ki* (nM) | t <sub>R</sub> (h) | PAE at 4X (h) | PAE at 8X (h) | PAE at 16X (h) |
|----------|--|----------|--------------------|---------------|---------------|----------------|
| PT504    | 1.06                                     | < 0.01   | 10                 | 12.3          | 10.9          | 12.4           |

The PAE studies of the first-line antituberculosis drugs rifampicin, ethambutol and isoniazid are reported to be 156 hrs, 8 hrs and 22 hrs, respectively (13). More recently, the PAE of a novel class of nitrofuranylamides were evaluated against slow-growing *M. bovis* giving a PAE comparable to rifampicin and much longer than ethambutol or isoniazid (4). However, very limited information could be found from the literature that links the drug-target kinetics with post-antibiotic effect.

#### Theoretical target engagement

The theoretical target engagement was calculated based on the model described above. Based on the assumption that the target was 100% occupied at 16X MIC,  $k_{\max}$  was 0.75 Log CFU/mL/h for PT04 (Table 4.2). As given by the model, the target occupancy  $\times k_{\max}$  at 8X MIC was 0.64, therefore the target occupancy at the corresponding concentration was 85%. This suggests that InhA needs to be engaged by at least 85% to achieve the bactericidal effect. This observation might indicate that InhA is possibly not a very vulnerable target as a high level of target engagement is required for cellular readout. However, target turnover is still a missing yet pivotal piece of information which could drastically affect in addressing the vulnerability of InhA.

## CONCLUSION

We have demonstrated that the diphenyl ether compounds are active against both *M. smeg* and *M. tb*, and that the triazole series gives better MIC values possibly due to a better cellular permeability. Two representative compounds, PT04 and PT504 were chosen to investigate the effect of drug-target kinetics on killing kinetics. The results suggest that a slower association rate constant of the drug may translate to a longer lag phase for recovery of growth. A cellular kinetic model was successfully established and reveals that the lag-phase time is largely affected by the inhibitor association kinetics while the maximum killing rate is more related to the binding affinity of the inhibitor. PAE experiments reveal that inhibitors with 10-hr residence time correspond to a 10-hr PAE. However, further investigation needs to be completed to build a thorough relationship between residence time and PAE in the InhA system.

## Chapter 5 InhA inhibitor discovery: novel fragment-hits and scaffolds

This chapter is based on part of the work that has been published in:

**Perryman, A.L., Yu, W.,** Ekins, S., Forli, S., Freundlich, J.S., Tonge, P.J., and Olson, A.J., “A Virtual Screen Discovers Novel, Fragment-sized Inhibitors of *Mycobacterium tuberculosis* InhA ”, *Journal of Chemical Information and Modeling*, 2015

Manjunatha, U., Rao, S.P.S., Kondreddi, R., Noble, C.G., Camacho, L.R., Tan, B.H., Ng, S.H., Ng, P., Ma, N.L., Lakshminarayana, S.B., Herve, M., Barnes, S.W., **Yu, W.**, Kuhlen, Kelli., Blasco, F., Beer, D., Walker, J.R., Tonge, P.J., Glynn, R., Smith, P.W., and Diagana, T., “Discovery of novel direct InhA inhibitors active against *Mycobacterium tuberculosis*”, *Science Translational Medicine*, 2015

### INTRODUCTION

Tuberculosis (TB), caused by *Mycobacterium tuberculosis* (*M. tb*), kills 1.3 million people each year (1). According to the World Health Organization, *M. tb* infects approximately two billion people (1). Since a third of the global population has a latent *M. tb* infection, this creates an immense reservoir of disease due to the potential for reactivation (1). There are 8.3 to 9 million new cases of TB annually, and half a million children get TB each year (1). *M. tb* kills more people in the world than any other bacteria. Of all infectious diseases, only HIV kills more people than *M. tb*, and TB is the leading cause of death for HIV/AIDS patients (1).

Although effective TB drugs have existed for over 60 years, and drug-resistant TB was not a major issue twenty years ago (2), cases of multi drug-resistant TB (MDR-TB) and extensively drug-resistant TB (XDR-TB) continue to increase throughout the world in both frequency and distribution (1-7). Cases of MDR-TB, which is defined as resistance to both isoniazid and rifampicin, have nearly doubled in just a few years (4). The global treatment success rate for TB is now less than 50% (1), and each year, one-half million new MDR-TB cases occur (*i.e.*, *M. tb* infections that are resistant to INH and rifampicin). In addition, XDR strains evade fluoroquinolones and at least one of the 2<sup>nd</sup>-line injectable drugs (amikacin, capreomycin, or kanamycin) (1) (Chapter 1). Finally, with the emergence of totally drug-resistant TB (TDR-TB) in several countries, no effective treatment options exist for these patients (3, 5-8).

#### Novel InhA inhibitors effective against isoniazid-resistant strains are critical for treating MDR and XDR-TB

InhA, the *M. tb* enoyl acyl-carrier protein reductase, is the primary target of the front-line drug isoniazid (INH) (9, 10) (Structure shown in Chapter 1). While it is one of the two most important antitubercular drugs and the only drug used for TB prophylaxis, INH suffers from resistance that continues to increase (1, 9, 11, 12). Data collected by the WHO indicate that up to 28% of all TB cases are INH-resistant, and in previously treated TB patients, up to 60% exhibit resistance, making it extremely difficult, time-consuming, and expensive to treat these patients (if they can be treated at all) (1, 2, 13).



INH must be activated by the *M. tb* catalase-peroxidase (KatG) (14-16), and most clinically relevant INH-resistant *M. tb* strains involve mutations in or deletions of *katG*, which abrogate activation of the INH prodrug (17, 18). In some areas, 70% of MDR-TB strains have mutations in *katG*, as do 100% of sequenced XDR-TB strains (19, 20). Although *katG* mutations are generally responsible for high-level resistance to INH in clinical isolates, those mutations can be enhanced by additional mutations in the promoter region of *inhA*, which cause low-level INH-resistance by increasing the amount of InhA produced (21, 22), and are found in up to 28% of INH-resistant clinical isolates (depending on the location of the study) (21-31). KatG activates INH to enable formation of a covalent adduct with NAD<sup>+</sup> or NADH (14) (Inhibition scheme shown in Chapter 1). As has been previously demonstrated, novel InhA inhibitors that do not require prior activation by KatG are not vulnerable to this key mechanism of INH resistance (11, 17).

### Current InhA inhibitors

There have been a lot of efforts to identify direct InhA inhibitors to overcome KatG-mediated resistance and many inhibitors have been yielded that block the lipid-binding site. He *et al.* reported the discovery of a series of pyrrolidine carboxamides (Structure shown in Figure 1.11 in Chapter 1) as a novel class of direct InhA inhibitors through a combination strategy of high-throughput screening and microarray parallel synthesis (32). AstraZeneca reported methyl-thiazoles as InhA inhibitors that displayed a novel inhibition mechanism where the protein adopted an “Y158-out” conformation upon binding (Figure 5.1). In addition, these methyl-thiazoles were NADH-preferred inhibitors, as opposed to the previously reported NAD<sup>+</sup>-preferred inhibitors (33). Subsequently, GSK reported a class of aminoproline as potent and

selective InhA direct inhibitors by means of DNA encoded library technology. Hit-to-lead optimization further yielded a compound with good InhA inhibition as well as pharmacokinetic profile (34). Remarkably, Hartkoorn *et al.* discovered the natural product pyridomycin with potent anti-TB activity. They also determined the crystal structure of pyridomycin in complex with InhA and found that pyridomycin adopted a unique binding mode that blocked both the cofactor substrate and the lipid substrate (35) (Crystal structure shown in Figure 1.12 in Chapter 1).

Although several novel classes of direct InhA inhibitors have been discovered, lack of *in vivo* efficacy compared to the front-line anti-TB drugs hints at the underlying hurdle of developing novel antituberculosis drugs.

#### Virtual screening to identify novel inhibitor scaffolds

High-throughput docking virtual screening (VS) studies have been used extensively in both academia and the pharmaceutical industry to discover inhibitors of select drug targets (median hit rate of 13% (36)) and are complementary to experimental target-based HTS (37). “Docking” flexible models of small molecules computationally probes the energetic landscape governing macromolecular recognition with a target protein, to help guide the discovery and design of novel inhibitors (38-45). By docking flexible models of ligands into atomic-scale protein targets the prediction of a) how tightly these compounds can bind; b) where they prefer to bind; and c) what specific interactions they can form at the binding site.

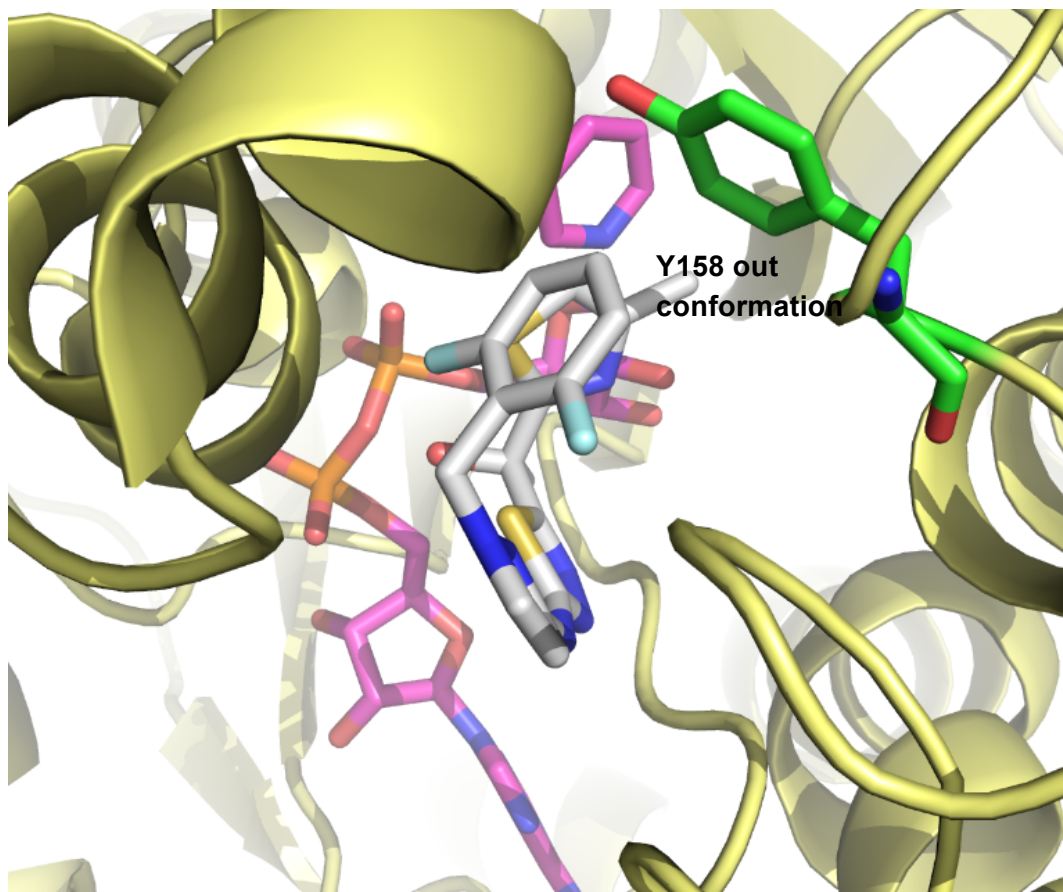


**Figure 5.1 InhA in complex with methyl-thiazole**  
Residue Y158 adopts the “Y158-out conformation (33).

Many VS studies, including some against InhA, have involved computational studies in the absence of experimental validation of their predictions (46-52). In contrast, some pioneering VS against InhA have yielded predictions that were experimentally validated with enzyme inhibition assays (53) and/or whole-cell growth assays against *M. tb* (54, 55), *M. vanbaalenii* (56), or *M. smegmatis* (57). These previous, experimentally validated VS against InhA helped

establish the feasibility of computer-aided drug discovery against this system and laid the foundation for the research we will present.

#### Whole-cell screening in identifying novel scaffold

Although high-throughput virtual screening has been highly productive in general, it usually requires the knowledge of the therapeutic target as a basis for chemical screens. Sometimes, these target-based screens reveal small molecules with potent activity against the enzyme target yet fail to inhibit the target in the *in vivo* environment (58). Due to the difficulty of converting compounds lacking whole-cell activity into ones with such activity, an alternative approach is to perform whole-cell screens against living organisms in the first place, where small molecules are tested against all targets simultaneously. Once the hit compound is identified, the challenge is to identify the target as further lead optimization will be hindered without knowing which protein target the compound inhibits (58). Various strategies for target deconvolution have been developed, such as selection of resistance mutants, biochemical affinity-based methods, gene overexpression and underexpression, and microarray technologies (58, 59).

Although target deconvolution is generally challenging, the whole-cell screening strategy has been widely utilized in many different systems. Using a recombinant strain of *M. tb* that underexpresses DHFR, Kumar *et al.* reported the discovery of a quinazoline-ring based DHFR inhibitor that had whole-cell activity (60). Stanley *et al.* also described the investigation of novel MmpL3 and DprE 1 inhibitors using whole-cell based high-throughput screening (61). In addition, this strategy has also been widely adopted in other Gram-positive and Gram-negative bacteria as well as fungal systems (62).

In the current chapter, we will discuss the discovery of novel InhA inhibitors based on heterocyclic and 4-pyridone scaffolds using both virtual screening and whole-cell activity profiling.

## MATERIALS AND METHODS

### Discovery of novel fragment-sized inhibitors of InhA using virtual screening

#### The Global Online Fight Against Malaria project and its relevance to TB research

The Global Online Fight Against Malaria (or “GO Fight Against Malaria,” GO FAM) was a project on the World Community Grid that Dr. Alexander L. Perryman designed and executed while at The Scripps Research Institute (63-65). Utilizing compound libraries such as NCI, Enamine, Asinex, ChemBridge, and Vitas-M Labs with 3-D models obtained from the ZINC server (66), GO FAM has performed virtual screens of 5.6 million commercially available compounds against over 200 structures of targets from 22 classes of validated and potential drug targets for the treatment of malaria and other diseases. In addition, it has also generated a total of 1.16 billion docking results.

In this work we used GO FAM to dock a much larger number of compounds against InhA than all previous VS combined (48-57). The results presented here encompass only 5.6% of the compounds screened on GO FAM against InhA—we began with the NCI library, because NCI compounds are available to researchers for free, through the NCI’s Developmental Therapeutics Program (DTP).

Screening the NCI library of compounds against InhA using the GO Fight Against  
Malaria World Community Grid

The docking was performed by Dr. Alex L. Perryman. AutoDock Vina (45) 1.1.2 (or “AD Vina”), which was grid-enabled for World Community Grid by IBM staff, was used to dock each compound from the NCI library against the crystallographic conformation of InhA-PT70 (pdb code: 2X23) (67). In positive control re-docking experiments, the co-crystallized inhibitor PT70 docked to the target model of 2X23 with an RMSD of 0.49 Å. Additional (successful) positive control re-docking and cross-docking experiments that utilized AD Vina against other crystal structures of InhA bound to different ligands have been published recently elsewhere (68).

InhA inhibition and kinetics experiments

An InhA inhibition assay was performed on the hit compounds that were identified from docking by AD VINA. Briefly, the candidate inhibitor was assayed at 100 µM in a reaction buffer (30 mM PIPES, 150 mM NaCl, 1 mM EDTA, at pH 6.8) containing 30 µM trans-2-dodecenoyl coenzyme A (DD CoA), 250 µM NADH, and 100 nM InhA. The enzymatic activity at 100 µM inhibitor concentration was quantified, and the three compounds that displayed the largest inhibition of enzyme activity were selected for further IC<sub>50</sub> measurements. In general, IC<sub>50</sub> values were determined by varying the concentration of inhibitors in the aforementioned reaction mixture. The data were analyzed using equation 5.1, where I is the inhibitor concentration and y is percent activity.

$$y = \frac{100\%}{1 + \frac{I}{IC_{50}}}$$

Equation 5.1

To provide mechanistic insight, the top two compounds were chosen for subsequent measurements of their inhibition constants ( $K_i$ ). The third best inhibitor displayed solubility problems at  $> 200 \mu\text{M}$  concentrations. The  $K_i$  value was calculated by determining the  $k_{\text{cat}}$  and  $K_m$  (DD CoA) values at several fixed inhibitor concentrations using the same assay conditions described above. The data were analyzed using the standard equations for competitive and non-competitive inhibition (equations 5.2 and 5.3).

$$v_o = \frac{v_{max}[S]}{K_M \left(1 + \frac{[I]}{K_i}\right) + [S]}$$

Equation 5.2

$$v_o = \frac{v_{max}[S]}{K_M \left(1 + \frac{[I]}{K_i}\right) + [S] \left(1 + \frac{[I]}{K_i'}\right)}$$

Equation 5.3

#### Comparison with known InhA inhibitors.

Dr. Sean Elkins performed the Principal Component Analysis (PCA) on the combination of the 157 known InhA inhibitors in TB Mobile 2 (Version 2 of a mobile application for antituberculosis drugs with known target) and the hit InhA compounds discovered from NCI



library from this study (69, 70). The file generated from the TB Mobile data set was used for the Principal Component Analysis (PCA), which was calculated using Discovery Studio 3.5 (71) and used eight interpretable descriptors (AlogP, molecular weight, number of rotatable bonds, number of rings, number of aromatic rings, number of hydrogen bond acceptors, number of hydrogen bond donors, and molecular fractional polar surface area).

#### Minimum inhibitory concentration (MIC) assay vs. *M. tb*

MIC assays were performed by Dr. Alex L. Perryman. For whole-cell *in vitro* studies, new batches of the NCI hit compounds were obtained from NCI. The compound structure, molecular weight and purity were confirmed by <sup>1</sup>H NMR (600 MHz), LC-MS and HPLC. MIC values of NCI 99389 and 111591 were determined following the microplate-based Alamar Blue assay (MABA) method as previously described (72). Fifty mM compound stock in DMSO was dissolved in sterile Middlebrook 7H9-OADC broth, making a 1 mM pre-test solution. One hundred μL pre-test solution was added into wells in column 1 of a sterile polystyrene 96-well round-bottom plate (CLS3795, Corning, NY). Wells in column 2 to 12 received 50 μL of sterile 7H9-OADC broth. Serial two-fold dilutions of compounds were performed, and column 12 was set as drug-free (inoculum-only) control. Final concentrations of compounds were as follows: for INH, 0.012 to 25 μg/mL; for NCI compounds, 0.50 to 500 μM. *M. tb* wild type strain H37Rv and *InhA* over-expression strain mc<sup>2</sup>4914 (10) were 1:1000 diluted in 7H9+OADC medium at mid-logarithmic stage of growth (OD<sub>595nm</sub>=0.4). Fifty μL of diluted bacterial suspensions were placed in each well, and the plates were sealed with Parafilm and incubated at 37 °C for seven days. Twenty μL of alamarBlue<sup>®</sup> reagent (Invitrogen, Frederick, MD) freshly mixed with 12.5 μL 20% Tween 80 was added into each well, followed by 24-hr incubation in 37 °C. The absorbance was read at 570 nm, using a reference wavelength of 600 nm, with a microplate reader (ELX808,

Biotek Instruments). The MIC endpoint was defined as the lowest concentration of the test agent that produced at least 90% reduction in absorbance compared with that of the drug-free control.

#### Cellular toxicity assay

Cytotoxicity assays were performed by Dr. Alex L. Perryman. The cytotoxicity of the 2 most promising NCI compounds was determined using the 3-(4,5-dimethylthiazol-2-yl)-2,5-diphenyltetrazolium bromide (MTT) cytotoxicity assay with the Vybrant MTT Cell Proliferation Assay Kit (Molecular Probes) (13). Vero cells (African green monkey kidney epithelial cells; ATCC) were plated in a sterilized 96-well plates (Costar 3595, Corning, NY) at  $2 \times 10^5$  cells/well with a volume of 50  $\mu$ L and incubated for 3 hrs in a 37 °C incubator. NCI compounds were dissolved in DMSO at a final concentration of 10 mg/mL. In a separate 96-well plate, two-fold serial dilutions of the compounds were prepared using Dulbecco's modified eagle medium (Gibco) supplemented with 10% fetal bovine serum. Fifty  $\mu$ L of diluted compounds were added to appropriate test plate wells to generate final concentrations ranging from 0.78 to 100  $\mu$ g/mL. Column 12 was utilized for a drug-free control. After 48 hrs treatment, 10  $\mu$ L of 12 mM MTT stock solution was added into each well and incubated at 37 °C for 4 hrs. One hundred  $\mu$ L of 0.1 g/mL SDS•HCl solution was subsequently added to each well in order to halt the reaction, followed by 4-hr incubation at 37 °C. The absorbance at 570 nm was determined with a VersaMax ELISA microplate reader (Molecular Devices), and the  $CC_{50}$  was calculated by plotting absorbance at 570 nm against concentration of untreated Vero cells control.

#### Discovery of 4-hydroxy-2-pyridone InhA inhibitors using whole-cell high-throughput profiling

### High-throughput cell-based screening and MIC determination

High-throughput screening and determination of MIC values were performed by Novartis. High-throughput screening of the Novartis compound collection was carried out using *M. tb* H37Rv, and MIC values against *M. tb* H37Rv were determined as previously described (73).

### Generation of drug-resistant mutants and whole genome sequencing

Selection of resistance mutations was performed by Novartis. *M. tb* H37Rv strain was plated on 7H11 agar plates containing 10x and 20x MIC of the test compounds. After 3 weeks of incubation at 37 °C single isolated colonies were propagated in drug free 7H9 broth. The resistance phenotype of the pyridone InhA inhibitors was confirmed by determining MIC values against compounds NITD-529, 564 and 916. Whole genome sequencing and single-nucleotide polymorphism analysis of the spontaneous resistant mutants was carried out as described before (73, 74).

### Binding Assay

Isothermal titration calorimetry (ITC) experiments were performed by Novartis using an ITC200 (GE Healthcare) at 25 °C, with 10-20 µM InhA in 20 mM HEPES pH 7.0, 150 mM NaCl and 2 mM TCEP in the sample cell. The compound at 125-500 µM was diluted, from a 10 mM stock in DMSO, into the same buffer and titrated into the InhA sample supplemented with the same concentration of DMSO. NADH from a 5 mM stock dissolved in water was added to both the cell and syringe at a final concentration of 50 µM. Typically, 15 injections of 2.6 µL of

compound were injected into the sample cell at 2.5 min intervals. The data were fit to a single-site binding equation using Origin.

#### Thermo shift assay

Thermofluor protein stability shift assays were performed to determine the cofactor preference of the compounds as previously described (75). A total volume of 20  $\mu\text{L}$  containing 7.4  $\mu\text{M}$  InhA, 2.5 mM cofactor (NADH or  $\text{NAD}^+$ ) and 25  $\mu\text{M}$  inhibitor (2% DMSO) was added to a 96-well thick-wall PCR plate (Concord) in the aforementioned reaction buffer. After 1.5 hrs incubation at 25  $^{\circ}\text{C}$ , 1  $\mu\text{L}$  of 100 x Sypro Orange (Sigma) was added and the plate was sealed with microseal “B” Film (Bio-Rad). The samples were heated from 25 to 90  $^{\circ}\text{C}$  in increments of 0.2  $^{\circ}\text{C}/10$  s. Data was processed on Bio-Rad CFX manager.

#### InhA enzyme assay

InhA inhibition assays were performed as described above to determine  $\text{IC}_{50}$  values for the compounds.

#### Crystallization and structure determination

Crystal structures were solved by Novartis. Crystallization conditions and data processing details were described in the corresponding paper (76).

## RESULTS AND DISCUSSION

### Discovery of novel fragment-sized inhibitors of InhA using virtual screening

#### Workflow of novel InhA inhibitor discovery by virtual screening

We characterized the predicted binding mode of each compound in the NCI library, by the number and types of energetically favorable interactions with the InhA active site and the estimated free energy of binding, using a software-automated workflow (python and tc-shell scripts) and established protocols (78-80). The results were filtered to harvest compounds that displayed critical interactions (based on analyses of the features displayed by nanomolar inhibitors of InhA in existing crystal structures) (11, 33, 67, 81). These filters selected compounds for which the top-scoring binding mode/compound displayed base-stacking interactions between the candidate compound and the NAD<sup>+</sup>/NADH co-factor and at least two predicted hydrogen bonds to the active site. The selected compounds also had to display an estimated free energy of binding (FEB)  $\leq$  -8.0 kcal/mol, according to the AD Vina scoring function. This set of docking filters harvested 91 compounds, whose binding modes were then visually inspected (Figure 5.2).

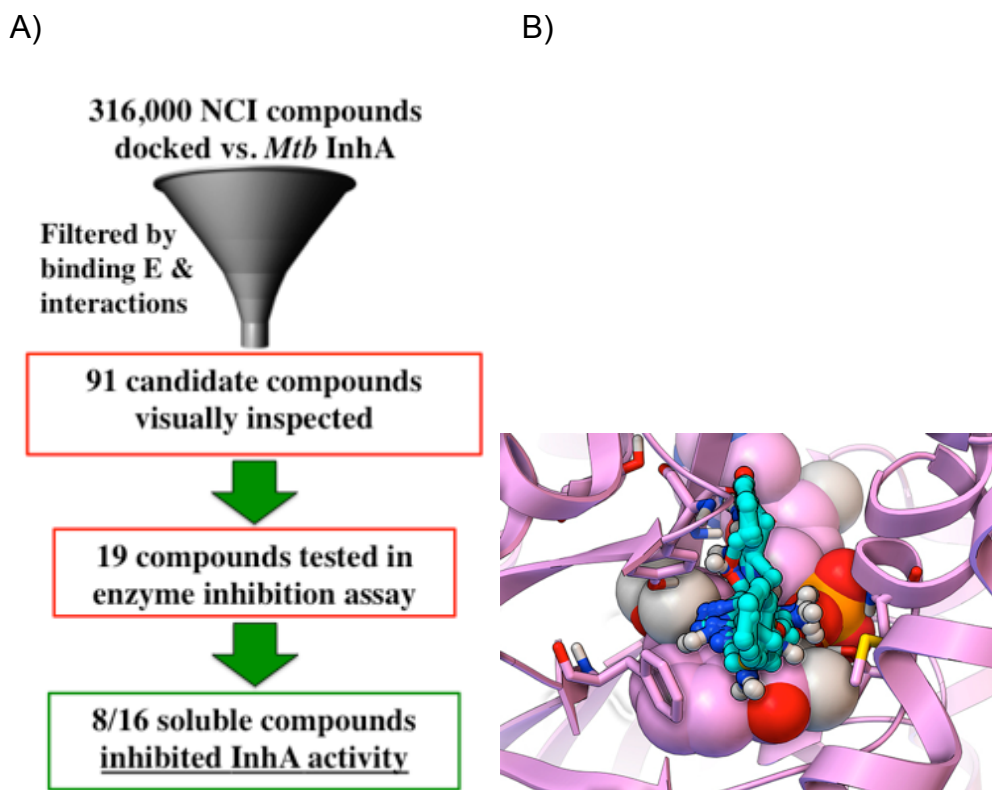


**Figure 5.2 Workflow Used to Discover Novel InhA Inhibitors in the Virtual Screen with the NCI Library on GO FAM**

(A) The workflow used energetic and interaction-based filters (e.g., requiring compounds to display an estimated free energy of binding  $\leq -8.0$  kcal/mol, base stack with the NAD cofactor, and form at least two hydrogen bonds with the active site) to filter the VS results and harvest NCI compounds for visual inspection. Candidates that passed visual inspection were then ordered and tested in InhA inhibition assays. Eight of the sixteen soluble compounds inhibited InhA activity by 27 to 71% at 100  $\mu$ M. (B) The predicted binding modes for all eight novel InhA inhibitors are displayed as sticks-and-balls with cyan carbons, while the InhA target is shown in magenta. The NAD cofactor is rendered as CPK, and the key residues Gly96, Ser123, Phe149, Tyr158, Thr196, and Met199 are shown as thin sticks

Visual inspection is a subjective process, but experience in macromolecular recognition and knowledge of the strengths and weaknesses of different modeling approaches used to view,

measure, and judge/prioritize the docked results can be helpful. The use of human knowledge (“*in cerebro*” quality control) to prioritize computer-aided (“*in silico*”) predictions has been a successful strategy in previous blind docking challenges, such as SAMPL2 and SAMPL4 (80, 82, 83). Our visual inspection process incorporated multiple criteria, in an attempt to decrease the number of false positives that often result from virtual screens. Unfavorable aspects of a docking result included compounds that (a) have docked modes displaying distorted geometries (*i.e.*, peptide bonds in the ligand models were allowed to freely rotate during docking, since the target was rigid, but docked modes displaying peptide bonds that were 30 to 90° from *cis* or *trans* were rejected); (b) have one or more large hydrophobic groups (*e.g.*, phenyl or t-butyl) exposed to solvent; or (c) display more than three unfavorable electrostatic repulsion interactions with polar or charged groups in the target. Favorable aspects of a docked pose included compounds where (d) a majority of their heteroatoms are involved in favorable electrostatic interactions or hydrogen bonds (as discussed in our recent manuscript) (68), since heteroatoms will likely need to be added during the optimization process, without violating Lipinski’s rules (84); (e) the hydrophobic groups displayed van der Waals interactions with non-polar regions of the target (as measured by the AD Vina scoring function (45), characterized using distance-dependent and atom pair-specific criteria implemented in the Fox software (78)); and (f) aromatic rings displayed pi-pi (base-stacking or T-stacking) (85-87) or pi-cation interactions with the target (86-88), as characterized by the Fox software (78). The AD Vina scoring function uses ambiguous atom types (*i.e.*, hydrogen bond donors are treated as donor and/or acceptor) and a spherical hydrogen bond potential (instead of an angle-dependent potential) (45). Consequently, to verify the number of hydrogen bonds that the docking filters detected, the donor-acceptor distance and donor-hydrogen-acceptor angle (which should be between 120-

180°) for predicted hydrogen bonds were all measured manually in PMV (89). Because rotatable polar hydrogen atoms in the ligands are placed in arbitrary torsion angles by AD Vina (45) and since the model of the target was rigid, structural intuition was also employed when deciding which hydrogen bonds the docked mode displayed. Special emphasis was placed on candidates that (g) displayed hydrogen bonds with invariant residues and backbone atoms, since previous studies with MDR HIV protease and MDR *P. falciparum* DHFR have shown that displaying these features renders the evolution of drug resistance less likely (90-106).

The visual inspection led to the discovery of several novel inhibitors (Table 5.1). Nineteen compounds were ordered, but three of them were insoluble at 100 µM in DMSO and could not be assayed (Table 5.1). Eight of the 16 soluble candidates were modest inhibitors of InhA (*i.e.*, showed 27% to 71% inhibition at 100 µM). Using the same assay conditions and protocol (*i.e.*, without pre-incubating the compound with InhA), the very potent positive control compound PT70 displayed 75% inhibition at 100 nM (*i.e.*, the well-optimized lead compound PT70 was >1000 times more potent than our best new inhibitor).

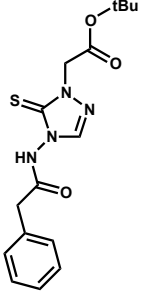
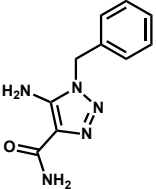
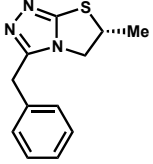
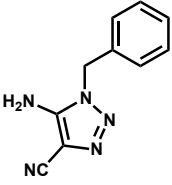
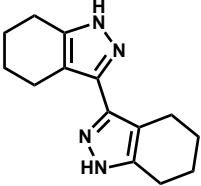
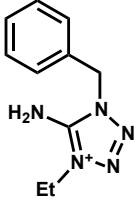
The pairwise Tanimoto similarity (107) was calculated for each of the 8 new InhA inhibitors versus each of the 7 other compounds in order to determine the number of distinct scaffolds, according to a cut off > 0.7(108) (Table 5.2). In addition, to assess the chemical property space of the eight InhA inhibitors found, the pairwise Tanimoto similarity (107) was also calculated for each of the new InhA inhibitors discovered in the NCI library versus each of the 157 known InhA inhibitors from TB Mobile (69). This again used the TB Mobile dataset sdf for which MDL descriptors were calculated, followed by Tanimoto similarity using the “find

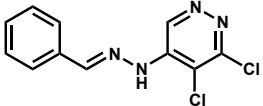
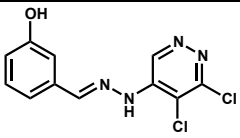
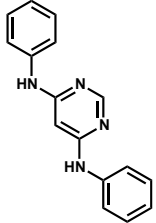
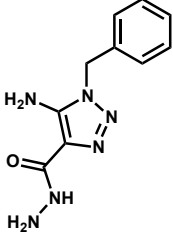
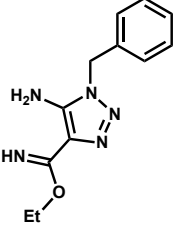
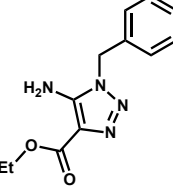
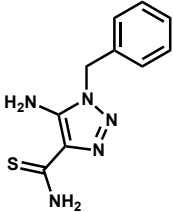


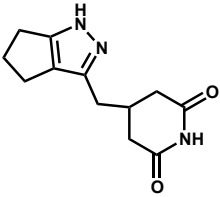
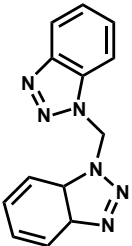
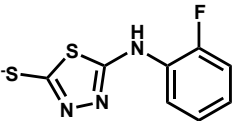
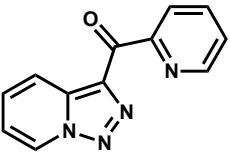
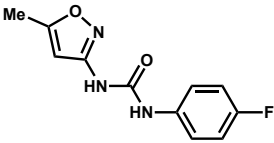
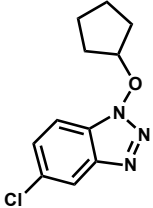
similar molecules by fingerprints” protocol in Discovery Studio 3.5 (71). This then enabled us to calculate the minimum, maximum and average similarity as measures of proximity to known InhA inhibitors.

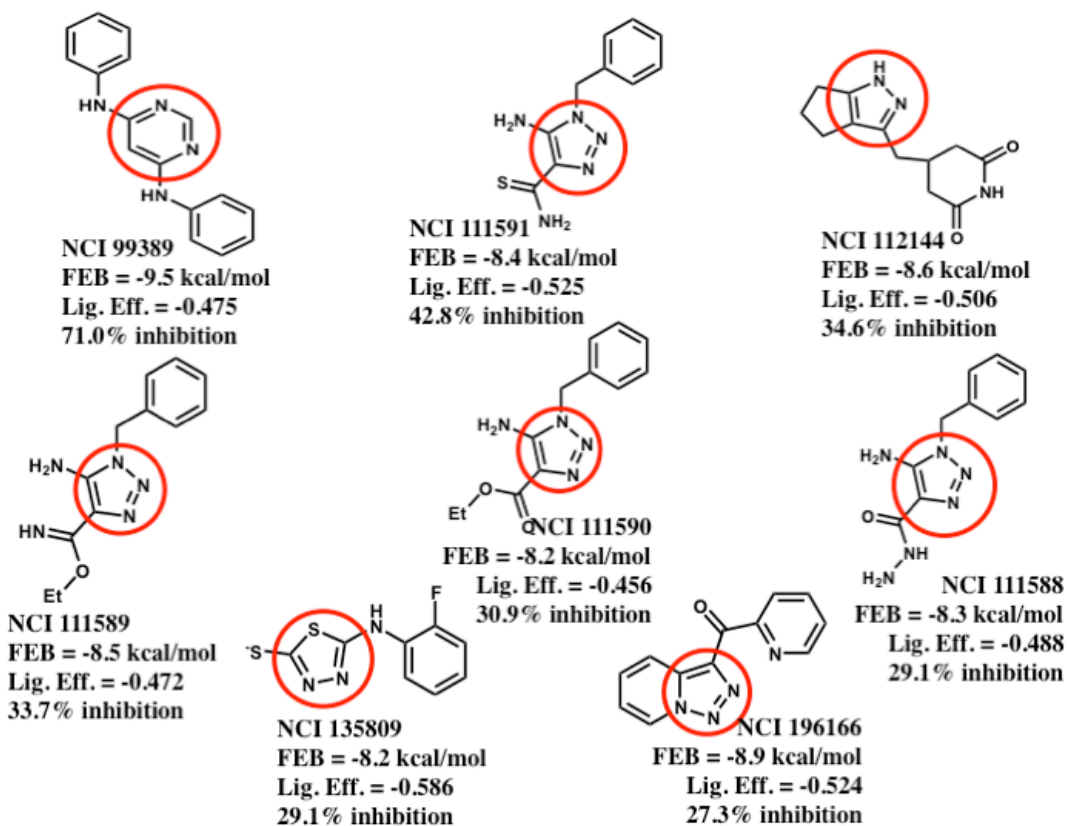
If scaffolds are defined as small molecule chemotypes that possess less than 70% similarity according to Tanimoto values (108), these eight inhibitors represent five novel InhA inhibitor scaffolds (see Figure 5.3 and Table 5.2). As required by the docking filters, all eight compounds are predicted to base stack with the NAD cofactor (Figures 5.4 - 5.5), instead of forming a covalent adduct with it. As demonstrated by the InhA activity assays, they do not require prior activation by *M. tb* KatG. “Hits” were classified in a way that involved the potency for a particular size of compound. “Fragment hits” (novel inhibitors with a  $M_w < 300$  Daltons) (109) tend to display a potency in the 100’s of  $\mu\text{M}$  to low mM range (according to  $K_i$  or  $K_d$ ) (82, 109-115). Consequently, we defined fragment hits as novel inhibitors with a  $M_w < 300$  g/mol that displayed a  $K_i$  value  $< 100 \mu\text{M}$ . Therefore, using a more stringent metric, 2 out of 16 compounds were novel fragment hits against InhA (*i.e.*, a 12.5% hit rate), representing two promising new scaffolds which will be discussed below.

Table 5.1 Compound ID's, 2D structures, and InhA inhibition data

| NCI ID | Structure   | $K_i^{app}$ ( $\mu$ M) & mechanism | InhA inhibition at 100 $\mu$ M inhibitor |
|--------|---|------------------------------------|--|
| 660846 |    |                                    | 2.7%                                     |
| 683622 |    |                                    | 9.2%                                     |
| 609097 |   |                                    | 10.3%                                    |
| 314884 |  |                                    | 10.3%                                    |
| 371850 |  |                                    | Not soluble                              |
| 11142  |  |                                    | 4.5%                                     |

|  |   |  |  |
|--|---|--|--|
| 75300                                  |    |  | Inhibitor precipitated in buffer                               |
| 75301                                  |    |  | Inhibitor precipitated in buffer                               |
| <b>99389</b><br><b>(ZINC01654204)</b>  |    | <b>54.1 ± 5.4</b><br><br><b>competitive</b>    | <b>71.0%</b><br><br><b>(estimated IC<sub>50</sub> ~ 40 μM)</b> |
| 111588<br><b>(ZINC0135077)</b>         |    |  | 29.1%  |
| 111589<br><b>(ZINC04994329)</b>        |  |  | 33.7%  |
| 111590<br><b>(ZINC00129134)</b>        |  |  | 30.9%  |
| <b>111591</b><br><b>(ZINC01703321)</b> |  | <b>59.2 ± 8.7</b><br><br><b>noncompetitive</b> | <b>42.8%</b>   |

|                          |   |   |       |
|--------------------------|---|---|-------|
| 112144<br>(ZINC04878446) |    | 205.6 ± 46<br><br>(precipitation observed at high concentrations) | 34.6% |
| 130836                   |    |   | 9.1%  |
| 135809<br>(ZINC01722139) |    |   | 29.1% |
| 196166<br>(ZINC01734860) |   |   | 27.3% |
| 213837                   |  |   | 10.9% |
| 293934                   |  |   | 9.1%  |



**Figure 5.3 Summary of the 2D structures, docking scores, and InhA inhibitory activities of the eight new inhibitors discovered**

The most potent new InhA inhibitor discovered is shown in the top-left corner, while the least potent new inhibitor is displayed in the bottom-right corner. These eight new inhibitors correspond to five novel scaffolds versus InhA (i.e., NCI 111588 – 111591 represent analogs of one scaffold, according to a Tanimoto cut-off of 0.7; see Table 5.2). FEB signifies the estimated free energy of binding value from AutoDock Vina's scoring function, in kcal/mol. The Lig. Eff. is the calculated ligand efficiency from AutoDock Vina, in kcal/mol/heavy atom. The % inhibition of InhA activity was produced when each compound was present at 100  $\mu$ M. The region of each compound that was predicted to base stack with the NAD cofactor is highlighted with a red circle.

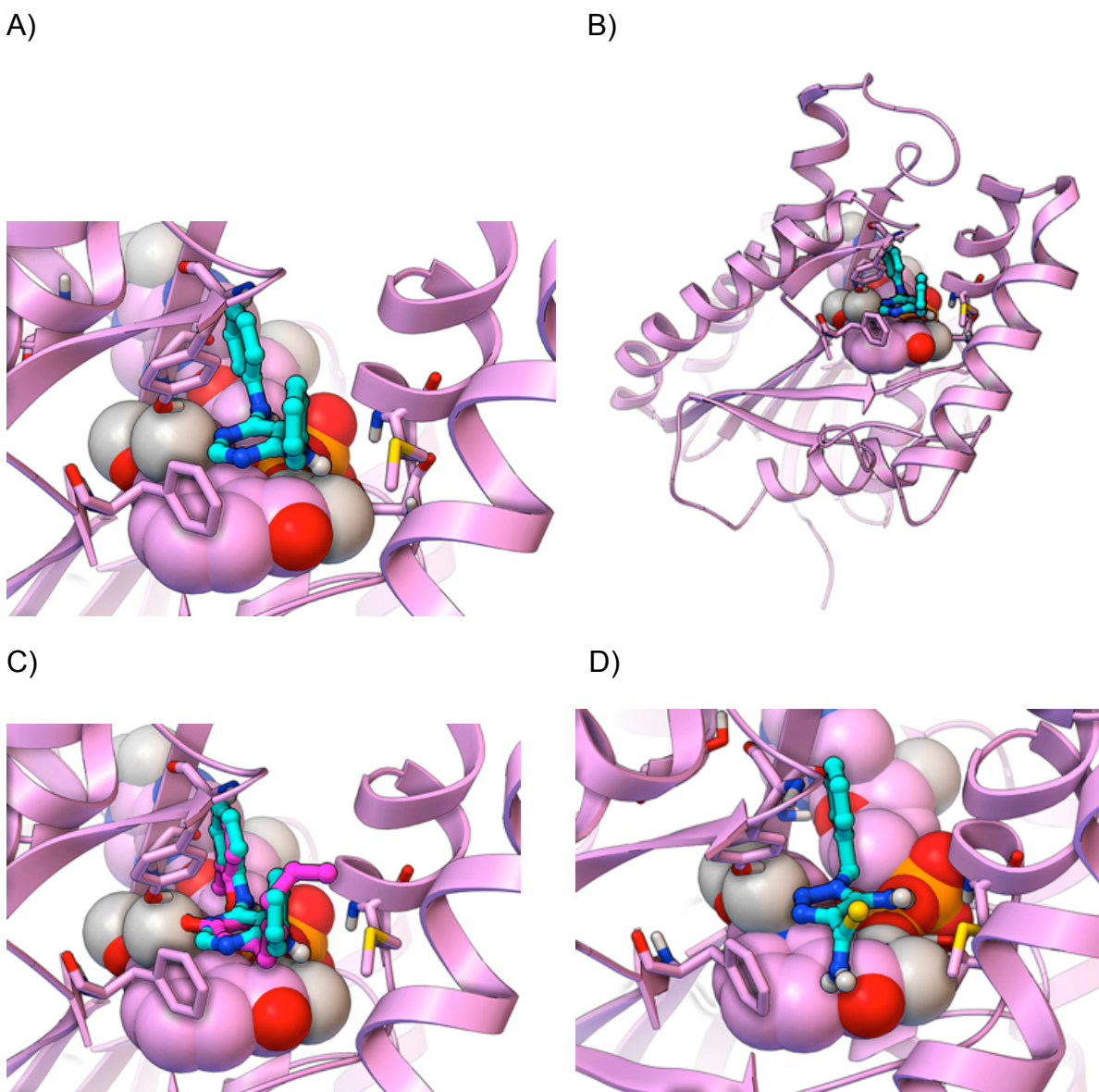


**Figure 5.4 Predicted binding modes of the two most potent new InhA inhibitors discovered in GO FAM experiment**

The docked modes produced by AutoDock Vina are displayed as ball-and-sticks with cyan carbon atoms, and the InhA target (2X23.pdb) is displayed as magenta ribbons. The NAD cofactor is displayed in CPK, and the key residues Gly96, Ser123, Phe149, Tyr158, Thr196, and Met199 are shown as thin sticks. A close-up view of the predicted binding mode of the top fragment hit, NCI 99389 ( $K_i^{\text{app}} = 54.1 \pm 5.4 \mu\text{M}$ ), is shown in (A), while the full view is displayed in (B). In (C) the docked mode of NCI 99389 is compared to the experimentally-determined binding mode of PT70, the inhibitor that crystallized with InhA in 2X23.pdb, which is displayed as ball-and-sticks with magenta carbons. In (D) the predicted binding mode of the 2<sup>nd</sup> most potent fragment hit, NCI 111591 ( $K_i^{\text{app}} = 59.2 \pm 8.7 \mu\text{M}$ ), is displayed.

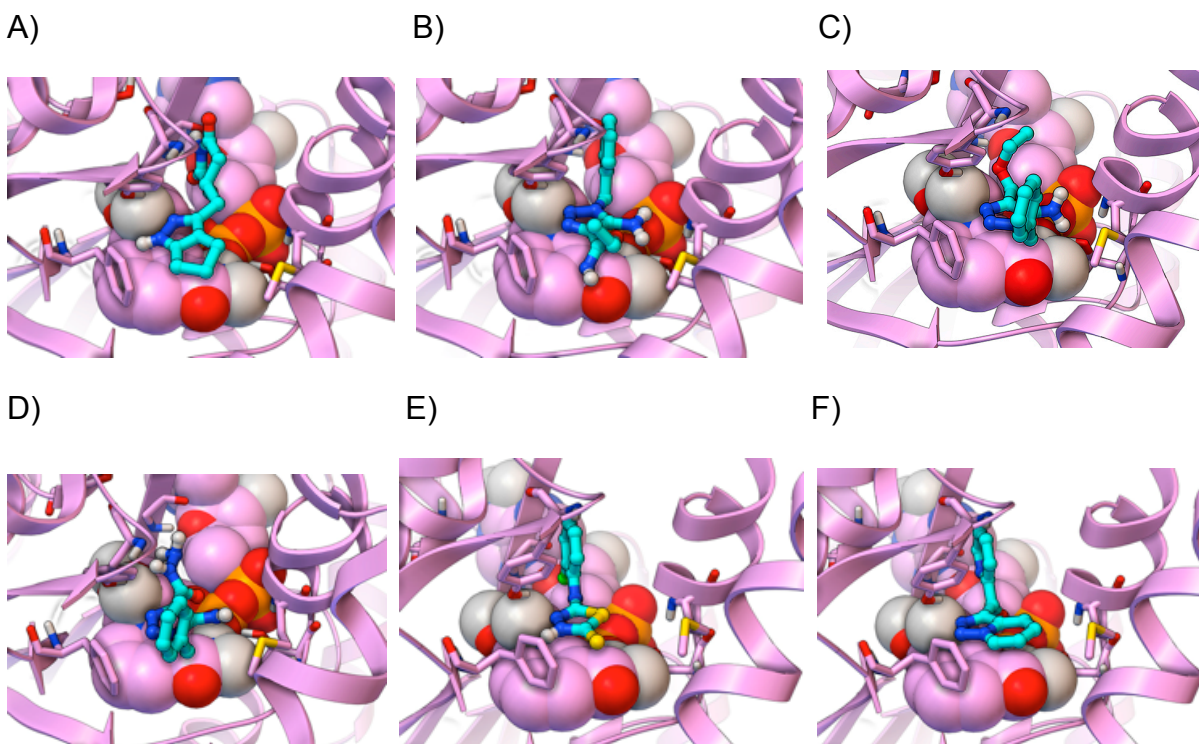


**Figure 5.5 Predicted binding modes of the least potent new InhA inhibitors discovered in GO FAM experiment**

The docked modes produced by AutoDock Vina are displayed as ball-and-sticks with cyan carbon atoms. The InhA target (2X23.pdb) is displayed as magenta ribbons, with the NAD cofactor as CPK. The key residues Gly96, Ser123, Phe149, Tyr158, Thr196, and Met199 are shown as thin sticks. The predicted binding modes of the following new InhA inhibitors are depicted: (A) NSC 112144 ( $K_i^{app} = 205.6 \pm 46 \mu\text{M}$ ), (B) NSC 111589, (C) NSC 111590, (D) NSC 111588, (E) NSC 135809, and (F) NSC 196166.

Table 5.2 Tanimoto Similarity of Each Novel Inhibitor Compared to the Other 7 New Inhibitors

| <b>NCI ID</b>                             | <b>111590</b> | <b>111588</b> | <b>99389</b> | <b>111591</b> | <b>135809</b> | <b>196166</b> | <b>112144</b> | <b>111589</b> |
|---|---------------|---------------|--------------|---------------|---------------|---------------|---------------|---------------|
| <b>111590</b>                             | 1.00          | 0.78          | 0.39         | 0.71          | 0.39          | 0.54          | 0.39          | 0.83          |
| <b>111588</b>                             | 0.78          | 1.00          | 0.45         | 0.78          | 0.46          | 0.55          | 0.48          | 0.84          |
| <b>99389</b>                              | 0.39          | 0.45          | 1.00         | 0.49          | 0.43          | 0.41          | 0.33          | 0.41          |
| <b>111591</b>                             | 0.71          | 0.78          | 0.49         | 1.00          | 0.57          | 0.48          | 0.38          | 0.72          |
| <b>135809</b>                             | 0.39          | 0.46          | 0.43         | 0.57          | 1.00          | 0.36          | 0.34          | 0.45          |
| <b>196166</b>                             | 0.54          | 0.55          | 0.41         | 0.48          | 0.36          | 1.00          | 0.41          | 0.48          |
| <b>112144</b>                             | 0.39          | 0.48          | 0.33         | 0.38          | 0.34          | 0.41          | 1.00          | 0.41          |
| <b>111589</b>                             | 0.83          | 0.84          | 0.41         | 0.72          | 0.45          | 0.48          | 0.41          | 1.00          |
| <b>Average similarity to the Other 7</b>  | 0.6           | 0.6           | 0.4          | 0.6           | 0.4           | 0.5           | 0.4           | 0.6           |
| <b>Maximum Similarity to the Other 7</b>  | 0.8           | 0.8           | 0.5          | 0.8           | 0.6           | 0.6           | 0.5           | 0.8           |
| <b>Scaffold # Using a Cutoff &gt; 0.7</b> | 2             | 2             | 1            | 2             | 4             | 5             | 3             | 2             |

2 fragment hits – NCI 99389 and NCI 111591

The most promising new scaffold, NCI 99389, is a 4,6-diaminopyrimidine and was predicted to form the following quaternary interactions in the docking studies: base stacking with the nicotinamide ring of the NAD cofactor (similar to the crystallographic binding mode of PT70) (67); T-stacking with the side-chain of Phe149; hydrogen-bonding with the hydroxyl of Tyr158 (similar to PT70) (67); hydrogen-bonding with the 2'-hydroxyl of the ribose adjacent to the nicotinamide ring of NAD (similar to PT70) (67); hydrogen-bonding with the sulfur in the



side-chain of Met199; favorable electrostatic interactions with the hydroxyl of Tyr158; and favorable electrostatic interactions with the phosphate group proximal to the ribose of NAD (Figure 5.4 A). As a reference, in addition to the aforementioned hydrogen bonding and base stacking interactions that the crystallographic binding mode of PT70 displays, PT70 also contains a six carbon alkyl tail that packs very well into a hydrophobic pocket of InhA. Despite using a large grid box in these docking calculations, the predicted binding mode of 99389 occupies a similar location to the crystallographic binding mode of PT70 (Figure 5.4 C). Experimental structure verification will be necessary to firmly establish the actual binding mode. Since this compound is an un-optimized fragment hit and lacks the long alkyl tail that PT70 contains, it might not induce the same “closed” conformation that PT70 induces (67, 116) (which might give 99389 a different binding mode than what these docking calculations predicted), and/or it might have to pay a larger enthalpic penalty to induce the ligand-bound conformation that InhA forms (which, when combined with the numerous hydrophobic contacts that it lacks, might also explain part of the >1,000-fold difference in potency versus PT70). NCI 99389 displayed an IC<sub>50</sub> of approximately 40 μM against InhA (Table 5.1). In subsequent kinetic experiments (Figure 5.6 and Table 5.1), it displayed an apparent K<sub>i</sub> of 54.1 ± 5.4 μM, and it demonstrated a competitive mechanism of inhibition with respect to substrate.

The second most promising new scaffold discovered, NCI 111591, is a 5-amino-1*H*-1,2,3-triazole and had a docked mode that displayed the following quaternary interactions with InhA: base stacking with the nicotinamide ring of the NAD cofactor; hydrogen-bonding with the hydroxyl of Tyr158; hydrogen-bonding with the 2'-hydroxyl of the ribose adjacent to the nicotinamide ring of NAD; hydrogen-bonding with the carbonyl oxygen of the nicotinamide

ring; favorable electrostatic interactions with the sulfur in the side-chain of Met199; favorable electrostatic interactions with the phosphate group proximal to the ribose of NAD; and favorable electrostatic interactions with the 2'-hydroxyl of the ribose that is adjacent to the nicotinamide ring of NAD (Figure 5.4 D). When present at 100  $\mu\text{M}$ , NCI 11591 inhibited InhA activity 42.8%. It displayed an apparent  $K_i$  of  $59.2 \pm 8.7 \mu\text{M}$ . As shown in Figure 5.6, 111591 followed a non-competitive mechanism of inhibition (*i.e.*, it can bind when the substrate is “not on or on,” meaning it could potentially bind to the holo enzyme, to the InhA:substrate complex, and/or to the InhA:NAD<sup>+</sup>:product complex). To further confirm the inhibition mode, data were fit to both Equation 5.2 and Equation 5.3 for comparison. The  $K_i$  values generated from the non-competitive fit and competitive fit were  $59.2 \pm 8.7 \mu\text{M}$  and  $54.0 \pm 51.0 \mu\text{M}$ , respectively. The much greater error for the competitive fit unambiguously confirmed the inhibition mechanism as non-competitive.

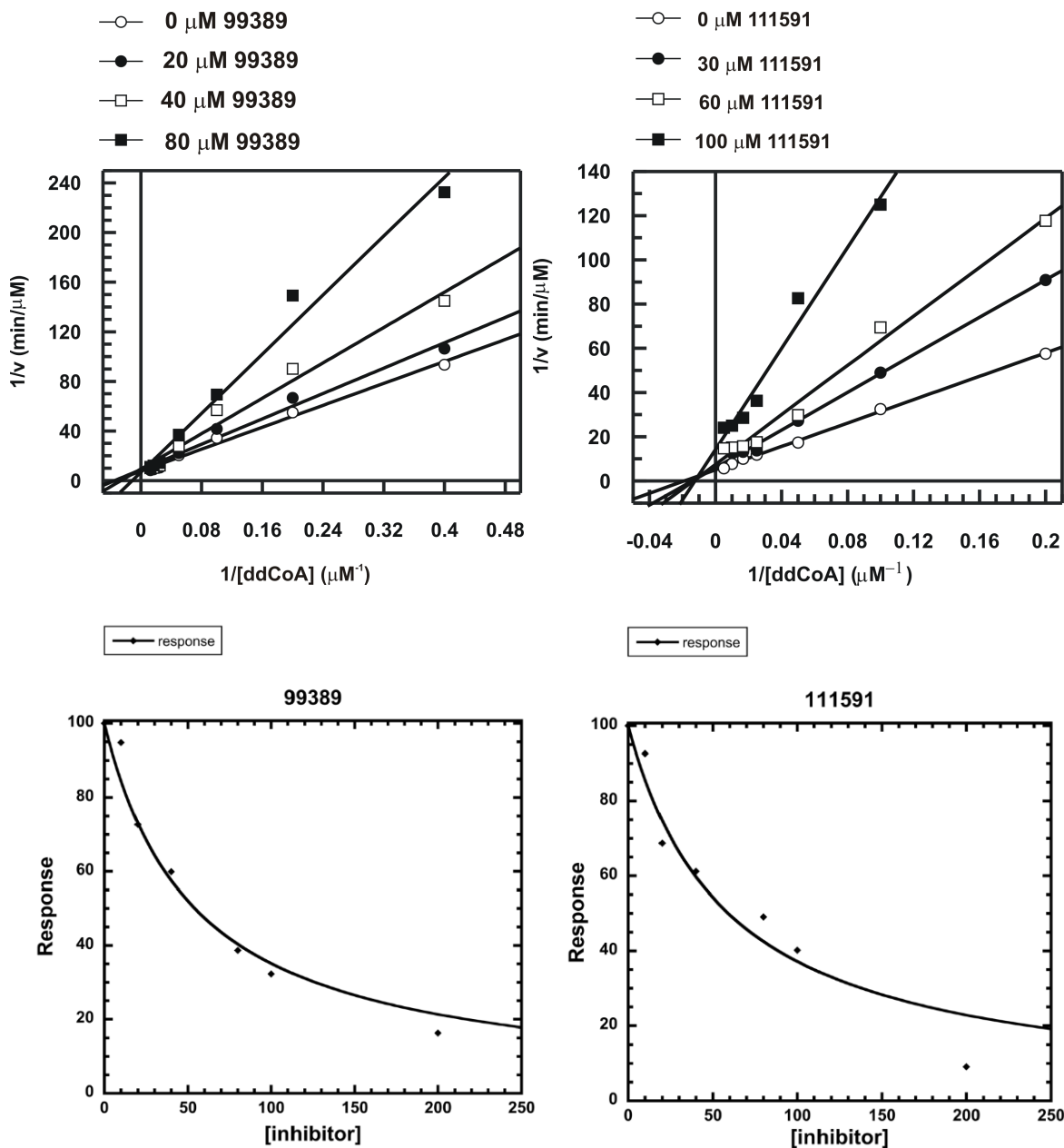


**Figure 5.6 Kinetic data for the two most potent InhA inhibitors**

NCI 99389 is a competitive inhibitor, while 111591 is noncompetitive inhibitor.  $\text{IC}_{50}$  values were measured for the top 2 fragment hits, followed by a detailed mechanistic study to measure the  $K_i$  values. NCI 99389 showed a  $K_i^{\text{app}}$  of  $54.1 \pm 5.4 \mu\text{M}$  and a competitive binding mechanism, indicating that the inhibitor competed with the CoA substrate and bound directly to the enzyme. Conversely, NCI111591 had a  $K_i^{\text{app}}$  of  $59.2 \pm 8.7 \mu\text{M}$  and a non-competitive binding mechanism, suggesting a more complex scenario where the inhibitor could bind to both the holo enzyme and to the substrate-enzyme complex.

### 6 less potent NCI inhibitors

The predicted binding modes for the six less potent new InhA inhibitors discovered are presented in Figure 5.5. They were all predicted to base-stack with the nicotinamide ring of the NAD cofactor and to form a hydrogen bond with the hydroxyl of Tyr158. Five of the six inhibitors (*i.e.*, all except NCI 111590) docked to form both a hydrogen bond and an additional favorable electrostatic interaction with the 2'-hydroxyl of the ribose adjacent to the nicotinamide ring of NAD, but the predicted pose of 111590 only formed a favorable electrostatic interaction with that hydroxyl. 112144 was also predicted to make a hydrogen bond with the carbonyl of Gly96, but it was predicted to display unfavorable electrostatic repulsion with both phosphate groups of the NAD cofactor. The amino and ether oxygen atoms of 111589 were predicted to form both favorable and unfavorable electrostatic interactions, respectively, with the sulfur in the side-chain of Met199, and it displayed an internal hydrogen bond between that amino and ether oxygen. The conserved regions of the scaffold in 111590 and 111588 had docked modes that superimposed, and they formed favorable electrostatic interactions with the sulfur in the side-chain of Met199 and with the hydroxyl of Ser123. If a slight conformational change occurs in the side-chain of Phe149, they could both T-stack with it. Docking of 135809 suggested favorable electrostatic interactions could be formed with the phosphate group adjacent to the ribose of the NAD cofactor, but it formed unfavorable electrostatic repulsion with both the sulfur in the side-chain of Met199 and the carbonyl of the nicotinamide ring of the NAD cofactor. The weaker InhA activity of 135809 compared to the other compounds with the most similar structures to it (Figure 5.3 and Table 5.1) might be due to these unfavorable electrostatic repulsions and perhaps to the less stable / less likely protonation state of the central thiadiazole

ring (*i.e.*, of the different independent models for the different protonation states of this compound that were screened, the model that passed the docking filters had a protonated thiadiazole, but ChemDraw predicts that this compound should be unprotonated at neutral pH). 196166 was the least potent InhA inhibitor, and its docked mode displayed three unfavorable electrostatic repulsions with the phosphate adjacent to the ribose of the NAD cofactor. The terminal pyridine also displayed unfavorable electrostatic repulsion with the sulfur in the side-chain of Met161, but the pyridine that is part of the two fused rings might T-stack with Phe149.

#### Principal Component Analysis (PCA) on the NCI compounds

The 8 inhibitors discovered were compared to a set of 157 previously-characterized InhA inhibitors available in TB Mobile 2 (69, 70). Principal Component Analysis (PCA) showed that these 8 InhA GO FAM inhibitors were generally not part of the main clusters of known InhA inhibitors, but they do have similar chemical properties to them (Figure 5.7). Each inhibitor was also individually compared to all known InhA inhibitors in the TB Mobile data set to obtain sets of pairwise Tanimoto coefficients, which were then averaged. Their average Tanimoto similarities ranged from 0.27 to 0.45 (with 1.0 indicating identical 2D structures) (Table 5.3). The two most promising new scaffolds discovered, NCI 99389 and 111591, had a maximum Tanimoto similarity to a known InhA inhibitor of 0.413 and 0.463, with a minimum similarity of 0.146 and 0.131, and average similarity values of 0.309 and 0.368, respectively (Table 5.3). These distinct cheminformatic analyses support these 8 GO FAM compounds as novel InhA inhibitors based on current literature data.

Table 5.3 Tanimoto Similarity to 154 Known InhA Inhibitors in the TB Mobile data set

| Compound IDs                  | Average Similarity | Maximum Similarity | Minimum Similarity |
|-------------------------------|--------------------|--------------------|--------------------|
| 1) NCI 99389<br>ZINC01654204  | 0.3087             | 0.4130             | 0.1458             |
| 2) NCI 111591<br>ZINC01703321 | 0.3681             | 0.4634             | 0.1311             |
| 3) NCI 112144<br>ZINC04878446 | 0.4503             | 0.5738             | 0.15               |
| 4) NCI 111589<br>ZINC04994329 | 0.4307             | 0.5732             | 0.1642             |
| 5) NCI 111590<br>ZINC00129134 | 0.4296             | 0.5522             | 0.1935             |
| 6) NCI 111588<br>ZINC0135077  | 0.4542             | 0.5897             | 0.1406             |
| 7) NCI 135809<br>ZINC01722139 | 0.2731             | 0.4366             | 0.1061             |
| 8) NCI 196166<br>ZINC01734860 | 0.3551             | 0.4833             | 0.1724             |

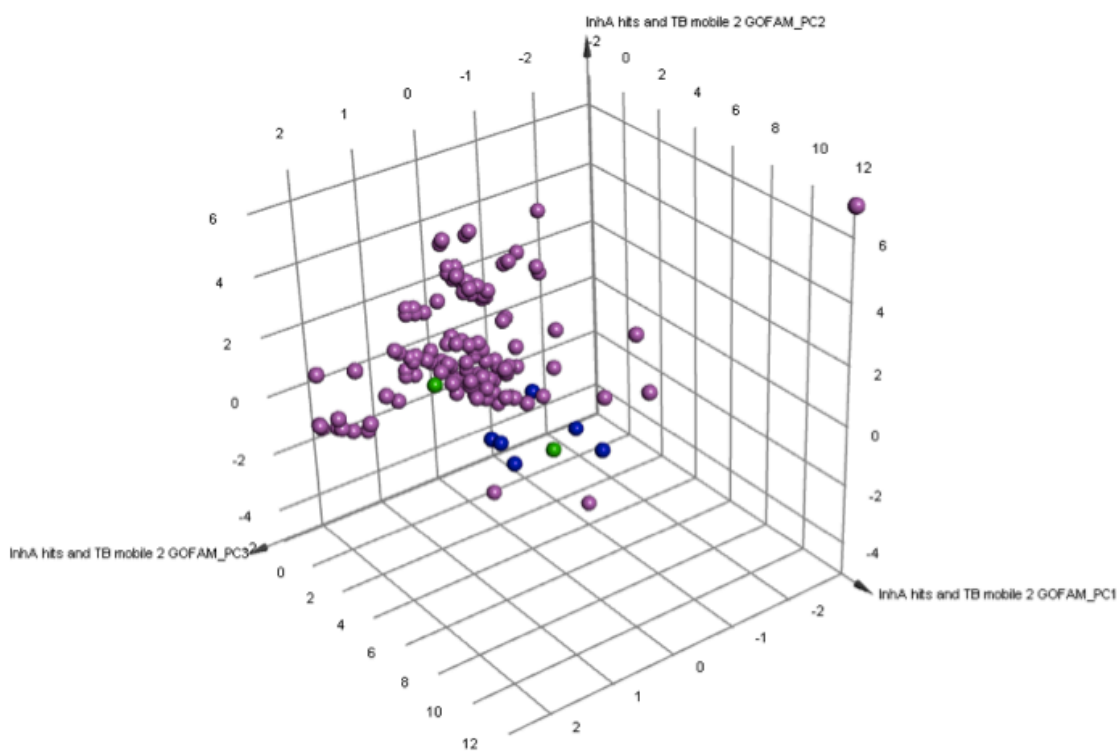


**Figure 5.7 Comparison of the chemical space of the new InhA inhibitors to known InhA inhibitors**

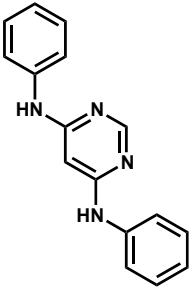
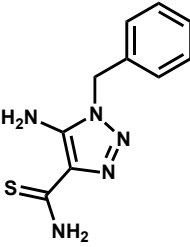
A Principal Component Analysis (PCA) was performed on the combination of the 157 known InhA inhibitors in the TB Mobile 2 data set and the 8 novel InhA inhibitors discovered. Three PCs explain 84.8% of the variance observed. The 157 InhA inhibitors in the TB Mobile 2 data set are displayed in magenta. The two most potent new InhA inhibitors discovered are depicted in green, and the other six novel InhA inhibitors identified are in blue. A red circle highlights the location of NCI 111591. The PCA indicates that the 8 new InhA inhibitors have similar chemical properties to known InhA inhibitors, but they are generally not within the main clusters of these previously characterized InhA inhibitors.

### Whole-cell evaluation on the NCI compounds

The top two fragment hits were then studied with (a) whole-cell *in vitro* *M. tb* growth experiments, using both the wild type strain H37Rv and the *inhA*-over-expressing strain mc<sup>2</sup>4914 (10) and with (b) Vero cell cytotoxicity experiments (Table 5.4). Unfortunately, the top InhA inhibitor discovered, 99389, displayed an MIC<sub>90</sub> of 500 μM against wild type *M. tb*. The MIC > 500 μM it exhibited against the *inhA*-overexpressor strain of *M. tb* suggests that InhA might be the primary target against whole-cell *M. tb*. However, this compound lacked sufficient efficacy against *M. tb* and displayed considerable cytotoxicity with Vero cells, with a CC<sub>50</sub> < 3.0 μM. As expected, the positive control INH displayed almost a 10-fold decrease in potency against the *inhA* overexpressor: MIC<sub>90</sub> of 0.4 μM (0.05 μg/mL) against wild type *M. tb* and 3 μM (0.4 μg/mL) against strain mc<sup>2</sup>4914. The second most promising InhA inhibitor discovered, NCI 111591, displayed an MIC<sub>90</sub> of 125 μM against both wild type *M. tb* and the *inhA*-overexpressing strain of *M. tb*. Although 111591 was 4-fold more potent against whole-cell *M. tb*, the lack of a shift in its potency against the *inhA* overexpressor indicates that InhA is likely not its primary target in *M. tb*. In the PCA that compared the new inhibitors to the 157 known InhA inhibitors in TB Mobile 2 (69, 70), 111591 was further from the main clusters of known InhA inhibitors, while 99389 was at the edge of the central cluster (Figure 5.7). NCI 111591 was less toxic against Vero cells, with a CC<sub>50</sub> of 26 μM; however, it still displayed an insufficient selectivity index of 0.21.



Table 5.4 Summary of Antitubercular Efficacy and Mammalian Cell Cytotoxicity

| NCI ID | Structure   | Vero cell<br>cytotoxicity:<br>CC <sub>50</sub> (μM) | MIC <sub>90</sub> vs <i>Mtb</i><br>(μM) |  |
|--------|---|---|---|--|
|        |   |   | H37Rv<br>wild type                      | mc <sup>2</sup> 4914<br><i>inhA</i><br>overexpressor |
| 99389  |    | < 3.0   | 500                                     | > 500  |
| 111591 |  | 26  | 125                                     | 125  |

Although several InhA inhibitors with nM potency have been reported previously (11, 15, 81, 117), novel chemotypes that inhibit InhA are needed for the following reasons: (a) the presence of the phenol group in triclosan derivatives (11, 81, 117) poses a metabolic liability for *in vivo* applications (118-120), (b) other advanced InhA leads have fared poorly when administered in mouse models of TB (15) and (c) drug-resistant strains of *M. tb* (*i.e.*, MDR-TB, XDR-TB, and TDR-TB) continue to evolve and spread throughout the world (1-7). In addition,

since 28% to 60% of TB cases are INH-resistant (1, 2, 13), and InhA is one of the most validated targets for treating TB, new chemotypes that inhibit InhA without displaying cross-resistance with INH could eventually seed the development of urgently needed new drug combinations for the treatment of active and latent TB infections.

The novel fragment hits we discovered against InhA displayed low  $\mu\text{M}$  potency, with  $K_i$  values of 54.1 and 59.2  $\mu\text{M}$  for the two most promising new scaffolds. Using stringent criteria to define a hit (a  $K_i$  value  $< 100 \mu\text{M}$  for a fragment-sized compound), this VS had a 12.5% hit rate. Thus, from a computational chemistry perspective, this VS was a success, since the median hit rate from hundreds of published VS is  $\sim 13\%$  (36). More importantly, these novel InhA inhibitors are all predicted to base stack with the NAD cofactor (instead of forming a covalent adduct with it). Our InhA inhibition assays demonstrated that these novel inhibitors do not require prior activation by *M. tb* KatG, which means that they should not be susceptible to the main mechanism of INH resistance found in clinical settings. In addition, the novel inhibitors discovered all lack the presence of the phenol group that poses a metabolic liability for triclosan derivatives. Consequently, the two most promising new chemotypes discovered might eventually enable the development of new InhA inhibitors that are effective against MDR-TB, XDR-TB, and TDR-TB. Since it is slightly weaker than NCI 99389, we consider NCI 11591 to be the second most promising new scaffold against InhA discovered in the present study. However, given its superior MIC against *Mtb* and its lower toxicity against Vero cells, NCI 11591 seems to be a more promising scaffold versus whole-cell *Mtb*.

Although these new chemotypes discovered against InhA are somewhat weak inhibitors (*i.e.*, they are “fragment hits” and not drug-sized “leads”), they were identified from a diverse, commercial library using freely available compounds. In addition, they are both fragment-sized compounds (*i.e.*,  $M_w < 300$  g/mol) (109). Fragment-based hit discovery was not our initial goal, but it was the ultimate result of this pilot study. Unlike traditional high-throughput screens, fragment-based drug discovery is founded on screening a smaller number of smaller-sized compounds, to advance the goal of discovering novel fragment hits with  $K_i$  or  $K_d$  values in the high  $\mu\text{M}$  to low mM range (110). Those initial novel fragments can then be optimized using structure-based and medicinal chemistry strategies to develop potent leads, some of which have advanced to become a clinical candidate (109) or an FDA approved drug (121). In the pioneering “SAR by NMR” study, the novel fragment hits discovered displayed  $K_d$  values of 100  $\mu\text{M}$  to 9.5 mM (115). Although a few studies have discovered fragment hits with potencies as great as 24  $\mu\text{M}$  (122), 49  $\mu\text{M}$  (122), 60  $\mu\text{M}$  (122) or 80  $\mu\text{M}$  (123). Most fragment hits have potencies (*i.e.*,  $K_i$  or  $K_d$  values) in the 100 to 300  $\mu\text{M}$  range, and many are in the low mM (82, 109-111, 113, 114, 122-124). Thus, although our two fragment hits have a very weak potency when compared to well-optimized lead compounds (such as PT70), our hits have not yet been optimized against the InhA target or against whole-cell *Mtb*, and they are actually more potent than most novel fragment hits.

Our most promising new fragment hit against InhA has a fairly simple structure and should be amenable to structure-based, medicinal chemistry-guided optimization. Due to their lack of whole-cell efficacy against *M. tb* and their inadequate selectivity indexes for Vero cell cytotoxicity, both of our top fragment hits will need considerable optimization before advancing

to the lead compound stage. Several previous studies performed structure-activity-relationship (SAR) experiments to guide the development of more potent InhA inhibitors (81, 117, 125-127). Those studies suggest that our most promising new fragment hit could perhaps be developed into a more potent InhA inhibitor by appending appropriate functionality off one or both of the phenyl rings to make additional energetically favorable interactions with residues such as Gly96, Phe97, Phe149, Met155, Pro156, Ala157, Pro193, Ala198, Met199, Ile202, Val203, Leu207, Gln214, Ile215, Leu218, or the NAD cofactor.

The similarity in the substructures that are predicted to base stack with the NAD cofactor (Figure 5.3) suggests that click chemistry, especially target-guided click chemistry (128-131), might be a useful approach to aid the discovery and development of novel InhA inhibitors. Target-guided click chemistry is based on the principle that the azide and alkyne-containing fragments will interact with each other and click together (to form the triazole ring) only if those fragments are correctly positioned and have high affinity and long residence times in the target enzyme (128-131). Since inhibitors that display long residence times with pathogenic targets can have more favorable properties *in vivo* (67, 75, 116, 132, 133), and since our computational results indicate that the triazole ring is predicted to form key base stacking and hydrogen bonding interactions with InhA (instead of just serving as a linker), we suggest that *in situ* click chemistry should be investigated in future studies against InhA.

## Discovery of 4-hydroxy-2-pyridones using microbiological profiling

### Identification of 4-hydroxy-2-pyridones and microbiological profiling

A whole-cell high-throughput screen of the nearly 2.3 million Novartis compound collection against *M. tb* H37Ra, resulted in 20,000 hits with activity > 50% inhibition at 12.5  $\mu\text{M}$  concentration. Promiscuous pan-active compounds (134), scaffolds of known anti-TB compounds, cytotoxic compounds against mammalian cells (Huh 7 or HepG2), compounds containing undesirable functional groups and compounds with  $M_w > 500$ ,  $\text{cLogP} < 1$  or  $> 4$  were deprioritized, resulting in one of the hits NITD-529, a novel anti-TB compound (Figure 5.8). NITD-529, 4-hydroxy-6-isobutyl-3-phenylpyridin-2(1H)-one, is a small polar molecule with moderate activity against *M. tb* H37Rv ( $\text{MIC}_{50}$  1.5  $\mu\text{M}$ ) and good solubility. Structure-activity-relationship studies with several 4-hydroxy-2-pyridone analogues revealed the importance of the pyridine core, 4-hydroxy group and R6 lipophilic group (Figure 5.8) for *M. tb* activity which led to the identification of NITD-564 and NITD 916 (Figure 5.8), a dimethylcyclohexyl derivative at the R6 position, and 30-fold more potent than isoniazid ( $\text{MIC}_{50}$  0.33  $\mu\text{M}$ ) and PA-824 (Structure shown in Chapter 1) ( $\text{MIC}_{50}$  0.4  $\mu\text{M}$ ) (135), and comparable activity to bedaquiline (Structure shown in Chapter 1) ( $\text{MIC}_{50}$  50 nM).

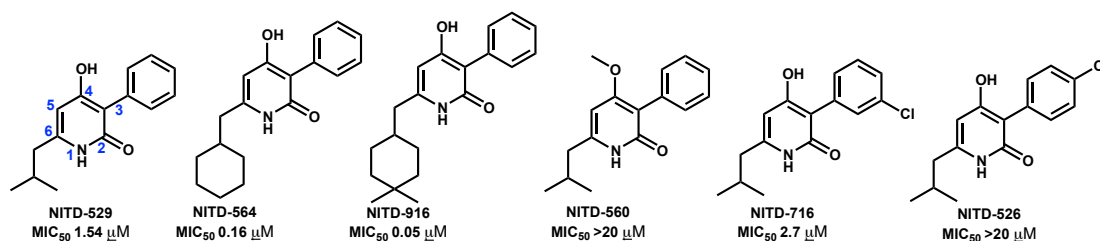


Figure 5.8 Chemical structures and  $\text{MIC}_{50}$  of 4-hydroxy-2-pyridone analogs

4-Hydroxy-2-pyridones were also active against six different clinical MDR-TB isolates that are distributed into five prominent clusters representing global populations of *M. tb* strains (136). The minimum concentration required to inhibit 99% growth of the diverse drug-resistant clinical isolates (MDR 1 to 6) by NITD-529, NITD-564 and NITD-916 was in a similar range to that of wild-type *M. tb* H37Rv (Table 5.5). The MIC activity of NITD-916 against the MDR-*M. tb* strains ranged from 0.04 to 0.16  $\mu$ M, demonstrating the potential of 4-hydroxy-2-pyridones for use against MDR-TB in the clinic.

#### Identification and validation of the molecular target

In order to identify the molecular target and elucidate the genetic basis of action of 4-hydroxy-2-pyridones, whole-genome sequencing was performed (WGS) on three of the *M. tb* mutant strains that were spontaneously resistant to NITD-529. WGS results revealed two independent single-nucleotide polymorphisms in the *InhA* gene encoding the NADH-dependent enoyl-ACP reductase compared to the parental strain *Mtb* H37Rv (Table 5.6). In the 529-B2 mutant, a missense mutation encoding S94A in *InhA* was observed, while 529-S1 and 529-S3 mutants shared a common D148G mutation in *InhA*. In addition, sequencing of *InhA* in the remaining *M. tb* mutants revealed more missense mutations i.e., G96A, D148E, M161I, M161A and T17A (Table 5.6). To genetically validate *InhA* as the molecular target of NITD-916, we over-expressed wild-type or mutated copies of *InhA* under the control of the *hsp60* promoter on a non-integrative plasmid pMV262. Over expression of mutated copies of *InhA* (D148G, D148E or S94A) in wild-type *M. tb* H37Rv resulted in > 10 fold shift in MIC, while over-expression of wild-type *InhA* resulted in a marginal 1.7 – 2.2-fold shift in MIC for both pyridines and isoniazid (Table 5.6). Thus resistance-conferring mutations seem to exert a dominant effect over wild-

type. None of the mutations affected the MIC for streptomycin. Together, these data suggest that a mutation in *InhA* is responsible for the resistance to 4-hydroxy-2-pyridones.

Table 5.5 Activity of 4-hydroxy-2-pyridone analogues against different drug resistance TB clinical isolates

| Strains                               | Resistance       | Genotype  | MIC <sub>99</sub> (μM) |                  |                  |          |          |          |          |
|---------------------------------------|------------------|---|------------------------|------------------|------------------|----------|----------|----------|----------|
|                                       |                  |   | NIT<br>D-<br>529       | NIT<br>D-<br>564 | NIT<br>D-<br>916 | M        | R        | I        | S        |
| MDR1                                  | SIR              | -   | 2.50                   | 0.16             | 0.04             | 0.3      | >5       | >20      | >5       |
| MDR2                                  | SIR              | -   | 2.50                   | 0.31             | 0.16             | 0.1<br>6 | >5       | 10       | >5       |
| MDR3                                  | SIRM PZA         | <i>rpoB</i> , (S531L)<br><i>katG</i> , (S315T)<br><i>rpsL</i> , (43AGC)<br><i>pncA</i> , (11 ups,<br>A>G) | 3.13                   | 0.16             | 0.08             | >5       | >5       | >20      | >5       |
| MDR4                                  | SIR PZA          | <i>rpoB</i> (S531L)<br><i>katG</i> (S315T)<br><i>pncA</i> (G132R)   | 2.50                   | 0.31             | 0.04             | 0.1<br>6 | >5       | >20      | >5       |
| MDR5                                  | SI               | -   | 2.50                   | 0.16             | 0.08             | 0.3<br>1 | 0.0<br>2 | >20      | 2.5      |
| MDR6                                  | SIR PZA          | <i>rpoB</i> (S531L)<br><i>katG</i> (S315T)<br><i>pnk</i> ΔCCA(P69)  | 2.50                   | 0.31             | 0.16             | 0.1<br>6 | >5       | >20      | >5       |
| MDR isolate with <i>InhA</i> mutation | IR               | <i>InhA</i> (I194T)   | 20                     | 2.5              | 1.25             |          |          | >20      | 0.6<br>3 |
| H37Rv                                 | None (wild-type) | -   | 2.50                   | 0.31             | 0.08             | 0.1<br>6 | 0.0<br>2 | 0.6<br>2 | 0.<br>31 |

Notes: S: Streptomycin; I: Isoniazid; R: Rifampicin; PZA: pyrazinamide; M: Moxifloxacin (Structures shown in Figure 1.6 in Chapter 1)

### *In vitro* inhibition and biophysical interaction of 4-hydroxy-2-pyridones with InhA

Enzyme-inhibition studies were performed to confirm that the 4-hydroxy-2-pyridones directly inhibit InhA. In these experiments, NITD-529 (MIC 1.54  $\mu\text{M}$ ) and NITD-564 (MIC 0.16  $\mu\text{M}$ ) inhibited InhA activity with an  $\text{IC}_{50}$  of  $9.60 \pm 0.72$   $\mu\text{M}$  and  $0.59 \pm 0.05$   $\mu\text{M}$ , respectively (Table 5.7). Though there was a 3-fold increase in cellular potency when comparing NITD-916 with NITD-564, no shift in the enzyme  $\text{IC}_{50}$  is observed, potentially due to the difference in cell permeability as NITD-916 has more than a log unit higher logP than NITD-564. The 4-methoxy cell-inactive analogue (NITD-560 MIC > 20  $\mu\text{M}$ ) is also inactive with the InhA enzyme (Figure 5.8 and Table 5.7). Similarly, a para-chloro substituted-analogue on the R3 position (NITD-520 MIC > 20  $\mu\text{M}$ ) is also inactive against the InhA enzyme unlike a meta-chloro substitution (NITD-716) (Table 5.7).

Overall, within this limited set of compounds, InhA inhibition by the 4-hydroxy-2-pyridones correlated with their *M. tb* MIC values. *In vitro* InhA enzyme  $\text{IC}_{50}$ s of 4-hydroxy-2-pyridone analogues are in general 4-10 fold higher than *M. tb* cellular activity. The difference in enzyme and cellular  $\text{IC}_{50}$  could be attributed to intracellular accumulation, differential sensitivity of InhA between *in vitro* and *in vivo* conditions and also potential direct or indirect effects including secondary molecular targets of 4-hydroxy-2-pyridones inside the cells.



Table 5.6 cross-resistance and whole genome sequencing analysis of 4-hydroxy-2-pyridone resistance mutants of *M. tb*

| Strains                               | InhA genotype           | Catalase phenotype | Compound MIC <sub>50</sub> (μM) |          |          |           |             |              |
|---------------------------------------|-------------------------|--------------------|---------------------------------|----------|----------|-----------|-------------|--------------|
|                                       |                         |                    | NITD-529                        | NITD-564 | NITD-916 | Isoniazid | ethionamide | Streptomycin |
| H37Rv<br>WT                           | WT                      | +                  | 1.54                            | 0.16     | 0.05     | 0.25      | 1.66        | 0.08         |
| 529-B2                                | TCG to<br>GCG<br>S94A   | +                  | >40                             | 4.04     | 0.78     | 0.86      | 9.74        | 0.06         |
| 529-S3                                | GAC to<br>GGC<br>D148G  | +                  | >40                             | 1.73     | 0.38     | 0.15      | -           | 0.08         |
| 529-B4                                | GGG to<br>GTG<br>G96V   | +                  | >40                             | 14.60    | >5.0     | 0.09      | 1.32        | 0.10         |
| 529-B6                                | -                       | +                  | >40                             | >40      | >5.0     | 0.11      | 1.41        | 0.09         |
| 529-B8                                | GAC to<br>GAA<br>D148E  | +                  | >40                             | >40      | >5.0     | 0.31      | 1.91        | 0.08         |
| H37Rv::<br>pMV262<br>-InhA            | InhA::<br>InhA          | nd                 | 2.59                            | -        | 0.11     | 0.51      | -           | 0.074        |
| H37Rv::<br>pMV262<br>-InhA::<br>D148G | InhA::<br>InhA<br>D148G | nd                 | >60                             | -        | 3.08     | -         | -           | 0.084        |
| H37Rv::<br>pMV262<br>-InhA::<br>D148E | InhA::<br>InhA<br>D148E | nd                 | >60                             | -        | >6.6     | -         | -           | 0.079        |
| H37Rv::<br>pMV262<br>-InhA::<br>S94A  | InhA::<br>InhA<br>S94A  | nd                 | 28.71                           | -        | 2.40     | -         | -           | 0.075        |

Isothermal titration calorimetry (ITC) revealed that NITD-529 binds to InhA only in the presence of NADH and no binding was observed in the presence of NAD or without any cofactor (Figure 5.9). NITD-529 and NITD-564 bind to the InhA-NADH complex with  $K_d$  values of 25 and 0.56  $\mu\text{M}$ , respectively (Figure 5.9, Table 5.7). Compound binding with NADH fits well with one binding site per monomer. Thermofluor experiment also confirmed that 4-hydroxy-2-pyridones preferentially bind to the InhA-NADH complex similar to PT166 (137), in contrast to PT70 (138) (Chapter 3), a diphenyl ether derivative which forms a stable ternary complex with  $\text{NAD}^+$  (Table 5.7). NITD-529 binding to the InhA-NADH complex lead to a modest increase ( $\Delta T_m + 4.4$  °C) in thermal stability compared to binding to the InhA- $\text{NAD}^+$  complex, whereas the thermal stability of the diphenyl ether was higher with  $\text{NAD}^+$  ( $\Delta T_m -6.6$  °C) (Table 5.7). Similar NADH-dependent binding has recently been shown for methyl-thiazoles (33). Collectively, the enzymology and biophysical-binding data have unambiguously demonstrated that 4-hydroxy-2-pyridones are direct InhA inhibitors and that they preferentially bind to the InhA-NADH complex.

#### Crystal Structure of cofactor-bound InhA with NITD-564 and NITD-916

To further understand the molecular interaction of 4-hydroxy-2-pyridones with InhA, co-crystal structures of ternary complexes with NADH-NITD5-64 and NADH-NITD-916 were solved by Novartis at a resolution of 2.9 and 3.2 Å, respectively (Figure 5.10). The ligands NITD-564 and NITD-916 are bound in the same position and orientation (Figure 5.10 A). Consistent with the ITC and thermal-shift data, both NITD-916 and NITD-564 bind to the E-NADH complex (Figure 5.10 B). The co-crystal structure revealed five key interactions of 4-hydroxy-2-pyridones with InhA and the NADH cofactor, namely i) the aromatic pyridone ring of

4-hydroxy-2-pyridones  $\pi$ -stacks against the pyridine ring of the cofactor NADH, ii) the oxygen at the 4-hydroxy group of NITD-916 hydrogen bonds with the 2'-hydroxyl moiety of the nicotinamide ribose sugar and the hydroxyl of Y158 of InhA, a conserved residue of the enoyl-reductase active-site triad; iii) the N- of the pyridine core interacts with the S of M199 (Figure 5.10 B and 5.10 C); iv) the R3 phenyl ring is exposed to a narrow pocket of the enzyme and v) the cyclohexyl or dimethyl cyclohexyl moiety of NITD-564

Table 5.7 Interaction of 4-hydroxy-2-pyridones with InhA

| Compound | <i>M. tb</i><br>MIC <sub>50</sub><br>( $\mu$ M) | InhA<br>IC <sub>50</sub><br>( $\mu$ M) | Thermofluor assay (T <sub>m</sub><br>°C) |                  |                         | ITC (NADH added)          |                         |                         |   |
|----------|---|--|--|------------------|-------------------------|---------------------------|-------------------------|-------------------------|---|
|          |   |  | E-<br>NAD <sup>+</sup><br>-I             | E-<br>NADH<br>-I | $\Delta$ T <sub>m</sub> | K <sub>d</sub> ( $\mu$ M) | $\Delta$ H<br>(cal/mol) | $\Delta$ S<br>(cal/mol) | N |
| NITD-529 | 1.54  | 9.6±0.7                                | 50.3                                     | 54.7             | 4.4                     | 25±7                      | 13100±420<br>2          | -22.9                   | 1 |
| NITD-564 | 0.16  | 0.59±0.0<br>5                          | 56.3                                     | 57.8             | 1.5                     | 0.56±0.0<br>7             | 11440±250               | -9.8                    | 1 |
| NITD-916 | 0.05  | 0.57±0.0<br>4                          | 55                                       | 56.3             | 1.3                     | -                         | -                       | -                       | - |
| NITD-560 | >20   | >20                                    | -  | -                | -                       | -                         | -                       | -                       | - |
| NITD-716 | 2.67  | 4.3±0.5                                | -  | -                | -                       | -                         | -                       | -                       | - |
| NITD-526 | >20   | >20                                    | -  | -                | -                       | -                         | -                       | -                       | - |
| PT70     | 11  | <0.05                                  | 66.7                                     | 60.1             | -6.6                    | -                         | -                       | -                       | - |
| PT166    | 10.5  | <0.05                                  | 52.3                                     | 71.5             | 19.<br>2                | -                         | -                       | -                       | - |

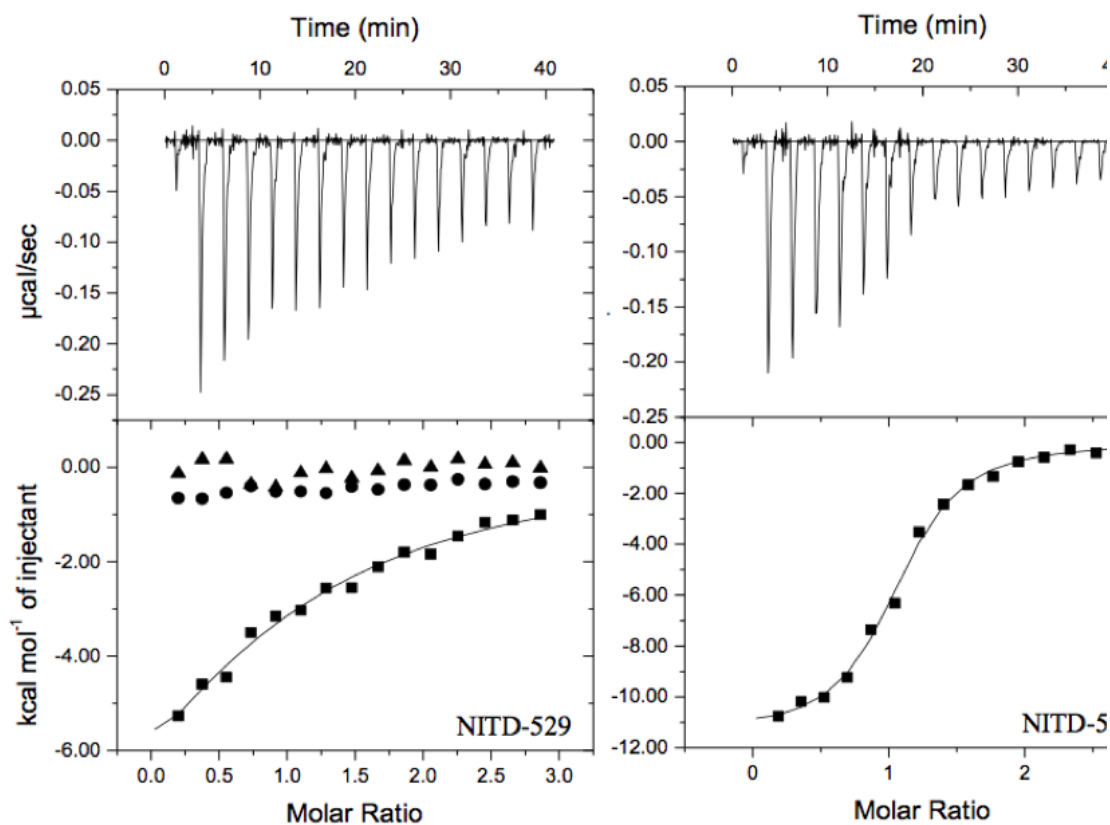


**Figure 5.9 Isothermal titration calorimetry binding of NITD-529 and NITD-564**  
 Binding to apo InhA (triangle), with InhA-NAD<sup>+</sup> complex (circles) and with InhA-NADH complex (squares)

and NITD-916 respectively occupies the large hydrophobic pocket comprising of the side chains of F149, M155, Y158, M199, G192, P193, I215, L218 and W222 (Figure 5.10 B). Consequently, at the R6 position, when the isopropyl group in NITD-529 is replaced by cyclohexyl (NITD-564), it provides a better interaction between the ligand and these hydrophobic side chains, leading to a 10-fold increase in antitubercular potency as well as in the potency against the InhA enzyme (Table 5.7). Replacing the cyclohexyl with the more

hydrophobic dimethyl-cyclohexyl (NITD-916) further enhances *M. tb* activity by 10 fold. NITD-916 binding to InhA leads to ordering of the substrate binding loop starting from residue 196 to 211 (Figure 5.10 A). All five pyridine-resistant mutations mapped in InhA, T17, S94, G06, D148 and M161 were within 6 Å of the NHAD binding site (Figure 5.10 C).

Superimposition of the InhA:NITD-916 structure with the enoyl substrate bound form (139) revealed that NITD-916 partly occupies the fatty acyl-substrate binding pocket and the dimethyl cyclohexyl group forms hydrophobic interactions with the substrate binding loop (Figure 5.10 D). Thus it is likely that the binding of NITD-916 to InhA-NADH complex prevents the enoyl substrate access to its binding site on the enzyme. Overlaying the structure of diphenyl ethers, pyrrolidine carboxamides and methyl-thiazoles (33) (126) (32, 140) along with the C-16 acyl substrate in NITD-916 structure revealed that these inhibitors all occupy the enoyl-substrate binding site (Figure 5.10 D). Recently, the natural product, pyridomycin (Structure shown in Figure 1.11 in Chapter 1) has also been shown to be a direct InhA inhibitor occupying both NADH and enoyl-substrate binding sites (141) (35). The InhA-NITD-916 complex has an open substrate binding loop conformation similar to the enoyl-substrate bound structure (139), unlike PT70 (140), which has a closed conformation (Figure 5.10 E). Thus, the co-crystal structures confirmed the NAD-dependent binding mode of 4-hydroxy-2-pyridones, and showed that these ligands partly occupy the enoyl-substrate binding pocket.

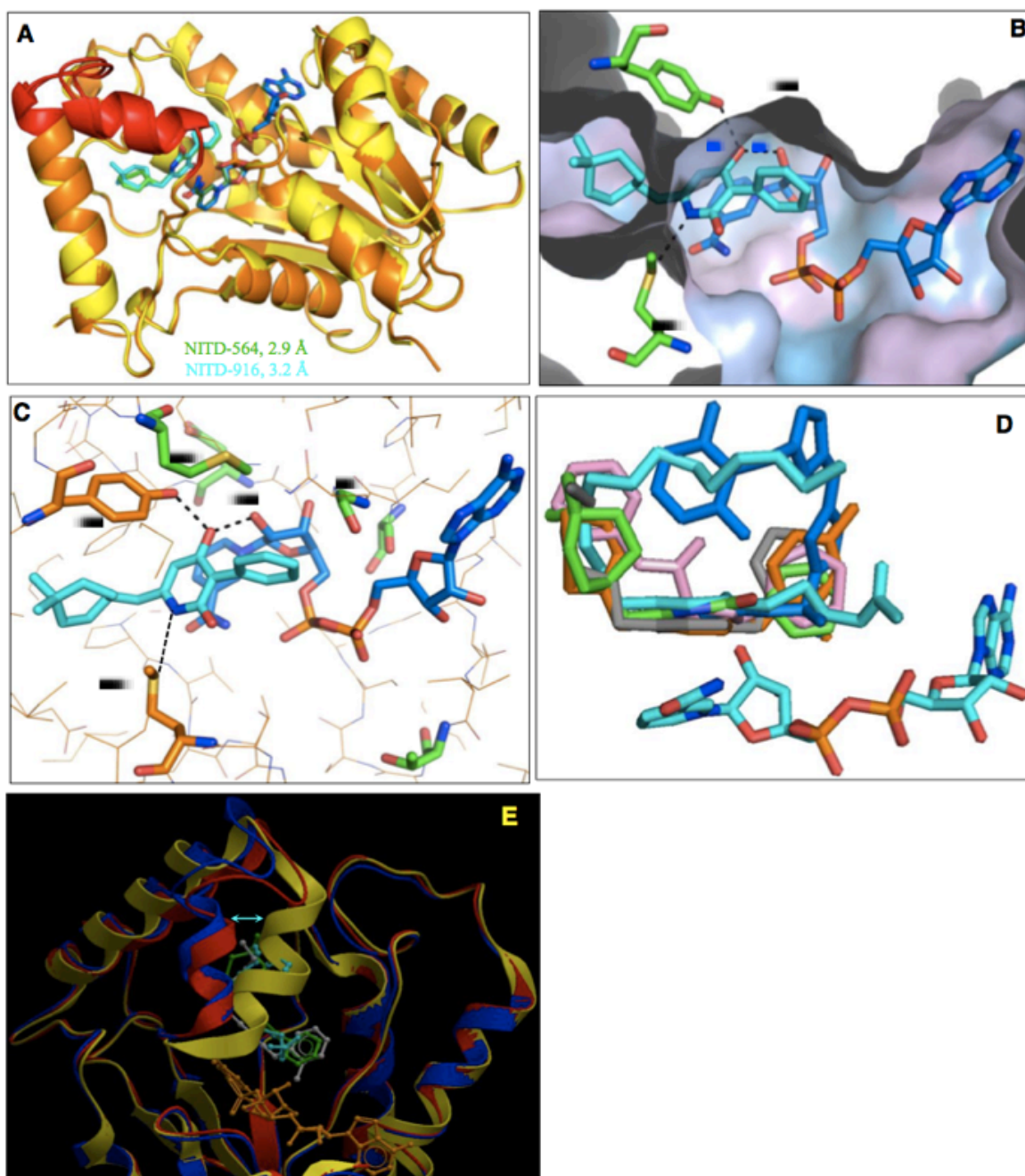


**Figure 5.10 Structural analysis of 2-pyridone binding site in InhA-NADH complex**

A) superimposed crystal structures of InhA-NADH-NITD564 (yellow) and InhA:NADH-NITD 916 (orange), respective 2-pyridone ligands are shown in green and cyan. Substrate binding loop encompassing residues 196 to 211 is shown in red. B) Close-up of NITD-916 (cyan) binding pocket InhA-NADH complex, with protein polar (cyan) and hydrophobic (grey) surfaces are colored. The side chains of Y158 and M199 residues are shown. The distance (in Å) between the ligand with Y158, M199 and NADH is highlighted dotted lines. C) Hydrogen bonding interactions of NITD-916 with critical residues in the active site of InhA. Side chains of amino acid residues responsible for NITD-916 resistance (T17, S94, G96, D148 and M161) are shown. D) The InhA-NITD 916 (green) structure overlaid with the fatty acyl substrate (cyan, 1BVR), along with other direct InhA inhibitors viz., triclosan derivative (orange, 3FNG), alkyl diphenyl ether (grey, 2X23), pyrrolidine carboxamides (Pink, 2H7I) and methyl-thiazoles (blue, 4BQP). E) The InhA-NITD 916 structure (red) overlaid with co-crystal structures of fatty acyl substrate (blue, 1BVR) and alkyl diphenyl ether (yellow, 2X23). Ligands are colored as above. The shift in the conformation of substrate binding loop is shown by an arrow.

## CONCLUSIONS

The Virtual Screen of the NCI library using the InhA-inhibitor structure PDB ID: 2X23 (67) led to the discovery of two promising and novel fragment hits that inhibit InhA activity. This pilot study demonstrated the utility of the (public domain / open access) GO FAM docking data against InhA and of our approach to its analysis. Novel inhibitors of the key TB drug target InhA were discovered in an efficient manner, requiring the experimental assessment of fewer than 20 candidate compounds. These open access GO FAM data against InhA and other targets for treating TB and malaria represent a valuable resource for the drug discovery community.

Utilizing phenotypic screening, identified series of 4-hydroxy-2-pyridone InhA inhibitors were also discovered. The antitubercular activity of this series does not require katG-mediated activation and that INH-resistant MDR/XDR-TB clinical isolates with katG mutations are fully susceptible to NITD-916. These efforts will facilitate further structure-guided rational approaches to identify preclinical candidates.

## Chapter 6 MUT056399 and *p*-Fluoro Diphenyl Ethers: Slow Binding Inhibitors of the Enoyl-ACP Reductase FabI from *Burkholderia pseudomallei*

This chapter is based on part of the work in the following manuscript under preparation:

Carla Neckles, Weixuan Yu, Gopal Reddy Bommineni, Maria Hirschbeck, Jason Cummings, Sandra Eltschkner, Fereidoon Daryaei, Zhuo Zhang, Minah Kim, Caroline Kisker, Richard Slayden, and Peter J. Tonge, “MUT056399 and *p*-Fluoro Diphenyl Ethers: Slow Binding Inhibitors of the Enoyl-ACP Reductase FabI from *Burkholderia pseudomallei*”, *under preparation*, 2015

### INTRODUCTION

#### Melioidosis

Melioidosis is a severe disease in Southeast Asia and Northern Australia. One of the most severe syndromes of this disease is melioidosis septic shock, which is often associated with pneumonia and bacteria that spread to distant sites (1). Melioidosis is caused by the Gram-negative organism *Burkholderia pseudomallei* (*B. pseudomallei*). While *B. pseudomallei* is susceptible to therapeutics such as ceftazidime, chloramphenicol, doxycycline, amoxicillin/clavulanate acid, trimethoprim/sulphamethoxazole, ureidopenicillins, and carbapenems (2, 3) (Figure 6.1), mortality is high because of frequent relapses (4). The ability to treat *B. pseudomallei* infections has become more relevant in recent years because of its



potential use as biological warfare. Currently, the Centers for Disease Control and Prevention (CDC) has claimed *B. pseudomallei* as a Tier 1 Biological Select Agent or Toxin (BSAT) (4, 5), which could be a potential threat to the public health if disseminated in large scale (5, 6). Therefore, novel therapeutics that can be used to treat *B. pseudomallei* infections effectively are urgently needed.

#### Fatty acid biosynthesis as drug target

Inhibition of the fatty acid biosynthesis (FAS) pathway is attractive because this pathway is responsible for the production of the bacterial phospholipid membrane, which is essential for bacterial survival. In addition, the low sequence homology and fundamental structural differences between the mammalian FAS system (FAS-I) and bacterial FAS system (FAS-II) open up the possibility to develop inhibitors with high selectivity and improved safety profile. Therefore the FAS-II pathway is known to be a good antimicrobial target (7, 8). In the FAS-II pathway, the enoyl-ACP reductase (ENR) is thought to be essential for bacterial viability, and also a key regulator of fatty acid biosynthesis (9). Hence, the ENR can be a promising drug target to treat *B. pseudomallei* infections.

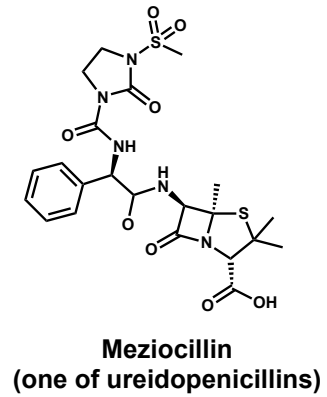
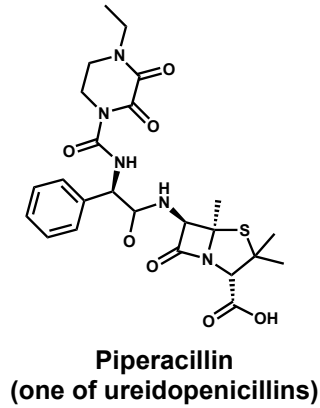
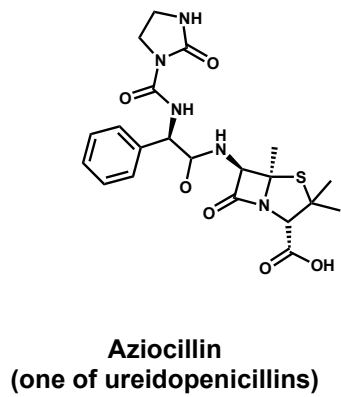
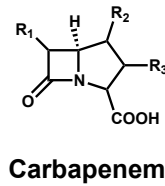
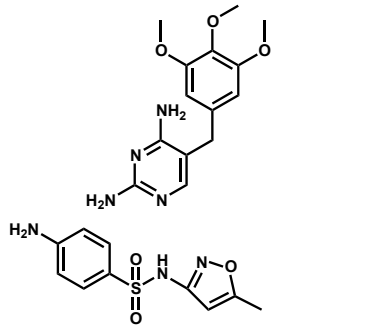
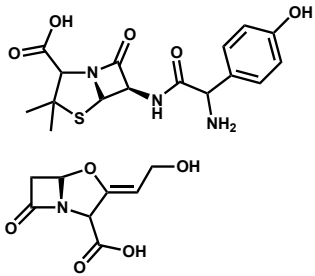
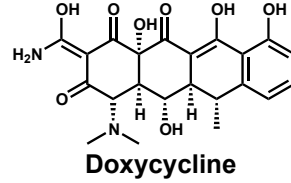
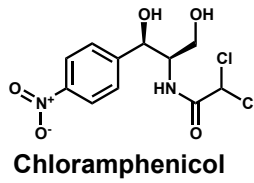
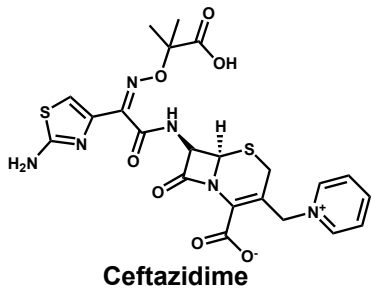


Figure 6.1 Frontline *B. pseudomallei* treatment

### Diversity of the ENR

There are four known isoforms of the ENR, namely FabI, FabK, FabL and FabV. FabK is a flavin-dependent oxidoreductase that utilizes NADH as the reductant to reduce the flavin cofactor FMN while employs FMNH<sub>2</sub> as an intermediate for the reductase (10). FabI, FabL and FabV isoforms belong to the short chain dehydrogenase superfamily, where FabI and FabL share the highly conserved active site motif Y-X<sub>6</sub>-K, while FabV has a slightly bigger active site motif Y-X<sub>8</sub>-K (11, 12). Interestingly, some bacteria species have more than one isoform of the ENR, for example, *Bacillus subtilis* expresses both FabI and FabL, while *Streptococcus pneumoniae* has FabK in addition to FabI (13, 14). The biological reasons for bacteria species to express a combination of different ENR isoforms are currently unknown.

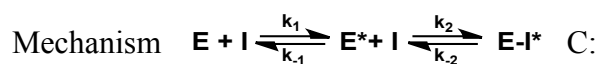
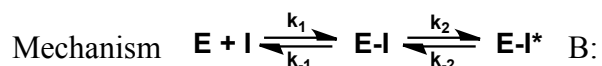
Although both FabI and FabV ENR isoforms coexist in *B. pseudomallei*, studies by Liu *et al* and Cummings *et al* demonstrated that FabI was a suitable drug target and compounds that targeted FabI showed a reduction in MIC values in *B. pseudomallei* efflux pump mutant strains (15, 16). The lead compounds in these studies were diphenyl ethers, analogues of the broad-spectrum inhibitor triclosan (Figure 6.2 A). These diphenyl ethers were shown to be potent inhibitors with binding constants ( $K_i$ ) ranging between 0.5 to 2 nM. Moreover, these compounds demonstrated slow binding inhibition (15).

### Time-dependent inhibition

Traditional drug discovery has focused on thermodynamic parameters, i.e. IC<sub>50</sub>, K<sub>i</sub> or MICs. However there is a growing interest in understanding and incorporating the kinetic aspects of

drug-target interactions into the pipeline, as the rate of breakdown of the enzyme-inhibitor complex is a critical factor under *in vivo* conditions where the inhibitor concentration is not constant (17-19). The kinetic lifetime of an enzyme-inhibitor complex can be described by the dissociation rate constant ( $k_{\text{off}}$ ), residence time ( $1/k_{\text{off}}$ ) or dissociative half-life ( $0.693/k_{\text{off}}$ ) (18, 20, 21). As discussed in Chapter 3, there are three possible mechanisms for a slow binding inhibition: (1) one-step binding mechanism (Scheme 6.1, Mechanism A); (2) an induced-fit, two-step mechanism (Mechanism B); and (3) conformational selection, two-step mechanism (Mechanism C). In the one-step binding mechanism, the inhibitor can bind to the enzyme to form the binary complex (EI), where the association ( $k_{\text{on}}$ ) and dissociation ( $k_{\text{off}}$ ) rate constant of the inhibitor correspond to  $k_1$  and  $k_{-1}$  (20, 22). In the induced-fit, two-step mechanism, the inhibitor originally binds to the enzyme in a conformation that is not optimized for enzyme-inhibitor interactions. Subsequently, the initial enzyme-inhibitor complex (EI) isomerizes to yield the final state (EI\*), in which enzyme-inhibitor interactions are maximized. The binding affinity for the initial enzyme-inhibitor complex is depicted by  $K_d$  ( $k_{-1}/k_1$ ), while the binding affinity of the final enzyme-inhibitor complex is represented by  $K_d^*$ , ( $k_{-1}/(k_1 + k_1k_2/k_{-2})$ ) (20, 22). In the conformational selection, two-step mechanism, the enzyme interconverts between two conformational states (E and E\*) and only one conformation (E\*) is able to bind the inhibitor. The increasing concentration of inhibitor drives the formation of E\*I, leading to a decrease on the population of free E\* state. Comparing to the binding step, the interconversion between the two enzyme states is relatively slower along the reaction coordinate, representing the rate-limiting step. In this mechanism, the binding affinity of the inhibitor for the final complex ( $K_d^*$ ) is depicted by  $k_{-2}/k_2$  (20, 22). Although conformational selection mechanism has been reported in some biological systems (23), the one-step and two-step induced-fit models are more commonly

seen. the most common slow binding mechanisms are the one-step and two-step induced-fit models. Liu *et al* demonstrated that the diphenyl ethers that target BpFabI were slow-onset inhibitors that followed an induced fit, two-step mechanism (15).



Scheme 6.1 Three different types of slow onset inhibition

#### Mutabilis compound – potent FabI drug candidate

Mutabilis FabI inhibitor, MUT37307, (Figure 6.2 B) is a diphenyl ether that targets the FabI ENRs (24). The addition of a *p*-fluoro group in the *Gerusz et al* compound series led to a 2-fold improvement on the IC<sub>50</sub> value against *S. aureus* FabI (25). Further optimization resulted in the second-generation inhibitor MUT056399 (Figure 6.2 C), which is potent antistaphylococcal clinical candidate (25, 26). Translation of MUT056399 inhibitory activity to other FabI enzymes, such as *Bp*FabI, would help determine if this compound can be potentially used as broad-spectrum antimicrobial agent. Further SAR studies will shed light on the significance of the *p*-fluorine introduction in modulating the kinetic and thermodynamic properties of diphenyl ether. Therefore, we performed SAR studies with MUT056399 and other *p*-fluoro diphenyl ether derivatives to address structural features that were favorable for inhibition of *Bp*FabI. Based on our thorough analysis unraveling the transition and ground

states of the enzyme-inhibitor complexes, we have successfully yielded lead compounds with optimized kinetic and thermodynamic properties against bpFabI. Finally, the antibacterial activity of the lead BpFabI inhibitor was evaluated in an acute *B. pseudomallei* mouse model of infection.

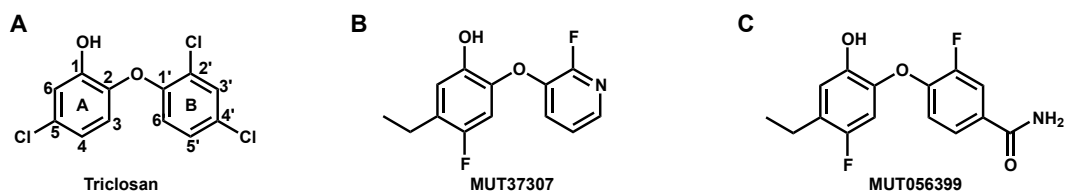


**Figure 6.2 FabI inhibitors**

A) Broad-spectrum inhibitor Triclosan B) MUT37037 C) MUT056399

## MATERIALS AND METHODS

### Materials

Luria broth was purchased from VWR and His-bind Ni<sup>2+</sup>-NTA resin was purchased from Invitrogen. Crotonyl coenzyme A (Cro-CoA) was purchased from Sigma-Aldrich and *trans*-2-octenoic acid was purchased from TCI. MUT056399 was a gift from Anacor Pharmaceuticals. All other chemical reagents were obtained from Fisher Scientific. All curve fitting was performed using KaleidaGraph Version 4.1.

### Expression and purification of *Bp*FabI

The FabI enoyl-ACP reductase from *Burkholderia pseudomallei* was expressed and purified as previously described (15). Briefly, the protein expression was performed using the *E. coli* BL21(DE3) pLysS cells in Luria Broth containing 0.2 mg/mL ampicillin. The cell culture was inoculated at 37 °C and induced at OD<sub>600</sub> of 0.8 with 1 mM isopropyl-1-thio-β-D-galactopyranoside (IPTG). Cells were incubated for an additional 16 h at 25 °C and harvested by centrifugation at 5000 rpm for 20 min at 4 °C. After the cell lysed by sonication, *Bp*FabI was purified using His affinity chromatography. The protein purity was confirmed by 15% SDS-PAGE, which gave an apparent molecular weight of ~28 kDa.

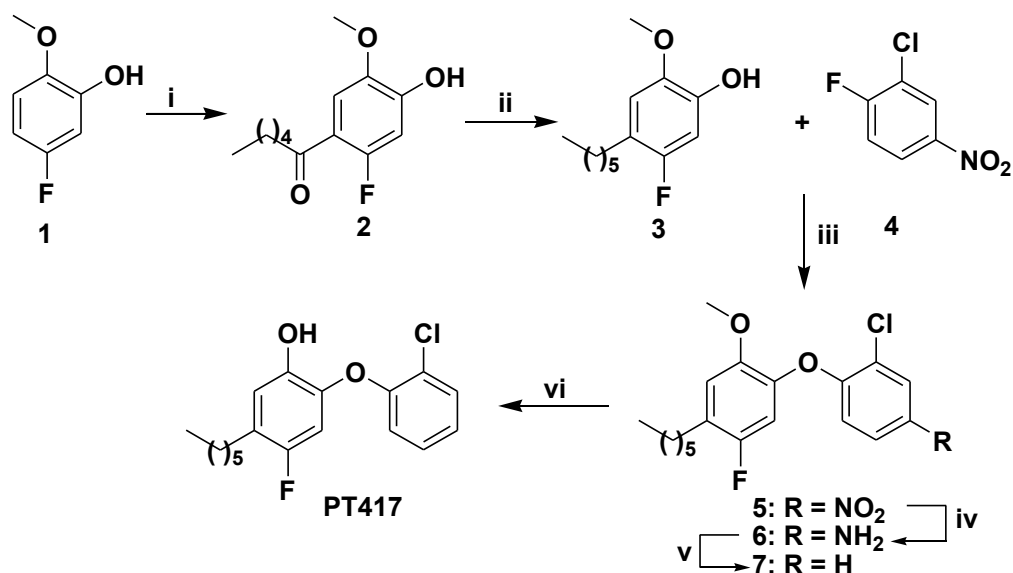
### Synthesis of substrates

The substrate *trans*-2-octenoyl-CoA (Oct-CoA) was synthesized from *trans*-2-octenoic acid, respectively, using the mixed anhydride method (27) as described in Chapter 2 (28).

## Synthesis of diphenyl ethers

Compounds PT01 and PT91 were synthesized as previously published (29). The syntheses of fluoro-diphenyl ethers (PT403, PT404, PT411, PT412 and PT417) were synthesized as recently published (28). Briefly, the Friedel-Crafts acylation of 1 was performed with appropriate acid chlorides in the presence of aluminum chloride under reflux conditions for 3 days to form 2 and 8. Metal catalyzed reduction of 2 and 8 with Zn/AcOH/HCl resulted in compounds 3 and 9 in 60-80% yield, respectively. Coupling of the resulting phenol (3 and 9) with nitrobenzenes (4, 10 and 11), followed by functional group transformations including reduction of nitro group, deamination, and demethylation resulted in the target molecules PT403, PT404, PT411, PT412, and PT417 (Scheme 6.2 and 6.3). PT406, PT407 and PT409 were synthesized by Dr. Fereidoon Daryae and Mr. Zhuo Zhang.

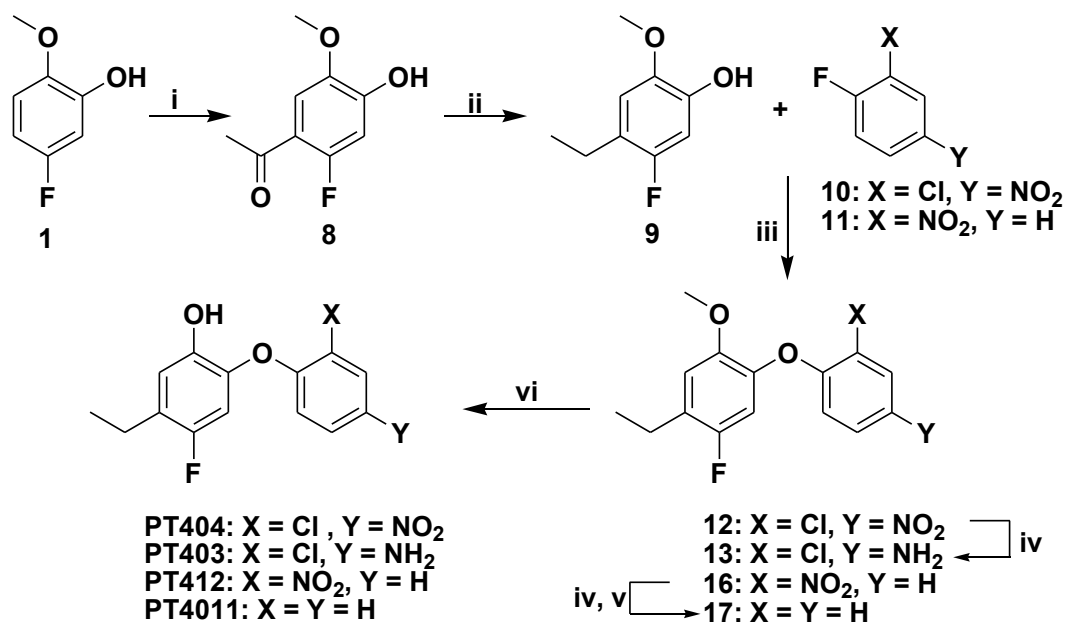




Scheme 6.2 Synthesis of PT417. Reagents and Conditions: i. AlCl<sub>3</sub>, hexanoyl chloride, DCE, reflux, 3 days, 60%; ii. Excess of Zn, conc HCl, AcOH, rt, 8 h, 75%; iii. K<sub>2</sub>CO<sub>3</sub>, DMF, 18-Crown-6, 120 °C, 2 h, 96%; iv. Zn, NH<sub>4</sub>Cl, MeOH/H<sub>2</sub>O, reflux, 1 h; v. t-BuONO<sub>2</sub>, DMF, 65 °C, overnight, 57% (two steps); vi. BBr<sub>3</sub>, DCM, -78 °C to rt, overnight, 98%.

### Thermal shift assay

ThermoFluoro experiments were performed as previously described to determine inhibitor cofactor preference (30). A mixture of 7.4 μM enzyme, 2.5 mM cofactor (NADH or NAD<sup>+</sup>) and 25 μM inhibitor (2% DMSO) was added to a 96-well thin-wall PCR plate (Concord) containing a buffer solution of 30 mM PIPES, 150 mM NaCl and 1.0 mM EDTA at pH 8.0. After 1.5 h incubation at 25 °C, 1 μL of 100 × Sypro Orange (Sigma) was added and the plate was sealed with Microseal 'B' Film (Bio-Rad). The samples were heated from 25 to 90 °C in increments of 0.2 °C/10 s. Bio-Rad CFX Manager was used to process the data.



Scheme 6.3 Synthesis of fluoro-diphenyl ether. Reagents and Conditions: i. AlCl<sub>3</sub>, Acetyl chloride, DCE, reflux, 3 days, 80%; ii. Excess of Zn, conc HCl, AcOH, rt, 8 h, 78%; iii. K<sub>2</sub>CO<sub>3</sub>, DMF, 18-Crown-6, 120 °C, 3 h, 97%; iv. Zn, NH<sub>4</sub>Cl, MeOH/H<sub>2</sub>O, reflux, 1 h; v. t-BuONO<sub>2</sub>, DMF, 65 °C, overnight, 58% (two steps); vi. BBr<sub>3</sub>, DCM, -78 °C to rt, overnight, 98%.

### Preincubation inhibition assay

Dr. Carla Neckles completed the pre-incubation inhibition assay. The preincubation inhibition assays were performed as previously described using a Cary 100 Bio (Varian) spectrophotometer at 25 °C in 30 mM PIPES, 150 mM NaCl and 1.0 mM EDTA at pH 8.0 (31). Assays were performed to determine the apparent inhibition constants for slow binding inhibitors. BpFabI (30 nM) was preincubated with fixed concentrations of DMSO (2%), bovine serum albumin (0.1 mg/mL), NAD<sup>+</sup> (10-200 μM), NADH (250 μM), and inhibitor (0-1000 nM) for 16 h at 4 °C. The reaction mixture was warmed to room temperature, and initiated by the addition of oct-CoA (30 μM). The apparent inhibition constant  $K_i^{app}$ , was determined using

Equation 6.1, where  $v$  and  $v_o$  are the initial velocities in the presence and absence of inhibitor, respectively, and  $[I]$  is the inhibitor concentration.

$$v = \frac{v_o}{1 + \frac{[I]}{K_i^{app}}}$$

Equation 6.1

The  $K_i^{app}$  values obtained at different  $\text{NAD}^+$  concentrations were the fit to Equation 6.2 to describe the binding of the inhibitor to  $\text{E-NAD}^+$  ( $K_1$ ).

$$K_i^{app} = K_1 \left( 1 + \frac{K_{m,NAD}}{[NAD]} \right)$$

Equation 6.2

### Progress curve analysis

Slow-onset inhibition kinetics were monitored at 340 nM on a Cary 100 spectrophotometer (Varian) at 25 °C. The reactions were initiated by the addition of enzyme (2 nM) to a mixture containing glycerol (8% v/v), bovine serum albumin (0.1 mg/mL), DMSO (2% v/v), crot-CoA (750  $\mu\text{M}$ ), NADH (250  $\mu\text{M}$ ),  $\text{NAD}^+$  (200  $\mu\text{M}$ ) and inhibitor (0-2000 nM). All reactions were monitored until the steady-state was reached, indicated by the linearity of the progress curve. Moreover, low enzyme and high substrate concentrations ensured substrate depletion would not significantly affect the reaction rates, such that in the absence of inhibitor the progress curves were linear for over a period of 30 min (30, 32, 33). Data were analyzed as previously described (31, 34), and fit to the Morrison & Walsh integrated rate equation (Equation 6.3), where;  $A_t$  and

$A_0$  are the absorbance at time  $t$  and  $0$ ;  $v_i$  and  $v_s$  are the initial and steady-state velocities; and  $k_{obs}$  is the observed pseudo-first rate order constant for the approach to steady-state.

$$A_t = A_0 - v_s t - (v_i - v_s) * \frac{1 - e^{-k_{obs} t}}{k_{obs}}$$

Equation 6.3

The plot of fractional steady-state velocities as a function of inhibitor concentration was fit to the isotherm equation (Equation 6.4) to determine the  $K_i^{app}$ , such that the values corresponded to the steady-state inhibition  $IC_{50}$ . The parameters  $v_s$ ,  $v_c$ ,  $[I]$  represent the steady-state velocity, the uninhibited reaction velocity, and the inhibitor concentration, respectively.

$$\frac{v_s}{v_c} = \frac{1}{1 + \frac{[I]}{K_i^{app}}}$$

Equation 6.4

The dissociation rate of the inhibitor,  $k_{-1}$ , was calculated from each progress curve using Equation 6.5.

$$k_{-1} = k_{obs} * \frac{v_s}{v_i}$$

Equation 6.5

The association rate of the inhibitor,  $k_1$ , was calculated from each progress curve using Equation 6.6.

$$k_1 = \frac{k_{-1}}{K_i^{app}}$$

Equation 6.6

The inhibition constant,  $K_i$ , was then calculated by Equation 6.7.

$$K_i = \frac{k_{-1}}{k_1}$$

Equation 6.7

### Direct dissociation assay

Using  $^{32}\text{P-NAD}^+$ , the direct dissociation rate,  $k_{\text{off}}$  was determined as previously published (28). A mixture of 15  $\mu\text{M}$  bpFabI, 20  $\mu\text{M}$   $\text{NAD}^+$ ,  $^{32}\text{P-NAD}^+$  (800 Ci/mmol) and 200  $\mu\text{M}$  inhibitor was pre-incubated at 4  $^\circ\text{C}$  overnight in the reaction buffer containing 30 mM PIPES, 150 mM NaCl and 1.0 mM EDTA at pH 8.0. Excess free ligand was removed by gel filtration and the 500  $\mu\text{L}$  reaction mixture was diluted into 60 mL reaction buffer to initiate inhibitor dissociation. 600  $\mu\text{L}$  aliquots from the diluted mixture were withdrawn at different time points, followed by an immediate ultracentrifugation at 13,400 rpm for 90 s. The radioactivity in the flow-through was quantified by LS5801 scintillation counter. Data were fitted to Equation 6.8.

$$C_{(t)} = C_{(0)} + C_{max} * (1 - e^{-k_{off}t})$$

Equation 6.8

### Minimum inhibitory concentration determination

Dr. Jason Cummings from Colorado State University performed the MIC measurement. *B. pseudomallei* 1026b (efflux-proficient) and *B. pseudomallei* Bp400 (1026b  $\Delta[bpeAB-oprB]$   $\Delta[amrAB-oprA]$ ) were grown to an OD600 of  $\sim 0.6$ , frozen at  $-80$   $^\circ\text{C}$  in 10% glycerol and were

used as standard bacterial stocks for these studies. For each evaluation bacteria were prepared fresh by growth from the standard stocks on Luria-Bertani (LB) Agar, Miller (BD) grown at 37 °C for 48-72 h. Bacteria recovered from the LB plates were used to inoculate 10 mL LB Broth. Broth cultures were then incubated for 18 h at 37 °C passed 1:100 and incubated for an additional 6 h at 37 °C. Bacteria were then diluted to a concentration of  $1 \times 10^6$  colony forming units (CFU)/mL in cation-adjusted Mueller-Hinton broth (CAMHB; BD, Franklin Lakes, NJ) and 50  $\mu$ L added to each well for each test plate. For MIC determination, compounds were added to a 96-well plate starting at 256  $\mu$ g/mL in the first column and serially diluted 1:2 to column 12 for a final concentration of 0.125  $\mu$ g/mL in CAMHB. MIC plates were incubated at 37 °C for 18 h at which MIC was determined as the lowest concentration that inhibits visible growth.

#### Evaluation of efficacy in acute *B. pseudomallei* mouse model of infection

Dr. Jason Cummings from Colorado State University completed the *in vivo* efficacy studies. 5-6 week old BALB/c female mice (Charles River Laboratories, Wilmington, MA) were challenged by intranasal infection with 5,000 CFU/mouse *B. pseudomallei* Bp400 ( $\Delta$ [amrAB-oprA]  $\Delta$ [bpeAB-oprB]) (35). Animals were anesthetized with a mixture of 100 mg/kg ketamine and 10 mg/kg xylazine delivered intraperitoneally. The bacteria were diluted to the appropriate concentration in PBS to achieve an inoculum concentration of  $2.5 \times 10^5$  CFU/mL. This inoculum was then delivered dropwise in alternating nostrils. Ceftazidime was formulated in PBS and test compounds in a lipid-based delivery system as previously described (16). Compounds were delivered intraperitoneally, b.i.d. (twice daily) starting at time of infection. The number of viable bacteria in lung and spleen was determined at 60 h post-infection by plating

serial 10-fold dilutions of homogenates on LB agar and incubating for 48 h at 37 °C. Bacterial burden was assessed and difference in group means was determined using a one-way analysis of variance (ANOVA) followed by Tukey's multiple comparisons test. Significance was determined by a P value < 0.05.

## RESULTS AND DISCUSSION

Mutabilis compound, MUT056399, is a slow-onset inhibitor of BpFabI that follows one-step binding mechanism

Mutabilis FabI inhibitor, MUT37307, is a first-generation *p*-fluoro analog of triclosan, and it was found to be specific for organisms that contain only FabI ENRs (24). MUT056399 was later synthesized as a second-generation *p*-fluoro diphenyl ether inhibitor (25, 26). The  $K_i$  and residence time for MUT056399 against *S. aureus* FabI (saFabI) were  $\sim 0.08$  nM and  $\sim 223$  min, respectively (36) and the compound is currently undergoing clinical development to treat *Staph* infections in humans (25, 26). As BpFabI was suggested to be sensitive to diphenyl ethers, in which these compounds were slow-onset inhibitors with  $K_i$  values of 0.5-2 nM (15), we expanded our study on MUT056399 to investigate the potentiality of broad-spectrum inhibition on bpFabI. As suggested in Table 6.1, the apparent binding affinity ( $K_i^{\text{app}}$ ) and residence time of MUT056399 for BpFabI were  $209 \pm 28$  nM and  $35 \pm 8$  min, respectively. This compound exhibited a weaker binding affinity and shorter residence time for bpFabI compared to *S. aureus* FabI. This is expected as the compound is optimized for the inhibition on saFabI. Comparing to the uninhibited progress curves, the initial velocity ( $v_i$ ) under different inhibitor concentrations remained unchanged (data not shown). In addition, a plot of pseudo-first order rate constant ( $k_{\text{obs}}$ ) as a function of inhibitor concentration revealed a linear fit for this compound (Figure 6.3). These observations are characteristic of a simple one-step binding mechanism and it unambiguously rules out the possibility of a conformational selection mechanism. In addition, these trends were consistent for all tested compounds in this study. Therefore, the data suggest *p*-fluoro diphenyl ethers bind to BpFabI via one-step binding mechanism.



It is important to note that Liu *et al* demonstrated slow-onset diphenyl ethers target BpFabI through an induced-fit, two-step model (15). However, a special case induced-fit, two-step mechanism is kinetically indistinguishable from a one-step binding mechanism. In such special case of the induced-fit model, the energy level of the initial complex EI is much higher than the final complex EI\*. Under this circumstance, initial inhibition cannot be detected at low inhibitor concentrations while steady-state velocity can be affected. It is not unusual for slow-onset inhibitors to follow a special case induced-fit model with FabI ENRs, as suggested in the saFabI system (30). It is possible that bpFabI presents a similar scenario, yet unfortunately this factor is not kinetically distinguishable in our system. According to the data on MUT056399, further SAR studies were then conducted to understand kinetic and thermodynamic properties of *p*-fluorine introduction and how this modulated binding to BpFabI.

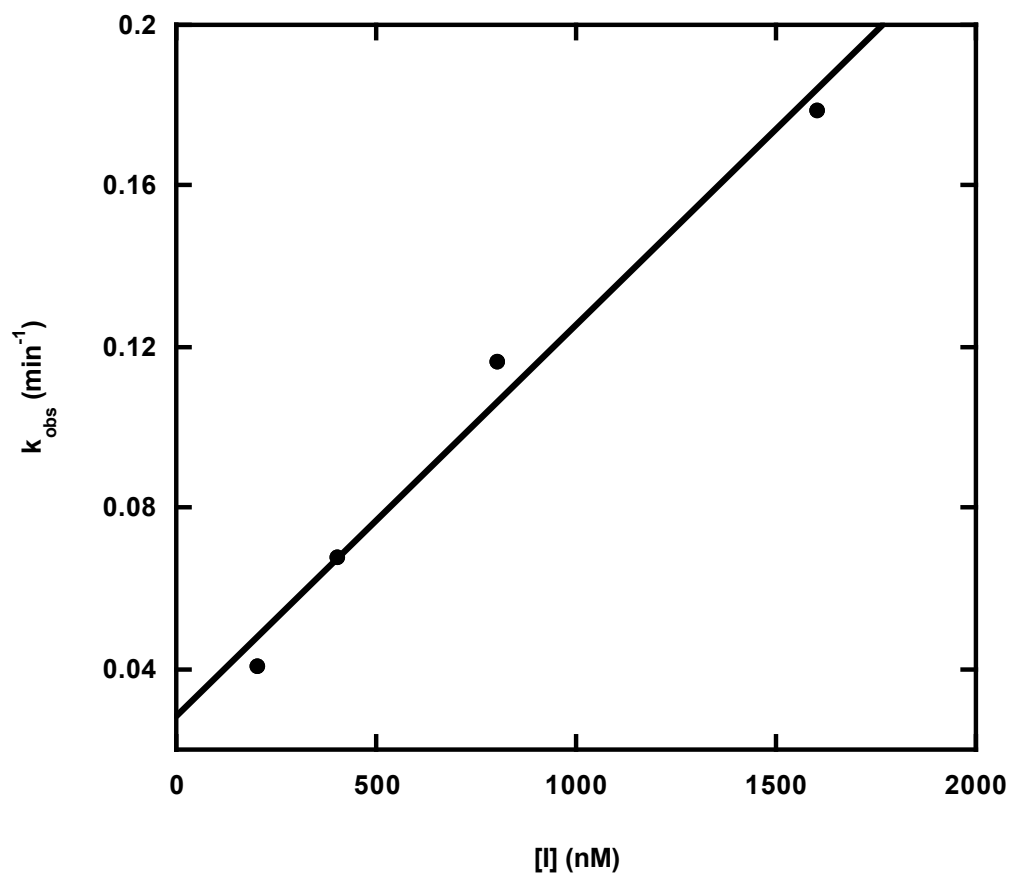


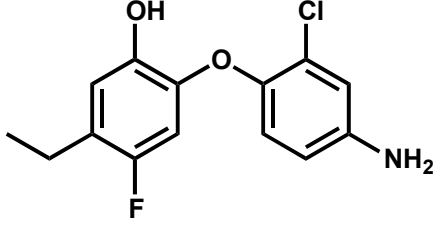
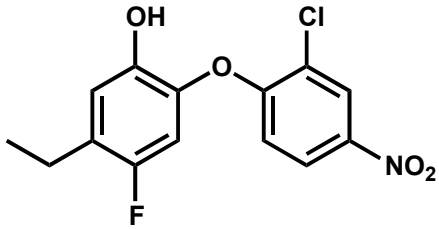
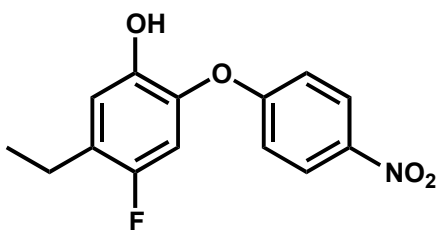
**Figure 6.3** Representative plot of pseudo-first order rate constant ( $k_{obs}$ ) as a function of inhibitor concentration

Selected compound MUT056399 reveals a linear fit with  $R^2 = 0.98$  for  $k_{obs}$  plot.

Table 6.1 Kinetic and thermodynamic parameters for inhibitors against bpFabI

| Compound      | Structure | $K_i^{app}$<br>(nM)                    | $K_i$<br>(nM)           | $k_{on}^{a}$<br>$PP (M^{-1} min^{-1})^b$ | $k_{off}$ (min <sup>-1</sup> )         | $t_R$<br>(min)                         |
|---------------|-----------|--|-------------------------|--|--|--|
| MUT056<br>399 |           | 209±2<br>8 <sup>b</sup>                | 177±4<br>4 <sup>d</sup> | 1.60<br>x 10 <sup>5</sup>                | 0.0284±0.007<br>b                      | 35±8 <sup>b</sup>                      |
| PT01          |           | 28±2 <sup>b</sup>                      | 22±4 <sup>d</sup>       | 2.08<br>x 10 <sup>6</sup>                | 0.0466±0.009<br>b                      | 19±9 <sup>b</sup>                      |
| PT411         |           | 26±3 <sup>a</sup><br>26±3 <sup>b</sup> | 17±3 <sup>d</sup>       | 1.36<br>x 10 <sup>6</sup>                | 0.0235±0.004<br>b<br>0.0344±0.002<br>c | 41±7 <sup>b</sup><br>29±1 <sup>c</sup> |
| PT91          |           | 26±3 <sup>b</sup>                      | 20±6 <sup>d</sup>       | 2.80<br>x 10 <sup>5</sup>                | 0.00551±0.00<br>169 <sup>b</sup>       | 196±71<br>b                            |

|       |  |  |                          |                           |   |   |
|-------|--|--|--------------------------|---------------------------|---|---|
| PT417 |  | 164±2<br>5 <sup>a</sup><br>130±1<br>1 <sup>b</sup> | 100±1<br>2 <sup>e</sup>  | 5.00<br>x 10 <sup>4</sup> | 0.00515±0.00<br>2 <sup>b</sup><br>0.00504±0.00<br>06 <sup>c</sup> | 227±30<br>b<br>198±26<br>c              |
| PT409 |  | 26±2 <sup>b</sup>                                  | 28±2 <sup>d</sup>        | 4.05<br>x 10 <sup>5</sup> | 0.0113±0.000<br>9 <sup>b</sup>                                    | 89±7 <sup>b</sup>                       |
| PT412 |  | 51±8 <sup>a</sup><br>102±7<br>b                    | 100±2<br>8 <sup>d</sup>  | 1.40<br>x 10 <sup>5</sup> | 0.0133±0.004<br>b<br>0.0125±0.000<br>9 <sup>c</sup>               | 91±16 <sup>b</sup><br>80±6 <sup>c</sup> |
| PT405 |  | 4.0±0.<br>2 <sup>b</sup>                           | 4.0±0.<br>3 <sup>d</sup> | 1.01<br>x 10 <sup>6</sup> | 0.00446±0.00<br>033 <sup>b</sup>                                  | 225±16<br>b                             |
| PT406 |  | 2.0±0.<br>3 <sup>b</sup>                           | 3.0±0.<br>1 <sup>d</sup> | 8.60<br>x 10 <sup>5</sup> | 0.0023±0.000<br>6 <sup>b</sup>                                    | 436±11<br>b                             |

|       |   |  |                                |                         |  |  |
|-------|---|--|--------------------------------|-------------------------|--|--|
| PT403 |  | $50 \pm 6^a$<br>$27 \pm 3^b$                               | $27 \pm 5^d$                   | $6.10$<br>$\times 10^5$ | $0.0167 \pm 0.003$<br><sub>b</sub><br>$0.0163 \pm 0.001$<br><sub>c</sub>   | $66 \pm 5^b$<br>$61 \pm 4^c$                                   |
| PT404 |  | $364 \pm 7$<br><sub>a</sub><br>$66 \pm 12$<br><sub>b</sub> | $20 \pm 7^e$                   | $7.00$<br>$\times 10^4$ | $0.0029 \pm 0.002$<br><sub>b</sub><br>$0.0014 \pm 0.000$<br><sub>5^c</sub> | $400 \pm 25$<br><sub>0^b</sub><br>$713 \pm 25$<br><sub>c</sub> |
| PT407 |  | $138 \pm 2$<br><sub>4^b</sub>                              | $173 \pm 0.$<br><sub>1^d</sub> | $2.20$<br>$\times 10^5$ | $0.038 \pm 0.0002$<br><sub>b</sub>   | $27 \pm 3^b$   |

<sup>a</sup> Determined by fitting data obtained from pre-incubation assays.

<sup>b</sup> Determined by fitting progress curves.

<sup>c</sup> Determined by fitting the <sup>32</sup>P-NAD<sup>+</sup> dissociation kinetics.

<sup>d</sup> Affinity was calculated using  $k_{-1}$  and  $k_1$  values obtained from progress curve analysis.

<sup>e</sup> Affinity was calculated using the  $k_{-2}$  value obtained from the <sup>32</sup>P-NAD dissociation assay since the dissociation rate was very slow. The  $k_1$  value was obtained from forward progress curve analysis.

### The *p*-fluorine introduction may destabilize the transition state and ground state.

Our previous work indicated that the diphenyl ether PT01 was a potent nanomolar slow-onset inhibitor for bpFabI, as well as FabI homologs from *S. aureus* and *Francisella tularensis* (30, 34, 37). Optimization of this compound series on the A ring alkyl chain and B ring led to the synthesis of PT91, in which we demonstrated a significantly improved binding affinity and residence time against *M. tuberculosis* FabI homolog (InhA) (Chapter 3). In addition, PT91 also showed efficacy in a *M. tuberculosis* infection model (29). Therefore, both PT01 and PT91 were selected to examine the effect of *p*-fluorine introduction on the inhibitor's kinetic and thermodynamic properties.

Addition of a *p*-fluorine substituent to PT91 (PT417) showed no significant effect on the  $k_{\text{off}}$  or residence time ( $t_{\text{R}}$ ) in comparison to PT91 (Table 6.1). However, as discussed in detail in Chapter 3,  $k_{\text{off}}$  depends on both binding affinity  $K_{\text{i}}$  and association rate constant  $k_{\text{on}}$ . Therefore, despite similar  $k_{\text{off}}$  values for PT91 and PT417, further analysis indicated that binding affinity weakened by 5-fold, from ~20 nM to ~100 nM after the introduction of *p*-fluorine, and the association rate ( $k_{\text{on}}$ ) decreased by ~5 fold, from  $2.8 \times 10^5 \text{ M}^{-1} \text{ min}^{-1}$  to  $5.0 \times 10^4 \text{ M}^{-1} \text{ min}^{-1}$  suggesting a higher transition state energy barrier. Thus, the  $k_{\text{off}}$  was not affected as a result of kinetic-thermodynamic compensation between the ground state and transition state.

### *p*-Fluoro diphenyl ethers' B-ring substituents may affect ground and/or transition states.

We speculated that a similar trend in ground and transition states destabilization would occur on fluoro-substitution of PT01 to create PT411 (Table 6.1) (25). However, the kinetic and thermodynamic parameters  $k_{\text{off}}$ ,  $k_{\text{on}}$  and  $K_{\text{i}}$  were comparable between PT01 and PT411. As PT01

and PT411 lack the substituent on the B ring, we speculated that both a *p*-fluoro group on the inhibitor's A-ring and an *ortho*- substituent on the inhibitor's B-ring were essential for destabilization of the ground and/or transition states of EI\*, as observed for PT91/PT417. Therefore, PT412 and PT409 were synthesized which contained an *o*-NO<sub>2</sub> group on the inhibitor's B-ring with and without a *p*-fluorine on the A-ring. Similar to the trends observed between PT91 and PT417, the *p*-fluorine introduction on the PT409/PT412 group showed no significant effect on  $k_{\text{off}}$  or  $t_{\text{R}}$  (Table 6.1). The binding affinity weakened by ~3-fold, from ~30 nM to 100 nM after the introduction of *p*-fluorine on PT412, and the  $k_{\text{on}}$  decreased by ~3-fold, from  $4.05 \times 10^5 \text{ M}^{-1} \text{ min}^{-1}$  to  $1.41 \times 10^5 \text{ M}^{-1} \text{ min}^{-1}$ . The data support that both *p*-fluoro group on the inhibitor's A-ring and an *ortho*- substituent on the inhibitor's B-ring are important for destabilization of the ground and/or transition states of EI\*.

Comparing PT412 with PT411, the introduction of an *o*-NO<sub>2</sub> group on the B-ring on the *p*-fluoro diphenyl ether weakened the binding affinity by approximately 6-fold, and decreased the  $k_{\text{on}}$  by ~10-fold, respectively. As a result, the  $k_{\text{off}}$  was only altered by 2-fold from  $(0.024 \pm 0.004) \text{ min}^{-1}$  (PT411) to  $(0.013 \pm 0.004) \text{ min}^{-1}$  (PT412). Interestingly, while a bulky group such as nitro decreases the binding affinity as well as the association rate constant, such effect can be alleviated or inverted when a less bulky substituent is introduced on the B ring. For example, when an *o*-fluoro group was introduced on the B-ring (PT405), the  $K_{\text{i}}$  was improved by approximately 4-fold compared to PT411, leading to the same magnitude change in  $k_{\text{off}}$  while  $k_{\text{on}}$  stayed the same. When an *o*-chloro group was introduced on the B-ring (PT406), the  $K_{\text{i}}$  was enhanced by approximately 6-fold compared to PT411, similar to the *o*-fluoro substituent. Yet a 2-fold decrease in  $k_{\text{on}}$  was observed, from  $1.36 \times 10^6 \text{ M}^{-1} \text{ min}^{-1}$  (PT411) to  $8.6 \times 10^5 \text{ M}^{-1} \text{ min}^{-1}$

(PT406). Consequently, the improved  $K_i$  and decreased  $k_{on}$  played a synergistic effect on  $k_{off}$ , resulting in a ~10-fold slower  $k_{off}$  of PT406. In general, the larger the substituent at the *ortho*-position on the inhibitor's B-ring, the smaller the  $k_{on}$ , resulting in slower  $k_{off}$  or longer residence time. Yet the bulkier group can also weaken the binding affinity, mitigating the overall outcome on the improvement of  $k_{off}$ . Ideally, the medium-sized *ortho*-substituent such as chloro should be incorporated on B ring for a slower  $k_{off}$  due to the enhanced binding affinity and a slower association rate.

According to the above observation, SAR studies were continued with a medium-sized substituent at the *ortho*-position on the B-ring (*o*-Cl group) in analogs that also contained a *p*-NH<sub>2</sub> (PT403) or *p*-NO<sub>2</sub> (PT404) group. Both PT403 and PT404 weakened the  $K_i$  by 6-9-fold compared to PT406 and had comparable  $K_i$  values to no substituents on the B-ring (PT411). As the electron-donating substituent (-NH<sub>2</sub>) at the *para*-position had little effect on  $k_{on}$  (PT403 vs. PT406), the residence time was shortened by ~7-fold as a consequence of the weakened binding affinity (PT403 vs. PT406). On the other hand, the electron-withdrawing substituent (-NO<sub>2</sub>) at the *para*-position significantly decreased the  $k_{on}$  by 12-fold (PT404 vs. PT406). Despite the fact that  $K_i$  was weakened by 6-9 fold compared to PT406, the residence time was still enhanced by 1.6-fold in comparison to PT406 due to a significant decrease in  $k_{on}$ . To confirm that the enhanced residence time was predominately due to the *o*-Cl not the *p*-NO<sub>2</sub> on the inhibitor's B-ring, we synthesized a *p*-fluoro diphenyl ether containing only *p*-NO<sub>2</sub> on the inhibitor's B-ring (PT407). Compared to PT406, the  $K_i$  of PT407 was weakened by 58-fold and  $k_{on}$  decreased by 4-fold. As a result, the residence time was shortened by 17-fold. Since the residence time for



PT407 was only  $27 \pm 3$  min, the long residence time for PT404 ( $713 \pm 25$  min) is predominantly due to the *o*-Cl not the *p*-NO<sub>2</sub> on the inhibitor's B-ring.

SAR studies that included modifications to the inhibitor's B-ring revealed changes in the  $K_i$ ,  $k_{on}$ , or  $k_{off}$  values. Remarkably, both the association and dissociation kinetics of the *p*-fluoro diphenyl ethers displayed a moderate linear correlation to binding affinity in a double logarithmic plot (Figure 6.4). This suggests that the energetics involved in residence time differentiation for the *p*-fluoro diphenyl ethers is based on the kinetic-thermodynamic compensation between the ground state and transition state for this inhibitor series. This is interesting because the conventional strategy to improve  $k_{off}$  is through the enhancement of binding affinity  $K_i$ ; in contrast destabilization of the transition state energy barrier upon inhibitor binding has been overlooked and has been rarely reported in other biological systems (18, 20, 21). Tian *et al* reported a series of benzothiazole transition state analog inhibitors of fatty acid amide hydrolase (FAAH) that display long residence time through an increased kinetic barrier (38). In our system we are able to interrogate the impact of the transition state barrier on the dissociation of the drug-target complex and this is the first time we have observed a correlation between transition state destabilization and  $k_{off}$  in the FabI system. We believe this trend is unique to analogs of Mutabilis second-generation compounds since studies by Chang *et al* revealed a strong correlation between only the dissociation rates and thermodynamic affinity in a logarithmic plot for other diphenyl ethers (39).

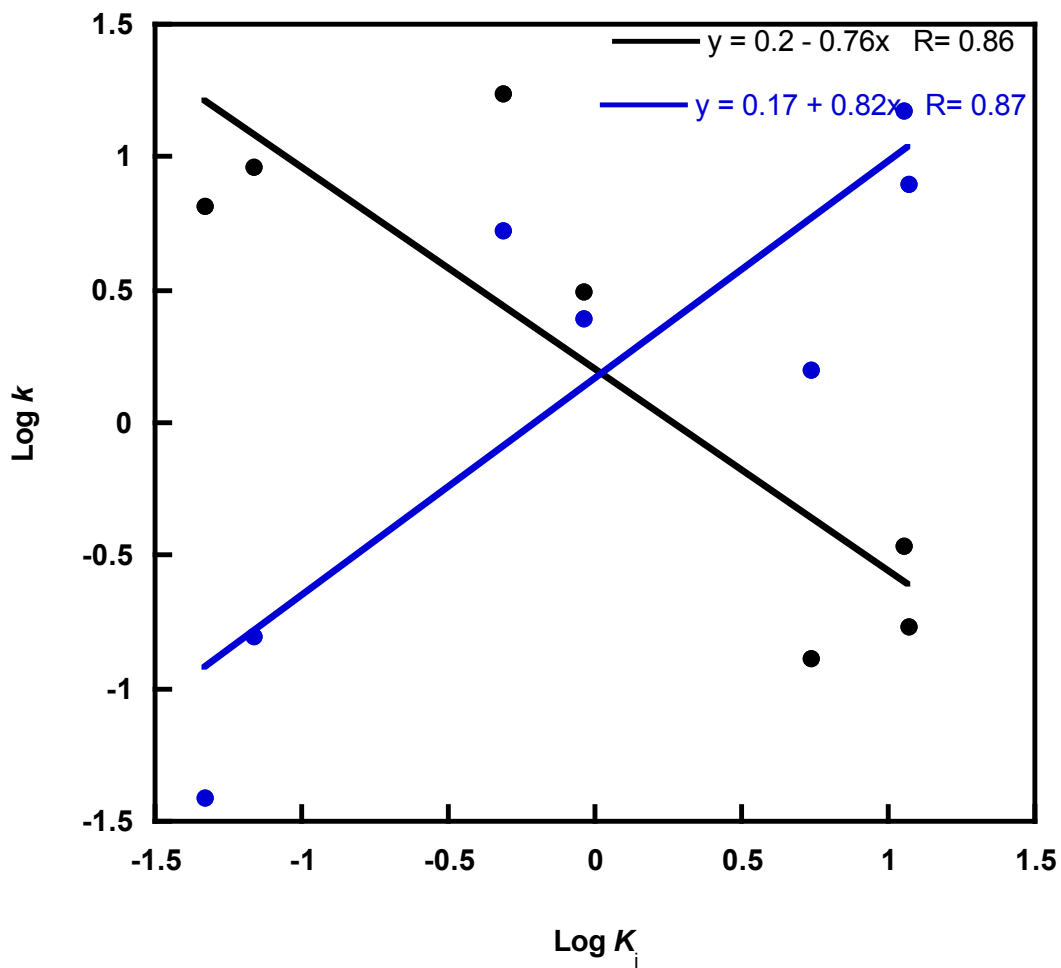


**Figure 6.4 Kinetic and thermodynamic correlation**

A double logarithmic plot depicts a moderate correlation between both association kinetics  $\log k_{on}$  (black), dissociation kinetics  $\log k_{off}$  (blue) and thermodynamic affinity ( $\log K_i$ ). On each axis, logarithmic values were normalized such that their mean is approaching zero.

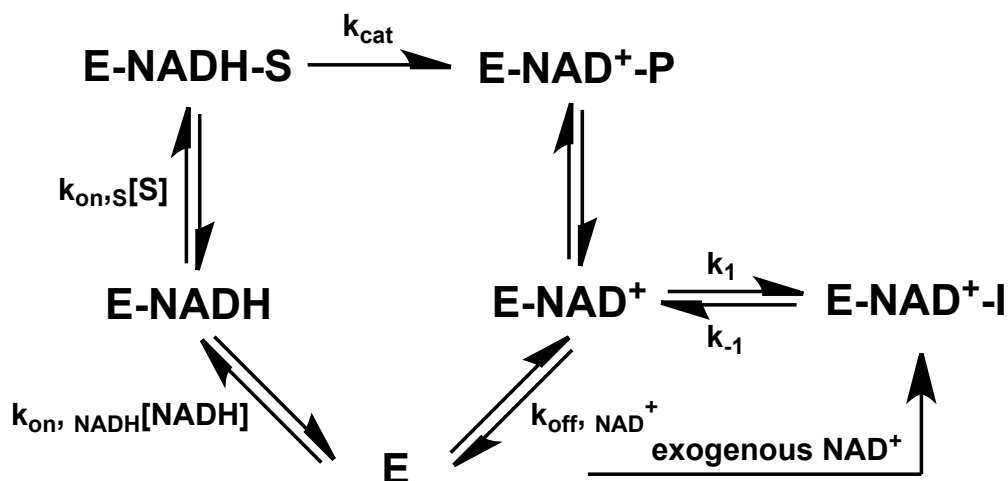
*p*-Fluoro diphenyl ethers form an E-NAD<sup>+</sup>-I complex with NAD<sup>+</sup> generated from catalysis and exogenous NAD<sup>+</sup>.

Thermal shift assays were performed to determine the preferred ternary complex that is formed in the presence of the inhibitor and either excess NADH or NAD<sup>+</sup>. Cofactor preference was determined by shifts in the midpoint temperatures of the protein-unfolding transition ( $T_m$ ). For example, there was a 10 °C shift in  $T_m$  when PT412 was incubated in the presence of NAD<sup>+</sup> in comparison to NADH (Figure 6.5). Furthermore, all compounds of interest in this study suggested a preference in NAD<sup>+</sup> when formed ternary complex with the enzyme. The  $T_m$  shift between E-NAD<sup>+</sup> complex and E-NADH complex were comparable as PT412 (data not shown).

To examine the resource of the NAD<sup>+</sup> that is responsible for the formation of E-NAD<sup>+</sup> product complex, we varied the concentration of enzyme or NAD<sup>+</sup> to interrogate whether the NAD<sup>+</sup> is generated from catalysis or from exogenous NAD<sup>+</sup>. First, progress curves were performed at 200  $\mu$ M and 1000  $\mu$ M NAD<sup>+</sup>, while the concentration of enzyme and inhibitor (PT403) were held constant. The best-fit parameters for  $k_{obs}$  and steady-state velocity ( $v_s$ ) were 0.033  $\text{min}^{-1}$  and 0.0091  $\mu\text{M}^{-1} \text{min}^{-1}$  at 200  $\mu$ M NAD<sup>+</sup>, and 0.048  $\text{min}^{-1}$  and 0.0098  $\mu\text{M}^{-1} \text{min}^{-1}$  at 1000  $\mu$ M NAD<sup>+</sup>, respectively. Although  $v_s$  at both NAD<sup>+</sup> concentrations remained relatively unchanged with only a 7% difference,  $k_{obs}$  changed by approximately 31%. This observation suggests that inhibitors not only bind to the E-NAD<sup>+</sup> binary complex generated from catalysis, but also from E-NAD<sup>+</sup> formed by direct binding of exogenous NAD<sup>+</sup> to the enzyme. This is distinct from other FabI homologs (e.g. InhA, saFabI and ecFabI), where the inhibitors bind exclusively to E-NAD<sup>+</sup> originating from catalytic turnover (36, 39). In addition, the percent change for the rate constant conversion, from initial velocity phase to the steady state velocity

phase, was similar to the  $k_{\text{obs}}$  observed when only inhibitor concentration was doubled. Moreover, the residence time decreased insignificantly by 1.4-fold, from approximately 70 to 50 min.

The next set of progress curves were performed at different enzyme concentrations, 2 nM and 8 nM with compound PT417, with the expectation that increasing the enzyme concentration would accelerate the approach to steady-state (a faster  $k_{\text{obs}}$ ). This 4-fold change in enzyme concentration led to a decrease in residence time approximately 4.5-fold from  $227 \pm 30$  min to  $64 \pm 2$  min. To confirm if we are underestimating or overestimating residence time, the residence time was also measured by the  $^{32}\text{P}$  direct dissociation assay. The residence time was  $198 \pm 26$  min, which agrees with the residence time measured from progress curve analysis at lower enzyme concentration. Taken together the two sets of data demonstrate that the formation of E-NAD<sup>+</sup>-I complex is dependent primarily on oxidized cofactor generated from catalysis but still can take exogenous NAD<sup>+</sup>. (Scheme 6.4).



Scheme 6.4 Detailed kinetic mechanism for inhibition of BpFabI by F-diphenyl ether

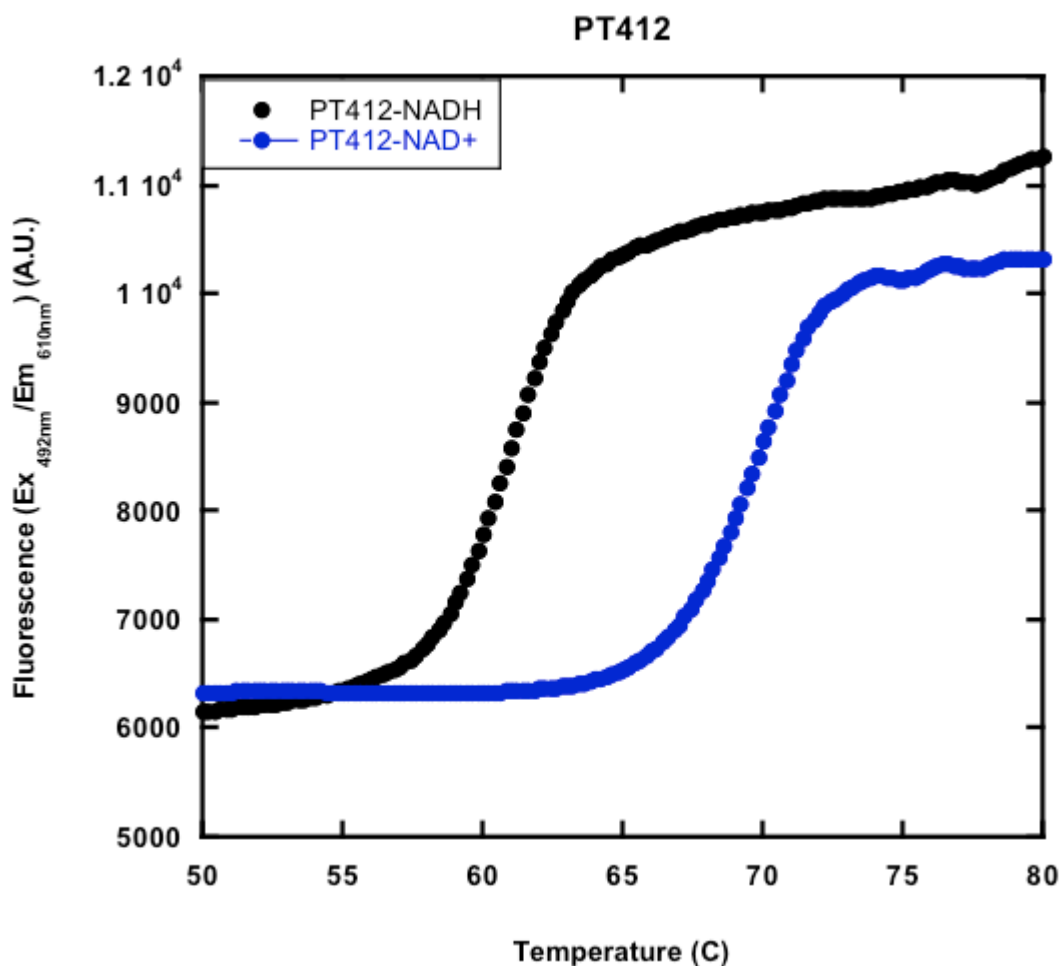


**Figure 6.5** Midpoint temperatures of the protein-unfolding transition ( $T_m$ ) for PT412 In the presence of NADH is shown in black or NAD<sup>+</sup> in blue

### Structural insights of PT404 in complex with BpFabI

Although there were no significant differences in inhibitor conformations between triclosan and PT404 bound to *BpFabI* (Figure 6.6 A), investigators have shown that the C–OH rotational barrier height in *p*-fluorophenols decreases as well as the –OH torsional

vibration frequency (40, 41). Therefore, increasing the degree of freedom of -OH may be unfavorable for the  $k_{on}$  of *p*-fluoro diphenyl ethers. It is possible that the removal of the fluoro-group on the A-ring allows the C-OH to be more rigid and positioned in a favorable conformation to hydrogen bond to the active site Y156 (Figure 6.6 B). Therefore, we speculate the slower  $k_{on}$  and weakened binding affinity for the *p*-fluoro diphenyl ethers may be due to the time it takes to form a favorable hydrogen bond with the active site tyrosine.

Additionally, the *p*-fluoro group in PT404 is in proximity to hydrophobic residues A197, I200, and F203 (Figure 6.6 C). Thus longer alkyl chain substituents next to *p*-fluorine on the inhibitor's A-ring may adopt conformations that could enhance hydrophobic interactions between the C-F and alkyl chain. This can be unfavorable for the inhibitor's alkyl chain to initially enter the hydrophobic substrate binding tunnel, which will eventually weaken the binding affinity as seen in the comparison of PT91 and PT417. These unfavorable inhibitor conformations may be circumvented by having a shorter alkyl chains next to the *p*-fluorine (PT01 vs. PT411).

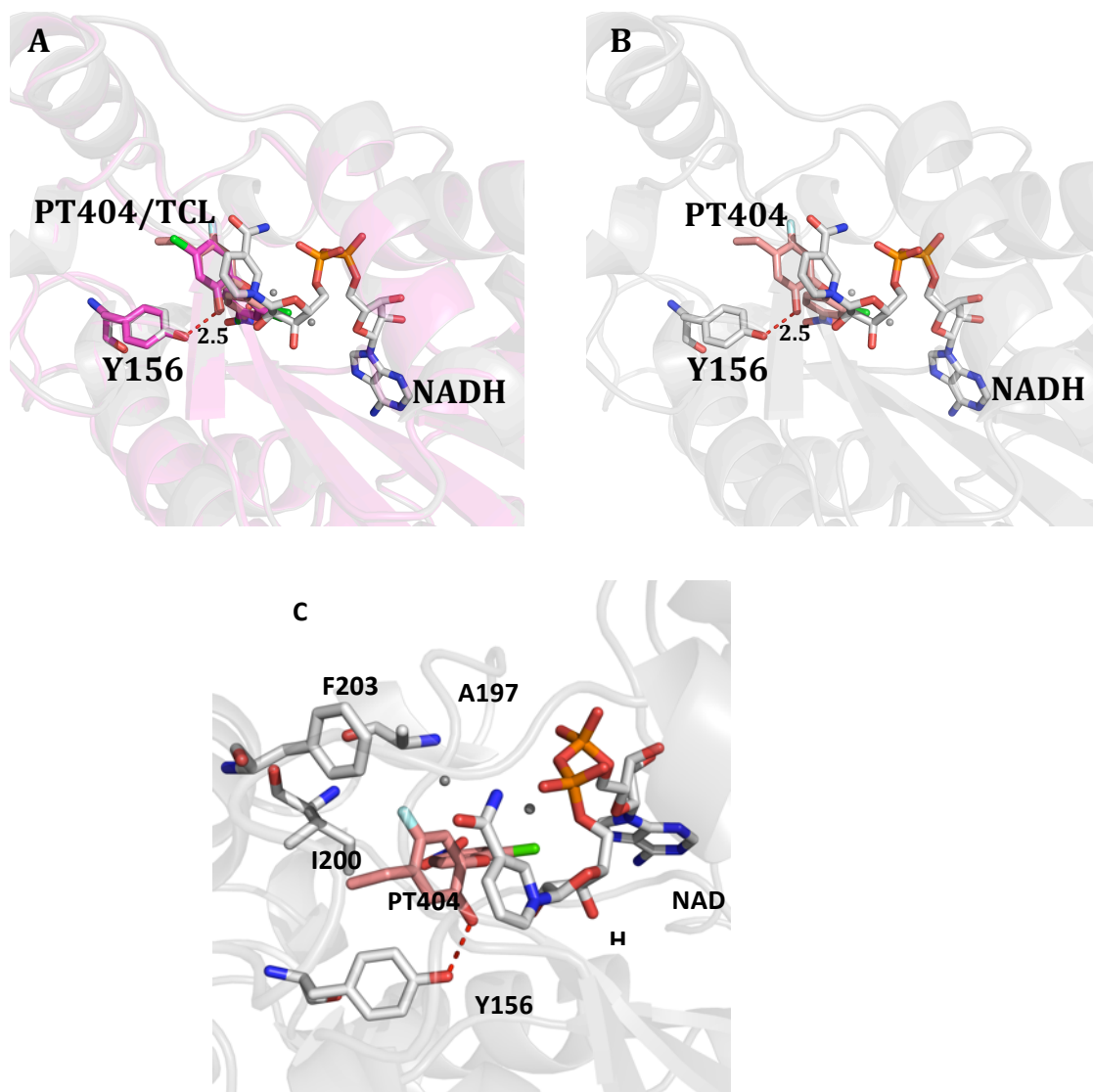


**Figure 6.6 Differences in the structures for PT404 and Triclosan in complex with *BpFabI* and NADH**

(A) Superposition of *BpFabI* bound to PT404 and triclosan (TCL), along with NADH (unpublished structures). (B) PT404 in complex with *BpFabI* and NADH (unpublished structure). (C) Hydrophobic residues in proximity to the *p*-fluoro group. TCL in complex with *BpFabI* is shown in dark pink; PT404 in complex with *BpFabI* is shown in grey; and hydrogen bonding interactions are represented by dashes.

### In vivo efficacy of PT405

Throughout our SAR studies, we evaluated optimal values for the parameters  $K_i^{\text{app}}$ ,  $k_{\text{on}}$ , and  $k_{\text{off}}$ , with a focus on  $k_{\text{on}}$ . It is important to note that one limitation in decreasing  $k_{\text{on}}$  is that *in vivo* metabolism will have a greater impact on the rate of target engagement, which is important since diphenyl ethers are susceptible to Phase II conjugation reactions (42). Rest on these considerations, lead compound PT405 was later selected for animal studies for three reasons. First, it had a strong thermodynamic affinity to BpFabI with a  $K_i^{\text{app}}$  value of  $4 \pm 0.2$  nM. Second, it had a long residence time of  $225 \pm 16$  min. Third, it had antimicrobial activity with MIC values of 128  $\mu\text{g}/\text{mL}$  and 16  $\mu\text{g}/\text{mL}$  towards wild-type *B. pseudomallei* (Bp1026b) and an efflux pump knockout strain (Bp 400), respectively.

Based on the above rationale, the efficacy of PT405 was evaluated in the acute *B. pseudomallei* animal model using the efflux knockout strain Bp400 (Figure 6.7). Mice were challenged with 5000 CFU and bacterial burden was assessed at 60 h post infection in lung and spleen homogenates. The efficacy of PT405 was determined relative to an untreated control group and a positive control group in which animals were treated with 200 mg/kg ceftazidime. There was no significant reduction in lung burden; however, PT405 showed a significant reduction ( $P < 0.001$ ) of 1.69  $\text{Log}_{10}$  CFU/mL in bacterial burden in the spleen. These data were compared with efficacy studies that used other diphenyl ether compounds. However, although previous studies suggested that these other diphenyl ethers should be active against pump mutant strains *in vivo*, the reduction in CFUs was insignificant in spleen. We speculated that the improved efficacy of PT405 could be a combination of its optimized binding



affinity and prolonged residence time. Further optimization on the similar classes of these inhibitors might open up possibilities of novel drug candidates to treat Melioidosis.

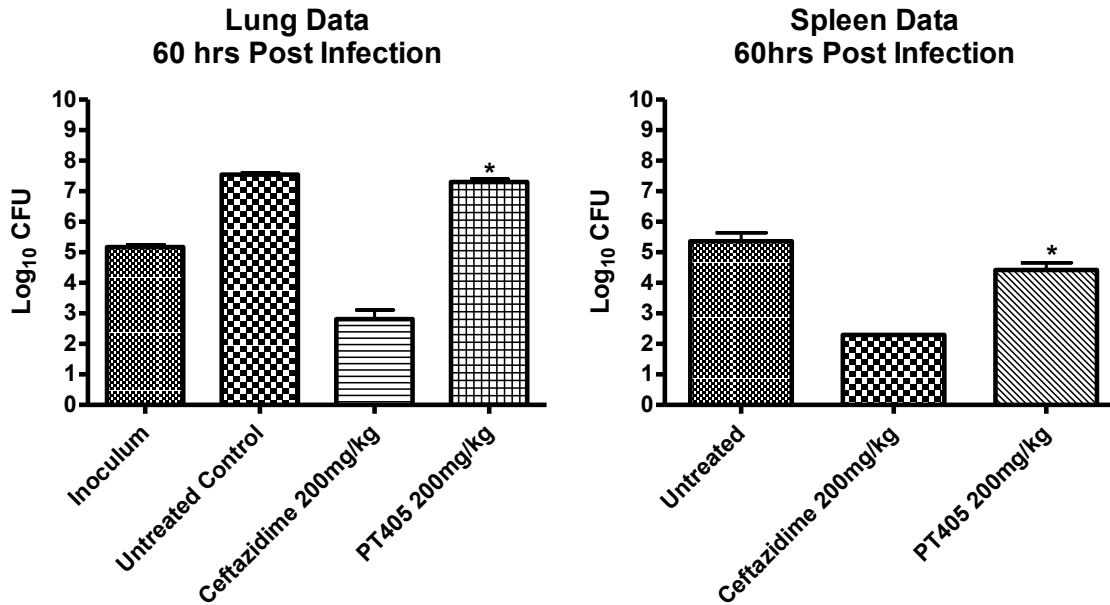


**Figure 6.7** *In vivo* efficacy of PT405 in the animal model of melioidosis.

The mean of each group was plotted and error bars indicating +/- standard deviation. Significance was determined by unpaired t-test analysis between untreated and treated groups. *In vivo* efficacy studies were performed using *B. pseudomallei* bp400 (1026b  $\Delta$ bpeAB-oprB;  $\Delta$ amrAB-oprA strain).

## CONCLUSION

SAR studies on fluoro-substituted diphenyl ethers that target BpFabI provide unique mechanistic insight, in which  $k_{\text{on}}$  plays a pivotal role in governing the drug-target residence time. Optimization of the kinetic and thermodynamic properties allowed us to examine the transition and ground states of the enzyme-inhibitor ternary complexes, and yielded compound PT404 which has a 10-fold slower association rate constant and residence time of up to 700 min. Structural studies of the longest residence time inhibitor PT404 bound to BpFabI revealed interactions that could affect predominantly  $k_{\text{off}}$ . Further optimization of these promising candidates can provide potential drug candidates for anti-bacterial activity against *B. pseudomallei*, which was shown in our *in vivo* efficacy animal model with lead BpFabI inhibitor PT405.

## Bibliography

### Chapter 1

1. Zumla, A., Nahid, P., and Cole, S. T. (2013) Advances in the development of new tuberculosis drugs and treatment regimens, *Nat Rev Drug Discov* 12, 388-404.
2. Lawn, S. D., and Zumla, A. I. (2011) Tuberculosis, *Lancet* 378, 57-72.
3. Organization, W. H. (2009) Global Tuberculosis Control - A Short Update to the 2009 Report, World Health Organization.
4. Gandhi, N. R., Moll, A., Sturm, A. W., Pawinski, R., Govender, T., Lalloo, U., Zeller, K., Andrews, J., and Friedland, G. (2006) Extensively drug-resistant tuberculosis as a cause of death in patients co-infected with tuberculosis and HIV in a rural area of South Africa, *Lancet* 368, 1575-1580.
5. Dheda, K., Shean, K., Zumla, A., Badri, M., Streicher, E. M., Page-Shipp, L., Willcox, P., John, M. A., Reubenson, G., Govindasamy, D., Wong, M., Padanilam, X., Dziwiecki, A., van Helden, P. D., Siwendu, S., Jarand, J., Menezes, C. N., Burns, A., Victor, T., Warren, R., Grobusch, M. P., van der Walt, M., and Kvasnovsky, C. (2010) Early treatment outcomes and HIV status of patients with extensively drug-resistant tuberculosis in South Africa: a retrospective cohort study, *Lancet* 375, 1798-1807.
6. Albert Schatz, E. B., Selman A. Waksman. (1944) Streptomycin, a Substance Exhibiting Antibiotic Activity Against Gram-Positive and Gram-Negative Bacteria, *Experimental Biology and Medicine* 55, 66 - 69.
7. Zhang, Y., Heym, B., Allen, B., Young, D., and Cole, S. (1992) The catalase-peroxidase gene and isoniazid resistance of *Mycobacterium tuberculosis*, *Nature* 358, 591-593.
8. Lei, B., Wei, C. J., and Tu, S. C. (2000) Action mechanism of antitubercular isoniazid. Activation by *Mycobacterium tuberculosis* KatG, isolation, and characterization of inhA inhibitor, *J Biol Chem* 275, 2520-2526.
9. Banerjee, A., Dubnau, E., Quemard, A., Balasubramanian, V., Um, K. S., Wilson, T., Collins, D., de Lisle, G., and Jacobs, W. R., Jr. (1994) inhA, a gene encoding a target for isoniazid and ethionamide in *Mycobacterium tuberculosis*, *Science* 263, 227-230.
10. Quemard, A., Sacchettini, J. C., Dessen, A., Vilcheze, C., Bittman, R., Jacobs, W. R., Jr., and Blanchard, J. S. (1995) Enzymatic characterization of the target for isoniazid in *Mycobacterium tuberculosis*, *Biochemistry* 34, 8235-8241.

11. Mdluli, K., Slayden, R. A., Zhu, Y., Ramaswamy, S., Pan, X., Mead, D., Crane, D. D., Musser, J. M., and Barry, C. E., 3rd. (1998) Inhibition of a Mycobacterium tuberculosis beta-ketoacyl ACP synthase by isoniazid, *Science* 280, 1607-1610.
12. Slayden, R. A., and Barry, C. E., 3rd. (2000) The genetics and biochemistry of isoniazid resistance in mycobacterium tuberculosis, *Microbes Infect* 2, 659-669.
13. Mitchison, D. A. (1985) The action of antituberculosis drugs in short-course chemotherapy, *Tubercle* 66, 219-225.
14. McCune, R. M., Jr., McDermott, W., and Tompsett, R. (1956) The fate of Mycobacterium tuberculosis in mouse tissues as determined by the microbial enumeration technique. II. The conversion of tuberculous infection to the latent state by the administration of pyrazinamide and a companion drug, *J Exp Med* 104, 763-802.
15. Heifets, L., and Lindholm-Levy, P. (1992) Pyrazinamide sterilizing activity in vitro against semidormant Mycobacterium tuberculosis bacterial populations, *Am Rev Respir Dis* 145, 1223-1225.
16. Konno, K., Feldmann, F. M., and McDermott, W. (1967) Pyrazinamide susceptibility and amidase activity of tubercle bacilli, *Am Rev Respir Dis* 95, 461-469.
17. Scorpio, A., and Zhang, Y. (1996) Mutations in pncA, a gene encoding pyrazinamidase/nicotinamidase, cause resistance to the antituberculous drug pyrazinamide in tubercle bacillus, *Nat Med* 2, 662-667.
18. Shi, W., Zhang, X., Jiang, X., Yuan, H., Lee, J. S., Barry, C. E., 3rd, Wang, H., Zhang, W., and Zhang, Y. (2011) Pyrazinamide inhibits trans-translation in Mycobacterium tuberculosis, *Science* 333, 1630-1632.
19. Takayama, K., and Kilburn, J. O. (1989) Inhibition of synthesis of arabinogalactan by ethambutol in Mycobacterium smegmatis, *Antimicrob Agents Chemother* 33, 1493-1499.
20. Mikusova, K., Slayden, R. A., Besra, G. S., and Brennan, P. J. (1995) Biogenesis of the mycobacterial cell wall and the site of action of ethambutol, *Antimicrob Agents Chemother* 39, 2484-2489.
21. Hartmann, G., Honikel, K. O., Knusel, F., and Nuesch, J. (1967) The specific inhibition of the DNA-directed RNA synthesis by rifamycin, *Biochim Biophys Acta* 145, 843-844.
22. Floss, H. G., and Yu, T. W. (2005) Rifamycin-mode of action, resistance, and biosynthesis, *Chem Rev* 105, 621-632.
23. Diacon, A. H., Pym, A., Grobusch, M., Patientia, R., Rustomjee, R., Page-Shipp, L., Pistorius, C., Krause, R., Bogoshi, M., Churchyard, G., Venter, A., Allen, J., Palomino, J. C., De

- Marez, T., van Heeswijk, R. P., Lounis, N., Meyvisch, P., Verbeeck, J., Parys, W., de Beule, K., Andries, K., and Mc Neeley, D. F. (2009) The diarylquinoline TMC207 for multidrug-resistant tuberculosis, *N Engl J Med* 360, 2397-2405.
24. Zumla, A., Hafner, R., Lienhardt, C., Hoelscher, M., and Nunn, A. (2012) Advancing the development of tuberculosis therapy, *Nat Rev Drug Discov* 11, 171-172.
25. Andries, K., Verhasselt, P., Guillemont, J., Gohlmann, H. W., Neefs, J. M., Winkler, H., Van Gestel, J., Timmerman, P., Zhu, M., Lee, E., Williams, P., de Chaffoy, D., Huitric, E., Hoffner, S., Cambau, E., Truffot-Pernot, C., Lounis, N., and Jarlier, V. (2005) A diarylquinoline drug active on the ATP synthase of *Mycobacterium tuberculosis*, *Science* 307, 223-227.
26. Richard G. Wax, K. L., Abigail A. Salyers, Harry Taber (2007) *Bacterial Resistance to Antimicrobials*, second edition ed., CRC Press.
27. Chakraborty, S., Gruber, T., Barry, C. E., 3rd, Boshoff, H. I., and Rhee, K. Y. (2013) Para-aminosalicylic acid acts as an alternative substrate of folate metabolism in *Mycobacterium tuberculosis*, *Science* 339, 88-91.
28. Sirgel, F. A., Warren, R. M., Streicher, E. M., Victor, T. C., van Helden, P. D., and Bottger, E. C. (2012) *gyrA* mutations and phenotypic susceptibility levels to ofloxacin and moxifloxacin in clinical isolates of *Mycobacterium tuberculosis*, *J Antimicrob Chemother* 67, 1088-1093.
29. Sirgel, F. A., Tait, M., Warren, R. M., Streicher, E. M., Bottger, E. C., van Helden, P. D., Gey van Pittius, N. C., Coetzee, G., Hoosain, E. Y., Chabula-Nxiweni, M., Hayes, C., Victor, T. C., and Trollip, A. (2012) Mutations in the *rrs* A1401G gene and phenotypic resistance to amikacin and capreomycin in *Mycobacterium tuberculosis*, *Microb Drug Resist* 18, 193-197.
30. Salian, S., Matt, T., Akbergenov, R., Harish, S., Meyer, M., Duscha, S., Shcherbakov, D., Bernet, B. B., Vasella, A., Westhof, E., and Bottger, E. C. (2012) Structure-activity relationships among the kanamycin aminoglycosides: role of ring I hydroxyl and amino groups, *Antimicrob Agents Chemother* 56, 6104-6108.
31. Bruning, J. B., Murillo, A. C., Chacon, O., Barletta, R. G., and Sacchettini, J. C. (2011) Structure of the *Mycobacterium tuberculosis* D-alanine:D-alanine ligase, a target of the antituberculosis drug D-cycloserine, *Antimicrob Agents Chemother* 55, 291-301.
32. Stover, C. K., Warrener, P., VanDevanter, D. R., Sherman, D. R., Arain, T. M., Langhorne, M. H., Anderson, S. W., Towell, J. A., Yuan, Y., McMurray, D. N., Kreiswirth, B. N., Barry, C. E., and Baker, W. R. (2000) A small-molecule nitroimidazopyran drug candidate for the treatment of tuberculosis, *Nature* 405, 962-966.

33. Matsumoto, M., Hashizume, H., Tomishige, T., Kawasaki, M., Tsubouchi, H., Sasaki, H., Shimokawa, Y., and Komatsu, M. (2006) OPC-67683, a nitro-dihydro-imidazooxazole derivative with promising action against tuberculosis in vitro and in mice, *PLoS Med* 3, e466.
34. Manjunatha, U. H., Boshoff, H., Dowd, C. S., Zhang, L., Albert, T. J., Norton, J. E., Daniels, L., Dick, T., Pang, S. S., and Barry, C. E., 3rd. (2006) Identification of a nitroimidazooxazine-specific protein involved in PA-824 resistance in *Mycobacterium tuberculosis*, *Proc Natl Acad Sci U S A* 103, 431-436.
35. Singh, R., Manjunatha, U., Boshoff, H. I., Ha, Y. H., Niyomrattanakit, P., Ledwidge, R., Dowd, C. S., Lee, I. Y., Kim, P., Zhang, L., Kang, S., Keller, T. H., Jiricek, J., and Barry, C. E., 3rd. (2008) PA-824 kills nonreplicating *Mycobacterium tuberculosis* by intracellular NO release, *Science* 322, 1392-1395.
36. Manjunatha, U. H., Lahiri, R., Randhawa, B., Dowd, C. S., Krahenbuhl, J. L., and Barry, C. E., 3rd. (2006) *Mycobacterium leprae* is naturally resistant to PA-824, *Antimicrob Agents Chemother* 50, 3350-3354.
37. Hurdle, J. G., Lee, R. B., Budha, N. R., Carson, E. I., Qi, J., Scherman, M. S., Cho, S. H., McNeil, M. R., Lenaerts, A. J., Franzblau, S. G., Meibohm, B., and Lee, R. E. (2008) A microbiological assessment of novel nitrofuranylamides as anti-tuberculosis agents, *J Antimicrob Chemother* 62, 1037-1045.
38. Manjunatha, U., Boshoff, H. I., and Barry, C. E. (2009) The mechanism of action of PA-824: Novel insights from transcriptional profiling, *Commun Integr Biol* 2, 215-218.
39. Ma, Z., Lienhardt, C., McIlleron, H., Nunn, A. J., and Wang, X. (2010) Global tuberculosis drug development pipeline: the need and the reality, *Lancet* 375, 2100-2109.
40. Tahlan, K., Wilson, R., Kastrinsky, D. B., Arora, K., Nair, V., Fischer, E., Barnes, S. W., Walker, J. R., Alland, D., Barry, C. E., 3rd, and Boshoff, H. I. (2012) SQ109 targets MmpL3, a membrane transporter of trehalose monomycolate involved in mycolic acid donation to the cell wall core of *Mycobacterium tuberculosis*, *Antimicrob Agents Chemother* 56, 1797-1809.
41. Reddy, V. M., Einck, L., Andries, K., and Nacy, C. A. (2010) In vitro interactions between new antitubercular drug candidates SQ109 and TMC207, *Antimicrob Agents Chemother* 54, 2840-2846.
42. Grzegorzewicz, A. E., Pham, H., Gundi, V. A., Scherman, M. S., North, E. J., Hess, T., Jones, V., Gruppo, V., Born, S. E., Kordulakova, J., Chavadi, S. S., Morisseau, C., Lenaerts, A. J., Lee, R. E., McNeil, M. R., and Jackson, M. (2012) Inhibition of mycolic acid transport across the *Mycobacterium tuberculosis* plasma membrane, *Nat Chem Biol* 8, 334-341.

43. La Rosa V, P. G., Canseco JO, Buroni S, Pasca MR, Biava M, Raju RM, Porretta GC, Alfonso S, Battilocchio C, Javid B, Sorrentino F, Ioerger TR, Sacchettini JC, Manetti F, Botta M, De Logu A, Rubin EJ, De Rossi E. (2012) MmpL3 is the cellular target of the antitubercular pyrrole derivative BM212, *Antimicrob Agents Chemother* 56, 324 - 331.
44. Stanley, S. A., Grant, S. S., Kawate, T., Iwase, N., Shimizu, M., Wivagg, C., Silvis, M., Kazyanskaya, E., Aquadro, J., Golas, A., Fitzgerald, M., Dai, H., Zhang, L., and Hung, D. T. (2012) Identification of novel inhibitors of *M. tuberculosis* growth using whole cell based high-throughput screening, *ACS Chem Biol* 7, 1377-1384.
45. Rao, S. P., Lakshminarayana, S. B., Kondreddi, R. R., Herve, M., Camacho, L. R., Bifani, P., Kalapala, S. K., Jiricek, J., Ma, N. L., Tan, B. H., Ng, S. H., Nanjundappa, M., Ravindran, S., Seah, P. G., Thayalan, P., Lim, S. H., Lee, B. H., Goh, A., Barnes, W. S., Chen, Z., Gagaring, K., Chatterjee, A. K., Pethe, K., Kuhen, K., Walker, J., Feng, G., Babu, S., Zhang, L., Blasco, F., Beer, D., Weaver, M., Dartois, V., Glynn, R., Dick, T., Smith, P. W., Diagona, T. T., and Manjunatha, U. H. (2013) Indolcarboxamide is a preclinical candidate for treating multidrug-resistant tuberculosis, *Sci Transl Med* 5, 214ra168.
46. Benator, D., Bhattacharya, M., Bozeman, L., Burman, W., Cantazaro, A., Chaisson, R., Gordin, F., Horsburgh, C. R., Horton, J., Khan, A., Lahart, C., Metchock, B., Pachucki, C., Stanton, L., Vernon, A., Villarino, M. E., Wang, Y. C., Weiner, M., and Weis, S. (2002) Rifapentine and isoniazid once a week versus rifampicin and isoniazid twice a week for treatment of drug-susceptible pulmonary tuberculosis in HIV-negative patients: a randomised clinical trial, *Lancet* 360, 528-534.
47. Ashtekar, D. R., Costa-Periera, R., Shrinivasan, T., Iyyer, R., Vishvanathan, N., and Rittel, W. (1991) Oxazolidinones, a new class of synthetic antituberculosis agent. In vitro and in vivo activities of DuP-721 against *Mycobacterium tuberculosis*, *Diagn Microbiol Infect Dis* 14, 465-471.
48. Fortun, J., Martin-Davila, P., Navas, E., Perez-Elias, M. J., Cobo, J., Tato, M., De la Pedrosa, E. G., Gomez-Mampaso, E., and Moreno, S. (2005) Linezolid for the treatment of multidrug-resistant tuberculosis, *J Antimicrob Chemother* 56, 180-185.
49. Wallis, R. S., Jakubiec, W., Mitton-Fry, M., Ladutko, L., Campbell, S., Paige, D., Silvia, A., and Miller, P. F. (2012) Rapid evaluation in whole blood culture of regimens for XDR-TB containing PNU-100480 (sutezolid), TMC207, PA-824, SQ109, and pyrazinamide, *PLoS One* 7, e30479.
50. Marrakchi, H., Zhang, Y. M., and Rock, C. O. (2002) Mechanistic diversity and regulation of Type II fatty acid synthesis, *Biochem Soc Trans* 30, 1050-1055.

51. Payne, D. J., Warren, P. V., Holmes, D. J., Ji, Y., and Lonsdale, J. T. (2001) Bacterial fatty-acid biosynthesis: a genomics-driven target for antibacterial drug discovery, *Drug Discov Today* 6, 537-544.
52. Chirala, S. S., Huang, W. Y., Jayakumar, A., Sakai, K., and Wakil, S. J. (1997) Animal fatty acid synthase: functional mapping and cloning and expression of the domain I constituent activities, *Proc Natl Acad Sci U S A* 94, 5588-5593.
53. Polakis, S. E., Guchhait, R. B., Zwergel, E. E., Lane, M. D., and Cooper, T. G. (1974) Acetyl coenzyme A carboxylase system of *Escherichia coli*. Studies on the mechanisms of the biotin carboxylase- and carboxyltransferase-catalyzed reactions, *J Biol Chem* 249, 6657-6667.
54. Blanchard, C. Z., Amspacher, D., Strongin, R., and Waldrop, G. L. (1999) Inhibition of biotin carboxylase by a reaction intermediate analog: implications for the kinetic mechanism, *Biochem Biophys Res Commun* 266, 466-471.
55. Cronan, J. E., Jr., and Waldrop, G. L. (2002) Multi-subunit acetyl-CoA carboxylases, *Prog Lipid Res* 41, 407-435.
56. Choi-Rhee, E., and Cronan, J. E. (2003) The biotin carboxylase-biotin carboxyl carrier protein complex of *Escherichia coli* acetyl-CoA carboxylase, *J Biol Chem* 278, 30806-30812.
57. Janiyani, K., Bordelon, T., Waldrop, G. L., and Cronan, J. E., Jr. (2001) Function of *Escherichia coli* biotin carboxylase requires catalytic activity of both subunits of the homodimer, *J Biol Chem* 276, 29864-29870.
58. de Queiroz, M. S., and Waldrop, G. L. (2007) Modeling and numerical simulation of biotin carboxylase kinetics: implications for half-sites reactivity, *J Theor Biol* 246, 167-175.
59. Williamson, I. P., and Wakil, S. J. (1966) Studies on the mechanism of fatty acid synthesis. XVII. Preparation and general properties of acetyl coenzyme A and malonyl coenzyme A-acyl carrier protein transacylases, *J Biol Chem* 241, 2326-2332.
60. Ruch, F. E., and Vagelos, P. R. (1973) Characterization of a malonyl-enzyme intermediate and identification of the malonyl binding site in malonyl coenzyme A-acyl carrier protein transacylase of *Escherichia coli*, *J Biol Chem* 248, 8095-8106.
61. Tsay, J. T., Oh, W., Larson, T. J., Jackowski, S., and Rock, C. O. (1992) Isolation and characterization of the beta-ketoacyl-acyl carrier protein synthase III gene (*fabH*) from *Escherichia coli* K-12, *J Biol Chem* 267, 6807-6814.
62. Alberts, A. W., Majerus, P. W., Talamo, B., and Vagelos, P. R. (1964) Acyl-Carrier Protein. Ii. Intermediary Reactions of Fatty Acid Synthesis, *Biochemistry* 3, 1563-1571.



63. Brock, D. J., Kass, L. R., and Bloch, K. (1967) Beta-hydroxydecanoyl thioester dehydrase. II. Mode of action, *J Biol Chem* 242, 4432-4440.
64. Helmkamp, G. M., Jr., Brock, D. J., and Bloch, K. (1968) Beta-hydroxydecanoyl thioester dehydrase. Specificity of substrates and acetylenic inhibitors, *J Biol Chem* 243, 3229-3231.
65. Mohan, S., Kelly, T. M., Eveland, S. S., Raetz, C. R., and Anderson, M. S. (1994) An *Escherichia coli* gene (FabZ) encoding (3R)-hydroxymyristoyl acyl carrier protein dehydrase. Relation to fabA and suppression of mutations in lipid A biosynthesis, *J Biol Chem* 269, 32896-32903.
66. Bergler, H., Wallner, P., Ebeling, A., Leitinger, B., Fuchsbichler, S., Aschauer, H., Kollenz, G., Hogenauer, G., and Turnowsky, F. (1994) Protein EnvM is the NADH-dependent enoyl-ACP reductase (FabI) of *Escherichia coli*, *J Biol Chem* 269, 5493-5496.
67. D'Agnolo, G., Rosenfeld, I. S., and Vagelos, P. R. (1975) Multiple forms of beta-ketoacyl-acyl carrier protein synthetase in *Escherichia coli*, *J Biol Chem* 250, 5289-5294.
68. Takayama, K., Wang, C., and Besra, G. S. (2005) Pathway to synthesis and processing of mycolic acids in *Mycobacterium tuberculosis*, *Clin Microbiol Rev* 18, 81-101.
69. Heym, B., Zhang, Y., Poulet, S., Young, D., and Cole, S. T. (1993) Characterization of the katG gene encoding a catalase-peroxidase required for the isoniazid susceptibility of *Mycobacterium tuberculosis*, *J Bacteriol* 175, 4255-4259.
70. Hazbon, M. H., Brimacombe, M., Bobadilla del Valle, M., Cavatore, M., Guerrero, M. I., Varma-Basil, M., Billman-Jacobe, H., Lavender, C., Fyfe, J., Garcia-Garcia, L., Leon, C. I., Bose, M., Chaves, F., Murray, M., Eisenach, K. D., Sifuentes-Osornio, J., Cave, M. D., Ponce de Leon, A., and Alland, D. (2006) Population genetics study of isoniazid resistance mutations and evolution of multidrug-resistant *Mycobacterium tuberculosis*, *Antimicrob Agents Chemother* 50, 2640-2649.
71. Rawat, R., Whitty, A., and Tonge, P. J. (2003) The isoniazid-NAD adduct is a slow, tight-binding inhibitor of InhA, the *Mycobacterium tuberculosis* enoyl reductase: adduct affinity and drug resistance, *Proc Natl Acad Sci U S A* 100, 13881-13886.
72. Tonge, P. J., Kisker, C., and Slayden, R. A. (2007) Development of modern InhA inhibitors to combat drug resistant strains of *Mycobacterium tuberculosis*, *Curr Top Med Chem* 7, 489-498.
73. Levy, C. W., Baldock, C., Wallace, A. J., Sedelnikova, S., Viner, R. C., Clough, J. M., Stuitje, A. R., Slabas, A. R., Rice, D. W., and Rafferty, J. B. (2001) A study of the structure-

activity relationship for diazaborine inhibition of *Escherichia coli* enoyl-ACP reductase, *J Mol Biol* 309, 171-180.

74. Davis, M. C., Franzblau, S. G., and Martin, A. R. (1998) Syntheses and evaluation of benzodiazaborine compounds against *M. tuberculosis* H37Rv in vitro, *Bioorg Med Chem Lett* 8, 843-846.

75. He, X., Alian, A., Stroud, R., and Ortiz de Montellano, P. R. (2006) Pyrrolidine carboxamides as a novel class of inhibitors of enoyl acyl carrier protein reductase from *Mycobacterium tuberculosis*, *J Med Chem* 49, 6308-6323.

76. Shirude, P. S., Madhavapeddi, P., Naik, M., Murugan, K., Shinde, V., Nandishaiah, R., Bhat, J., Kumar, A., Hameed, S., Holdgate, G., Davies, G., McMiken, H., Hegde, N., Ambady, A., Venkatraman, J., Panda, M., Bandodkar, B., Sambandamurthy, V. K., and Read, J. A. (2013) Methyl-thiazoles: a novel mode of inhibition with the potential to develop novel inhibitors targeting InhA in *Mycobacterium tuberculosis*, *J Med Chem* 56, 8533-8542.

77. Encinas, L., O'Keefe, H., Neu, M., Remuinan, M. J., Patel, A. M., Guardia, A., Davie, C. P., Perez-Macias, N., Yang, H., Convery, M. A., Messer, J. A., Perez-Herran, E., Centrella, P. A., Alvarez-Gomez, D., Clark, M. A., Huss, S., O'Donovan, G. K., Ortega-Muro, F., McDowell, W., Castaneda, P., Arico-Muendel, C. C., Pajk, S., Rullas, J., Angulo-Barturen, I., Alvarez-Ruiz, E., Mendoza-Losana, A., Ballell Pages, L., Castro-Pichel, J., and Evindar, G. (2014) Encoded library technology as a source of hits for the discovery and lead optimization of a potent and selective class of bactericidal direct inhibitors of *Mycobacterium tuberculosis* InhA, *J Med Chem* 57, 1276-1288.

78. Hartkoorn, R. C., Sala, C., Neres, J., Pojer, F., Magnet, S., Mukherjee, R., Uplekar, S., Boy-Rottger, S., Altmann, K. H., and Cole, S. T. (2012) Towards a new tuberculosis drug: pyridomycin - nature's isoniazid, *EMBO Mol Med* 4, 1032-1042.

79. Hartkoorn, R. C., Pojer, F., Read, J. A., Gingell, H., Neres, J., Horlacher, O. P., Altmann, K. H., and Cole, S. T. (2014) Pyridomycin bridges the NADH- and substrate-binding pockets of the enoyl reductase InhA, *Nat Chem Biol* 10, 96-98.

80. Mattheus, W., Masschelein, J., Gao, L. J., Herdewijn, P., Landuyt, B., Volckaert, G., and Lavigne, R. (2010) The kalimantacin/batumin biosynthesis operon encodes a self-resistance isoform of the FabI bacterial target, *Chem Biol* 17, 1067-1071.

81. Copeland, R. A., Pompliano, D. L., and Meek, T. D. (2006) Drug-target residence time and its implications for lead optimization, *Nat Rev Drug Discov* 5, 730-739.

82. Tummino, P. J., and Copeland, R. A. (2008) Residence time of receptor-ligand complexes and its effect on biological function, *Biochemistry* 47, 5481-5492.

83. Lu, H., England, K., am Ende, C., Truglio, J. J., Luckner, S., Reddy, B. G., Marlenee, N. L., Knudson, S. E., Knudson, D. L., Bowen, R. A., Kisker, C., Slayden, R. A., and Tonge, P. J. (2009) Slow-onset inhibition of the FabI enoyl reductase from *francisella tularensis*: residence time and in vivo activity, *ACS Chem Biol* 4, 221-231.
84. A.Copeland, R. (2005) *Evaluation of Enzyme Inhibitors in Drug Discovery*, A John Wiley & Sons, Inc, Publication

## Chapter 2

1. Taubes, G. (2008) The bacteria fight back, *Science* 321, 356-361.
2. McDevitt, D., and Rosenberg, M. (2001) Exploiting genomics to discover new antibiotics, *Trends Microbiol* 9, 611-617.
3. Marshall, E. (2008) Trench warfare in a battle with TB, *Science* 321, 362-364.
4. Wright, G. D. (2007) The antibiotic resistome: the nexus of chemical and genetic diversity, *Nat Rev Microbiol* 5, 175-186.
5. Copeland, R. A., Pompliano, D. L., and Meek, T. D. (2006) Drug-target residence time and its implications for lead optimization, *Nat Rev Drug Discov* 5, 730-739.
6. Tummino, P. J., and Copeland, R. A. (2008) Residence time of receptor-ligand complexes and its effect on biological function, *Biochemistry* 47, 5481-5492.
7. Vauquelin, G., and Charlton, S. J. (2010) Long-lasting target binding and rebinding as mechanisms to prolong in vivo drug action, *Br J Pharmacol* 161, 488-508.
8. Kola, I., and Landis, J. (2004) Can the pharmaceutical industry reduce attrition rates?, *Nat Rev Drug Discov* 3, 711-715.
9. Lu, H., England, K., am Ende, C., Truglio, J. J., Luckner, S., Reddy, B. G., Marlenee, N. L., Knudson, S. E., Knudson, D. L., Bowen, R. A., Kisker, C., Slayden, R. A., and Tonge, P. J. (2009) Slow-onset inhibition of the FabI enoyl reductase from *francisella tularensis*: residence time and in vivo activity, *ACS Chem Biol* 4, 221-231.
10. Lu, H., and Tonge, P. J. (2010) Drug-target residence time: critical information for lead optimization, *Curr Opin Chem Biol* 14, 467-474.
11. Van Aller, G. S., Nandigama, R., Petit, C. M., DeWolf, W. E., Jr., Quinn, C. J., Aubart, K. M., Zalacain, M., Christensen, S. B., Copeland, R. A., and Lai, Z. (2005) Mechanism of time-dependent inhibition of polypeptide deformylase by actinonin, *Biochemistry* 44, 253-260.
12. Copeland, R. A., Basavapathruni, A., Moyer, M., and Scott, M. P. (2011) Impact of enzyme concentration and residence time on apparent activity recovery in jump dilution analysis, *Anal Biochem* 416, 206-210.
13. Rajagopalan, R., Misialek, S., Stevens, S. K., Myszka, D. G., Brandhuber, B. J., Ballard, J. A., Andrews, S. W., Seiwert, S. D., and Kossen, K. (2009) Inhibition and binding kinetics of the hepatitis C virus NS3 protease inhibitor ITMN-191 reveals tight binding and slow dissociative behavior, *Biochemistry* 48, 2559-2568.

14. Cooper, M. A. (2004) Advances in membrane receptor screening and analysis, *J Mol Recognit* 17, 286-315.
15. Rich, R. L., and Myszka, D. G. (2000) Advances in surface plasmon resonance biosensor analysis, *Curr Opin Biotechnol* 11, 54-61.
16. Myszka, D. G., and Rich, R. L. (2000) Implementing surface plasmon resonance biosensors in drug discovery, *Pharm Sci Technolo Today* 3, 310-317.
17. Abdiche, Y., Malashock, D., Pinkerton, A., and Pons, J. (2008) Determining kinetics and affinities of protein interactions using a parallel real-time label-free biosensor, the Octet, *Anal Biochem* 377, 209-217.
18. Karlsson, R., Katsamba, P. S., Nordin, H., Pol, E., and Myszka, D. G. (2006) Analyzing a kinetic titration series using affinity biosensors, *Anal Biochem* 349, 136-147.
19. H. Q. Zhang, S. B., and N. J. Tao. (2003) High-performance differential surface plasmon resonance sensor using quadrant cell photodetector, *REVIEW OF SCIENTIFIC INSTRUMENTS* 74.
20. Penefsky, H. S. (1977) Reversible binding of Pi by beef heart mitochondrial adenosine triphosphatase, *J Biol Chem* 252, 2891-2899.
21. Penefsky, H. S. (1979) A centrifuged-column procedure for the measurement of ligand binding by beef heart F1, *Methods Enzymol* 56, 527-530.
22. Tillotson, B., Slocum, K., Coco, J., Whitebread, N., Thomas, B., West, K. A., MacDougall, J., Ge, J., Ali, J. A., Palombella, V. J., Normant, E., Adams, J., and Fritz, C. C. (2010) Hsp90 (Heat Shock Protein 90) Inhibitor Occupancy Is a Direct Determinant of Client Protein Degradation and Tumor Growth Arrest in Vivo, *Journal of Biological Chemistry* 285, 39835-39843.
23. Quemard, A., Sacchettini, J. C., Dessen, A., Vilcheze, C., Bittman, R., Jacobs, W. R., Jr., and Blanchard, J. S. (1995) Enzymatic characterization of the target for isoniazid in *Mycobacterium tuberculosis*, *Biochemistry* 34, 8235-8241.
24. Ward, W. H., Holdgate, G. A., Rowsell, S., McLean, E. G., Pauptit, R. A., Clayton, E., Nichols, W. W., Colls, J. G., Minshull, C. A., Jude, D. A., Mistry, A., Timms, D., Camble, R., Hales, N. J., Britton, C. J., and Taylor, I. W. (1999) Kinetic and structural characteristics of the inhibition of enoyl (acyl carrier protein) reductase by triclosan, *Biochemistry* 38, 12514-12525.
25. Liu, N., Cummings, J. E., England, K., Slayden, R. A., and Tonge, P. J. (2011) Mechanism and inhibition of the FabI enoyl-ACP reductase from *Burkholderia pseudomallei*, *J Antimicrob Chemother* 66, 564-573.

26. Xu, H., Sullivan, T. J., Sekiguchi, J., Kirikae, T., Ojima, I., Stratton, C. F., Mao, W., Rock, F. L., Alley, M. R., Johnson, F., Walker, S. G., and Tonge, P. J. (2008) Mechanism and inhibition of saFabI, the enoyl reductase from *Staphylococcus aureus*, *Biochemistry* 47, 4228-4236.
27. Luckner, S. R., Liu, N., am Ende, C. W., Tonge, P. J., and Kisker, C. (2010) A slow, tight binding inhibitor of InhA, the enoyl-acyl carrier protein reductase from *Mycobacterium tuberculosis*, *J Biol Chem* 285, 14330-14337.
28. Schiebel, J., Chang, A., Lu, H., Baxter, M. V., Tonge, P. J., and Kisker, C. (2012) *Staphylococcus aureus* FabI: inhibition, substrate recognition, and potential implications for in vivo essentiality, *Structure* 20, 802-813.
29. Parikh, S., Moynihan, D. P., Xiao, G., and Tonge, P. J. (1999) Roles of tyrosine 158 and lysine 165 in the catalytic mechanism of InhA, the enoyl-ACP reductase from *Mycobacterium tuberculosis*, *Biochemistry* 38, 13623-13634.
30. am Ende, C. W., Knudson, S. E., Liu, N., Childs, J., Sullivan, T. J., Boyne, M., Xu, H., Gegina, Y., Knudson, D. L., Johnson, F., Peloquin, C. A., Slayden, R. A., and Tonge, P. J. (2008) Synthesis and in vitro antimycobacterial activity of B-ring modified diaryl ether InhA inhibitors, *Bioorg Med Chem Lett* 18, 3029-3033.
31. Sivaraman, S., Sullivan, T. J., Johnson, F., Novichenok, P., Cui, G., Simmerling, C., and Tonge, P. J. (2004) Inhibition of the bacterial enoyl reductase FabI by triclosan: a structure-reactivity analysis of FabI inhibition by triclosan analogues, *J Med Chem* 47, 509-518.
32. Sullivan, T. J., Truglio, J. J., Boyne, M. E., Novichenok, P., Zhang, X., Stratton, C. F., Li, H. J., Kaur, T., Amin, A., Johnson, F., Slayden, R. A., Kisker, C., and Tonge, P. J. (2006) High affinity InhA inhibitors with activity against drug-resistant strains of *Mycobacterium tuberculosis*, *ACS Chem Biol* 1, 43-53.
33. Pan, P. (2012) Lead optimization and slow-onset inhibition of the enoyl-ACP reductase (InhA) from *Mycobacterium tuberculosis*, PhD dissertation.
34. Chang, A., Schiebel, J., Yu, W., Bommineni, G. R., Pan, P., Baxter, M. V., Khanna, A., Sottriffer, C. A., Kisker, C., and Tonge, P. J. (2013) Rational Optimization of Drug-Target Residence Time: Insights from Inhibitor Binding to the *Staphylococcus aureus* FabI Enzyme-Product Complex, *Biochemistry* 52, 4217-4228.
35. Yu, W., Neckles, C., Chang, A., Bommineni, G. R., Spagnuolo, L., Zhang, Z., Liu, N., Lai, C., Truglio, J., and Tonge, P. J. (2015) A [P]NAD-based method to identify and quantitate long residence time enoyl-acyl carrier protein reductase inhibitors, *Anal Biochem* 474C, 40-49.

36. Rawat, R., Whitty, A., and Tonge, P. J. (2003) The isoniazid-NAD adduct is a slow, tight-binding inhibitor of InhA, the Mycobacterium tuberculosis enoyl reductase: adduct affinity and drug resistance, *Proc Natl Acad Sci U S A* 100, 13881-13886.
37. Wang, A., Dorso, C., Kopcho, L., Locke, G., Langish, R., Harstad, E., Shipkova, P., Marcinkeviciene, J., Hamann, L., and Kirby, M. S. (2012) Potency, selectivity and prolonged binding of saxagliptin to DPP4: maintenance of DPP4 inhibition by saxagliptin in vitro and ex vivo when compared to a rapidly-dissociating DPP4 inhibitor, *BMC Pharmacol* 12, 2.
38. Anderson, K., Lai, Z., McDonald, O. B., Stuart, J. D., Nartey, E. N., Hardwicke, M. A., Newlander, K., Dhanak, D., Adams, J., Patrick, D., Copeland, R. A., Tummino, P. J., and Yang, J. (2009) Biochemical characterization of GSK1070916, a potent and selective inhibitor of Aurora B and Aurora C kinases with an extremely long residence time, *Biochem J* 420, 259-265.
39. Garvey, E. P., Schwartz, B., Gartland, M. J., Lang, S., Halsey, W., Sathe, G., Carter, H. L., 3rd, and Weaver, K. L. (2009) Potent inhibitors of HIV-1 integrase display a two-step, slow-binding inhibition mechanism which is absent in a drug-resistant T66I/M154I mutant, *Biochemistry* 48, 1644-1653.
40. Copeland, R. A. (2005) *Evaluation of enzyme inhibitors in drug discovery a guide for medicinal chemists and pharmacologists*, 2nd ed., John Wiley & Sons, Inc, Hoboken.
41. Vauquelin, G., and Van Liefde, I. (2012) Radioligand dissociation measurements: potential interference of rebinding and allosteric mechanisms and physiological relevance of the biological model systems, *Expert Opin Drug Discov* 7, 583-595.
42. Wu, J. T., Wu, L. H., and Knight, J. A. (1986) Stability of NADPH: effect of various factors on the kinetics of degradation, *Clin Chem* 32, 314-319.
43. Hofmann, D., Wirtz, A., Santiago-Schubel, B., Disko, U., and Pohl, M. (2010) Structure elucidation of the thermal degradation products of the nucleotide cofactors NADH and NADPH by nano-ESI-FTICR-MS and HPLC-MS, *Anal Bioanal Chem* 398, 2803-2811.
44. Gooljarsingh, L. T., Fernandes, C., Yan, K., Zhang, H., Grooms, M., Johanson, K., Sinnamon, R. H., Kirkpatrick, R. B., Kerrigan, J., Lewis, T., Arnone, M., King, A. J., Lai, Z., Copeland, R. A., and Tummino, P. J. (2006) A biochemical rationale for the anticancer effects of Hsp90 inhibitors: slow, tight binding inhibition by geldanamycin and its analogues, *Proc Natl Acad Sci U S A* 103, 7625-7630.
45. Uitdehaag, J. C., Sunnen, C. M., van Doornmalen, A. M., de Rouw, N., Oubrie, A., Azevedo, R., Ziebell, M., Nickbarg, E., Karstens, W. J., and Ruygrok, S. (2011) Multidimensional profiling of CSF1R screening hits and inhibitors: assessing cellular activity,

target residence time, and selectivity in a higher throughput way, *J Biomol Screen* 16, 1007-1017.

46. Vauquelin, G. (2012) Determination of drug–receptor residence times by radioligand binding and functional assays: experimental strategies and physiological relevance, *Medicinal chemistry communications*, 645-651.

47. Motulsky, H. J., and Mahan, L. C. (1984) The kinetics of competitive radioligand binding predicted by the law of mass action, *Mol Pharmacol* 25, 1-9.



### Chapter 3

1. Copeland, R. A., Pompliano, D. L., and Meek, T. D. (2006) Drug-target residence time and its implications for lead optimization, *Nat Rev Drug Discov* 5, 730-739.
2. Lu, H., and Tonge, P. J. (2010) Drug-target residence time: critical information for lead optimization, *Curr Opin Chem Biol* 14, 467-474.
3. Tummino, P. J., and Copeland, R. A. (2008) Residence time of receptor-ligand complexes and its effect on biological function, *Biochemistry* 47, 5481-5492.
4. Swinney, D. C. (2008) Applications of Binding Kinetics to Drug Discovery, *Pharmaceutical Medicine* 22, 23 - 34.
5. Holdgate, G. A., and Gill, A. L. (2011) Kinetic efficiency: the missing metric for enhancing compound quality?, *Drug Discov Today* 16, 910-913.
6. Swinney, D. C. (2006) Biochemical mechanisms of New Molecular Entities (NMEs) approved by United States FDA during 2001-2004: mechanisms leading to optimal efficacy and safety, *Curr Top Med Chem* 6, 461-478.
7. Walkup, G. K., You, Z., Ross, P. L., Allen, E. K., Daryaei, F., Hale, M. R., O'Donnell, J., Ehmann, D. E., Schuck, V. J., Buurman, E. T., Choy, A. L., Hajec, L., Murphy-Benenato, K., Marone, V., Patey, S. A., Grosser, L. A., Johnstone, M., Walker, S. G., Tonge, P. J., and Fisher, S. L. (2015) Translating slow-binding inhibition kinetics into cellular and in vivo effects, *Nat Chem Biol*.
8. Wagner, F. F., Zhang, Y. L., Fass, D. M., Joseph, N., Gale, J. P., Weiwer, M., McCarren, P., Fisher, S. L., Kaya, T., Zhao, W. N., Reis, S. A., Hennig, K. M., Thomas, M., Lemercier, B. C., Lewis, M. C., Guan, J. S., Moyer, M. P., Scolnick, E., Haggarty, S. J., Tsai, L. H., and Holson, E. B. (2015) Kinetically Selective Inhibitors of Histone Deacetylase 2 (HDAC2) as Cognition Enhancers, *Chem Sci* 6, 804-815.
9. Jin, M., Petronella, B. A., Cooke, A., Kadalbajoo, M., Siu, K. W., Kleinberg, A., May, E. W., Gokhale, P. C., Schulz, R., Kahler, J., Bittner, M. A., Foreman, K., Pachter, J. A., Wild, R., Epstein, D., and Mulvihill, M. J. (2013) Discovery of novel insulin-like growth factor-1 receptor inhibitors with unique time-dependent binding kinetics, *Acs Med Chem Lett* 4, 627-631.
10. Garvey, E. P. (2010) Structural mechanisms of slow-onset, two- step enzyme inhibition, *Current Chemical Biology* 4, 64 - 73.
11. Guan, R., Ho, M. C., Brenowitz, M., Tyler, P. C., Evans, G. B., Almo, S. C., and Schramm, V. L. (2011) Entropy-driven binding of picomolar transition state analogue inhibitors to human 5'-methylthioadenosine phosphorylase, *Biochemistry* 50, 10408-10417.

12. Fioulaine, S., Boularot, A., Artaud, I., Desmadril, M., Dardel, F., Meinnel, T., and Giglione, C. (2011) Trapping conformational states along ligand-binding dynamics of peptide deformylase: the impact of induced fit on enzyme catalysis, *PLoS Biol* 9, e1001066.
13. Carroll, M. J., Mauldin, R. V., Gromova, A. V., Singleton, S. F., Collins, E. J., and Lee, A. L. (2012) Evidence for dynamics in proteins as a mechanism for ligand dissociation, *Nat Chem Biol* 8, 246-252.
14. Lu, H., England, K., am Ende, C., Truglio, J. J., Luckner, S., Reddy, B. G., Marlenee, N. L., Knudson, S. E., Knudson, D. L., Bowen, R. A., Kisker, C., Slayden, R. A., and Tonge, P. J. (2009) Slow-onset inhibition of the FabI enoyl reductase from *francisella tularensis*: residence time and in vivo activity, *ACS Chem Biol* 4, 221-231.
15. Pan, P., Knudson, S. E., Bommineni, G. R., Li, H. J., Lai, C. T., Liu, N., Garcia-Diaz, M., Simmerling, C., Patil, S. S., Slayden, R. A., and Tonge, P. J. (2014) Time-dependent diaryl ether inhibitors of InhA: structure-activity relationship studies of enzyme inhibition, antibacterial activity, and in vivo efficacy, *ChemMedChem* 9, 776-791.
16. Li, H. J., Lai, C. T., Pan, P., Yu, W., Liu, N., Bommineni, G. R., Garcia-Diaz, M., Simmerling, C., and Tonge, P. J. (2014) A structural and energetic model for the slow-onset inhibition of the *Mycobacterium tuberculosis* enoyl-ACP reductase InhA, *ACS Chem Biol* 9, 986-993.
17. Luckner, S. R., Liu, N., am Ende, C. W., Tonge, P. J., and Kisker, C. (2010) A slow, tight binding inhibitor of InhA, the enoyl-acyl carrier protein reductase from *Mycobacterium tuberculosis*, *J Biol Chem* 285, 14330-14337.
18. Yu, W., Neckles, C., Chang, A., Bommineni, G. R., Spagnuolo, L., Zhang, Z., Liu, N., Lai, C., Truglio, J., and Tonge, P. J. (2015) A [P]NAD-based method to identify and quantitate long residence time enoyl-acyl carrier protein reductase inhibitors, *Anal Biochem* 474C, 40-49.
19. Quemard, A., Sacchettini, J. C., Dessen, A., Vilcheze, C., Bittman, R., Jacobs, W. R., Jr., and Blanchard, J. S. (1995) Enzymatic characterization of the target for isoniazid in *Mycobacterium tuberculosis*, *Biochemistry* 34, 8235-8241.
20. Parikh, S., Moynihan, D. P., Xiao, G., and Tonge, P. J. (1999) Roles of tyrosine 158 and lysine 165 in the catalytic mechanism of InhA, the enoyl-ACP reductase from *Mycobacterium tuberculosis*, *Biochemistry* 38, 13623-13634.
21. Parikh, S. L., Xiao, G., and Tonge, P. J. (2000) Inhibition of InhA, the enoyl reductase from *Mycobacterium tuberculosis*, by triclosan and isoniazid, *Biochemistry* 39, 7645-7650.
22. Chang, A., Schiebel, J., Yu, W., Bommineni, G. R., Pan, P., Baxter, M. V., Khanna, A., Sotriffer, C. A., Kisker, C., and Tonge, P. J. (2013) Rational Optimization of Drug-Target

Residence Time: Insights from Inhibitor Binding to the *Staphylococcus aureus* FabI Enzyme-Product Complex, *Biochemistry* 52, 4217-4228.

23. Ward, W. H., Holdgate, G. A., Rowsell, S., McLean, E. G., Pauptit, R. A., Clayton, E., Nichols, W. W., Colls, J. G., Minshull, C. A., Jude, D. A., Mistry, A., Timms, D., Camble, R., Hales, N. J., Britton, C. J., and Taylor, I. W. (1999) Kinetic and structural characteristics of the inhibition of enoyl (acyl carrier protein) reductase by triclosan, *Biochemistry* 38, 12514-12525.
24. Liu, N., Cummings, J. E., England, K., Slayden, R. A., and Tonge, P. J. (2011) Mechanism and inhibition of the FabI enoyl-ACP reductase from *Burkholderia pseudomallei*, *J Antimicrob Chemother* 66, 564-573.
25. Xu, H., Sullivan, T. J., Sekiguchi, J., Kirikae, T., Ojima, I., Stratton, C. F., Mao, W., Rock, F. L., Alley, M. R., Johnson, F., Walker, S. G., and Tonge, P. J. (2008) Mechanism and inhibition of saFabI, the enoyl reductase from *Staphylococcus aureus*, *Biochemistry* 47, 4228-4236.
26. Schiebel, J., Chang, A., Shah, S., Lu, Y., Liu, L., Pan, P., Hirschbeck, M. W., Tareilus, M., Eltschkner, S., Yu, W., Cummings, J. E., Knudson, S. E., Bommineni, G. R., Walker, S. G., Slayden, R. A., Sottriffer, C. A., Tonge, P. J., and Kisker, C. (2014) Rational design of broad spectrum antibacterial activity based on a clinically relevant enoyl-acyl carrier protein (ACP) reductase inhibitor, *J Biol Chem* 289, 15987-16005.
27. Perryman, A. L., Yu, W., Wang, X., Ekins, S., Forli, S., Li, S. G., Freundlich, J. S., Tonge, P. J., and Olson, A. J. (2015) A Virtual Screen Discovers Novel, Fragment-Sized Inhibitors of *Mycobacterium tuberculosis* InhA, *J Chem Inf Model*.
28. Stec, J., Fomovska, A., Afanador, G. A., Muench, S. P., Zhou, Y., Lai, B. S., El Bissati, K., Hickman, M. R., Lee, P. J., Leed, S. E., Auschwitz, J. M., Sommerville, C., Woods, S., Roberts, C. W., Rice, D., Prigge, S. T., McLeod, R., and Kozikowski, A. P. (2013) Modification of triclosan scaffold in search of improved inhibitors for enoyl-acyl carrier protein (ACP) reductase in *Toxoplasma gondii*, *ChemMedChem* 8, 1138-1160.
29. Menendez, C., Chollet, A., Rodriguez, F., Inard, C., Pasca, M. R., Lherbet, C., and Baltas, M. (2012) Chemical synthesis and biological evaluation of triazole derivatives as inhibitors of InhA and antituberculosis agents, *Eur J Med Chem* 52, 275-283.
30. Menendez, C., Gau, S., Lherbet, C., Rodriguez, F., Inard, C., Pasca, M. R., and Baltas, M. (2011) Synthesis and biological activities of triazole derivatives as inhibitors of InhA and antituberculosis agents, *Eur J Med Chem* 46, 5524-5531.
31. Rawat, R., Whitty, A., and Tonge, P. J. (2003) The isoniazid-NAD adduct is a slow, tight-binding inhibitor of InhA, the *Mycobacterium tuberculosis* enoyl reductase: adduct affinity and drug resistance, *Proc Natl Acad Sci U S A* 100, 13881-13886.

32. Winqvist, J., Geschwindner, S., Xue, Y., Gustavsson, L., Musil, D., Deinum, J., and Danielson, U. H. (2013) Identification of structural-kinetic and structural-thermodynamic relationships for thrombin inhibitors, *Biochemistry* 52, 613-626.
33. Reynolds, C. H., and Holloway, M. K. (2011) Thermodynamics of ligand binding and efficiency, *Acs Med Chem Lett* 2, 433-437.

## Chapter 4

1. Copeland, R. A., Pompliano, D. L., and Meek, T. D. (2006) Drug-target residence time and its implications for lead optimization, *Nat Rev Drug Discov* 5, 730-739.
2. Tummino, P. J., and Copeland, R. A. (2008) Residence time of receptor-ligand complexes and its effect on biological function, *Biochemistry* 47, 5481-5492.
3. Kola, I., and Landis, J. (2004) Can the pharmaceutical industry reduce attrition rates?, *Nat Rev Drug Discov* 3, 711-715.
4. Lu, H., and Tonge, P. J. (2010) Drug-target residence time: critical information for lead optimization, *Curr Opin Chem Biol* 14, 467-474.
5. Lu, H., England, K., am Ende, C., Truglio, J. J., Luckner, S., Reddy, B. G., Marlenee, N. L., Knudson, S. E., Knudson, D. L., Bowen, R. A., Kisker, C., Slayden, R. A., and Tonge, P. J. (2009) Slow-onset inhibition of the FabI enoyl reductase from *francisella tularensis*: residence time and in vivo activity, *ACS Chem Biol* 4, 221-231.
6. Walkup, G. K., You, Z., Ross, P. L., Allen, E. K., Daryaei, F., Hale, M. R., O'Donnell, J., Ehmann, D. E., Schuck, V. J., Buurman, E. T., Choy, A. L., Hajec, L., Murphy-Benenato, K., Marone, V., Patey, S. A., Grosser, L. A., Johnstone, M., Walker, S. G., Tonge, P. J., and Fisher, S. L. (2015) Translating slow-binding inhibition kinetics into cellular and in vivo effects, *Nat Chem Biol*.
7. Chang, A. (2013) *S. aureus* FabI: Linking Catalysis, Inhibition and Cellular Effects, Dissertation.
8. Wei, J. R., Krishnamoorthy, V., Murphy, K., Kim, J. H., Schnappinger, D., Alber, T., Sasseti, C. M., Rhee, K. Y., and Rubin, E. J. (2011) Depletion of antibiotic targets has widely varying effects on growth, *Proc Natl Acad Sci U S A* 108, 4176-4181.
9. Lei, B., Wei, C. J., and Tu, S. C. (2000) Action mechanism of antitubercular isoniazid. Activation by *Mycobacterium tuberculosis* KatG, isolation, and characterization of inha inhibitor, *J Biol Chem* 275, 2520-2526.
10. Kai Johnsson, D. S. K., and Peter G. Schultz. (1995) Studies on the Mechanism of Action of Isoniazid and Ethionamide in the Chemotherapy of Tuberculosis, *Journal of American Chemistry Society* 117, 5009 - 2010.
11. Pan, P., Knudson, S. E., Bommineni, G. R., Li, H. J., Lai, C. T., Liu, N., Garcia-Diaz, M., Simmerling, C., Patil, S. S., Slayden, R. A., and Tonge, P. J. (2014) Time-dependent diaryl ether inhibitors of InhA: structure-activity relationship studies of enzyme inhibition, antibacterial activity, and in vivo efficacy, *ChemMedChem* 9, 776-791.

12. Yu, W., Neckles, C., Chang, A., Bommineni, G. R., Spagnuolo, L., Zhang, Z., Liu, N., Lai, C., Truglio, J., and Tonge, P. J. (2015) A [P]NAD-based method to identify and quantitate long residence time enoyl-acyl carrier protein reductase inhibitors, *Anal Biochem* 474C, 40-49.
13. Hurdle, J. G., Lee, R. B., Budha, N. R., Carson, E. I., Qi, J., Scherman, M. S., Cho, S. H., McNeil, M. R., Lenaerts, A. J., Franzblau, S. G., Meibohm, B., and Lee, R. E. (2008) A microbiological assessment of novel nitrofuranyl amides as anti-tuberculosis agents, *J Antimicrob Chemother* 62, 1037-1045.
14. Bundtzen, R. W., Gerber, A. U., Cohn, D. L., and Craig, W. A. (1981) Postantibiotic suppression of bacterial growth, *Rev Infect Dis* 3, 28-37.
15. Li, R. C. (1996) Simultaneous pharmacodynamic analysis of the lag and bactericidal phases exhibited by beta-lactams against *Escherichia coli*, *Antimicrob Agents Chemother* 40, 2306-2310.
16. Sato, N., Suzuki, H., Hayashi, H., Shibasaki, S., Sugano, T., Maebashi, K., Kurosawa, T., Shiomi, M., and Ogata, H. (2008) New concept and a theoretical consideration of the mechanism-based pharmacokinetics/ pharmacodynamics (PK/PD) modeling for antimicrobial agents, *Jpn J Antibiot* 61, 314-338.
17. GOPINATHAN, R. G. a. K. P. (1980) Growth of *Mycobacterium smegmatis* in minimal and complete media, *Journal of Bioscience* 2, 337 - 348.

## Chapter 5

1. WHO. (2013) Global Tuberculosis Report, World Health Organization, Geneva.
2. Abubakar, I., Zignol, M., Falzon, D., Raviglione, M., Ditiu, L., Masham, S., Adetifa, I., Ford, N., Cox, H., Lawn, S. D., Marais, B. J., McHugh, T. D., Mwaba, P., Bates, M., Lipman, M., Zijenah, L., Logan, S., McNerney, R., Zumla, A., Sarda, K., Nahid, P., Hoelscher, M., Pletschette, M., Memish, Z. A., Kim, P., Hafner, R., Cole, S., Migliori, G. B., Maeurer, M., Schito, M., and Zumla, A. (2013) Drug-resistant tuberculosis: time for visionary political leadership, *The Lancet Infectious Diseases* 13, 529-539.
3. Velayati, A. A., Farnia, P., and Masjedi, M. R. (2013) The totally drug resistant tuberculosis (TDR-TB), *Int J Clin Exp Med* 6, 307-309.
4. Dheda, K., and Migliori, G. B. (2012) The global rise of extensively drug-resistant tuberculosis: is the time to bring back sanatoria now overdue?, *The Lancet* 379, 773-775.
5. Gothi, D., and Joshi, J. M. (2011) Resistant TB: Newer Drugs and Community Approach, *Recent Pat Antiinfect Drug Discov* 6, 27-37.
6. Udhwadia, Z. F., Amale, R. A., Ajbani, K. K., and Rodrigues, C. (2012) Totally Drug-Resistant Tuberculosis in India, *Clinical Infectious Diseases* 54, 579-581.
7. Velayati, A. A., Masjedi, M. R., Farnia, P., Tabarsi, P., Ghanavi, J., ZiaZarifi, A. H., and Hoffner, S. E. (2009) Emergence of new forms of totally drug-resistant tuberculosis bacilli: Super extensively drug-resistant tuberculosis or totally drug-resistant strains in iran, *CHEST Journal* 136, 420-425.
8. Shah, N. S., Richardson, J., Moodley, P., Babaria, P., Ramtahal, M., Heysell, S. K., Li, X., Moll, A. P., Friedland, G., Sturm, A. W., and Gandhi, N. R. (2011) Increasing drug resistance in extensively drug-resistant tuberculosis, South Africa, *Emerg Infect Dis* 17, 510-513.
9. Vilchèze, C., and Jacobs Jr, W. R. (2007) The mechanism of isoniazid killing: clarity through the scope of genetics., *Ann Rev Microbiol* 61, 35-50.
10. Vilcheze, C., Wang, F., Arai, M., Hazbon, M. H., Colangeli, R., Kremer, L., Weisbrod, T. R., Alland, D., Sacchettini, J. C., and Jacobs, W. R. (2006) Transfer of a point mutation in *Mycobacterium tuberculosis inhA* resolves the target of isoniazid, *Nat Med* 12, 1027-1029.
11. Freundlich, J. S., Wang, F., Vilchèze, C., Gulten, G., Langley, R., Schiehser, G. A., Jacobus, D. P., Jacobs, W. R., and Sacchettini, J. C. (2009) Triclosan Derivatives: Towards Potent Inhibitors of Drug-Sensitive and Drug-Resistant *Mycobacterium tuberculosis*, *ChemMedChem* 4, 241-248.

12. North, E. J., Jackson, M., and Lee, R. E. (2014) New Approaches to Target the Mycolic Acid Biosynthesis Pathway for the Development of Tuberculosis Therapeutics, *Curr Pharm Des* 20, 4357-4378.
13. Vilcheze, C., Baughn, A. D., Tufariello, J., Leung, L. W., Kuo, M., Basler, C. F., Alland, D., Sacchettini, J. C., Freundlich, J. S., and Jacobs, W. R., Jr. (2011) Novel inhibitors of InhA efficiently kill *Mycobacterium tuberculosis* under aerobic and anaerobic conditions, *Antimicrob Agents Chemother* 55, 3889-3898.
14. Heym, B., Zhang, Y., Poulet, S., Young, D., and Cole, S. T. (1993) Characterization of the *katG* gene encoding a catalase-peroxidase required for the isoniazid susceptibility of *Mycobacterium tuberculosis*, *Journal of Bacteriology* 175, 4255-4259.
15. Encinas, L., O'Keefe, H., Neu, M., Remuinan, M. J., Patel, A. M., Guardia, A., Davie, C. P., Perez-Macias, N., Yang, H., Convery, M. A., Messer, J. A., Perez-Herran, E., Centrella, P. A., Alvarez-Gomez, D., Clark, M. A., Huss, S., O'Donovan, G. K., Ortega-Muro, F., McDowell, W., Castaneda, P., Arico-Muendel, C. C., Pajk, S., Rullas, J., Angulo-Barturen, I., Alvarez-Ruiz, E., Mendoza-Losana, A., Pages, L. B., Castro-Pichel, J., and Evindar, G. (2014) Encoded library technology as a source of hits for the discovery and lead optimization of a potent and selective class of bactericidal direct inhibitors of *Mycobacterium tuberculosis* InhA, *J Med Chem* 57, 1276-1288.
16. Zhang, L., Ye, Y., Duo, L., Wang, T., Song, X., Lu, X., Ying, B., and Wang, L. (2011) Application of genotype MTBDRplus in rapid detection of the *Mycobacterium tuberculosis* complex as well as its resistance to isoniazid and rifampin in a high volume laboratory in Southern China, *Mol Biol Rep* 38, 2185-2192.
17. Tonge, P. J., Kisker, C., and Slayden, R. A. (2007) Development of modern InhA inhibitors to combat drug resistant strains of *Mycobacterium tuberculosis*, *Curr Top Med Chem* 7, 489-498.
18. Hazbon, M. H., Brimacombe, M., Bobadilla del Valle, M., Cavatore, M., Guerrero, M. I., Varma-Basil, M., Billman-Jacobe, H., Lavender, C., Fyfe, J., Garcia-Garcia, L., Leon, C. I., Bose, M., Chaves, F., Murray, M., Eisenach, K. D., Sifuentes-Osornio, J., Cave, M. D., Ponce de Leon, A., and Alland, D. (2006) Population genetics study of isoniazid resistance mutations and evolution of multidrug-resistant *Mycobacterium tuberculosis*, *Antimicrob Agents Chemother* 50, 2640-2649.
19. Ajbani, K., Rodrigues, C., Shenai, S., and Mehta, A. (2011) Mutation Detection and Accurate Diagnosis of Extensively Drug-Resistant Tuberculosis: Report from a Tertiary Care Center in India, *Journal of Clinical Microbiology* 49, 1588-1590.



20. Chia, B.-S., Lanzas, F., Rifat, D., Herrera, A., Kim, E. Y., Sailer, C., Torres-Chavolla, E., Narayanaswamy, P., Einarsson, V., Bravo, J., Pascale, J. M., Ioerger, T. R., Sacchettini, J. C., and Karakousis, P. C. (2012) Use of Multiplex Allele-Specific Polymerase Chain Reaction (MAS-PCR) to Detect Multidrug-Resistant Tuberculosis in Panama, *PLoS ONE* 7, e40456.
21. Fenner, L., Egger, M., Bodmer, T., Altpeter, E., Zwahlen, M., Jaton, K., Pfyffer, G. E., Borrell, S., Dubuis, O., Bruderer, T., Siegrist, H. H., Furrer, H., Calmy, A., Fehr, J., Stalder, J. M., Ninet, B., Bottger, E. C., and Gagneux, S. (2012) Effect of mutation and genetic background on drug resistance in *Mycobacterium tuberculosis*, *Antimicrob Agents Chemother* 56, 3047-3053.
22. Tessema, B., Beer, J., Emmrich, F., Sack, U., and Rodloff, A. C. (2012) Analysis of gene mutations associated with isoniazid, rifampicin and ethambutol resistance among *Mycobacterium tuberculosis* isolates from Ethiopia, *BMC Infect Dis* 12, 37.
23. Shubladze, N., Tadumadze, N., and Bablshvili, N. (2013) Molecular patterns of multidrug resistance of in Georgia, *Int J Mycobacteriol* 2, 73-78.
24. Hung, N. V., Ando, H., Thuy, T. T., Kuwahara, T., Hang, N. T., Sakurada, S., Thuong, P. H., Lien, L. T., and Keicho, N. (2013) Clonal expansion of *Mycobacterium tuberculosis* isolates and coexisting drug resistance in patients newly diagnosed with pulmonary tuberculosis in Hanoi, Vietnam, *BMC Res Notes* 6, 444.
25. Tseng, S. T., Tai, C. H., Li, C. R., Lin, C. F., and Shi, Z. Y. (2013) The mutations of *katG* and *inhA* genes of isoniazid-resistant *Mycobacterium tuberculosis* isolates in Taiwan, *J Microbiol Immunol Infect*, 163-171.
26. Huyen, M. N., Cobelens, F. G., Buu, T. N., Lan, N. T., Dung, N. H., Kremer, K., Tiemersma, E. W., and van Soolingen, D. (2013) Epidemiology of isoniazid resistance mutations and their effect on tuberculosis treatment outcomes, *Antimicrob Agents Chemother* 57, 3620-3627.
27. Yadav, R., Sethi, S., Dhatwalia, S. K., Gupta, D., Mewara, A., and Sharma, M. (2013) Molecular characterisation of drug resistance in *Mycobacterium tuberculosis* isolates from North India, *Int J Tuberc Lung Dis* 17, 251-257.
28. Varghese, B., Hillemann, A., Wijayanti, D. R., Shoukri, M., Al-rabiah, F., Al-Omari, R., and Al-Hajoj, S. (2012) New insight into the molecular characterization of isoniazid and rifampicin resistant *Mycobacterium tuberculosis* strains from Saudi Arabia, *Infect Genet Evol* 12, 549-556.
29. Ali, A., Hasan, R., Jabeen, K., Jabeen, N., Qadeer, E., and Hasan, Z. (2011) Characterization of mutations conferring extensive drug resistance to *Mycobacterium tuberculosis* isolates in Pakistan, *Antimicrob Agents Chemother* 55, 5654-5659.

30. Balabanova, Y., Nikolayevskyy, V., Ignatyeva, O., Kontsevaya, I., Rutterford, C. M., Shakhmistova, A., Malomanova, N., Chinkova, Y., Mironova, S., Fedorin, I., and Drobniowski, F. A. (2011) Survival of civilian and prisoner drug-sensitive, multi- and extensive drug-resistant tuberculosis cohorts prospectively followed in Russia, *PLoS ONE* 6, e20531.
31. Kozhamkulov, U., Akhmetova, A., Rakhimova, S., Belova, E., Alenova, A., Bismilda, V., Chingissova, L., Ismailov, S., Ramanculov, E., and Momynaliev, K. (2011) Molecular characterization of rifampicin- and isoniazid-resistant *Mycobacterium tuberculosis* strains isolated in Kazakhstan, *Jpn J Infect Dis* 64, 253-255.
32. He, X., Alian, A., Stroud, R., and Ortiz de Montellano, P. R. (2006) Pyrrolidine carboxamides as a novel class of inhibitors of enoyl acyl carrier protein reductase from *Mycobacterium tuberculosis*, *J Med Chem* 49, 6308-6323.
33. Shirude, P. S., Madhavapeddi, P., Naik, M., Murugan, K., Shinde, V., Nandishaiah, R., Bhat, J., Kumar, A., Hameed, S., Holdgate, G., Davies, G., McMiken, H., Hegde, N., Ambady, A., Venkatraman, J., Panda, M., Bandodkar, B., Sambandamurthy, V. K., and Read, J. A. (2013) Methyl-thiazoles: a novel mode of inhibition with the potential to develop novel inhibitors targeting InhA in *Mycobacterium tuberculosis*, *J Med Chem* 56, 8533-8542.
34. Encinas, L., O'Keefe, H., Neu, M., Remuinan, M. J., Patel, A. M., Guardia, A., Davie, C. P., Perez-Macias, N., Yang, H., Convery, M. A., Messer, J. A., Perez-Herran, E., Centrella, P. A., Alvarez-Gomez, D., Clark, M. A., Huss, S., O'Donovan, G. K., Ortega-Muro, F., McDowell, W., Castaneda, P., Arico-Muendel, C. C., Pajk, S., Rullas, J., Angulo-Barturen, I., Alvarez-Ruiz, E., Mendoza-Losana, A., Ballell Pages, L., Castro-Pichel, J., and Evindar, G. (2014) Encoded library technology as a source of hits for the discovery and lead optimization of a potent and selective class of bactericidal direct inhibitors of *Mycobacterium tuberculosis* InhA, *J Med Chem* 57, 1276-1288.
35. Hartkoorn, R. C., Sala, C., Neres, J., Pojer, F., Magnet, S., Mukherjee, R., Uplekar, S., Boy-Rottger, S., Altmann, K. H., and Cole, S. T. (2012) Towards a new tuberculosis drug: pyridomycin - nature's isoniazid, *EMBO Mol Med* 4, 1032-1042.
36. Zhu, T., Cao, S., Su, P.-C., Patel, R., Shah, D., Chokshi, H. B., Szukala, R., Johnson, M. E., and Hevener, K. E. (2013) Hit Identification and Optimization in Virtual Screening: Practical Recommendations Based on a Critical Literature Analysis, *J Med Chem* 56, 6560-6572.
37. Tanrikulu, Y., Kruger, B., and Proschak, E. (2013) The holistic integration of virtual screening in drug discovery, *Drug Discov Today* 18, 358-364.
38. Goodsell, D. S., and Olson, A. J. (1990) Automated docking of substrates to proteins by simulated annealing, *Proteins* 8, 195-202.

39. Goodsell, D. S., Lauble, H., Stout, C. D., and Olson, A. J. (1993) Automated docking in crystallography: analysis of the substrates of aconitase, *Proteins* 17, 1-10.
40. Goodsell, D. S., Morris, G. M., and Olson, A. J. (1996) Automated docking of flexible ligands: applications of AutoDock, *J Mol Recognit* 9, 1-5.
41. Morris, G. M., Goodsell, D. S., Huey, R., and Olson, A. J. (1996) Distributed automated docking of flexible ligands to proteins: parallel applications of AutoDock 2.4, *J Comput Aided Mol Des* 10, 293-304.
42. Olson, A. J., and Goodsell, D. S. (1998) Automated docking and the search for HIV protease inhibitors, *SAR QSAR Environ Res* 8, 273-285.
43. Soares, T. A., Goodsell, D. S., Briggs, J. M., Ferreira, R., and Olson, A. J. (1999) Docking of 4-oxalocrotonate tautomerase substrates: implications for the catalytic mechanism, *Biopolymers* 50, 319-328.
44. Osterberg, F., Morris, G. M., Sanner, M. F., Olson, A. J., and Goodsell, D. S. (2002) Automated docking to multiple target structures: incorporation of protein mobility and structural water heterogeneity in AutoDock, *Proteins* 46, 34-40.
45. Trott, O., and Olson, A. J. (2010) AutoDock Vina: improving the speed and accuracy of docking with a new scoring function, efficient optimization, and multithreading, *J Comput Chem* 31, 455-461.
46. Kumar, M., Vijayakrishnan, R., and Subba Rao, G. (2010) In silico structure-based design of a novel class of potent and selective small peptide inhibitor of Mycobacterium tuberculosis Dihydrofolate reductase, a potential target for anti-TB drug discovery, *Mol Divers* 14, 595-604.
47. Kumar, A., and Siddiqi, M. I. (2008) Virtual screening against Mycobacterium tuberculosis dihydrofolate reductase: suggested workflow for compound prioritization using structure interaction fingerprints, *J Mol Graph Model* 27, 476-488.
48. Lu, X. Y., Chen, Y. D., Jiang, Y. J., and You, Q. D. (2009) Discovery of potential new InhA direct inhibitors based on pharmacophore and 3D-QSAR analysis followed by in silico screening, *Eur J Med Chem* 44, 3718-3730.
49. Lu, X. Y., Chen, Y. D., and You, Q. D. (2010) 3D-QSAR studies of arylcarboxamides with inhibitory activity on InhA using pharmacophore-based alignment, *Chem Biol Drug Des* 75, 195-203.
50. Subba Rao, G., Vijayakrishnan, R., and Kumar, M. (2008) Structure-based design of a novel class of potent inhibitors of InhA, the enoyl acyl carrier protein reductase from Mycobacterium tuberculosis: a computer modelling approach, *Chem Biol Drug Des* 72, 444-449.

51. Punkvang, A., Saparpakorn, P., Hannongbua, S., Wolschann, P., and Pungpo, P. (2010) Elucidating drug-enzyme interactions and their structural basis for improving the affinity and potency of isoniazid and its derivatives based on computer modeling approaches, *Molecules* 15, 2791-2813.
52. Kinnings, S. L., Liu, N., Tonge, P. J., Jackson, R. M., Xie, L., and Bourne, P. E. (2011) A machine learning-based method to improve docking scoring functions and its application to drug repurposing, *Journal of Chemical Information and Modeling* 51, 408-419.
53. Pauli, I., dos Santos, R. N., Rostirolla, D. C., Martinelli, L. K., Ducati, R. G., Timmers, L. F., Basso, L. A., Santos, D. S., Guido, R. V., Andricopulo, A. D., and Norberto de Souza, O. (2013) Discovery of new inhibitors of *Mycobacterium tuberculosis* InhA enzyme using virtual screening and a 3D-pharmacophore-based approach, *J Chem Inf Model* 53, 2390-2401.
54. Mohan, S. B., Ravi Kumar, B. V., Dinda, S. C., Naik, D., Prabu Seenivasan, S., Kumar, V., Rana, D. N., and Brahmshatriya, P. S. (2012) Microwave-assisted synthesis, molecular docking and antitubercular activity of 1,2,3,4-tetrahydropyrimidine-5-carbonitrile derivatives, *Bioorg Med Chem Lett* 22, 7539-7542.
55. Muddassar, M., Jang, J. W., Hong, S. K., Cho, Y. S., Kim, E. E., Keum, K. C., Oh, T., Cho, S. N., and Pae, A. N. (2010) Identification of novel antitubercular compounds through hybrid virtual screening approach, *Bioorg Med Chem* 18, 6914-6921.
56. Izumizono, Y., Arevalo, S., Koseki, Y., Kuroki, M., and Aoki, S. (2011) Identification of novel potential antibiotics for tuberculosis by in silico structure-based drug screening, *Eur J Med Chem* 46, 1849-1856.
57. Kinjo, T., Koseki, Y., Kobayashi, M., Yamada, A., Morita, K., Yamaguchi, K., Tsurusawa, R., Gulten, G., Komatsu, H., Sakamoto, H., Sacchettini, J. C., Kitamura, M., and Aoki, S. (2013) Identification of compounds with potential antibacterial activity against *Mycobacterium* through structure-based drug screening, *J Chem Inf Model* 53, 1200-1212.
58. Payne, D. J., Gwynn, M. N., Holmes, D. J., and Pompliano, D. L. (2007) Drugs for bad bugs: confronting the challenges of antibacterial discovery, *Nat Rev Drug Discov* 6, 29-40.
59. Plouffe, D., Brinker, A., McNamara, C., Henson, K., Kato, N., Kuhen, K., Nagle, A., Adrian, F., Matzen, J. T., Anderson, P., Nam, T. G., Gray, N. S., Chatterjee, A., Janes, J., Yan, S. F., Trager, R., Caldwell, J. S., Schultz, P. G., Zhou, Y., and Winzeler, E. A. (2008) In silico activity profiling reveals the mechanism of action of antimalarials discovered in a high-throughput screen, *Proc Natl Acad Sci U S A* 105, 9059-9064.
60. Kumar, A., Zhang, M., Zhu, L., Liao, R. P., Mutai, C., Hafsat, S., Sherman, D. R., and Wang, M. W. (2012) High-throughput screening and sensitized bacteria identify an *M. tuberculosis* dihydrofolate reductase inhibitor with whole cell activity, *PLoS One* 7, e39961.

61. Stanley, S. A., Grant, S. S., Kawate, T., Iwase, N., Shimizu, M., Wivagg, C., Silvis, M., Kazyanskaya, E., Aquadro, J., Golas, A., Fitzgerald, M., Dai, H., Zhang, L., and Hung, D. T. (2012) Identification of novel inhibitors of *M. tuberculosis* growth using whole cell based high-throughput screening, *ACS Chem Biol* 7, 1377-1384.
62. Katzianer, D. S., Yano, T., Rubin, H., and Zhu, J. (2014) A high-throughput small-molecule screen to identify a novel chemical inhibitor of *Clostridium difficile*, *Int J Antimicrob Agents* 44, 69-73.
63. Perryman, A. L. (2011) I'll take "Curing Malaria" for \$1,000, Alex, In *Citizen IBM* (Fishkind, A., and Gordon, R., Eds.), IBM.
64. Perryman, A. L. (2011) GO Fight Against Malaria, In *World Community Grid* (IBM, Ed.), p World Community Grid's GO FAM section, IBM Corporation.
65. Perryman, A. L., and Olson, A. J. (2013) Global Online Fight Against Malaria project.
66. Irwin, J. J., and Shoichet, B. K. (2005) ZINC--a free database of commercially available compounds for virtual screening, *J Chem Inf Model* 45, 177-182.
67. Luckner, S. R., Liu, N., am Ende, C. W., Tonge, P. J., and Kisker, C. (2010) A slow, tight binding inhibitor of InhA, the enoyl-acyl carrier protein reductase from *Mycobacterium tuberculosis*, *J Biol Chem* 285, 14330-14337.
68. Stec, J., Vilcheze, C., Lun, S., Perryman, A. L., Wang, X., Freundlich, J. S., Bishai, W., Jacobs, W. R., Jr., and Kozikowski, A. P. (2014) Biological evaluation of potent triclosan-derived inhibitors of the enoyl-acyl carrier protein reductase InhA in drug-sensitive and drug-resistant strains of *Mycobacterium tuberculosis*, *ChemMedChem* 9, 2528-2537.
69. Ekins, S., Clark, A. M., and Sarker, M. (2013) TB Mobile: a mobile app for anti-tuberculosis molecules with known targets, *J Cheminform* 5, 13.
70. Clark, A. M., Sarker, M., and Ekins, S. (2014) New target prediction and visualization tools incorporating open source molecular fingerprints for TB Mobile 2.0, *Journal of Cheminformatics* 6, 38-54.
71. Inc., A. S. (2013) *Discovery Studio Modeling Environment*, Release 4.0 ed., Accelrys Software Inc., San Diego, CA.
72. Franzblau, S. G., Witzig, R. S., McLaughlin, J. C., Torres, P., Madico, G., Hernandez, A., Degnan, M. T., Cook, M. B., Quenzer, V. K., Ferguson, R. M., and Gilman, R. H. (1998) Rapid, low-technology MIC determination with clinical *Mycobacterium tuberculosis* isolates by using the microplate Alamar Blue assay, *J Clin Microbiol* 36, 362-366.

73. Rao, S. P., Lakshminarayana, S. B., Kondreddi, R. R., Herve, M., Camacho, L. R., Bifani, P., Kalapala, S. K., Jiricek, J., Ma, N. L., Tan, B. H., Ng, S. H., Nanjundappa, M., Ravindran, S., Seah, P. G., Thayalan, P., Lim, S. H., Lee, B. H., Goh, A., Barnes, W. S., Chen, Z., Gagaring, K., Chatterjee, A. K., Pethe, K., Kuhen, K., Walker, J., Feng, G., Babu, S., Zhang, L., Blasco, F., Beer, D., Weaver, M., Dartois, V., Glynne, R., Dick, T., Smith, P. W., Diagana, T. T., and Manjunatha, U. H. (2013) Indolcarboxamide is a preclinical candidate for treating multidrug-resistant tuberculosis, *Sci Transl Med* 5, 214ra168.
74. Leeds, J. A., Sachdeva, M., Mullin, S., Barnes, S. W., and Ruzin, A. (2014) In vitro selection, via serial passage, of *Clostridium difficile* mutants with reduced susceptibility to fidaxomicin or vancomycin, *J Antimicrob Chemother* 69, 41-44.
75. Chang, A., Schiebel, J., Yu, W., Bommineni, G. R., Pan, P., Baxter, M. V., Khanna, A., Sotriffer, C. A., Kisker, C., and Tonge, P. J. (2013) Rational Optimization of Drug-Target Residence Time: Insights from Inhibitor Binding to the *Staphylococcus aureus* FabI Enzyme-Product Complex, *Biochemistry* 52, 4217-4228.
76. Manjunatha, U. H., SP, S. R., Kondreddi, R. R., Noble, C. G., Camacho, L. R., Tan, B. H., Ng, S. H., Ng, P. S., Ma, N. L., Lakshminarayana, S. B., Herve, M., Barnes, S. W., Yu, W., Kuhen, K., Blasco, F., Beer, D., Walker, J. R., Tonge, P. J., Glynne, R., Smith, P. W., and Diagana, T. T. (2015) Direct inhibitors of InhA are active against *Mycobacterium tuberculosis*, *Sci Transl Med* 7, 269ra263.
77. Yu, W., Neckles, C., Chang, A., Bommineni, G. R., Spagnuolo, L., Zhang, Z., Liu, N., Lai, C., Truglio, J., and Tonge, P. J. (2015) A [P]NAD-based method to identify and quantitate long residence time enoyl-acyl carrier protein reductase inhibitors, *Anal Biochem* 474C, 40-49.
78. Forli, S., and Olson, A. J. (2010) Raccoon, Molecular Graphics Laboratory.
79. Cosconati, S., Forli, S., Perryman, A. L., Harris, R., Goodsell, D. S., and Olson, A. J. (2010) Virtual screening with AutoDock: theory and practice, *Expert Opin Drug Discov* 5, 597-607.
80. Perryman, A. L., Santiago, D. N., Forli, S., Santos-Martins, D., and Olson, A. J. (2014) Virtual screening with AutoDock Vina and the common pharmacophore engine of a low diversity library of fragments and hits against the three allosteric sites of HIV integrase: participation in the SAMPL4 protein-ligand binding challenge, *J Comput Aided Mol Des* 28, 429-441.
81. Sullivan, T. J., Truglio, J. J., Boyne, M. E., Novichenok, P., Zhang, X., Stratton, C. F., Li, H. J., Kaur, T., Amin, A., Johnson, F., Slayden, R. A., Kisker, C., and Tonge, P. J. (2006) High affinity InhA inhibitors with activity against drug-resistant strains of *Mycobacterium tuberculosis*, *ACS Chem Biol* 1, 43-53.

82. Mobley, D. L., Liu, S., Lim, N. M., Wymer, K. L., Perryman, A. L., Forli, S., Deng, N., Su, J., Branson, K., and Olson, A. J. (2014) Blind prediction of HIV integrase binding from the SAMPL4 challenge, *J Comput Aided Mol Des* 28, 327-345.
83. Voet, A. R., Kumar, A., Berenger, F., and Zhang, K. Y. (2014) Combining in silico and in cerebro approaches for virtual screening and pose prediction in SAMPL4, *J Comput Aided Mol Des* 28, 363-373.
84. Lipinski, C. A., Lombardo, F., Dominy, B. W., and Feeney, P. J. (2001) Experimental and computational approaches to estimate solubility and permeability in drug discovery and development settings, *Advanced Drug Delivery Reviews* 46, 3-26.
85. Hunter, C. A. (1993) Sequence-dependent DNA structure. The role of base stacking interactions, *J Mol Biol* 230, 1025-1054.
86. Jiang, X., Loo, D. D., Hirayama, B. A., and Wright, E. M. (2012) The importance of being aromatic: pi interactions in sodium symporters, *Biochemistry* 51, 9480-9487.
87. Durrant, J. D., and McCammon, J. A. (2011) BINANA: a novel algorithm for ligand-binding characterization, *J Mol Graph Model* 29, 888-893.
88. Sponer, J., Leszczynski, J., and Hobza, P. (2001) Electronic properties, hydrogen bonding, stacking, and cation binding of DNA and RNA bases, *Biopolymers* 61, 3-31.
89. Morris, G. M., Huey, R., Lindstrom, W., Sanner, M. F., Belew, R. K., Goodsell, D. S., and Olson, A. J. (2009) AutoDock4 and AutoDockTools4: Automated docking with selective receptor flexibility, *J Comput Chem* 30, 2785-2791.
90. Lefebvre, E., and Schiffer, C. A. (2008) Resilience to resistance of HIV-1 protease inhibitors: profile of darunavir, *AIDS Rev* 10, 131-142.
91. Nalam, M. N., Ali, A., Altman, M. D., Reddy, G. S., Chellappan, S., Kairys, V., Ozen, A., Cao, H., Gilson, M. K., Tidor, B., Rana, T. M., and Schiffer, C. A. (2010) Evaluating the substrate-envelope hypothesis: structural analysis of novel HIV-1 protease inhibitors designed to be robust against drug resistance, *J Virol* 84, 5368-5378.
92. Kairys, V., Gilson, M. K., Lather, V., Schiffer, C. A., and Fernandes, M. X. (2009) Toward the design of mutation-resistant enzyme inhibitors: further evaluation of the substrate envelope hypothesis, *Chem Biol Drug Des* 74, 234-245.
93. Altman, M. D., Ali, A., Reddy, G. S., Nalam, M. N., Anjum, S. G., Cao, H., Chellappan, S., Kairys, V., Fernandes, M. X., Gilson, M. K., Schiffer, C. A., Rana, T. M., and Tidor, B. (2008) HIV-1 protease inhibitors from inverse design in the substrate envelope exhibit subnanomolar binding to drug-resistant variants, *J Am Chem Soc* 130, 6099-6113.

94. Chellappan, S., Kiran Kumar Reddy, G. S., Ali, A., Nalam, M. N., Anjum, S. G., Cao, H., Kairys, V., Fernandes, M. X., Altman, M. D., Tidor, B., Rana, T. M., Schiffer, C. A., and Gilson, M. K. (2007) Design of mutation-resistant HIV protease inhibitors with the substrate envelope hypothesis, *Chem Biol Drug Des* 69, 298-313.
95. Prabu-Jeyabalan, M., King, N. M., Nalivaika, E. A., Heilek-Snyder, G., Cammack, N., and Schiffer, C. A. (2006) Substrate envelope and drug resistance: crystal structure of RO1 in complex with wild-type human immunodeficiency virus type 1 protease, *Antimicrob Agents Chemother* 50, 1518-1521.
96. King, N. M., Prabu-Jeyabalan, M., Nalivaika, E. A., Wigerinck, P., de Bethune, M. P., and Schiffer, C. A. (2004) Structural and thermodynamic basis for the binding of TMC114, a next-generation human immunodeficiency virus type 1 protease inhibitor, *J Virol* 78, 12012-12021.
97. King, N. M., Prabu-Jeyabalan, M., Nalivaika, E. A., and Schiffer, C. A. (2004) Combating susceptibility to drug resistance: lessons from HIV-1 protease, *Chem Biol* 11, 1333-1338.
98. Nalam, M. N., Ali, A., Reddy, G. S., Cao, H., Anjum, S. G., Altman, M. D., Yilmaz, N. K., Tidor, B., Rana, T. M., and Schiffer, C. A. (2013) Substrate envelope-designed potent HIV-1 protease inhibitors to avoid drug resistance, *Chem Biol* 20, 1116-1124.
99. Shen, Y., Altman, M. D., Ali, A., Nalam, M. N., Cao, H., Rana, T. M., Schiffer, C. A., and Tidor, B. (2013) Testing the substrate-envelope hypothesis with designed pairs of compounds, *ACS Chem Biol* 8, 2433-2441.
100. Nalam, M. N., and Schiffer, C. A. (2008) New approaches to HIV protease inhibitor drug design II: testing the substrate envelope hypothesis to avoid drug resistance and discover robust inhibitors, *Curr Opin HIV AIDS* 3, 642-646.
101. Chusacultanachai, S., Thiensathit, P., Tarnchompoo, B., Sirawaraporn, W., and Yuthavong, Y. (2002) Novel antifolate resistant mutations of *Plasmodium falciparum* dihydrofolate reductase selected in *Escherichia coli*, *Mol Biochem Parasitol* 120, 61-72.
102. Japrun, D., Leartsakulpanich, U., Chusacultanachai, S., and Yuthavong, Y. (2007) Conflicting requirements of *Plasmodium falciparum* dihydrofolate reductase mutations conferring resistance to pyrimethamine-WR99210 combination, *Antimicrob Agents Chemother* 51, 4356-4360.
103. Kamchonwongpaisan, S., Vanichtanankul, J., Taweechai, S., Chitnumsub, P., and Yuthavong, Y. (2007) The role of tryptophan-48 in catalysis and binding of inhibitors of *Plasmodium falciparum* dihydrofolate reductase, *Int J Parasitol* 37, 787-793.



104. Maitarad, P., Kamchonwongpaisan, S., Vanichtanankul, J., Vilaivan, T., Yuthavong, Y., and Hannongbua, S. (2009) Interactions between cycloguanil derivatives and wild type and resistance-associated mutant Plasmodium falciparum dihydrofolate reductases, *J Comput Aided Mol Des* 23, 241-252.
105. Yuthavong, Y., Yuvaniyama, J., Chitnumsub, P., Vanichtanankul, J., Chusacultanachai, S., Tarnchompoo, B., Vilaivan, T., and Kamchonwongpaisan, S. (2005) Malarial (Plasmodium falciparum) dihydrofolate reductase-thymidylate synthase: structural basis for antifolate resistance and development of effective inhibitors, *Parasitology* 130, 249-259.
106. Lin, Y. C., Perryman, A. L., Olson, A. J., Torbett, B. E., Elder, J. H., and Stout, C. D. (2011) Structural basis for drug and substrate specificity exhibited by FIV encoding a chimeric FIV/HIV protease, *Acta Crystallogr D Biol Crystallogr* 67, 540-548.
107. Willett, P. (2006) Similarity-based virtual screening using 2D fingerprints, *Drug Discov Today* 11, 1046-1053.
108. Ballell, L., Bates, R. H., Young, R. J., Alvarez-Gomez, D., Alvarez-Ruiz, E., Barroso, V., Blanco, D., Crespo, B., Escribano, J., Gonzalez, R., Lozano, S., Huss, S., Santos-Villarejo, A., Martin-Plaza, J. J., Mendoza, A., Rebollo-Lopez, M. J., Remuinan-Blanco, M., Lavandera, J. L., Perez-Herran, E., Gamo-Benito, F. J., Garcia-Bustos, J. F., Barros, D., Castro, J. P., and Cammack, N. (2013) Fueling open-source drug discovery: 177 small-molecule leads against tuberculosis, *ChemMedChem* 8, 313-321.
109. Chessari, G., and Woodhead, A. J. (2009) From fragment to clinical candidate--a historical perspective, *Drug Discovery Today* 14, 668-675.
110. Hajduk, P. J., and Greer, J. (2007) A decade of fragment-based drug design: strategic advances and lessons learned, *Nat Rev Drug Discov* 6, 211-219.
111. Austin, C., Pettit, S. N., Magnolo, S. K., Sanvoisin, J., Chen, W., Wood, S. P., Freeman, L. D., Pengelly, R. J., and Hughes, D. E. (2012) Fragment screening using capillary electrophoresis (CEfrag) for hit identification of heat shock protein 90 ATPase inhibitors, *Journal of biomolecular screening* 17, 868-876.
112. Teotico, D. G., Babaoglu, K., Rocklin, G. J., Ferreira, R. S., Giannetti, A. M., and Shoichet, B. K. (2009) Docking for fragment inhibitors of AmpC  $\beta$ -lactamase, *Proceedings of the National Academy of Sciences* 106, 7455-7460.
113. Murray, C. W., Callaghan, O., Chessari, G., Cleasby, A., Congreve, M., Frederickson, M., Hartshorn, M. J., McMenamin, R., Patel, S., and Wallis, N. (2007) Application of fragment screening by X-ray crystallography to beta-secretase, *J Med Chem* 50, 1116-1123.

114. Chen, Y., and Shoichet, B. K. (2009) Molecular docking and ligand specificity in fragment-based inhibitor discovery, *Nat Chem Biol* 5, 358-364.
115. Shuker, S. B., Hajduk, P. J., Meadows, R. P., and Fesik, S. W. (1996) Discovering high-affinity ligands for proteins: SAR by NMR, *Science* 274, 1531-1534.
116. Li, H. J., Lai, C. T., Pan, P., Yu, W., Liu, N., Bommineni, G. R., Garcia-Diaz, M., Simmerling, C., and Tonge, P. J. (2014) A Structural and Energetic Model for the Slow-Onset Inhibition of the Mycobacterium tuberculosis Enoyl-ACP Reductase InhA, *ACS Chem Biol* 9, 986-993.
117. am Ende, C. W., Knudson, S. E., Liu, N., Childs, J., Sullivan, T. J., Boyne, M., Xu, H., Gegina, Y., Knudson, D. L., Johnson, F., Peloquin, C. A., Slayden, R. A., and Tonge, P. J. (2008) Synthesis and in vitro antimycobacterial activity of B-ring modified diaryl ether InhA inhibitors, *Bioorg Med Chem Lett* 18, 3029-3033.
118. England, K., am Ende, C., Lu, H., Sullivan, T. J., Marlenee, N. L., Bowen, R. A., Knudson, S. E., Knudson, D. L., Tonge, P. J., and Slayden, R. A. (2009) Substituted diphenyl ethers as a broad-spectrum platform for the development of chemotherapeutics for the treatment of tularaemia, *J Antimicrob Chemother* 64, 1052-1061.
119. Wu, J. L., Liu, J., and Cai, Z. (2010) Determination of triclosan metabolites by using in-source fragmentation from high-performance liquid chromatography/negative atmospheric pressure chemical ionization ion trap mass spectrometry, *Rapid Commun Mass Spectrom* 24, 1828-1834.
120. Wang, L. Q., Falany, C. N., and James, M. O. (2004) Triclosan as a substrate and inhibitor of 3'-phosphoadenosine 5'-phosphosulfate-sulfotransferase and UDP-glucuronosyl transferase in human liver fractions, *Drug metabolism and disposition: the biological fate of chemicals* 32, 1162-1169.
121. Bollag, G., Hirth, P., Tsai, J., Zhang, J., Ibrahim, P. N., Cho, H., Spevak, W., Zhang, C., Zhang, Y., Habets, G., Burton, E. A., Wong, B., Tsang, G., West, B. L., Powell, B., Shellooe, R., Marimuthu, A., Nguyen, H., Zhang, K. Y., Artis, D. R., Schlessinger, J., Su, F., Higgins, B., Iyer, R., D'Andrea, K., Koehler, A., Stumm, M., Lin, P. S., Lee, R. J., Grippo, J., Puzanov, I., Kim, K. B., Ribas, A., McArthur, G. A., Sosman, J. A., Chapman, P. B., Flaherty, K. T., Xu, X., Nathanson, K. L., and Nolop, K. (2010) Clinical efficacy of a RAF inhibitor needs broad target blockade in BRAF-mutant melanoma, *Nature* 467, 596-599.
122. de Kloe, G. E., Bailey, D., Leurs, R., and de Esch, I. J. (2009) Transforming fragments into candidates: small becomes big in medicinal chemistry, *Drug Discovery Today* 14, 630-646.
123. Congreve, M., Chessari, G., Tisi, D., and Woodhead, A. J. (2008) Recent developments in fragment-based drug discovery, *J Med Chem* 51, 3661-3680.

124. Teotico, D. G., Babaoglu, K., Rocklin, G. J., Ferreira, R. S., Giannetti, A. M., and Shoichet, B. K. (2009) Docking for fragment inhibitors of AmpC beta-lactamase, *Proceedings of the National Academy of Sciences of the United States of America* 106, 7455-7460.
125. Boyne, M. E., Sullivan, T. J., amEnde, C. W., Lu, H., Gruppo, V., Heaslip, D., Amin, A. G., Chatterjee, D., Lenaerts, A., Tonge, P. J., and Slayden, R. A. (2007) Targeting fatty acid biosynthesis for the development of novel chemotherapeutics against *Mycobacterium tuberculosis*: evaluation of A-ring-modified diphenyl ethers as high-affinity InhA inhibitors, *Antimicrob Agents Chemother* 51, 3562-3567.
126. Freundlich, J. S., Wang, F., Vilcheze, C., Gulten, G., Langley, R., Schiehsler, G. A., Jacobus, D. P., Jacobs, W. R., Jr., and Sacchettini, J. C. (2009) Triclosan derivatives: towards potent inhibitors of drug-sensitive and drug-resistant *Mycobacterium tuberculosis*, *ChemMedChem* 4, 241-248.
127. Kuo, M. R., Morbidoni, H. R., Alland, D., Sneddon, S. F., Gourlie, B. B., Staveski, M. M., Leonard, M., Gregory, J. S., Janjigian, A. D., Yee, C., Musser, J. M., Kreiswirth, B., Iwamoto, H., Perozzo, R., Jacobs, W. R., Jr., Sacchettini, J. C., and Fidock, D. A. (2003) Targeting tuberculosis and malaria through inhibition of Enoyl reductase: compound activity and structural data, *J Biol Chem* 278, 20851-20859.
128. Krasinski, A., Radic, Z., Manetsch, R., Raushel, J., Taylor, P., Sharpless, K. B., and Kolb, H. C. (2005) In situ selection of lead compounds by click chemistry: target-guided optimization of acetylcholinesterase inhibitors, *J Am Chem Soc* 127, 6686-6692.
129. Mamidyala, S. K., and Finn, M. G. (2010) In situ click chemistry: probing the binding landscapes of biological molecules, *Chem Soc Rev* 39, 1252-1261.
130. Manetsch, R., Krasinski, A., Radic, Z., Raushel, J., Taylor, P., Sharpless, K. B., and Kolb, H. C. (2004) In situ click chemistry: enzyme inhibitors made to their own specifications, *J Am Chem Soc* 126, 12809-12818.
131. Sharpless, K. B., and Manetsch, R. (2006) In situ click chemistry: a powerful means for lead discovery, *Expert Opin Drug Discov* 1, 525-538.
132. Lu, H., England, K., am Ende, C., Truglio, J. J., Luckner, S., Reddy, B. G., Marlenee, N. L., Knudson, S. E., Knudson, D. L., Bowen, R. A., Kisker, C., Slayden, R. A., and Tonge, P. J. (2009) Slow-onset inhibition of the FabI enoyl reductase from *francisella tularensis*: residence time and in vivo activity, *ACS Chem Biol* 4, 221-231.
133. Lu, H., and Tonge, P. J. (2010) Drug-target residence time: critical information for lead optimization, *Curr Opin Chem Biol* 14, 467-474.

134. Baell, J. B., and Holloway, G. A. (2010) New substructure filters for removal of pan assay interference compounds (PAINS) from screening libraries and for their exclusion in bioassays, *J Med Chem* 53, 2719-2740.
135. Manjunatha, U. H., Boshoff, H., Dowd, C. S., Zhang, L., Albert, T. J., Norton, J. E., Daniels, L., Dick, T., Pang, S. S., and Barry, C. E., 3rd. (2006) Identification of a nitroimidazo-oxazine-specific protein involved in PA-824 resistance in *Mycobacterium tuberculosis*, *Proc Natl Acad Sci U S A* 103, 431-436.
136. Gutacker, M. M., Mathema, B., Soini, H., Shashkina, E., Kreiswirth, B. N., Graviss, E. A., and Musser, J. M. (2006) Single-nucleotide polymorphism-based population genetic analysis of *Mycobacterium tuberculosis* strains from 4 geographic sites, *J Infect Dis* 193, 121-128.
137. Schiebel, J., Chang, A., Shah, S., Lu, Y., Liu, L., Pan, P., Hirschbeck, M. W., Tareilus, M., Eltschkner, S., Yu, W., Cummings, J. E., Knudson, S. E., Bommineni, G. R., Walker, S. G., Slayden, R. A., Sotriffer, C. A., Tonge, P. J., and Kisker, C. (2014) Rational design of broad spectrum antibacterial activity based on a clinically relevant enoyl-acyl carrier protein (ACP) reductase inhibitor, *J Biol Chem* 289, 15987-16005.
138. Pan, P., Knudson, S. E., Bommineni, G. R., Li, H. J., Lai, C. T., Liu, N., Garcia-Diaz, M., Simmerling, C., Patil, S. S., Slayden, R. A., and Tonge, P. J. (2014) Time-dependent diaryl ether inhibitors of InhA: structure-activity relationship studies of enzyme inhibition, antibacterial activity, and in vivo efficacy, *ChemMedChem* 9, 776-791.
139. Rozwarski, D. A., Vilcheze, C., Sugantino, M., Bittman, R., and Sacchettini, J. C. (1999) Crystal structure of the *Mycobacterium tuberculosis* enoyl-ACP reductase, InhA, in complex with NAD<sup>+</sup> and a C16 fatty acyl substrate, *J Biol Chem* 274, 15582-15589.
140. Sullivan, T. J., Truglio, J. J., Boyne, M. E., Novichenok, P., Zhang, X., Stratton, C. F., Li, H. J., Kaur, T., Amin, A., Johnson, F., Slayden, R. A., Kisker, C., and Tonge, P. J. (2006) High affinity InhA inhibitors with activity against drug-resistant strains of *Mycobacterium tuberculosis*, *ACS Chem Biol* 1, 43-53.
141. Hartkoorn, R. C., Pojer, F., Read, J. A., Gingell, H., Neres, J., Horlacher, O. P., Altmann, K. H., and Cole, S. T. (2014) Pyridomycin bridges the NADH- and substrate-binding pockets of the enoyl reductase InhA, *Nat Chem Biol* 10, 96-98.
142. Payne, D. J., Warren, P. V., Holmes, D. J., Ji, Y., and Lonsdale, J. T. (2001) Bacterial fatty-acid biosynthesis: a genomics-driven target for antibacterial drug discovery, *Drug Discov Today* 6, 537-544.
143. Hogenauer, G., and Woisetschlager, M. (1981) A diazaborine derivative inhibits lipopolysaccharide biosynthesis, *Nature* 293, 662-664.

144. Levy, C. W., Baldock, C., Wallace, A. J., Sedelnikova, S., Viner, R. C., Clough, J. M., Stuitje, A. R., Slabas, A. R., Rice, D. W., and Rafferty, J. B. (2001) A study of the structure-activity relationship for diazaborine inhibition of *Escherichia coli* enoyl-ACP reductase, *J Mol Biol* 309, 171-180.

## Chapter 6

1. Wiersinga, W. J., van der Poll, T., White, N. J., Day, N. P., and Peacock, S. J. (2006) Melioidosis: insights into the pathogenicity of *Burkholderia pseudomallei*, *Nat Rev Microbiol* 4, 272-282.
2. White, N. J. (2003) Melioidosis, *Lancet* 361, 1715-1722.
3. Cheng, A. C., and Currie, B. J. (2005) Melioidosis: Epidemiology, pathophysiology, and management, *Clin Microbiol Rev* 18, 383-+.
4. Gilad, J., Harary, I., Dushnitsky, T., Schwartz, D., and Amsalem, Y. (2007) *Burkholderia mallei* and *Burkholderia pseudomallei* as bioterrorism agents: National aspects of emergency preparedness, *Israel Med Assoc J* 9, 499-503.
5. Rotz, L. D., Khan, A. S., Lillibrige, S. R., Ostroff, S. M., and Hughes, J. M. (2002) Public health assessment of potential biological terrorism agents, *Emerg Infect Dis* 8, 225-230.
6. Gilad, J., Harary, I., Dushnitsky, T., Schwartz, D., and Amsalem, Y. (2007) *Burkholderia mallei* and *Burkholderia pseudomallei* as bioterrorism agents: national aspects of emergency preparedness, *Isr Med Assoc J* 9, 499-503.
7. Baldock, C., Rafferty, J. B., Sedelnikova, S. E., Baker, P. J., Stuitje, A. R., Slabas, A. R., Hawkes, T. R., and Rice, D. W. (1996) A mechanism of drug action revealed by structural studies of enoyl reductase, *Science* 274, 2107-2110.
8. Lu, H., and Tonge, P. J. (2008) Inhibitors of FabI, an enzyme drug target in the bacterial fatty acid biosynthesis pathway, *Acc Chem Res* 41, 11-20.
9. Heath, R. J., and Rock, C. O. (1995) Enoyl-acyl carrier protein reductase (fabI) plays a determinant role in completing cycles of fatty acid elongation in *Escherichia coli*, *J Biol Chem* 270, 26538-26542.
10. Massengo-Tiasse, R. P., and Cronan, J. E. (2009) Diversity in enoyl-acyl carrier protein reductases, *Cell Mol Life Sci* 66, 1507-1517.
11. Parikh, S., Moynihan, D. P., Xiao, G., and Tonge, P. J. (1999) Roles of tyrosine 158 and lysine 165 in the catalytic mechanism of InhA, the enoyl-ACP reductase from *Mycobacterium tuberculosis*, *Biochemistry* 38, 13623-13634.
12. Massengo-Tiasse, R. P., and Cronan, J. E. (2008) *Vibrio cholerae* FabV defines a new class of enoyl-acyl carrier protein reductase, *J Biol Chem* 283, 1308-1316.
13. Marrakchi, H., Dewolf, W. E., Jr., Quinn, C., West, J., Polizzi, B. J., So, C. Y., Holmes, D. J., Reed, S. L., Heath, R. J., Payne, D. J., Rock, C. O., and Wallis, N. G. (2003)

Characterization of *Streptococcus pneumoniae* enoyl-(acyl-carrier protein) reductase (FabK), *Biochem J* 370, 1055-1062.

14. Heath, R. J., Su, N., Murphy, C. K., and Rock, C. O. (2000) The enoyl-[acyl-carrier-protein] reductases FabI and FabL from *Bacillus subtilis*, *J Biol Chem* 275, 40128-40133.
15. Liu, N., Cummings, J. E., England, K., Slayden, R. A., and Tonge, P. J. (2011) Mechanism and inhibition of the FabI enoyl-ACP reductase from *Burkholderia pseudomallei*, *J Antimicrob Chemother.* 66, 564-573.
16. Cummings, J. E., Beaupre, A. J., Knudson, S. E., Liu, N., Yu, W., Neckles, C., Wang, H., Khanna, A., Bommineni, G. R., Trunck, L. A., Schweizer, H. P., Tonge, P. J., and Slayden, R. A. (2014) Substituted diphenyl ethers as a novel chemotherapeutic platform against *Burkholderia pseudomallei*, *Antimicrob Agents Chemother* 58, 1646-1651.
17. Copeland, R. A., Pompliano, D. L., and Meek, T. D. (2006) Drug-target residence time and its implications for lead optimization, *Nat Rev Drug Discov* 5, 730-739.
18. Tummino, P. J., and Copeland, R. A. (2008) Residence time of receptor-ligand complexes and its effect on biological function, *Biochemistry* 47, 5481-5492.
19. Lu, H., and Tonge, P. J. (2010) Drug-target residence time: critical information for lead optimization, *Curr Opin Chem Biol* 14, 467-474.
20. Copeland, R. A., Pompliano, D. L., and Meek, T. D. (2006) Drug-target residence time and its implications for lead optimization, *Nature reviews. Drug discovery* 5, 730-739.
21. Zhang, R., and Monsma, F. (2009) The importance of drug-target residence time, *Current opinion in drug discovery & development* 12, 488-496.
22. Tummino, P. J., and Copeland, R. A. (2008) Residence time of receptor-ligand complexes and its effect on biological function, *Biochemistry* 47, 5481-5492.
23. Halford, S. E. (1971) *Escherichia coli* alkaline phosphatase. An analysis of transient kinetics, *Biochem J* 125, 319-327.
24. Silver, L. L. (2011) Challenges of antibacterial discovery, *Clin Microbiol Rev* 24, 71-109.
25. Gerusz, V., Denis, A., Faivre, F., Bonvin, Y., Oxoby, M., Briet, S., LeFralliec, G., Oliveira, C., Desroy, N., Raymond, C., Peltier, L., Moreau, F., Escaich, S., Vongsouthi, V., Floquet, S., Drocourt, E., Walton, A., Prouvensier, L., Saccomani, M., Durant, L., Genevard, J. M., Sam-Sambo, V., and Soulama-Mouze, C. (2012) From triclosan toward the clinic: discovery of nonbiocidal, potent FabI inhibitors for the treatment of resistant bacteria, *J Med Chem* 55, 9914-9928.

26. Escaich, S., Prouvensier, L., Saccomani, M., Durant, L., Oxoby, M., Gerusz, V., Moreau, F., Vongsouthi, V., Maher, K., Morrissey, I., and Soulama-Mouze, C. (2011) The MUT056399 inhibitor of FabI is a new antistaphylococcal compound, *Antimicrob Agents Chemother* 55, 4692-4697.
27. Parikh, S. L., Xiao, G., and Tonge, P. J. (2000) Inhibition of InhA, the enoyl reductase from *Mycobacterium tuberculosis*, by triclosan and isoniazid, *Biochemistry* 39, 7645-7650.
28. Yu, W., Neckles, C., Chang, A., Bommineni, G. R., Spagnuolo, L., Zhang, Z., Liu, N., Lai, C., Truglio, J., and Tonge, P. J. (2015) A [P]NAD-based method to identify and quantitate long residence time enoyl-acyl carrier protein reductase inhibitors, *Anal Biochem* 474C, 40-49.
29. Pan, P., Knudson, S. E., Bommineni, G. R., Li, H. J., Lai, C. T., Liu, N., Garcia-Diaz, M., Simmerling, C., Patil, S. S., Slayden, R. A., and Tonge, P. J. (2014) Time-dependent diaryl ether inhibitors of InhA: structure-activity relationship studies of enzyme inhibition, antibacterial activity, and in vivo efficacy, *ChemMedChem* 9, 776-791.
30. Chang, A., Schiebel, J., Yu, W. X., Bommineni, G. R., Pan, P., Baxter, M. V., Khanna, A., Sottriffer, C. A., Kisker, C., and Tonge, P. J. (2013) Rational Optimization of Drug-Target Residence Time: Insights from Inhibitor Binding to the *Staphylococcus aureus* FabI Enzyme-Product Complex, *Biochemistry* 52, 4217-4228.
31. Copeland, R. A. (2005) Evaluation of enzyme inhibitors in drug discovery. A guide for medicinal chemists and pharmacologists, *Methods of biochemical analysis* 46, 1-265.
32. Ward, W. H. J., Holdgate, G. A., Rowsell, S., McLean, E. G., Pauptit, R. A., Clayton, E., Nichols, W. W., Colls, J. G., Minshull, C. A., Jude, D. A., Mistry, A., Timms, D., Camble, R., Hales, N. J., Britton, C. J., and Taylor, I. W. F. (1999) Kinetic and structural characteristics of the inhibition of enoyl (acyl carrier protein) reductase by triclosan, *Biochemistry* 38, 12514-12525.
33. Kapoor, M., Reddy, C. C., Krishnasastri, M. V., Surolia, N., and Surolia, A. (2004) Slow-tight-binding inhibition of enoyl-acyl carrier protein reductase from *Plasmodium falciparum* by triclosan, *Biochem J* 381, 719-724.
34. Lu, H., England, K., Ende, C. A., Truglio, J. J., Luckner, S., Reddy, B. G., Marlenee, N. L., Knudson, S. E., Knudson, D. L., Bowen, R. A., Kisker, C., Slayden, R. A., and Tonge, P. J. (2009) Slow-Onset Inhibition of the FabI Enoyl Reductase from *Francisella tularensis*: Residence Time and in Vivo Activity, *Acs Chem Biol* 4, 221-231.
35. Mima, T., and Schweizer, H. P. (2010) The BpeAB-OprB efflux pump of *Burkholderia pseudomallei* 1026b does not play a role in quorum sensing, virulence factor production, or extrusion of aminoglycosides but is a broad-spectrum drug efflux system, *Antimicrob Agents Chemother* 54, 3113-3120.



36. Chang, A. (2013) *S. aureus* FabI: Linking Catalysis, Inhibition and Cellular Effects, Dissertation.
37. Liu, N., Cummings, J. E., England, K., Slayden, R. A., and Tonge, P. J. (2011) Mechanism and inhibition of the FabI enoyl-ACP reductase from *Burkholderia pseudomallei*, *J Antimicrob Chemother* 66, 564-573.
38. Tian, G., Paschetto, K. A., Gharahdaghi, F., Gordon, E., Wilkins, D. E., Luo, X., and Scott, C. W. (2011) Mechanism of inhibition of fatty acid amide hydrolase by sulfonamide-containing benzothiazoles: long residence time derived from increased kinetic barrier and not exclusively from thermodynamic potency, *Biochemistry* 50, 6867-6878.
39. Chang, A., Schiebel, J., Yu, W., Bommineni, G. R., Pan, P., Baxter, M. V., Khanna, A., Sotriffer, C. A., Kisker, C., and Tonge, P. J. (2013) Rational Optimization of Drug-Target Residence Time: Insights from Inhibitor Binding to the *Staphylococcus aureus* FabI Enzyme-Product Complex, *Biochemistry* 52, 4217-4228.
40. Zierkiewicz, W. M., Danuta; and Hobza, Pavel (2004) The barrier to internal rotation and electronic effects in para-halogenophenols: theoretical study, *Chemical Physics Letters* 386, 95-100.
41. Zierkiewicz, W. M., Danuta; Czarnik-Matusiewicz, Bogusłwa; and Rospenk, Maria (2003) Molecular Structure and Infrared Spectra of 4-Fluorophenol: A Combined Theoretical and Spectroscopic Study, *J. Phys. Chem.* 107, 4547-4554.
42. Wang, L. Q., Falany, C. N., and James, M. O. (2004) Triclosan as a substrate and inhibitor of 3'-phosphoadenosine-5'-phosphosulfate-sulfotransferase and UDP-glucuronosyl transferase in human liver fractions, *Drug Metab Dispos* 32, 1162-1169.